

# **Drug Delivery Systems for Glioblastoma Therapy**

**By**

**Mohammad Norouzi**

A Thesis Submitted to the Faculty of Graduate Studies of  
The University of Manitoba  
in partial fulfillment of the requirements for the degree of

**DOCTOR OF PHILOSOPHY**

Graduate Program of Biomedical Engineering  
University of Manitoba  
Winnipeg, MB, Canada  
Copyright © 2020 by Mohammad Norouzi

## ABSTRACT

Many chemotherapeutics suffer from an inability to penetrate the blood-brain barrier (BBB) and to reach the target site within the brain at the therapeutically levels to treat Gliomas. In the present study, various drug delivery systems were developed and characterized with the goal of overcoming the BBB and delivering chemotherapeutics (i.e. doxorubicin, and salinomycin) for the treatment of glioblastoma multiforme (GBM).

In the first scenario, biocompatible magnetic iron oxide nanoparticles (IONPs) with negative and positive charge coatings were developed as drug delivery systems of doxorubicin and salinomycin, respectively. The drug-loaded IONPs exhibited a gradual release of both doxorubicin and salinomycin within 4 days and were found to be effective in ROS induction, and activation of both caspases and tumor suppressors (i.e. p53, MEG3 and GAS5) in human GBM cells. Utilizing an *in vitro* BBB-GBM co-culture model, the permeability of both salinomycin- and doxorubicin-loaded IONPs through the confluent cell monolayer was significantly enhanced using an external magnetic field and transient enhanced permeability of the BBB (using either hyperosmotic mannitol or a cyclic cadherin binding peptide).

In the second scenario, injectable thermosensitive hydrogels were developed as local drug delivery systems of salinomycin at the tumor site. The drug-loaded Pluronic released salinomycin over a week and decreased GBM cell viability by ca. 90% within 48 hours of treatment, which was significantly more effective than that of free salinomycin (cell viability reduction of ca. 50%). Animal studies in subcutaneous U251 xenografted nude mice also revealed that salinomycin -

loaded Pluronic reduced the tumor growth compared to the free salinomycin- and PBS-treated mice by 2-fold and 2.6-fold, respectively within 11 days.

Taken together, it is envisaged that the developed drug-loaded IONPs in combination with an external magnetic field and transient enhanced permeability of the BBB can provide an efficient approach to overcome the limited BBB permeability and deliver chemotherapeutics at the tumor site within the brain. Also, the salinomycin-loaded Pluronic hydrogel provides a local drug delivery approach to treat brain tumors by which not only the BBB is bypassed, but also the systemic drug exposure and toxicity are diminished and high doses of the chemotherapeutic can locally be administered at the tumor site.

## **Acknowledgment**

First and foremost, I would like to express my sincere gratitude to my supervisor Prof. Donald W. Miller for all his great supports during my Ph.D. study. I also acknowledge him for financial support of me. This project was not possible without his guidance and encouragement.

Also, I would like to thank my thesis committee: Prof. Zahra Moussavi, Prof. Xiaochen Gu, Dr. Rodrigo Franca and Prof. Jayanth Panyam for their insightful comments and support.

I thank Prof. James A. Thliveris for taking the TEM images, Prof. Thomas Klonisch for providing the GBM cells, Prof. Teruna J. Siahaan and Mr. Brian M. Kopec for providing the Cadherin peptide, Dr. Marzieh Ebrahimi and Mr. Javad Firouzi for their contribution in animal study, Dr. Niloufar Sodeifi for pathological analyses and Dr. Lida Fallah for consultation in statistical analyses. I also thank Dr. Vinith Yathindranath for contribution in the synthesis, formulation and physicochemical characterization of the iron oxide nanoparticles.

I extend my gratitude to our lab members Wei Xiong, Eman Alraddadi, and Marlyn Laksitorini.

Last but not least, I would like to thank my family and friends for their great supports.

This research was supported by grants from the Canadian Institutes of Health Research and Natural Science and Engineering Research Council – Canada.

## **Dedication**

*This work is dedicated to  
my family*

# Table of Contents

## 1. Chapter 1: Introduction

1.1. Rationale	2
1.2. Objectives	2
1.3. Organizations	4
1.4. Literature Review: Iron Oxide Nanoparticles in Glioma Theranostics	5
1.4.1. Introduction	5
1.4.2. Physiochemical Properties of IONPs	8
1.4.3. How IONPs can overcome the BBB	12
1.4.4. IONPs Applications in Glioma Imaging	17
1.4.5. IONPs Applications as Drug Delivery System in Glioma Therapy	27
1.4.6. Magnetic Hyperthermia effect of IONPs	39
1.4.7. Concluding Remarks and Future Prospects	45
1.4.8. References	50

## 2. Chapter 2

### **Doxorubicin-loaded Iron Oxide Nanoparticles for Glioblastoma Therapy**

2.1. Introduction	63
2.2. Materials and methods	66
2.3. Results and discussion	75
2.4. Conclusion	98
2.5. References	100

### **3. Chapter 3**

#### **Salinomycin-loaded Iron Oxide Nanoparticles for Glioblastoma Therapy**

3.1. Introduction	109
3.2. Materials and methods	112
3.3. Results and discussion	120
3.4. Conclusion	138
3.5. References	139

### **4. Chapter 4**

#### **Salinomycin-loaded Injectable Thermosensitive Hydrogels for Glioblastoma Therapy**

4.1. Introduction	146
4.2. Materials and methods	148
4.3. Results and discussion	154
4.4. Conclusion	172
4.5. References	173

### **5. Chapter 5**

#### **Conclusion and Future Directions**

5.1. Conclusion	178
5.2. Future direction	184
5.3. References	186

## List of Tables

Table 2.1. Sequences of human primers	73
Table 3.1. Sequences of human primers	119
Table 4.1. Sequences of human primers	153
Table 4.2. $n$ and $k$ values for salinomycin release from the hydrogels	156

## List of Figures

Fig. 1.1. A: The line graph exhibits the average diameter changes of Ferumoxytol enhancement over time (*solid line*) in comparison to that of Gd (*dashed*) and T2-weighted signal abnormalities (*dashed-dotted*). MRI images of (B) Gd T1-weighted, (C) T2-weighted, and (D-H) post-Ferumoxytol T1-weighted MRI images at five time points (*D*, 4–6 h; *E*, 6–20 h; *F*, 24–28 h; *G*, 48–52 h; *H*, > 72 h). Reproduced with permission from Ref [1]. 21

Fig. 1.2. (a) MRI of U87MG tumor-bearing mice injected with either RGD–TPIONPs or TPIONPs before and 4 h-post-injection. Only RGD–TPIONPs could specifically home to the tumor vicinity and induced significant T2 reduction. (b) Optical imaging of U87MG tumor-bearing mice injected with either RGD–TPIONPs or TPIONPs at 4 and 24 h-post-administration. The RGD–TPIONPs injected mice exhibited desirable contrast at tumor vicinity within 24 h. (c) *Ex vivo* NIRF imaging of major organs harvested from mice got injection of either TPIONP or RGD–TPIONP. Higher tumor contrast was seen in RGD–TPIONP injected, while distribution of both nanoparticles in other organs was comparable. “TPIONPs” is considered as the synonym of IONPs. Reproduced with permission from Ref [2]. 25

Fig. 1.3. Distribution of NF-SIONs in the brain tumor region (A-C) and non-tumor region (D-F), by immunofluorescence staining, 8 h post-injection. The samples were stained with two monoclonal antibodies (mAbs; green and red) against GFAP (A,C,D and F, astrocyte), CD11b (A,B,D and E, monocytes/macrophages), and Iba1(C and F, microglia). In comparison to the non-tumoral region, macrophages and microglial cells extensively appeared in the tumor region, while the nanoparticles-binding cells were considerably overlapped with tumor-associated macrophages/microglia (CD11b+ or Iba-1+ cells), albeit not with astrocytes (GFAP+ cells). Blue and magenta signals indicate the location of cell nucleus and NF-SIONs, respectively. White circles demonstrate co-localization of tumor-associated macrophages and NF-SIONs. Scale bar: 50  $\mu\text{m}$  ( $\times 40$ ). Reproduced with permission from Ref [3]. 26

Fig. 1.4. (a) transporting efficiency across BBB *in vitro* at 4 h; (b) *in vivo* distribution of the nanoparticles after injection via tail vein at 4 h. The dissected brains showed a tendency of the NP accumulation as follows: MNP/T7-PLGA NPs + MAG > MNP/T7-PLGA NPs > MNP/PLGA NPs + MAG > MNP/PLGA NPs. (c) overall survival of glioma-bearing mice (n = 8). Reproduced with permission from Ref [4]. 36

Fig. 1.5. (a) Representative micro SPECT/CT images of GBM tumor-bearing mice. Distribution of  $^{99\text{mTc}}$ -TMZ shows rapid clearance from the brain. Distribution of  $^{99\text{mTc}}$ -STAT exhibits a significantly extended and localized retention at the tumor vicinity compared to  $^{99\text{mTc}}$ -STAP.  $^{99\text{mTc}}$ -STT demonstrates minimal uptake at the tumor site, indicating the necessity of anti-nestin antibody as a targeting moiety. (b) images of GBM tumor-bearing mice; a rapid increase in intracerebral tumor volume in the untreated group of animals (control) is observed, while the animals treated with STAT exhibited a significantly greater regression in tumor volume compared to TMZ and STAP-treated animals over a period of 21 days. (c) graph illustrating the tumor regression volume post-treatment with TMZ, STAT and STAP against untreated control. The STAT-treated animals demonstrated better intracerebral tumor regression compared to TMZ treated animals. Reproduced partially with permission from Ref [5]. 38

Fig. 1.6. (a) MRI of tumors in C6 glioma-bearing rats. (b) tumor volumes upon treatment. (The relative tumor volume i.e. day 7 vs day 28 in saline, DOX, DOX@Ps 80-SPIONs, and DOX@Ps 80-SPIONs with an MF were 69.78, 60.39, 50.46 and 0.9, respectively. (c) cumulative survival of animals upon treatment. The animal in saline, DOX, DOX@Ps 80-SPIONs, and DOX@Ps 80-SPIONs with an MF showed 17.8, 32.4, 38.5, and 79.2 days of survival, respectively. Reproduced with permission from Ref [6].

40

Fig. 1.7. (A) intraoperative picture of NanoPaste® application onto the resection cavity wall. (B) representative CT scans of a patient prior (left side) and post-thermotherapy (right side) with remarkable edema around nanoparticle deposits. (C) Representative pictures from a patient demonstrating enhanced Caspase-3 and HSP70 expression after treatment. (D) Representative pictures of immunohistochemical staining. They demonstrate a significant infiltration of CD3+, CD8+ and CD68+ cells after intracavitary thermotherapy, while the pre-treatment samples do not exhibit T-cell immune cell infiltrates (magnification  $\times 200$ ). Reproduced with permission from Ref [7].

42

Fig. 2.1. characterization of nanoparticles: (a) photographs of EDT-IONP (left) and DOX- EDT-IONP (right) solutions in PBS; TEM images of (b) EDT-IONPs, and (c) DOX- EDT-IONPs; (d) histogram of EDT-IONP size distribution from 100 measurements; (e) FTIR spectrum of EDT-IONP, (f) release of DOX from the DOX-EDT-IONPs in pH 7.4 and 4.5.

76

Fig. 2.2. Biocompatibility of EDT-IONPs on b.End3, MDCK-MDR and U251 cell lines after 48 hour treatment using MTT assay (n=5). The Y-axis represents cell viability compared to the control.

79

Fig. 2.3. Uptake of EDT-IONPs and DOX-EDT-IONPs by (a) b.End 3, (b) U251, and (c) MDCK-MDR after 4-hour treatment. (d) uptake of DOX by U251 cells treated with either DOX, DOX-EDT-IONPs, or DOX-EDT-IONPs + Magnet after 2 h. \* indicates a significant difference compared to DOX at  $p < 0.05$ . Data is presented as mean  $\pm$  S.D, and  $n = 3$  (three replications). IONPs and DOX-IONPs represent for EDT-IONPs and DOX-EDT-IONPs.

81

Fig. 2.4. TEM images of nanoparticles uptake by U251 cells cell after 4 h of the treatment, (a) EDT-IONPs and (b) DOX-EDT-IONPs.

82

Fig. 2.5. Cytotoxicity assessment of various concentrations of DOX and DOX-EDT-IONPs (250, 500 and 1  $\mu\text{g/mL}$ ) on U251 after 48 h treatment. \* indicates a significant difference at  $p < 0.05$ . Data is presented as mean  $\pm$  S.D, and  $n=6$ . The Y-axis represents cell viability compared to the control. IONPs and DOX-IONPs represent for EDT-IONPs and DOX-EDT-IONPs.

84

Fig. 2.6. Flow cytometer analysis for cell apoptosis/necrosis of U251 upon 48-hour treatment, stained with Annexin V-FITC and PI. (a) Control, (b) EDT-IONPs (c) DOX, and (d) DOX-EDT-IONPs. (Q4) demonstrates Live, (Q3) early apoptotic, (Q2) late apoptotic and (Q1) necrotic cells.

85

Fig. 2.7. Flow cytometer analysis for cell proliferation assay of carboxyfluorescein succinimidyl ester (CFSE)-labelled U251 upon treatment with EDT-IONPs, DOX and DOX-EDT-IONPs. (a) CFSE flow cytometry graph, and (b) the relative cell proliferation inhibition calculated by (mean

CFSE control/mean CFSE treated). \* shows a significant difference compared to the control group at  $p < 0.05$ . IONPs and DOX-IONPs represent for EDT-IONPs and DOX-EDT-IONPs. 86

Fig. 2.8. Fluorescence microscopy images of U251 with or without treatment after 48 h. Red, blue and green fluorescence colours represent Alexa Fluor@ 488 phalloidin-stained F-actin, DAPI-stained cell nuclei, and  $\gamma$ -H2AX, a marker of DNA double-strand breaks, respectively. IONPs and DOX-IONPs represent for EDT-IONPs and DOX-EDT-IONPs. 87

Fig. 2.9. ROS induction by EDT-IONPs, DOX or DOX-EDT-IONPs in U251 at different time-points. \* indicates a significant difference compared to the control group at  $p < 0.05$ . Data is presented as mean  $\pm$ S.D, and  $n = 5$ . IONPs and DOX-IONPs represent for EDT-IONPs and DOX-EDT-IONPs. 90

Fig. 2.10. Relative gene expression of U251 cell upon treatment with either EDT-IONPs, DOX or DOX-EDT-IONPs for 48 h. \* indicates a significance difference compared to the control group, and \*\* compared to DOX-treated cells at  $p < 0.05$ . Data is presented as mean  $\pm$ S.D, and  $n=5$ . IONPs and DOX-IONPs represent for EDT-IONPs and DOX-EDT-IONPs. 91

Fig. 2.11. Anti-cancer efficacy of DOX-EDT-IONPs compared to the free DOX on an MDCK-MDR-GBM model *in vitro*. (a) DOX permeability across the MDCK-MDR monolayer with or without IONPs in the presence or absence of magnet and ADTC5 (b) cytotoxicity of each formulation on U251 cells after penetrating the monolayer. (c) DOX-IONPs permeability across the MDCK-MDR monolayer with or without magnet and ADTC5. \* indicates a significant difference at  $p < 0.05$  with the other treated groups. Data is presented as mean  $\pm$ S.D, and  $n=3$ . IONPs and DOX-IONPs represent for EDT-IONPs and DOX-EDT-IONPs. 98

Fig. S 2.1. IC50 curve of DOX on U251 cells. The cells were treated with DOX solution in cell culture media for 48 h and the MTT assay was then conducted. The IC50 of DOX was found to be ca. 300 ng/mL. 106

Fig. S 2.2. IRDye permeability across the MDCK-MDR monolayer upon 4-h treatment with peptide or mannitol within the uptake study. \* indicates a significance difference compared to the control (no disrupting agent) and cadherin peptide groups ( $p < 0.01$ ). 106

Fig. 3.1. PEI-PEG-IONPs characterization: (a) TEM images, (b) size distribution histogram, (c) FTIR spectrum, (d) release of salinomycin from the nanoparticles in pHs 7.4 (physiological pH), and 4.5 (pH of acidic intracellular compartments such as endosomes). 121

Fig. 3.2. Biocompatibility of different concentrations of PEI-PEG-IONPs on (a) bEnd.3 and (b) U251 cell lines after 48 h treatment using MTT assay ( $n=5$ ). The Y-axis represents cell viability compared to the control. 124

Fig. 3.3. Uptake of IONPs and Sali-IONPs by (a) b.End 3 and (b) U251 after 4 h treatment. \* indicates a significant difference at  $p < 0.05$  between the specified groups. Data was presented as mean  $\pm$ S.D, and  $n = 3$ . 126

Fig. 3.4. TEM images of a) IONPs and b) Sali-IONPs uptake by U251 cell after 4 h of the treatment. 126

Fig. 3.5. Cytotoxicity evaluation of salinomycin and Sali-IONPs on U251 after 48 h treatment. \* indicates a significant difference compared to the control group at  $p < 0.05$ . Data was presented as mean  $\pm$ S.D, and  $n = 6$ . 128

Fig. 3.6. Cell apoptosis/necrosis of U251 upon treatment, stained with Annexin V-FITC and PI. (a) Control, (b) IONPs (c) salinomycin, and (d) Sali-IONPs. (Q4) shows live, (Q3) early apoptotic, (Q2) late apoptotic and (Q1) necrotic cells. 129

Fig. 3.7. Cell proliferation analysis of CFSE-labelled U251 upon treatment with IONPs, salinomycin and Sali-IONPs. (a) CFSE flow cytometry graph, and (b) the relative cell proliferation inhibition by (mean CFSE control/mean CFSE treated). \* indicates a significant difference compared to the control group at  $p < 0.05$ . 130

Fig. 3.8. Fluorescence microscopy images of U251 treated with either salinomycin or Sali-IONPs after 48 h of the treatment. Red and blue fluorescence colours represent Alexa Fluor@ 488 phalloidin-stained F-actin and DAPI-stained cell nuclei, respectively. 130

Fig. 3.9. ROS generation in U251 treated with either IONPs, salinomycin or Sali-IONPs at different time-points. \* indicates a significant difference compared to the control group at  $p < 0.05$ . Data was presented as mean  $\pm$ S.D, and  $n = 5$ . 131

Fig. 3.10. Relative gene expression of U251 cell treated with either IONPs, salinomycin or Sali-IONPs after 48 h of the treatment. \* and \*\* indicate a significant difference compared to the control and salinomycin groups, respectively at  $p < 0.05$ . Data was presented as mean  $\pm$ S.D, and  $n = 5$ . 132

Fig. 3.11. Evaluation of anti-cancer efficacy of Sali-IONPs compared to the free salinomycin on a BBB-brain tumor model *in vitro*. (a) Sali-IONPs permeability across the bEnd.3 monolayer with or without magnet and mannitol (b) cytotoxicity of each formulation on U251 cells after penetrating the bEnd.3 monolayer. \* indicates a significant difference at  $p < 0.05$  with the other treated groups. Data was presented as mean  $\pm$ S.D, and  $n = 3$ . 137

Fig. 4.1. (a) hydrogel appearances at 4°C and 37°C (20 %wt solution in D.I water); (b) *in vitro* degradation profile as a function of incubation time in PBS (pH 7.4, 37°C). 155

Fig. 4.2. (a) *in vitro* release profile of salinomycin from Pluronic and PLGA-PEG-PLGA at pH 7.4; (b) mechanistic analysis of salinomycin release according to Korsmeyer–Peppas equation. 156

Fig. 4.3. Biocompatibility of Pluronic (a) and PLGA-PEG-PLGA (b) on U251 GBM, and ANA-1 macrophage cell lines. (c) cytotoxicity of salinomycin and hydrogels containing salinomycin on U251 cells after 48 h. Sali: salinomycin and PLGA: PLGA-PEG-PLGA; significant differences were shown by \* (compared to control) and \*\* (compared to salinomycin 1  $\mu$ g/mL) at  $p < 0.05$ . Sali represents salinomycin. 159

Fig. 4.4. Cell apoptosis/necrosis of treated U251 after 48 h, stained with Annexin V-FITC and PI. (a) Control, (b) salinomycin (c) PLGA-PEG-PLGA+salinomycin, and (d) Pluronic-salinomycin. Cell populations were sorted based on live (Q4), early apoptotic (Q3), late apoptotic (Q2) and necrotic cells (Q1). 161

Fig. 4.5. Cell proliferation assay of CFSE-labelled U251 after 48 h treatment. (a) CFSE flow cytometry graph, and (b) the relative cell proliferation as calculated by the mean CFSE<sub>control</sub>/mean CFSE<sub>treated</sub>. \* indicates a significant difference compared to the control group at  $p < 0.05$ . Sali represents salinomycin. 163

Fig. 4.6. Fluorescence microscopy images of U251 treated with salinomycin and the hydrogels containing salinomycin after 48 h. Red and blue fluorescence represents Alexa Fluor@ 488 phalloidin-stained F-actin and DAPI-stained cell nuclei, respectively. 164

Fig. 4.7. ROS level in U251 treated with salinomycin and the hydrogels containing salinomycin at different timepoints. \* indicates significant compared to the control group at  $p < 0.05$ . 165

Fig. 4.8. Relative gene expression of U251 cell treated with salinomycin and the hydrogels containing salinomycin after 48 h. \* indicates a significant difference compared to the control group at  $p < 0.05$ . 167

Fig. 4.9. (a) Tumor volumes of subcutaneous U251 xenografted nude mice treated with PBS, Pluronic, salinomycin, and Pluronic+salinomycin for 12 days. \* and \*\* indicate a significant difference compared to the control and salinomycin groups, respectively at  $p < 0.05$ , and n.s. means not significant compared to control. The data were reported as the mean $\pm$ standard error. (b) relative body weight of mice received different treatments. 169

Fig. 4.10. Images of H&E stained-tumor tissues of mice received (a) PBS, (b) Pluronic, (c) salinomycin, and (d) Pluronic-salinomycin, 12 days post-treatment. 171

## References

- 1 Neuwelt, E.A. et al. (2007) The potential of ferumoxytol nanoparticle magnetic resonance imaging, perfusion, and angiography in central nervous system malignancy: a pilot study. *Neurosurgery* 60 (4), 601-612
- 2 Chen, K. et al. (2009) Triblock copolymer coated iron oxide nanoparticle conjugate for tumor integrin targeting. *Biomaterials* 30 (36), 6912-6919
- 3 Lee, C. et al. (2018) In vivo delineation of glioblastoma by targeting tumor-associated macrophages with near-infrared fluorescent silica coated iron oxide nanoparticles in orthotopic xenografts for surgical guidance. *Scientific reports* 8
- 4 Cui, Y. et al. (2016) Dual-targeting magnetic PLGA nanoparticles for codelivery of paclitaxel and curcumin for brain tumor therapy. *ACS applied materials & interfaces* 8 (47), 32159-32169
- 5 Prabhu, S. et al. (2017) A polymeric temozolomide nanocomposite against orthotopic glioblastoma xenograft: tumor-specific homing directed by nestin. *Nanoscale* 9 (30), 10919-10932
- 6 Xu, H.-L. et al. (2016) Glioma-targeted superparamagnetic iron oxide nanoparticles as drug-carrying vehicles for theranostic effects. *Nanoscale* 8 (29), 14222-14236
- 7 Grauer, O. et al. (2019) Combined intracavitary thermotherapy with iron oxide nanoparticles and radiotherapy as local treatment modality in recurrent glioblastoma patients. *Journal of neuro-oncology* 141 (1), 83-94

## Glossary

ABC: ATP-binding cassette  
ACNU: Nitrosourea nimustine  
ADTC5: A cyclic cadherin binding peptide  
AMF: Alternating magnetic field  
AmS: Aminosilane  
ANOVA: Analysis of variance  
APTES: (3-aminopropyl) triethoxysilane  
BBB: Blood-brain barrier  
BBTB: Blood–brain tumor barrier  
BCNU: 1,3-bis(2-chloroethyl)-1-nitrosourea  
BCRP: Breast cancer resistance protein  
bEnd.3: Mouse brain endothelial cells  
BSA: Bovine serum albumin  
C6-ADR: DOX-resistant C6 glioma cells  
CASLNs: Catanionic solid lipid nanoparticles  
CDI: Coefficient of drug interaction  
CDDP: Cisplatin  
CED: Convection-enhanced delivery  
CFSE: Carboxyfluorescein succinimidyl ester dye  
CMC: Critical micellar concentration  
CT: Computed tomography  
CUR: Curcumin (CUR)  
Cyp-D: Cyclophilin D  
DAPI: 4',6-diamidino-2-phenylindole dihydrochloride  
DCF: 2',7'-dichlorofluorescein  
DCFDA: 2',7'-dichlorofluorescein diacetate

$D_H$ : Hydrodynamic diameter  
DLS: Dynamic light scattering  
DOX: Doxorubicin  
EDT: Trimethoxysilylpropyl-ethylenediamine triacetic acid  
EGF: Epidermal growth factor  
EGFRvIIIAb: Epidermal growth factor receptor variant III antibody  
EPR: Enhanced permeability and retention  
FBS: Fetal bovine serum  
FDA: Food and Drug Administration  
 $^{18}F$ -FDOPA: 3, 4-dihydroxy-6-[ $^{18}F$ ] fluoro-l phenylalanine  
FDX70000: 70 kDa Fluorescein isothiocyanate-dextran  
 $Fe_3O_4$ : Magnetite  
FUS: Focused ultrasound  
 $\gamma$ - $Fe_2O_3$ : Maghemite  
GBM: Glioblastoma multiforme  
Gd: Gadolinium  
Gd-DTPA: Gadopentetic acid  
Gas5: lncRNA-growth arrest-specific 5  
HAV: His-Ala-Val  
HAS: Human serum albumin  
Hsp70: 70-kDa heat shock protein  
IgG: Immunoglobulin G  
IONPs: Iron oxide nanoparticles  
I.V.: Intravenous  
Ku70: Essential enzyme for DNA repair and replication  
LDLR: Low-density lipoprotein receptor  
LncRNA: Long non-coding RNA  
LRP-1: Lipoprotein-related protein 1

MABVEGF: Monoclonal antibodies against vascular endothelial growth factor

MBs: Microbubbles

MDCK: Madin–Darby canine kidney

MDCK-MDR: Human multi-drug resistant protein 1

MDR: Multidrug resistance

MEG3: Maternally Expressed Gene 3

MHT: Magnetic hyperthermia therapy

M-PLL: Magnetosome coated with poly-L-lysine

MiR-155: Oncogene

MPS: Mononuclear phagocyte system

MRI: Magnetic resonance imaging

MRPs: Multidrug resistance-associated proteins

MSNs: Mesoporous silica nanoparticles

MTT: 3-(4,5-dimethylthiazol-2-yl)-2,5-diphenyltetrazoliumbromide

NFs: Nanofibers

NF-SIONs: Near-infrared fluorescent silica-coated iron oxide nanoparticles

NIRF: Near-infrared fluorescence

NP: Nanoparticle

NSF: Nephrogenic systemic fibrosis

OS-1: Overall survival after primary tumor diagnosis

OS-2: Overall survival following diagnosis of first tumor recurrence

p53: Tumor suppressor

PBS: Phosphate-buffered saline

PDI: Polydispersity index

PEG: Poly(ethylene) glycol

PEI: Polyethylenimine

PEO–PPO–PEO: Poly(ethylene oxide)-poly(propylene oxide)-poly(ethylene oxide)

PET: Positron emission tomography

P-gp: P-glycoprotein

PLGA: Poly(lactic-co-glycolic acid)

PLGA-PEG-PLGA: Poly(lactide-co-glycolide)-b-poly(ethylene glycol)-b-poly(lactide-co-glycolide)

PPZ: Poly(organophosphazene)

Ps 80: Polysorbate 80

PSMA: Prostate-specific membrane antigen

PTX: Paclitaxel

qRT-PCR: Quantitative reverse-transcript polymerase chain reaction

$r_1$ : Longitudinal relaxivity

$r_2$ : Transverse relaxivity

Rb: Retinoblastoma

RES: Reticuloendothelial system

RGD: Arg-Gly-Asp

Sali-PEI-PEG-IONPs: Salinomycin-loaded PEI-PEG-IONPs

SD: Standard deviation

SPECT: Single-photon emission computed tomography

SPIONs: Superparamagnetic iron oxide nanoparticles

SPION-NHs: SPION-loaded nanocapsule hydrogels

STAP: Anti-nestin antibody-polysorbate-80 nanocomposite

STAT: Anti-nestin antibody-transferrin conjugated nanocomposite

STT: Nanocomposite devoid of anti-nestin antibody

TEM: Transmission electron microscopy

TfR2: Transferrin receptor 2

$T_g$ : Glass-transition temperature

TMZ: Temozolomide

TOP2: Topoisomerase II

TRAIL: Tumor necrosis factor-related apoptosis-inducing ligand

U87: Human GBM cell line U87

U251: Human GBM cell line U251

USPIONs: Ultra-small SPIONs

V: Volume

WHO: World Health Organization

$\zeta$ : Zeta potential

$\gamma$ -H2AX: Phosphorylated H2AX

# **Chapter 1:**

## **Introduction**

## 1.1. Rationale

The blood-brain barrier (BBB) that restricts the penetration of many therapeutic agents into the brain remains a major challenge for the development of an efficacious therapeutic regimen for brain tumors. In fact, the tight junctions between adjacent brain endothelial cells form a physical barrier preventing paracellular diffusion of most therapeutic substances into the brain. Moreover, the presence of multiple drug efflux transporters on the brain endothelial cells contributes to the barrier function of the BBB by actively effluxing a wide range of therapeutic agents out of the BBB. Considering these hurdles, the current standard of care of glioblastoma multiforme (GBM, World Health Organization grade IV glioma) is limited to a single-agent chemotherapy with temozolomide in combination with radiotherapy. However, this regimen has not been successful enough in clinical practice and the median survival of GBM patients receiving the current standard of care is only 14.6 months post-diagnosis. Taken together, effective chemotherapy of malignant gliomas necessitates efficient drug delivery systems that can overcome the BBB and provide therapeutic doses of the chemotherapeutics within the brain. In fact, the clinical failure of many potentially effective therapeutic agents arises from the lack of an efficacious delivery system with the capability of bypassing the BBB and providing a therapeutic concentration of the drugs at the tumor site.

## 1.2. Objectives

Considering the limited permeability of the BBB that restricts the available chemotherapeutic options for GBM treatment to a single-agent temozolomide, the development of efficient drug delivery systems overcoming the BBB and providing therapeutic doses of more potent chemotherapeutics within the brain is of significant importance. In this study, we selected two

effective and more potent chemotherapeutics (i.e. doxorubicin, and salinomycin), whose indications are restricted in GBM chemotherapy *ipso facto* their inability to penetrate the BBB and low bioavailability in the brain. However, not only are doxorubicin (IC50: 330 ng/mL), and salinomycin (IC50: 700 ng/mL) more potent than temozolomide (IC50: 9600 ng/mL) in U251 GBM cells *in vitro*, but also they can be utilized in combination with temozolomide to show synergistic anti-cancer effects in GBM cells.

In this context, we developed and evaluated two different categories of drug delivery systems, enabling the chemotherapeutics to enter the brain. (1) Magnetic nanoparticles that can intravenously be administered in combination with the BBB transient disrupting methods (i.e. a cyclic ADT peptide or hyperosmotic mannitol solution) and an external magnetic field to enhance their penetration into the brain. (2) Thermosensitive hydrogels that can be administered intratumorally thereby bypassing the BBB and providing a high concentration of the drug at the tumor vicinity. Therefore, the main objectives of the current dissertation are:

- (1) Development, characterization and *in vitro* evaluation of negatively-charged trimethoxysilylpropyl-ethylenediamine triacetic acid (EDT)-IONP as a drug delivery system of Doxorubicin in combination with a cyclic ADT peptide as a transient disruption agent, and an external magnetic field.
  
- (2) Development, characterization and *in vitro* evaluation of positively charged polyethylenimine (PEI)-polyethylene glycol (PEG)-IONP as a drug delivery system of Salinomycin in combination with hyperosmotic transient disruption agent, and an external magnetic field.

(3) Development, characterization and evaluation (*in vitro* and *in vivo*) of injectable thermosensitive hydrogels as local drug delivery systems of Salinomycin in the treatment of brain tumors.

This study offers important implications in both nanoparticle-based systems for intravenous drug administration and injectable hydrogels for local intratumoral administration of chemotherapeutic agents into the brain in order to overcome the BBB and provide a therapeutic level of the drugs at the tumor site.

### **1.3. Organization**

This thesis consists of five chapters. Chapter 1 introduces the motivation and objectives, and provides a comprehensive literature review on the application of IONPs in diagnosis and therapy of glioma. The literature review on the application of injectable hydrogels in local chemotherapy of glioma is provided in Chapter 4 (in order to prevent further extension of Chapter 1). Chapter 2 presents the development, characterization and *in vitro* evaluation of DOX-EDT-IONPs on GBM cells. Chapter 3 describes the development, characterization and *in vitro* evaluation of Sali-PEI-PEG-IONPs on GBM cells. Chapter 4 presents the development, characterization and evaluation (*in vitro* and *in vivo*) of injectable thermosensitive hydrogels as local drug delivery systems of salinomycin in the treatment of GBM tumors. Chapter 5 concludes the thesis with a discussion of future work and final remarks.

## 1.4. Literature Review

### Iron Oxide Nanoparticles in Glioma Theranostics

#### 1.4.1. Introduction

Glioma is the most common primary tumor of the central nervous system, derived from astrocytes, oligodendrocytes or ependymal cells [1]. Glioma accounts for approximately 81% of primary malignant brain tumors, with an annual incidence of 6.6 per 100,000 persons in the USA [2]. According to the World Health Organization (WHO) classification, glioma is divided into four grades. Glioblastoma multiforme (GBM), the most aggressive form of malignant gliomas is a WHO grade IV, characterized by diffuse infiltration of the tumor cells into the brain parenchyma and a high recurrence rate [3]. The incidence of GBM is 3.19 per 100,000 people in the USA, and the median survival of GBM patients receiving the current standard of care is 14.6 months post-diagnosis [4,5].

The current standard of care for malignant gliomas is surgical resection of the tumor followed by postoperative radiation and adjuvant chemotherapy with temozolomide (TMZ) [5]. The infiltrative nature of high-grade gliomas, invading the surrounding brain parenchyma and essential neurological structures, renders a complete surgical resection unattainable. Thereof, the residual glioma cells at the tumor margins cause tumor recurrence resulting in a relapse of the disease [6-10]. Better depiction of the tumor boundaries through improved and multi-modal imaging techniques allows for more efficacious surgical removal of the tumor foci, leading to better therapeutic responses [7,11]. However, despite the surgical advancements, adjuvant chemo-

and radiotherapy are of significant importance to keep the essential neurological structures as much as possible.

Chemotherapy also exhibits modest clinical benefits inasmuch as most of the current systemically administered chemotherapeutics suffer from an inability to penetrate the blood-brain barrier (BBB) at therapeutically relevant levels [12,13]. The BBB is a physiological barrier with selective permeability regulating the passage of substances from the bloodstream into the brain. It consists of tight junctions between microvascular endothelial cells, the basement membrane, astrocytic foot processes, and pericytes [14,15].

With respect to imaging, although magnetic resonance imaging (MRI) is the current mainstay for brain tumor diagnosis, it has some limitations in delineating the brain tumor boundaries [16,17]. In fact, the contrast enhancement by the gadolinium (Gd)-based MRI relies on the leakiness of the Gd chelates as the contrast agents, out of the BBB into the brain. Since the leakiness of the BBB is a key feature in the detection of the brain tumors through the (Gd)-based MRI, the Gd chelates cannot enhance the contrast of the most peripheral portions of the tumor where the invading tumor cells infiltrate healthy brain parenchyma without an extensive BBB disruption and neoangiogenesis [18,19]. Therefore, the normal permeability of the BBB does not allow the Gd chelates to leak out into the interstitial tissues, leading to no or minimal enhancement within the areas of the peripheral tumor cells [19].

To address the limitations of the conventional imaging and chemotherapy of gliomas such as limited delivery of therapeutic/contrast agents to brain tumor and the invasive nature of the tumor cells, nanomedicines have emerged as promising tools. Generally, nanomedicine can enhance the half-life and bioavailability of their payload while preventing them from biodegradation and providing a controlled or sustained release of the bioactive agents at the tumor

site by conjugation of environmentally sensitive moieties [20-22]. Moreover, nanomedicine has the capability of amalgamating therapeutic and diagnostic modalities, serving as theranostic platforms [20,23]. Amidst various types of engineered nanocarriers, iron oxide nanoparticles (IONPs, magnetite ( $\text{Fe}_3\text{O}_4$ ) or maghemite ( $\gamma\text{-Fe}_2\text{O}_3$ )) have received increasing interest in various cancer theranostics. This is due to the properties of the IONPs that lend themselves as potential contrast enhancers for MRI, carriers for both small and large molecule drugs and genes as well as hyperthermia agents [16,20]. Generally, IONPs incorporate excellent biocompatibility with unique and tunable magnetic properties. In addition, IONPs are known to be biodegradable and cleared from the body through the endogenous iron metabolic pathway by which the released iron is metabolized in the liver and then either incorporated into the hemoglobin of erythrocytes or eliminated from the body through renal route [24,25].

Clinical studies on the safety profile of IONPs have shown no to moderate side effects. Various IONP formulations have been used clinically for imaging purposes. One such contrast agent of MRI, Ferumoxtran-10, was evaluated on 1777 adult patients using pooled data from 37 phase I to phase III clinical trials [26]. At least one adverse effect was reported in 23.2% of patients receiving Ferumoxtran-10 intravenously, of which 86.3% were mild-to-moderate in severity. The most common treatment-related adverse events were back pain, pruritus, headache, and urticaria. Only 7 patients (0.42%) reported serious treatment-related adverse events (including anaphylactic shock, chest pain, dyspnea, skin rash, oxygen saturation decreased, and 2 cases of hypotension). The only death reported from Ferumoxtran-10 imaging studies was due to unintended bolus injection of undiluted Ferumoxtran-10. Furthermore, in a 1-year retrospective study on 8666 patients who received Ferumoxytol intravenously, the total incidence of adverse events and serious adverse events was 1.25% and 0.21%, respectively. The most common serious adverse events were

hypotension (0.12%), hypersensitivity (0.06%), dyspnoea (0.05%), loss of consciousness (0.03%), anaphylactoid reaction (0.02%), syncope (0.02%) and unresponsive to stimuli (0.02%) [27,28]. Later, Ferumoxytol (up to 5 mg Fe/kg intravenously) was reported to be well-tolerated on 49 pediatric and 19 young adult patients suffering from various tumors or kidney transplants without major adverse events [29].

Currently, Ferumoxytol (Feraheme®) is an FDA-approved IONP formulation recommended for the treatment of iron deficiency anemia in adult patients [30,31]. Furthermore, several IONP formulations such as Ferumoxytol are under clinical trials as MRI contrast agent. NanoTherm®, an aminosilane-coated superparamagnetic IONP, is also an IONP formulation that has been introduced by MagForce, Inc., for magnetic hyperthermia treatment mainly in patients with recurrent GBM in clinical trials [30]. Although IONPs as drug carriers have not yet entered clinical trials, their advantages in site-specific and enhanced drug delivery of chemotherapeutics have widely been investigated in pre-clinical studies for glioma treatment [32,33]. This review paper focuses on the applications of IONPs in both imaging and therapeutic modalities (i.e. drug delivery and hyperthermia therapy) of malignant gliomas. Moreover, recent advances and optimizations of the current IONP-based formulations and their efficacy in pre-clinical models are discussed, which can pave the way for prospective clinical trials of IONPs in brain cancer theranostics.

## 1.4.2. Physicochemical Properties of IONPs

### 1.4.2.1. Surface Coating of IONPs

Generally, physicochemical properties of IONPs (like size, shape, surface coating and surface charge) can profoundly affect their biocompatibility, biodistribution as well as

functionality [34-36]. Surface features of IONPs are one of the prominent characteristics that profoundly impact on their pharmacokinetics and biodistribution. Upon intravenous administration of IONPs, plasma proteins adsorb non-specifically onto the surface of the nanoparticles. This results in formation of a stable protein layer around the surface of the nanoparticle called the “protein corona”. The protein corona can markedly change the biodistribution of nanoparticles and determines their fate *in vivo* [37]. Indeed, the protein corona is involved in the fast clearance of the nanoparticles by the mononuclear phagocyte system (MPS), particularly macrophages, and the reticuloendothelial system (RES), such as the liver and spleen [21,38]. To circumvent this, IONPs are often coated with hydrophilic macromolecules such as poly(ethylene) glycol (PEG) [39,40], dextran [41,42], chitosan [43], and starch [44], in an effort to reduce the non-specific protein adsorption *via* enhanced hydrophilicity and steric repulsion effects on the surface of the IONPs. Such a surface coating can result in prolonging the blood circulation time of the IONPs, preventing their intravascular aggregation and augmenting their accumulation in the brain tumor.

Among various coatings, PEG has been the most common option with an excellent anti-fouling characteristic to stabilize IONPs via enhancing both steric hindrance and hydrophilicity of the nanoparticles. In addition, PEG has the advantage of low molecular weight polydispersity index (PDI) compared to the natural polymers such as chitosan and dextran that is essential for a more uniform biodistribution of the nanoparticles [45]. IONPs coated with higher molecular weights of PEG generally demonstrate longer plasma half-life *in vivo*. For example, IONPs coated with 5 and 20 kDa of PEG exhibited half-lives of 7.29 and 11.75 h, respectively while the non-PEG coated IONPs had a half-life of 0.12 h [46]. Similarly, in one study, upon surface modification of starch-coated IONPs with PEG, glioma tumor concentration of the PEG-IONPs was augmented

by 15-fold (0.07% vs 1.0% injected dose/g tissue) under a magnetic field owing to the long-circulating feature of PEG-starch-IONPs [47].

With respect to the surface charge, it is believed that IONPs with neutral surface charge have a slower rate of opsonization and elimination due to reduced interactions with opsonin proteins, compared to either positive or negative ionic surface coatings [48,49]. Although positive charge IONPs typically demonstrate a higher cellular internalization compared to the negatively charged IONPs [50], their blood clearance is also faster than the negative ones, thanks to the higher affinity to adsorb the plasma proteins [51].

#### 1.4.2.2. Shape of IONPs

In addition to surface coating and charge, IONP shape can also play an important role in their pharmacokinetics and biodistribution. Generally, nanoparticles with elongated shapes exhibit more favorable pharmacokinetics and tumor-homing features compared to their spherical counterparts [21,52]. In fact, nanostructures with a higher length-to-width aspect ratio exhibit longer blood circulation time over the spherical counterparts that can be attributed to reduced uptake by macrophages owing to an opsonin-independent phagocytosis phenomenon [52], and reduced contact with the macrophage cell membrane [53]. Furthermore, higher surface area of elongated nanoparticles facilitates a multivalent interaction with target cell receptors compared to the curved shape of spherical particles with a limited number of the available binding sites, leading to higher accumulation of elongated nanoparticles within the tumors [52,54,55]. For example, gold nanorods were found to be distributed throughout tumors in breast cancer tumor-bearing mice, whereas gold nanospheres and nanodisks were only observed on the surface of the tumor [56]. Rod-shaped mesoporous silica nanoparticles (MSNs, aspect ratios of 1.5 with length of 185 nm; and 5 with length of 720 nm) also revealed different biodistributions *in vivo*. Indeed, short-rod

MSNs were easily trapped in the liver and showed faster clearance by urine and feces compared to the long-rod MSNs [57].

Similarly, *in vitro* studies on different cells exhibited greater cellular uptake and diffusion properties of elongated nanoparticles. For example, iron oxide nanobricks exhibited higher cellular uptake in cultured brain endothelial cells than iron oxide nanospheres with similar surface coatings, through caveolae-mediated endocytosis [58]. In another comparative study, whereas iron oxide nanospheres were found to be located in the vacuole of macrophage cells *in vitro* as aggregates, iron oxide nanorods were spread throughout the cytoplasm and exhibited higher necrosis owing to the higher degree of membrane damage and ROS production [59]. This suggests that nanoparticles' shape not only can change their pharmacokinetics and biodistribution, but also in turn can affect their cytotoxicity.

#### 1.4.2.3. Size of IONPs

Hydrodynamic size is another influential factor determining the characteristics and biodistribution of the nanoparticles. Generally, the blood half-life of IONPs is directly dependent on their size and typically larger nanoparticles show shorter blood half-life. For example, Roohi et al., [60] studied the effect of size on blood kinetics using different-sized IONPs and reported that IONPs with sizes of 20 and 70 nm showed  $t_{1/2}$  of 49 and 2.8 min, respectively, that was attributed to the less macrophage uptake. It has also been demonstrated that nanoparticles with a hydrodynamic size of greater than 100 nm are readily taken up by the RES and sequestered in the spleen through mechanical filtration followed by phagocytosis [61,62]. On the other hand, nanoparticles with a hydrodynamic size smaller than 10 nm are rapidly eliminated from the blood by the kidneys through glomerular filtration [63,64]. Therefore, a hydrodynamic size range of

IONPs between 10 and 100 nm is required to minimize their clearance and extend their blood half-life [65].

Moreover, within this optimum size range, smaller nanoparticles encounter a markedly less degree of diffusional hindrance resulting in a deeper penetration into the tumor core as well as a more homogeneous distribution within the tumor interstitium [66,67]. For example, gold nanoparticles smaller than 10 nm could distribute throughout cytoplasm and nucleus of cancer cells *in vivo*, while larger nanoparticles were found merely in the cytoplasm where they formed aggregates [68]. Therefore, it is envisaged that within the optimum size range of 10-100 nm in terms of better pharmacokinetic behaviours, smaller nanoparticles (i.e. < 50 nm) can be more efficacious options as both contrast agents and drug delivery systems due to their greater tissue penetration.

### 1.4.3. How IONPs can overcome the BBB

The BBB is a physiological barrier that controls the passage of substances from the bloodstream into the brain. The BBB is made of tight junctions between microvascular endothelial cells, the basement membrane, astrocytic end feet, and pericytes [14,15]. In fact, astrocyte end feet, spreading over the basal lamina of the brain endothelial cells, contribute to the barrier properties of the BBB [69]. The pericytes lie between the astrocyte end feet and capillary wall and show the similar function as smooth muscle, control vasculature tone and endothelial growth, and regulate BBB-specific gene expression patterns in endothelial cells. Dysfunction of pericytes has been shown to be associated with loss of BBB integrity and reduction in regional cerebral blood flow in animal models [70].

Moreover, the presence of complex tight junctions between adjacent brain endothelial cells forms a physical barrier that prevents paracellular diffusion of a majority of substances into the brain [71]. While transcellular diffusion of lipophilic solutes can occur, the presence of multiple drug efflux transporters including (i) P-glycoprotein (P-gp), (ii) various multidrug resistance-associated proteins (MRPs), and (iii) breast cancer resistance protein (BCRP) contribute to the barrier function of the BBB by actively effluxing a wide range of drugs out of the BBB. Therefore, the efflux transporters significantly limit the penetration of the chemotherapeutics into the brain even at high administered doses [20,72].

Similarly, imaging and treatment of brain tumors with nanoparticle-based formulations face the challenges of the BBB restricting their penetration into the brain. Once they entered, efficient and homogenous uptake of the nanoparticles by the tumor cells is necessary for an efficacious imaging/treatment [73]. This section deals with the mechanisms by which IONPs can overcome the BBB, enhancing their penetration into the brain and augmenting their uptake by the cancer cells.

#### 1.4.3.1. Passive Targeting

Nanoparticle accumulation at tumor sites is typically categorized into passive and active targeting strategies, while magnetic targeting can further enhance IONP's targeting capability [33]. In passive targeting, as the brain tumor progresses, both the BBB and the blood–brain tumor barrier (BBTB) become compromised structurally and functionally leading to formation of a leaky vasculature around and within the tumor, whereby IONPs in sub-100 nm size can extravasate through these leaky vessels into the tumor microenvironment *via* a mechanism known as the enhanced permeability and retention (EPR) effect [12,74]. The EPR effect generally provides higher local drug concentration at the tumor vicinity when the drug is delivered by nanovectors

due to the leaky vasculature around and within the tumor, furnishing extravasation of the nanovector with its payload [75]. Structural studies of brain tumor microvasculature *in vivo* have demonstrated that BBTB gaps have an upper limit of somewhere between 20 and 100 nm [76]. This gap size of the BBTB highlights the importance of engineering small nanoparticles capable of extravasation into the brain.

Although the BBTB has been reported to be compromised in primary brain tumors and would thus be amenable to nanoparticle accumulation *via* the EPR effect [77,78], studies suggest that the capillary leakiness is not uniform throughout the brain tumor [79]. Furthermore, for early stage of brain tumors, the EPR effect may not play an important role inasmuch as the BBB is still intact, and leakiness is observed at the stages when tumor volume is high and difficult to treat [80]. In addition, the infiltrating tumor cells are mostly associated with the intact BBB that would impede passive targeting of nanoparticles [81]. While there are several reports on improved nanoparticle accumulation due to the passive targeting of the EPR effect, this is likely to be more important in animal models compared to humans due to the heterogeneous tumor types, the inter-patient variabilities and the different disease stages in humans [75,77].

#### 1.4.3.2. Active Targeting

To overcome the passive targeting limitations, active targeting approaches can be exploited. Such targeting approaches involve decorating the surface of the nanoparticle with targeting ligands with the capability of binding to receptors overexpressed by cancer cells or angiogenic endothelial cells. Active targeting can enhance cellular uptake and tumor internalization of IONPs *via* receptor-mediated endocytosis, resulting in an augmented antitumor activity, and reduced off-target toxicity compared to free drug [82,83].

For glioma theranostic purposes, IONPs have been functionalized with several targeting ligands such as Arg-Gly-Asp (RGD) [84,85], epidermal growth factor (EGF) [86], epidermal growth factor receptor variant III antibody (EGFRvIIIAb) [87,88], and Transferrin [89] to target glioma cells. For example, EGF conjugated-superparamagnetic iron oxide nanoparticles (SPIONs) exhibited significantly greater accumulation and higher T2 signal reduction at the tumor site 24 h post-intravenous injection, compared to non-targeted SPIONs in C6 intracranial tumor-bearing mice [86].

Furthermore, to mediate transcytosis of IONPs across the BBB and enhance their penetration into the brain, IONPs can also be functionalized with various transcytosis-mediated ligands targeting angiogenic endothelial cells. To this end, IONPs have been functionalized with several ligands such as monoclonal antibodies against vascular endothelial growth factor (mAbVEGF) [90], Angiopep-2 [91], Transferrin [92], chlorotoxin [93,94], and lactoferrin [95,96]. For example, IONPs decorated with Angiopep-2 showed better permeability via transcytosis across the BBB through recognition of the low-density lipoprotein receptor-related protein in an *ex vivo* BBB model [91].

However, it is noteworthy to mention that drug delivery by nanoparticle-based formulations through active targeting has still not been successful in clinical practice. BIND-014, docetaxel-loaded PLGA-PEG nanoparticles decorated with anti-prostate-specific membrane antigen (PSMA), and MM-302, HER2-targeted PEGylated liposomal doxorubicin are two examples of active targeted nanomedicines for cancer chemotherapy that failed in late-stage clinical trials [97]. In this context, the EPR effect was reported to be a greater driver of BIND-014 access to the tumor cells than PSMA expression [98]. In fact, the expression of target receptors in some types of tumors, the tumor heterogeneity and the interpatient variability limit the benefit of

active targeted nanomedicines in clinical practice [99-101]. Therefore, other approaches such as site-specific magnetic targeting or transiently enhanced permeability of the BBB have attracted much attention as more effective platforms for delivery of therapeutic agents to the central nervous systems and treatment of malignant gliomas.

#### 1.4.3.3. Magnetic Targeting

IONPs uniquely provide a third mode for site-specific targeting due to the magnetic responsiveness of the iron oxide core. In terms of magnetic targeting, an external magnetic field is applied to draw IONPs to the site of action, regulating their systemic biodistribution and enhancing their imaging and treatment efficacy [102]. In fact, magnetic targeting is often utilized in combination with passive targeting, active targeting or BBB-disrupting approaches to further enhance passage of IONPs across the BBB and augment tumor exposure to the magnetic nanoparticles.

Chertok et al., [33] reported a fraction of IONPs that reaches the brain tumor site after systemic administration, can actively be retained by applying an external magnetic field, resulting in prolonging tumor exposure to the drug carrier. In fact, by applying an external magnetic field, overall orthotopic tumor exposure to magnetic nanoparticles was enhanced by 5-fold through the EPR effect *vis à vis* non-magnetic targeted tumors. Similarly, the target selectivity index of nanoparticle accumulation in glioma tissue over non-magnetic targeted normal brain parenchyma was augmented by 3.6-fold [33].

The same magnetic targeting effect was also reported in other types of cancers. For example, Guo et al.[103] prepared DOX-loaded IONPs and reported that DOX accumulation within tumor under an external magnetic field in subcutaneous osteosarcoma-bearing mice to be 2.3-fold higher than that in the tumors without an external magnetic field guidance and 5.1-fold

higher than that of the free administered DOX. In another study, utilizing an external magnetic field in rabbits bearing squamous cell carcinoma led to complete tumor remission with reduced doses of 20 and 50% mitoxantrone, when the drug was loaded to IONPs, due to holding of the drug at the site of action. However, 20 and 50% of mitoxantrone alone did not reduce tumor volume, and only at the doses of 75% and 100% of the mitoxantrone alone, tumor remission was observed [104].

#### 1.4.3.4. Other Methods

In addition to the passive, active, and magnetic targeting, some strategies have been recruited to overcome the BBB barrier functionality and enhance the delivery of IONPs into the brain, such as convection-enhanced delivery (CED), focused ultrasound (FUS), and transient disruption of the BBB. These strategies will be discussed in detail in section 1.5.

#### 1.4.4. IONPs Applications in Glioma Imaging

Effective imaging modalities are essential for preoperative planning, intraoperative tumor resection, as well as therapeutic monitoring in malignant gliomas. Depiction of tumor boundaries and differentiation of tumor from normal brain tissue are paramount for providing as complete surgical removal of the tumor foci as possible and reducing the tumor recurrence rate [7,102]. An assortment of imaging modalities is being utilized for the diagnosis of glioma in practice, such as MRI, computed tomography (CT), single-photon emission computed tomography (SPECT), and positron emission tomography (PET) [105]. MRI is the current mainstay for brain tumor diagnosis while it has some limitations particularly in differentiation between necrotic tissue and recurrent tumor [16,17]. The PET has also been used to provide additional insights into gliomas including malignancy grade, tumor delineation, and differentiation between necrotic tissue and recurrent tumor by means of metabolic activity measurement through the higher uptake of radiotracers by

the malignant cells [17,106]. A comparison of 3, 4-dihydroxy-6-[18F] fluoro-l phenylalanine (<sup>18</sup>F-FDOPA) PET and MRI for detection of glioma tumor recurrence in 35 patients revealed high sensitivity to detect recurrent glioma (100% vs. 92.3%) for both techniques, albeit much higher specificity of PET to differentiate recurrent glioma from radiation necrosis (88.9% vs. 44.4%) [107]. Moreover, PET offers higher spatial resolution (3–5 mm) with greater sensitivity than SPECT (spatial resolution: 8–10 mm) [108].

As mentioned earlier, MRI is still the current gold standard for brain tumor diagnosis, characterized by a high spatial resolution based on the detection of proton relaxation in an external magnetic field [16,109]. MRI contrast agents are recruited to reduce either longitudinal relaxation times, T1 (positive contrast, brighter images, signal enhancement), or transverse relaxations times, T2 (negative contrast, darker images, signal destruction) of surrounding water protons under an external magnetic field [110]. Currently, gadolinium (Gd) chelates are employed as T1 contrast agents, though they suffer from a short plasma half-life, a transient imaging time, a nonspecific biodistribution, and potential nephrotoxicity [20]. Although administration of Gd chelates in patients with the renal dysfunction is known to be associated with the development of nephrogenic systemic fibrosis (NSF) [111], more recent studies have revealed the accumulation of gadolinium in various tissues of patients without renal impairment such as bone, brain, and kidneys [112]. In fact, whilst gadolinium is mostly eliminated from the body through the kidneys, when it is dissociated into free Gd<sup>3+</sup>, it shows greater deposition in tissues. Kanda et al., [113] reported gadolinium accumulation in the brain, particularly in the dentate nucleus and globus pallidus (mean 0.44 μg/g of brain tissue ± 0.63), in post-mortem brain tissues of subjects without renal disease who received Gd chelates. Similarly, post-mortem neuronal tissue samples from 13 subjects who underwent at least four Gd-based MRI examinations during the last 14 years revealed

Gd accumulation (0.1–58.8  $\mu\text{g/g}$  of brain tissue) in a significant dose-dependent relationship [114]. Moreover, femoral head bone samples collected from patients who underwent total hip replacement surgery demonstrated Gd deposition 8 years after gadolinium exposure [115]. The concerns over the potential long-term toxicity in the central nervous system have led to re-examine the risk to benefit ratio of repeated administration of Gd-based contrast agents for MRI [116].

Superparamagnetic iron oxide nanoparticles (SPIONs) have an established history of use as T2 contrast agents due to their negative contrast enhancement by darkening T2- and T2\*-weighted images. In fact, IONPs with a core diameter of less than 20 nm exhibit superparamagnetism that is necessary for applications involving MRI contrast agents. By definition, superparamagnetic nanoparticles do not retain magnetization when the external magnetic field is removed, allowing their magnetization to be switched on and off by application of an external magnetic field [83,117]. Moreover, ultra-small SPIONs (USPIONs) have shown potential as dual T1 and T2 contrast agents [102]. Generally, SPIONPs provide several advantages over the traditional contrast agents including (i) higher longitudinal and transverse relaxation values ( $r_1 = 15$ ,  $r_2 = 89 \text{ mM}^{-1} \text{ second}^{-1}$  for Ferumoxytol vs  $r_1 = 4$ ,  $r_2 = 6 \text{ mM}^{-1} \text{ second}^{-1}$  for Gadoteridol in clinical trials) [118], (ii) slower clearance and longer circulation time (plasma half-life of 14 h for Ferumoxytol vs 1.6 h for Gd-DTPA in clinical trials) [119], (iii) improved tumor margin delineation due to enhanced cellular internalization by tumor cells, and (iv) relatively low cytotoxicity [75]. Furthermore, to augment the efficacy of SPIONs as MRI contrast agents for glioma monitoring, the nanoparticles can be functionalized exploiting various tumor biomarkers [120].

Since the last two decades, IONPs have been employed as MRI contrast agents in clinical practice [121]. Although some commercial IONP contrast agents such as Ferumoxide (Feridex),

and Ferumoxsil (Lumirem/ Gastromark) were discontinued, and Ferumoxtran-10 (Combidex/Sinerem) and Ferucarbotran (Resovist) applications are limited to a few countries [121-124], there are some ongoing clinical trials with IONP formulations for cancer detection. They include Ferumoxytol (Feraheme) (*ClinicalTrials.gov Identifier: such as NCT03179449, NCT03234309, NCT00659126 in brain tumors, and NCT03280277 in rectal cancer*) and Ferumoxtran-10 (*only in the Netherlands, ClinicalTrials.gov Identifier: NCT02751606 in rectal and breast cancers, and NCT03223064 in prostate cancer*) as MRI contrast agents. Ferumoxytol is a superparamagnetic iron oxide nanoparticle, coated with polyglucose sorbitol carboxymethylether (hydrodynamic diameter ( $D_H$ ):~ 30 nm), that has been approved by the FDA for treatment of iron deficiency anemia in patients with chronic kidney disease, and is employed off-label as an MRI contrast agent [125,126].

In a pilot study on 12 patients with malignant brain tumors, it was found that Ferumoxytol shows a delayed T1 enhancement with peak signal at 24–28 h post-injection (Fig. 1.1), while, standard Gd-based contrast agents display maximum enhancement within minutes after administration [110]. This means that Ferumoxytol did not show early vascular leakage like Gd-based contrast agent due to the larger size of the nanoparticles. Furthermore, the contrast enhancement provided by Ferumoxytol persisted up to 72 h post-injection (Fig. 1.1), which can be attributed to the persistence of the IONPs at the tumor vicinity after a single dose of Ferumoxytol. The application of Ferumoxytol as both T1- and T2-contrast agent was also reported as a potential alternative for GBM patients unable to tolerate Gd [118]. Furthermore, since Ferumoxytol is phagocytosed by tumor-associated macrophages, infiltrating the tumor microenvironment, Ferumoxytol to gadolinium contrast mismatch ratio in a dual Fe-and Gd-MRI was suggested as a biomarker for differentiating neuroinflammation-mediated pseudoprogession from disease

recurrence in GBM patients [127]. Pseudoprogression is a *de facto* treatment-related reaction with a transient contrast enhancement within the site of therapy that might mimic tumor recurrence. Due to the lack of diagnostic biomarkers, differentiation of tumor recurrence from pseudoprogression has remained a problem in neuro-oncology [128,129].

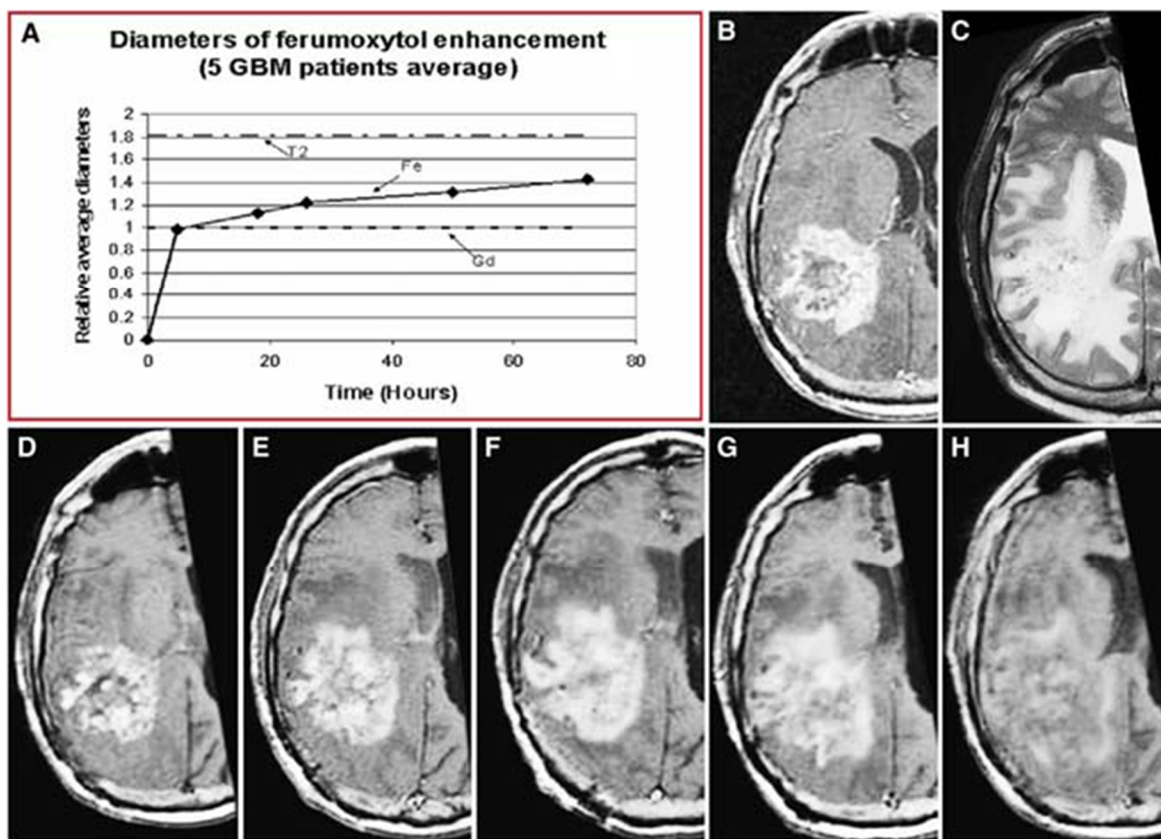


Fig. 1.1. A: The line graph exhibits the average diameter changes of Ferumoxytol enhancement over time (*solid line*) in comparison to that of Gd (*dashed*) and T2-weighted signal abnormalities (*dashed-dotted*). MRI images of (B) Gd T1-weighted, (C) T2-weighted, and (D-H) post-Ferumoxytol T1-weighted MRI images at five time points (D, 4–6 h; E, 6–20 h; F, 24–28 h; G, 48–52 h; H, > 72 h). Reproduced with permission from Ref [130].

Currently, there are many ongoing pre-clinical studies with IONP formulations to improve their characteristic and functionality as MRI contrast agents. For example, although IONPs are mainly employed as T2 contrast agents, a T1–T2 dual-modal MRI contrast agent can be fabricated

by conjugation/doping of T1 chelating agents on the surface of IONPs [131]. In a study, PEGylated-Gd-doped IONPs ( $D_H$ : 6.57 nm) were fabricated *via* the polyol method, with a transverse relaxivity ( $r_2$ ) and longitudinal relaxivity ( $r_1$ ) of 66.9 and 65.9  $\text{mM}^{-1} \text{s}^{-1}$ , respectively with the capability of contrast enhancement in both  $T_1$ - and  $T_2$ -weighted MRI images. In preclinical studies, glioma-bearing mice receiving PEG-Gd-IONPs had larger contrast areas in the  $T_1$  image, than that of the  $T_2$  image. This is likely due to the insufficient accumulation and retention of PEG-Gd-IONPs in glioma through the EPR effect [132].

To improve the selectivity of IONPs as MRI contrast agents for brain tumors, several active targeting ligands such as mAbVEGF [90], EGFRvIIIAb [88], RGD peptide [85,133,134], lactoferrin [135], and 70-kDa heat shock protein (Hsp70) [136] have been decorated on the nanoparticle surface. For example, bovine serum albumin (BSA)-coated IONPs decorated with mAbVEGF ( $D_H$ : 96 nm,  $T_2$  relaxivity: 172  $\text{mM}^{-1} \text{s}^{-1}$  vs  $160 \pm 10 \text{ mM}^{-1} \text{s}^{-1}$  for Feridex) were found to be more effective than the same doses of Feridex or non-specific murine immunoglobulin G (IgG)-BSA-IONPs as  $T_2$  contrast agent in rats bearing intracranial glioma C6 [90]. Although the signal intensity in the tumor tissue was similar for both targeted and non-targeted IONPs at 5 min and 2 h post-injection; in the case of mAbVEGF-BSA-IONPs, the signal intensity was significantly higher than that of IgG-BSA-IONPs at 24 h post-injection due to the effective accumulation of the targeted IONPs in the tumor tissue and the fast elimination of non-targeted IONPs and Feridex.

IONPs can also be utilized in multi-modal imaging *via* functionalization with other imaging probes to enhance visualization of glioma cells and overcome the limitations of a single imaging modality. The amalgamation of various imaging modalities can provide complementary information for early diagnosis, surgical resection and therapeutic follow-up of malignant gliomas

[137,138]. For instance, human serum albumin (HSA)-dopamine coated IONPs ( $D_H$ : 29 nm) were labelled with  $^{64}\text{Cu}$ -DOTA chelates and Cy5.5 dye and utilized for triple-modal imaging i.e. PET/near-infrared fluorescence (NIRF)/MRI in a subcutaneous U87MG human glioblastoma xenograft nude mouse model [139]. In another study, PEGylated IONPs ( $D_H$ :  $\sim 20$  nm,  $r_2$  relaxivity:  $190 \text{ mM}^{-1}\text{s}^{-1}$ ) were labelled with a NIRF dye (IRDye800) and functionalized with a RGD peptide [133], possessing a high affinity to  $\alpha_v\beta_3$  integrin receptors overexpressed on angiogenic endothelial cells and some tumor cells, such as malignant glioma cells [140]. The RGD-IONPs could selectively home to the tumor site compared to IONPs in subcutaneous U87MG tumor-bearing mice (Fig. 1.2a,b) showing a clear tumor contrast even after 24 h, while causing a significant reduction in T2 signal. However, despite the RGD tumor targeting, the biodistribution patterns of both types of nanoparticle in other organs were comparable. In fact, the nanoparticles were found in the liver and spleen due to the RES-mediated uptake, while the optical intensity in kidneys was attributed to the dissociation of the coating from the iron oxide core (Fig. 1.2b) [133].

Considering the infiltrative nature of GBM cells invading the surrounding brain parenchyma, fluorescence-guided surgery can be a technique of significant importance to improve intraoperative procedures and ensure the removal of microscopic tumor deposits [141]. For this purpose, near-infrared fluorescent silica-coated iron oxide nanoparticles (NF-SIONs,  $D_H$ : 37 nm) were fabricated for intraoperative imaging of GBM by targeting tumor-associated macrophages [142]. Immunofluorescence staining of excised brain tissue from orthotopic U87-MG tumor-bearing mice revealed that most of the NF-SIONs bound to macrophages (CD11b+) or microglia (Iba1+, brain macrophages), but not astrocytes (GFAP), indicating NF-SIONs were selectively taken up by tumoral region i.e. tumor-associated immune cells

(monocytes/macrophages/microglia) compared to non-tumor region i.e. brain parenchyma cells (astrocytes) (Fig. 1.3).

In summary, it is envisaged that IONPs with multi-modal imaging capability of MRI, PET, and NIRF can potentially be utilized as a nanoprobe for interoperative imaging, imaging-guided surgery of GBM tumor resection as well as therapeutic monitoring in future clinical trials. Moreover, IONPs as imaging nanoprobes are likely to overcome the BBB via either magnetic or active targeting thus addressing the limitations of current imaging techniques of glioma tumors that merely rely on the EPR effect.

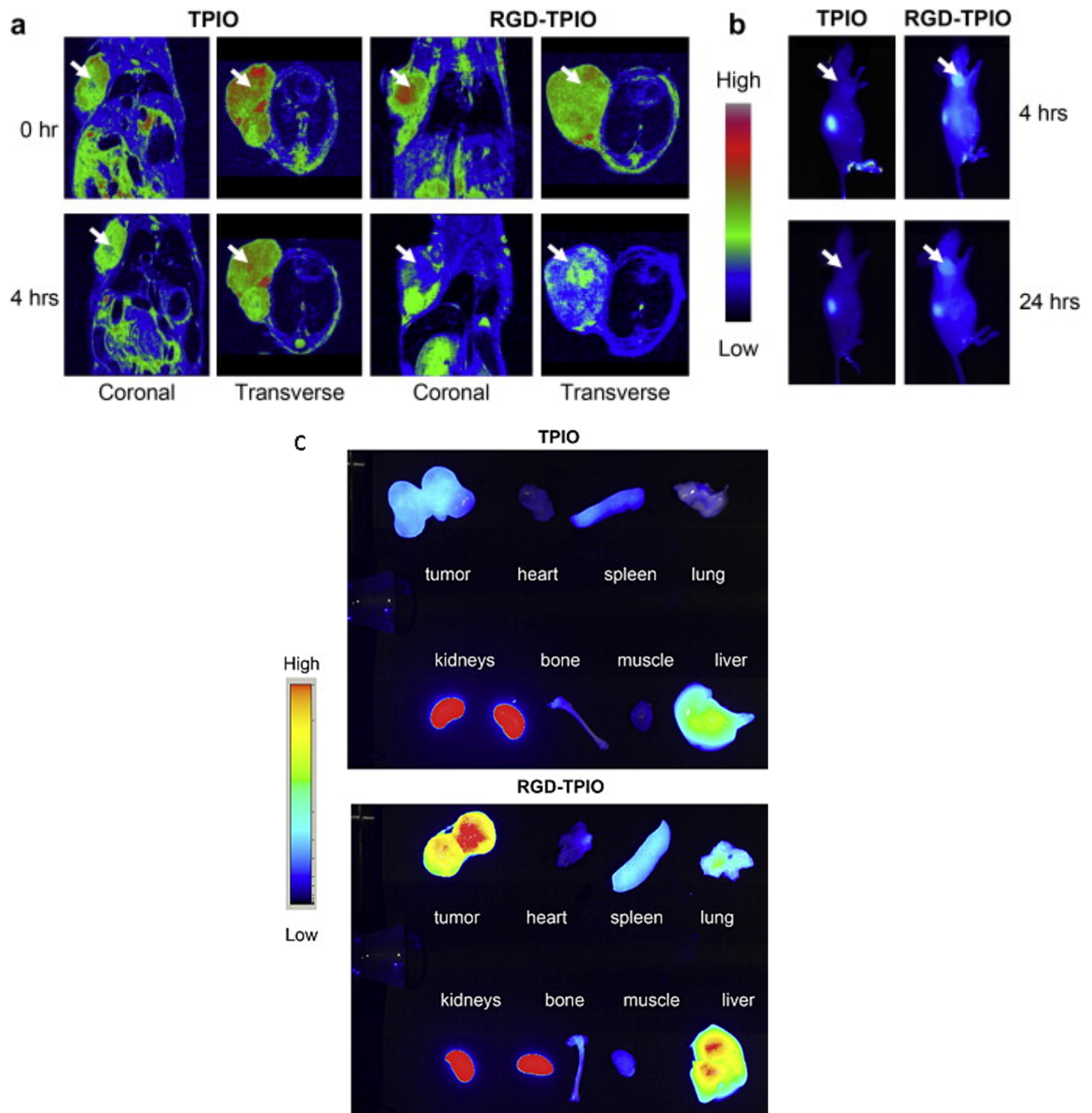


Fig. 1.2. (a) MRI of U87MG tumor-bearing mice injected with either RGD-TPIONPs or TPIONPs before and 4 h-post injection. Only RGD-TPIONPs could specifically home to the tumor vicinity and induced significant T2 reduction. (b) Optical imaging of U87MG tumor-bearing mice injected with either RGD-TPIONPs or TPIONPs at 4 and 24 h-post-administration. The RGD-TPIONPs injected mice exhibited desirable contrast at tumor vicinity within 24 h. (c) *Ex vivo* NIRF imaging of major organs harvested from mice got injection of either TPIONP or RGD-TPIONP. Higher tumor contrast was seen in RGD-TPIONP injected, while distribution of both nanoparticles in other organs was comparable. “TPIONPs” is considered as the synonym of IONPs. Reproduced with permission from Ref [133].

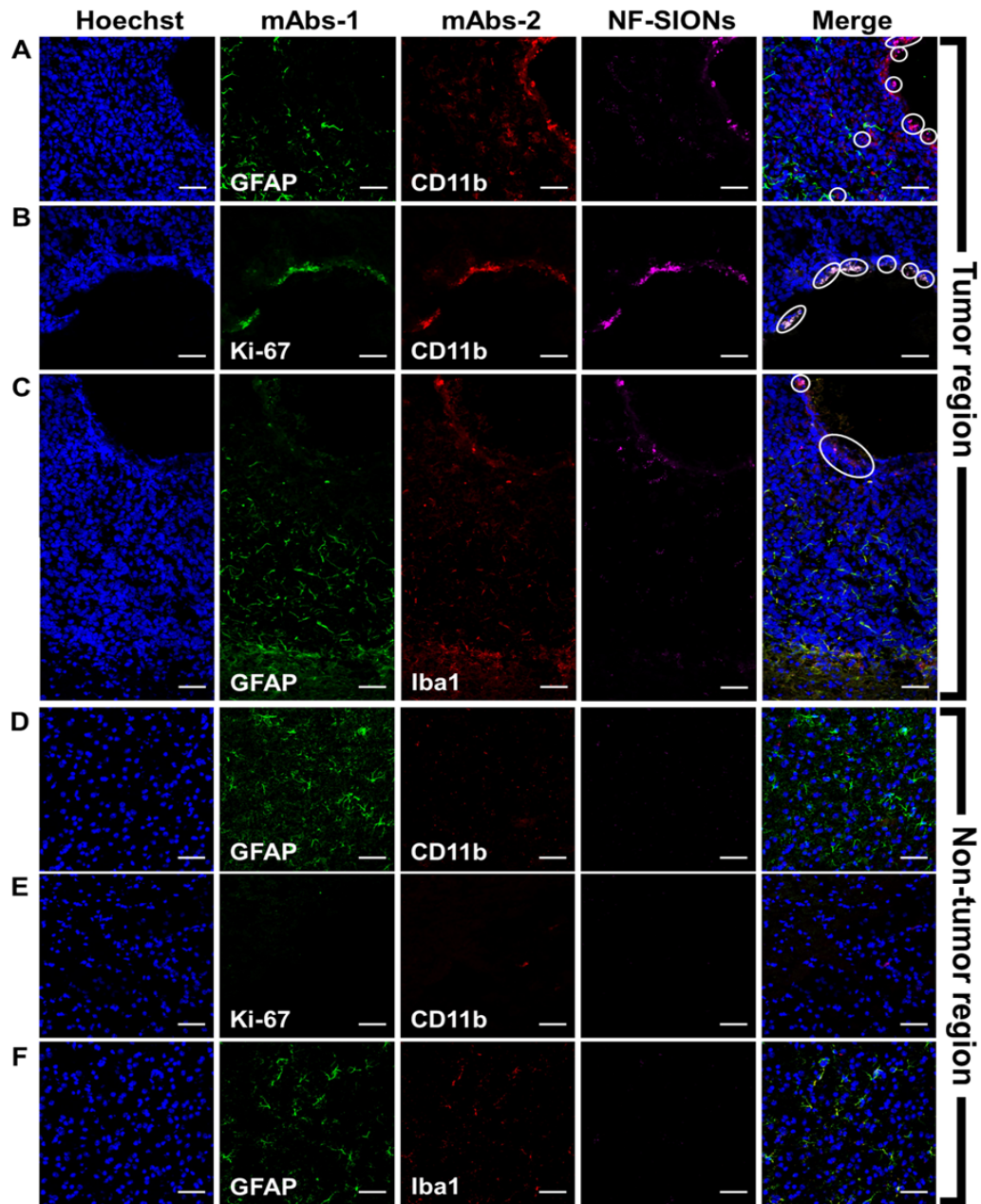


Fig. 1.3. Distribution of NF-SIONs in the brain tumor region (A-C) and non-tumor region (D-F), by immunofluorescence staining, 8 h post-injection. The samples were stained with two monoclonal antibodies (mAbs; green and red) against GFAP (A,C,D and F, astrocyte), CD11b (A,B,D and E, monocytes/macrophages), and Iba1 (C and F, microglia). In comparison to the non-tumoral region, macrophages and microglial cells extensively appeared in the tumor region, while the nanoparticles-binding cells were considerably overlapped with tumor-associated macrophages/microglia (CD11b+ or Iba-1+ cells), albeit not with astrocytes (GFAP+ cells). Blue and magenta signals indicate the location of cell nucleus and NF-SIONs, respectively. White circles demonstrate co-localization of tumor-associated macrophages and NF-SIONs. Scale bar: 50  $\mu\text{m}$  ( $\times 40$ ). Reproduced with permission from Ref [142].

#### 1.4.5. IONPs Applications as Drug Delivery System in Glioma Therapy

IONPs have been employed as efficient nanocarriers for chemotherapeutics, antibodies, peptides, DNA, siRNAs, and radionuclides to augment their transportation across the BBB and provide a site-specific magnetic targeting for glioma therapy [21,30]. Utilizing IONPs as nanocarriers can provide several advantages over conventional systemic administration of the therapeutic agents. These include (i) extended circulation time of the bioactive agents without being rapidly cleared from the body, (ii) protection of payload therapeutic agents from inactivation or biodegradation, (iii) passive, active or site-specific magnetic targeting to the tumor tissue by which the therapeutic efficiency is enhanced, while systemic biodistribution and systemic toxicity is diminished, (iv) controlled and sustained release of the bioactive agents at the tumor site by conjugation of environmentally sensitive moieties (e.g., pH and temperature-sensitive moieties) on IONPs, (v) delivery of multiple therapeutic agents for synergistic effects in one platform, (vi) overcoming multidrug resistance (MDR) and efflux transporters by masking the drugs entrapped within the nanoparticles, and (vii) combining multi-modal theranostic approaches to monitor treatment progress and synergistic therapeutic strategies (e.g. chemotherapy and hyperthermia therapy) [20-22].

Generally, drugs can be coupled to nanoparticle's surface either through chemical reactions (e.g., covalent bonding) or physical interactions (e.g., hydrophobic interaction or electrostatic attraction). Although the covalent bonding can secure drug molecules remaining on the nanoparticle's surface, this strategy has some limitations including (i) insufficient release of the payload drugs once nanoparticles delivered to tumor site, (ii) limited number of active functional groups on the nanoparticle's surface that can restrict the drug loading efficiency, and (iii) bioactivity of the loaded drugs might be affected during the chemical reactions [20,21]. To address

the insufficient release issue, a cleavable linkage between the drugs and nanoparticles' surface can be recruited to enable a selective and controlled release of the drug molecules triggered by some external stimuli such as acidic pH of tumor microenvironment (pH 6.5–6.8)/lysosomes (pH 4–6), temperature or enzymatic reactions [143-145].

An alternative strategy relies on the encapsulation of both IONPs and therapeutic agents within liposomes, polymeric or lipid nanoparticles, serving as magnetic responsive nanocarriers [146-148]. This strategy not only enhances the encapsulation efficiency for a wide range of molecules within the nanoparticles, but also can ameliorate the IONP stability in the bloodstream [149]. In fact, IONP's surface coatings can be degraded over time, particularly in biological media, leading to aggregation and precipitation of the nanoparticles. Loading IONPs into liposomes or lipids can protect them from degradation while offering well-defined *in vivo* behavior, independent of size or surface characteristics of IONPs [150,151]. Similar to PEGylated IONPs, lipid-anchored PEG stabilizes the liposomes/lipids and prevents them from being rapidly recognized and cleared by the MPS [152]. Furthermore, incorporation of magnetic IONPs into liposomes/lipids allows controlled release of payload that is triggered with an alternating magnetic field (AMF) [153].

Thus far, several IONP formulations have been developed as efficacious nanocarriers for some anti-cancer therapeutic agents such as temozolomide (TMZ) [154,155], doxorubicin (DOX) [95,156,157], paclitaxel (PTX) [158], gemcitabine [159], and cetuximab [160,161] through either chemical conjugation or physical entrapment that have been employed in glioma therapy.

In a study by Kievit et al., [156] DOX was covalently conjugated on amine terminated-PEG coated IONPs *via* pH labile hydrazone bonds, exhibiting 50% enhancement in DOX release at acidic pH ( $\text{pH} \leq 5.5$ ), suggesting that DOX can be released preferentially in the endosomal/lysosomal compartment of the cell where it is protected from the drug efflux.

Therefore, the DOX-IONPs could overcome the MDR associated with overexpression of ATP-binding cassette (ABC) transporters including ABCB1, ABCB5, ABCB8, and ABCC1, in DOX-resistant C6 (C6-ADR) glioma cells. This was consequently associated with greater retention of DOX-IONPs and reduction of cell viability compared to cells treated with free drug. However, DOX sensitive C6 cells were found more sensitive to free DOX that is likely due to the faster diffusion of free DOX to the nucleus, in comparison to the DOX-IONPs [156]. In addition, this can also be attributed to the fact that when the DOX-IONPs are internalized into cytoplasm, they are enclosed into endosomes followed by fusion to lysosomes [162]. Therefore, using DOX-IONPs might result in more DOX entrapped within the lysosomes, which cannot get released and diffused to the nucleus to induce cell apoptosis.

Conjugation of cetuximab, an EGFR inhibitor, with IONPs has already shown greater anti-tumor effect than that of cetuximab alone in both EGFR- and EGFRvIII-expressing human GBM neurospheres and GBM stem-like cells *in vitro*, owing to more efficient cellular targeting and uptake, EGFR signaling alterations, and apoptosis induction [160]. While these *in vitro* studies are promising, as the technology is moved into intracranial tumor models, the nanoparticle formulation faces the BBB and BBTB that would potentially limit brain penetration and tumor cell uptake efficiency. To address this issue, convection-enhanced delivery (CED) was employed in a pilot study in order to bypass the BBB/BBTB limited permeability [161]. CED is *de facto* an invasive stereotactically-guided drug delivery method. In CED, catheter(s) are inserted into the brain through burr hole(s) created in the skull and dura and the drug is actively pumped into the brain parenchyma through the catheter(s) via the positive hydrostatic pressure [163,164]. This procedure bypasses the BBB and allows the local delivery of high-molecular-weight therapeutic agents. The

convective nature of the infusion results in a greater volume of distribution than would be achieved by the simple diffusion [165,166].

Bernal et al., [167] reported that CED can significantly enhance IONP distribution even distant from the injection site, compared to bolus infusion in the rat brain as confirmed by fluorescence imaging, and MRI. Moreover, a single treatment with cetuximab-IONP and CED in spontaneously occurring intracranial gliomas in canines after surgical resection was found effective to decrease the tumor median size by 54.9% at 1-month, while the median survival after surgery was reported to be 248 days [161]. Thence, it was envisaged that this platform in combination with fractionated radiotherapy might show further enhanced treatment effect based on the preclinical studies [87,161]. In another study, iron oxide nanoparticles administered via CED to enhance their intratumoral and peritumoral distribution in the brain. To this end, IONPs were conjugated with EGFRvIIIAb, capable of selectively binding to (EGFRvIII) present on GBM cells. A significant increase in the median survival of intracranial GBM tumor-bearing mice underwent CED was observed from 11 days (no treatment) to 16 and 19 days for mice received IONPs and EGFRvIIIAb-IONPs, respectively [88].

#### 1.4.5.1. Disruption of the BBB for Drug Delivery

Alternative and non-invasive strategies to overcome the limited drug delivery into the brain, deploy techniques to transiently disrupt the BBB and permit the passage of therapeutic molecules into the brain. Moreover, transient disruption of the BBB can address the limitations of drug delivery into the brain that merely relies on the EPR effect or the active targeting. These transient disruption techniques can be either through chemical (like mannitol solution), molecular (like peptides that inhibit interactions of cell-adhesion proteins at the intercellular junctions), or physical (like FUS) approaches [168,169].

#### 1.4.5.2. Mannitol for Disruption of the BBB

In view of the chemical approaches, infusion of a mannitol solution is the most widely studied method for the BBB transient disruption. This hyperosmotically shrinks endothelial cells and opens the tight junctions of the BBB, which permits large molecules to passively diffuse into the brain across the BBB. Moreover, hyperosmotic treatment has been found to be effective in enhancing clathrin-mediated endocytosis and simultaneously attenuating exocytosis [170]. Mannitol has extensively been used in combination with anti-tumor agents in clinical trials for glioma therapy over the last three decades [171,172]. For example, in a clinical study, mannitol infusion prior to nitrosourea nimustine (ACNU) and cisplatin (CDDP) administration exhibited a significantly higher median survival time in patients with brain metastases compared to those received ACNU and CDDP without mannitol (47 vs 24 weeks) [172]. Mannitol was also studied in clinical trials in combination with bevacizumab for patients with recurrent malignant glioma. This therapeutic platform was well tolerated and showed a reduction in tumor volume [173].

Sun et al., [174] utilized mannitol to enhance the passage of IONPs across the confluent monolayers of mouse brain endothelial cells (bEnd.3) as a model of the BBB *in vitro*. Although the negatively-charged N-trimethoxysilylpropyl) ethylenediaminetriacetate [EDT]-IONPs were not permeable across an intact cell monolayer, using mannitol increased passage of EDT-IONPs across the bEnd.3 monolayer by 28% after 24 hours of treatment, which further enhanced to 44% when a magnetic field was present. Similarly, effective uptake of IONPs as contrast agents in Alzheimer's disease transgenic mice was reported upon intravenous [175] or intracarotid [176] injection of mannitol to visualize amyloid plaques in the brain. The intravenous administration of mannitol is currently preferred due to less invasive nature, and better tolerance in clinical practice [175,177]. However, the intracarotid injection of mannitol is associated with a more disruptive

effect on the BBB permeability for large protein and small molecules compared to the intravenous route. Moreover, the intracarotid injection of mannitol has been reported to be brain-specific with no significant change in extravasation of markers into other organs such as liver [178].

Generally, the maximum BBB disruption has been reported 5 min after administration of mannitol lasting about 20-30 min, in animal studies [177]. However, the major disadvantage with osmotic disruption in clinical practice, is the long recovery period required for the BBB to be restored to its normal barrier function [179]. This recovery period time has been reported to be 2 to 6 hours in the clinic, which can increase the risks of neurotoxicity [180]. Moreover, this long recovery period can be associated with entrance of immune cells as well as small and large molecules to the central nervous system and increased intra-cranial pressure [181].

#### 1.4.5.3. Focused Ultrasound for Disruption of the BBB

Focused Ultrasound (FUS) is a physical non-invasive approach for local and transient disruption of the BBB, thus enhancing the delivery of therapeutic agents into the brain [168]. For example, FUS was reported to augment 1,3-bis(2-chloroethyl)-1-nitrosourea (BCNU) delivery through the BBB in normal (by 340%) and tumor-implanted (by 202%) brains in rats. Correspondingly, median survival increased from 28.5 days (control), 25.5 days (FUS) and 32.5 days (BCNU) to 53 days for rats underwent FUS+BCNU [182]. The integration of FUS and magnetic field was also reported to synergistically enhance the delivery of epirubicin-conjugated IONPs across the BBB by which epirubicin deposition increased from  $1,336 \pm 1,182$  ng/gram of tissue for FUS treatment alone, to 21,738 ng/gram of tissue with a combination of FUS and magnetic field exposure [183]. Recently, FUS has also been employed with microbubbles (MBs) to enhance BBB disruption due to the additional mechanical forces produced by the oscillation of circulating MBs as a result of the focused ultrasound [184]. For example, PEG-coated gold

nanoparticles exhibited over 3-fold higher uptake in right hemispheres upon exposure to FUS and MBs, compared to non-sonicated left hemispheres in rat models [185]. Fan et al., [186], prepared multifunctional MBs loaded with DOX and conjugated with SPIONs. Deposition of DOX-SPIONs-MBs in the brain tumor region was enhanced by 2.28-fold, 2.67-fold and 4.04-fold, by magnetic field targeting, FUS exposure, and combined FUS exposure and magnetic field targeting, respectively. By facilitating the BBB opening, this developed platform can potentially be utilized as both drug delivery system, and dual MRI/ultrasound contrast agent.

However, it is noteworthy to mention that the intensity of the FUS beam decreases along gradients that extend out from the center point of the beam [187]. This may result in non-uniform opening of the BBB, while in this case, drug concentration gradient will be the only driving force to deliver the drug to the invading and metastatic tumor cells at the therapeutic levels. On the other hand, this gradient of the drug concentration may lead to rapid propagation of the drug, reducing the concentration of the drug to below the therapeutic levels at the tumor site. Last but not least, FUS administration relies on the localization of the tumors based on the MRI, while it has some limitations in delineating the brain tumor boundaries as well as the invading tumor cells infiltrating healthy brain parenchyma [19]. This may result in tumor recurrence after the treatment.

#### 1.4.5.4. Cadherin Peptides for Disruption of the BBB

A more novel approach to enhance the BBB permeability relies on the inhibition of the cell-adhesion protein interactions at the intercellular junctions. Generally, cadherin peptides can inhibit E-cadherin-mediated cell-cell adhesion at the biological barriers (i.e., the BBB and intestinal mucosa barrier) [188]. For example, a His-Ala-Val (HAV) peptide (HAV6) derived from E-cadherin has shown enhanced delivery of Gd-DTPA and NIRF dye R800 through the BBB into the brain in Balb/c mice [188]. In fact, HAV6 can bind to the external domain of cadherin and alter

paracellular diffusion of various marker molecules through the BBB. Laksitorini et al., [169] also utilized cyclic-ADT peptides to enhance the delivery of marker molecules (e.g.,  $^{14}\text{C}$ -mannitol, and Gd-DTPA) to the brain via the paracellular pathways across the BBB. Cyclic-ADT peptides have found to bind to the EC1 domain of E-cadherin, blocking the cadherin–cadherin interactions in the *adherens* junctions of the vascular endothelial cells of the BBB and thus enhancing paracellular delivery of molecules into the brain [169]. In a comparative study, ADTC5 was found superior to HAV peptides in terms of BBB modulatory activity due to the higher brain deposition of Gd-DTPA caused by ADTC5 compare to those of HAV peptide [169,179]. Although this approach of using cadherin peptides for enhancing permeability of the BBB have been reported for small molecules entering the brain [169,179], it has not still been established for enhanced penetration of nanoparticle-based formulations into the brain either *in vitro* or *in vivo*.

As mentioned earlier, although the extensive opening of the BBB by mannitol and the long recovery time for re-establishment of the BBB integrity, limits its application in clinical practice [189], the cadherin peptides are likely to show the advantage of not producing an extensive change in permeability of large molecules into the brain. Moreover, the time frame for BBB disruption with cadherin peptides was reported to be fast (3–6 min post-injection injection of the peptide), and the recovery time for re-establishment of the BBB integrity was reported to be within 60 min post-injection of the cadherin peptide *in vivo*. In addition, no change in cerebral blood flow of mice received cadherin peptide was observed [179]. Therefore, it is envisaged that the cadherin peptide approach for enhancing the BBB permeability has several advantages over either the osmotic disruption or FUS approaches. Moreover, this approach can address the limitations of drug delivery into the brain that merely relies on the EPR effect or active targeting in the clinical practices, as discussed earlier. This warrants future pre-clinical and clinical studies of utilization

of cadherin peptides for enhancing the BBB permeability in combination with various nanomedicines and therapeutic agents for glioma therapy.

#### 1.4.5.4. Encapsulation of IONPs for drug delivery

In terms of IONP formulation, nanoparticles and multiple therapeutic agents can be encapsulated within liposomes, polymeric or lipid nanoparticles, serving as magnetic responsive nanocarriers, as mentioned earlier. To exploit this feature, a dual-targeting, co-delivery platform was developed by co-encapsulation of magnetic IONPs, PTX, and curcumin (CUR) within PLGA nanoparticle (NP), whose surface was decorated with transferrin receptor-binding peptide T7 for ligand-mediated targeting in juxtaposition with the feasibility of magnetic-guided targeting. This dual-targeting yielded ~4-fold increment in BBB transport efficiency (Fig. 1.4a) and a greater brain accumulation (Fig. 1.4b) compared to the non-targeted PLGA NPs in orthotopic U87 glioma-bearing mice. Of note, no death was reported in the cohort of mice treated with MNP/T7-PLGA NPs (PTX + CUR) + MAG (within 35 days), while the survival rates were 83% and 67% for MNP/T7-PLGA NPs (PTX + CUR) without a magnetic field and free combo drugs, respectively (Fig. 1.4c) [190].

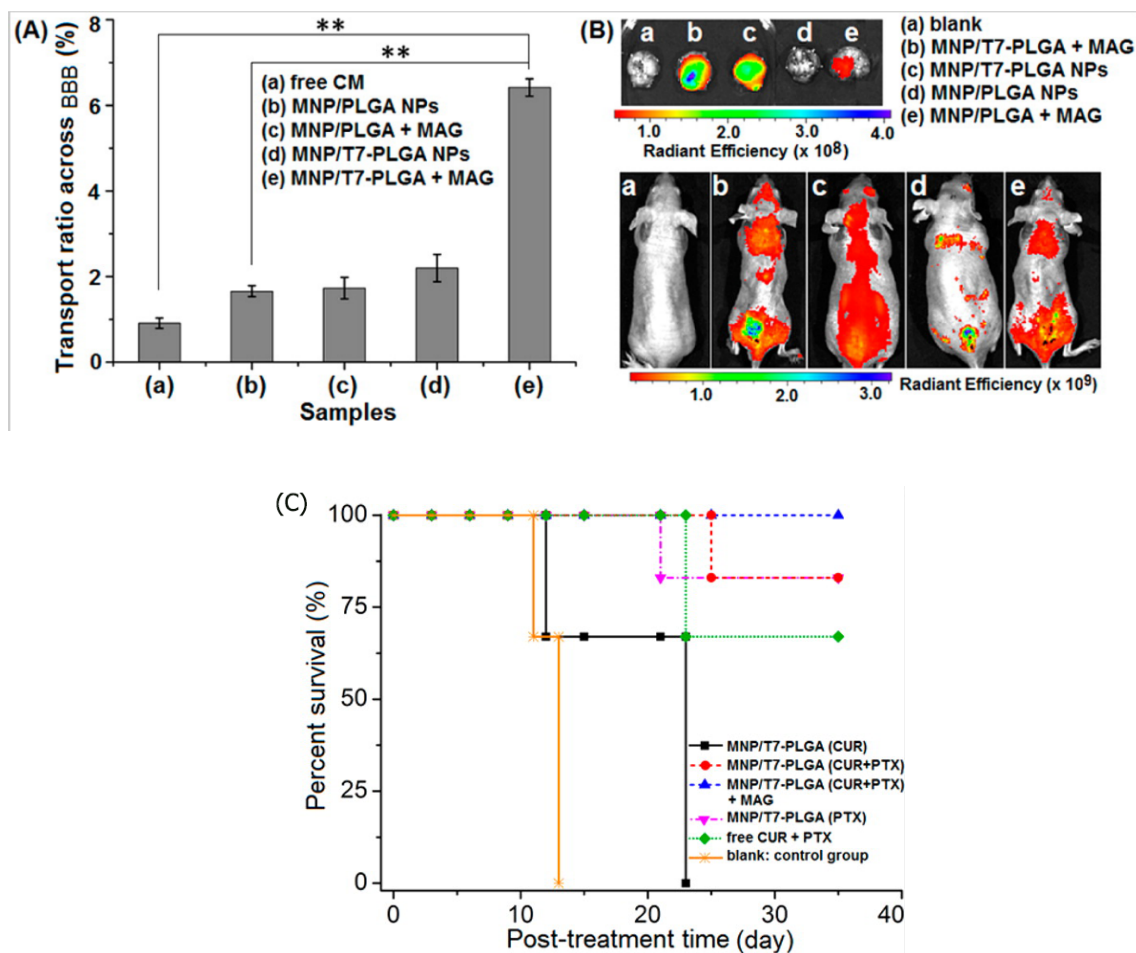


Fig. 1.4. (a) transporting efficiency across BBB *in vitro* at 4 h; (b) *in vivo* distribution of the nanoparticles after injection via tail vein at 4 h. The dissected brains showed a tendency of the NP accumulation as follows: MNP/T7-PLGA NPs + MAG > MNP/T7-PLGA NPs > MNP/PLGA NPs + MAG > MNP/PLGA NPs. (c) overall survival of glioma-bearing mice (n = 8). Reproduced with permission from [190].

In a similar work, polymeric nanocomposite embedding IONPs and TMZ were fabricated whose surface was decorated with an antibody against nestin, a marker for glioma stem cells, and either transferrin or polysorbate 80 (Ps 80) to permeate the BBB [155]. The transferrin was selected since transferrin receptor 2 (TfR2) is highly expressed in GBM cells [191]. In addition, since the BBB expresses low-density lipoprotein receptor (LDLR)-related proteins, enhanced accumulation of polysorbate-80-coated nanoparticles has been reported in the brain due to adsorption of apolipoprotein B or E, which are endocytosed by the LDLR on the endothelial cells of the BBB

[192,193]. This polymeric nanocomposite formulation could provide a sustained release with a significantly enhanced accumulation and prolonged retention of TMZ in the brain (Fig. 1.5a) as well as an augmented tumor cell death (Fig. 1.5b,c) in U-251 MG intracranial GBM tumor-bearing-mice, with a superiority of anti-nestin antibody-transferrin conjugated nanocomposite (STAT) *vis à vis* the anti-nestin antibody-polysorbate-80 nanocomposite (STAP), nanocomposite devoid of anti-nestin antibody (STT) and free TMZ [155].

#### 1.4.5.5. Theranostic Application of IONPs

As mentioned earlier, IONPs can be utilized in both therapeutic and diagnostic platforms, bridging diagnosis and therapeutic modalities such as imaging, drug delivery, and hyperthermia therapy, thus providing imaging-guided synergistic therapies for malignant gliomas [20,23].

To integrate the drug delivery capability, magnetic site-specific targeting, and real-time MRI imaging in one platform for the glioma theranostic in one study, multifunctional nanoparticles were designed with a core of IONPs and a shell made of PEG/PEI/polysorbate-80 encapsulating DOX ( $D_H$ : 58 nm). The nanoparticles enhanced DOX uptake by C6 glioma cells in rats bearing intracranial tumors, particularly in the presence of an external magnetic field, indicating effective magnetic targeting. In addition, the Ps 80-IONPs served as a contrast agent in T2-weighted MRI to monitor real-time therapeutic outcome. Thanks to the magnetic site-specific targeting and Ps 80-mediated endocytosis, the DOX@Ps 80-SPIONs in the presence of a magnetic field could suppress the tumor growth completely within 28 days (Fig. 1.6a,b) and prolonged the survival (17.8, 32.4, 38.5 and 79.2 days for saline, DOX, DOX@Ps 80-SPIONs, and DOX@Ps 80-SPIONs+Magnetic field treated mice, respectively) (Fig. 1.6c). Furthermore, DOX-associated heart toxicity was prevented upon administration of DOX@Ps 80-SPIONs, and no toxicity was observed in other major organs, i.e. lungs, spleen, kidneys and liver [32]. Therefore, the developed

DOX@Ps 80-SPIONs formulation plus magnetic field can potentially be utilized as a theranostic tool in glioma.

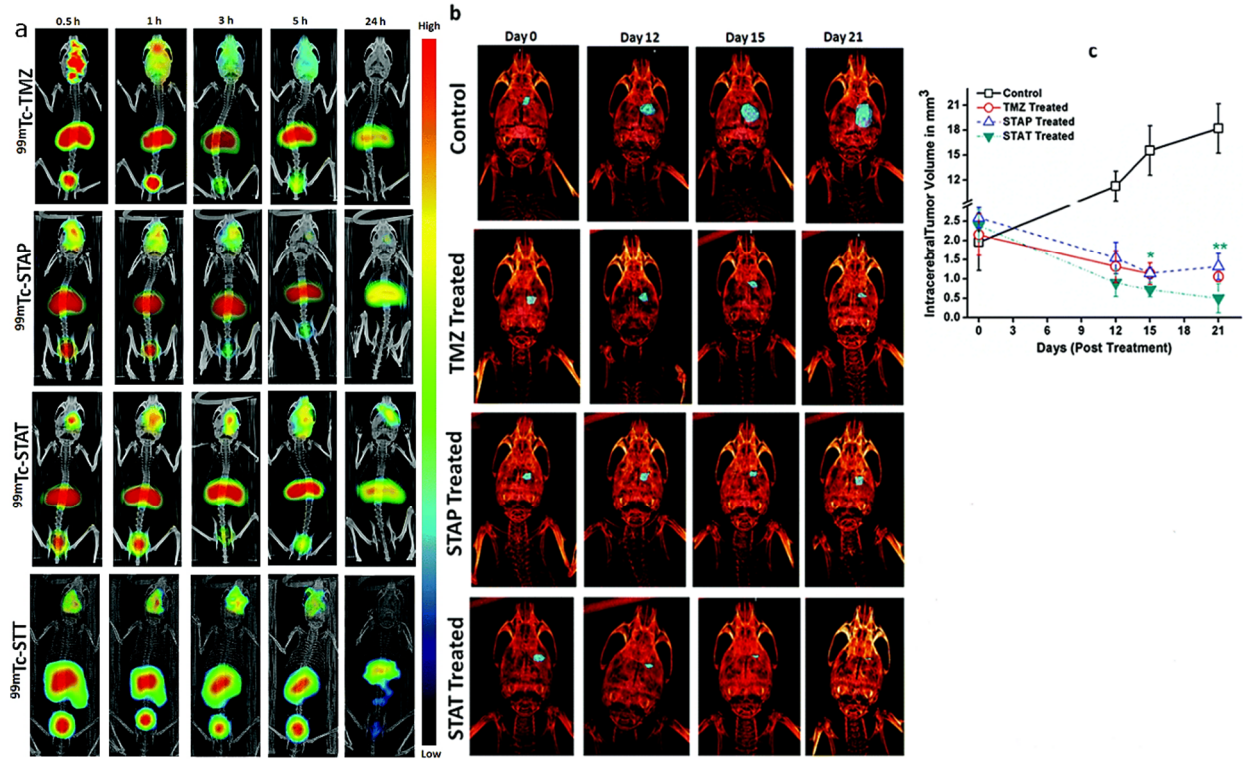


Fig. 1.5. (a) Representative micro SPECT/CT images of GBM tumor-bearing mice. Distribution of 99mTc-TMZ shows rapid clearance from the brain. Distribution of 99mTc-STAT exhibits a significantly extended and localized retention at the tumor vicinity compared to 99mTc-STAP. 99mTc-STT demonstrates minimal uptake at the tumor site, indicating the necessity of anti-nestin antibody as a targeting moiety. (b) images of GBM tumor-bearing mice; a rapid increase in intracerebral tumor volume in the untreated group of animals (control) is observed, while the animals treated with STAT exhibited a significantly greater regression in tumor volume compared to TMZ and STAP-treated animals over a period of 21 days. (c) graph illustrating the tumor regression volume post-treatment with TMZ, STAT and STAP against untreated control. The STAT-treated animals demonstrated better intracerebral tumor regression compared to TMZ treated animals. Reproduced partially with permission from [155].

## 1.4.6. Magnetic Hyperthermia Effect of IONPs

### 1.4.6.1. IONPs Applications in Magnetic Hyperthermia Therapy of Glioma

Hyperthermia therapy relies on the exposure of cancerous tissues to elevated temperatures (41 to 46 °C) to kill cancer cells or sensitize them to chemotherapy/radiotherapy [194,195]. Furthermore, hyperthermia therapy has been known to enhance drug delivery to the brain by inducing reversible BBB disruption [196]. Several techniques including radiofrequency, ultrasound, microwave, laser and magnetic nanoparticles can be recruited to provide localized hyperthermia effect [197].

The magnetic feature of IONPs can be harnessed to induce localized hyperthermia by applying an alternating magnetic field (AMF), termed as magnetic hyperthermia therapy (MHT). In this approach, IONPs that accumulate within the tumor vicinity are subjected to a high-frequency AMF, by which they absorb energy and generate heat through Néel and Brownian relaxations and hysteresis loss mechanisms, leading to a localized MHT [20,198]. The application of IONPs in MHT for various cancers such as glioma [197,199], prostate cancer [200], breast cancer [201], and lung cancer [202] have been reported in pre-clinical studies. A dose-dependent inhibitory effect of IONPs on proliferation of U251 [203], U87-MG [204], and U87-EGFRvIII [205] GBM cells has also been reported. Similarly, magnetite cationic liposomes exposed to AMF exhibited an anti-tumor effect on subcutaneous T-9 rat glioma models with a complete regression, and no regrowth of tumors over a period of 3 months. Moreover, this MHT was accompanied by a host immune response mediated by both CD8<sup>+</sup> and CD4<sup>+</sup> T cells and enhanced tumor-selective cytotoxic T lymphocyte activity [206].

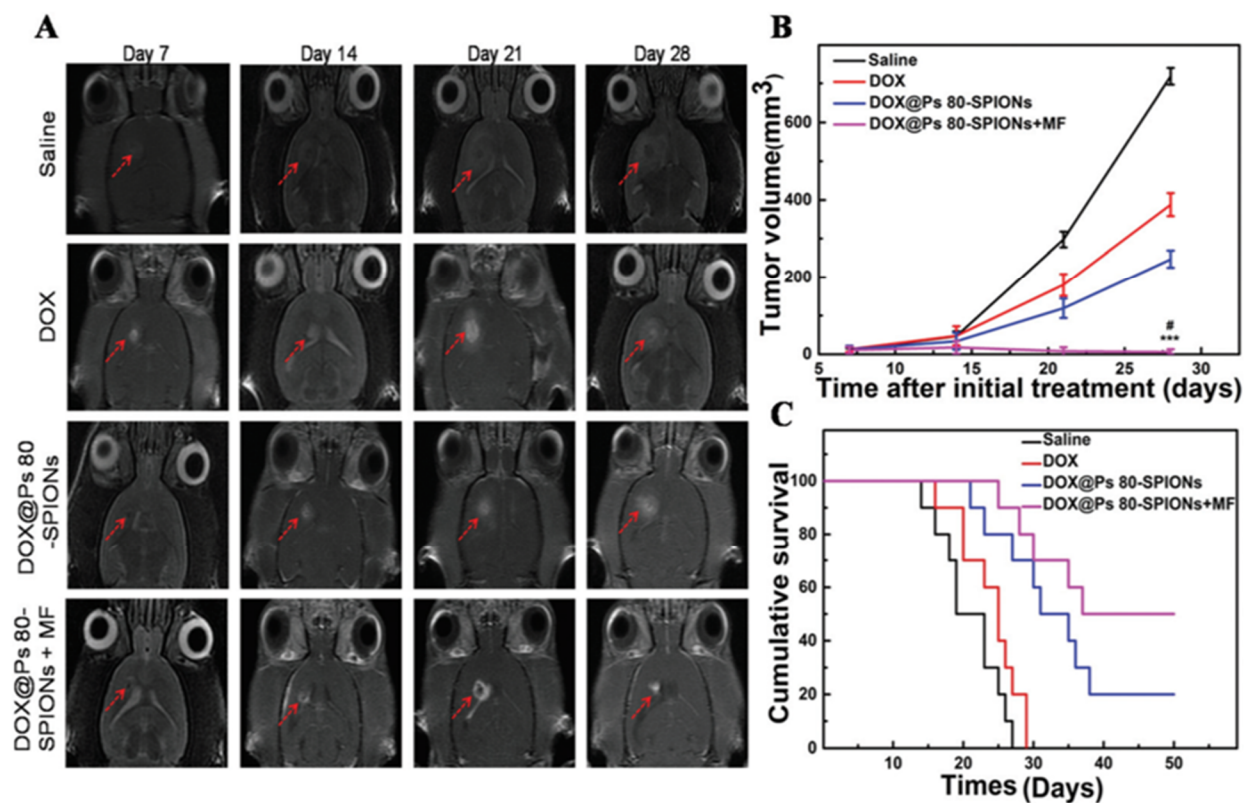


Fig. 1.6. (a) MRI of tumors in C6 glioma-bearing rats. (b) tumor volumes upon treatment. (The relative tumor volume i.e. day 7 vs day 28 in saline, DOX, DOX@Ps 80-SPIONs, and DOX@Ps 80-SPIONs with an MF were 69.78, 60.39, 50.46 and 0.9, respectively. (c) cumulative survival of animals upon treatment. The animal in saline, DOX, DOX@Ps 80-SPIONs, and DOX@Ps 80-SPIONs with an MF showed 17.8, 32.4, 38.5, and 79.2 days of survival, respectively. Reproduced with permission from Ref [32].

Currently, IONPs are being utilized in clinical trials for MHT of GBM [207] and prostate carcinoma [208]. In addition, the efficacy of MHT with IONPs in conjunction with radiotherapy has been reported in clinical studies [207,209]. NanoTherm® (MagForce Nanotechnologies AG, Berlin, Germany), aminosilane-coated superparamagnetic iron oxide nanoparticles with  $D_H$ :17 nm, has been approved in Europe for clinical trials in combination with radiotherapy in patients with recurrent GBM [31,210]. Generally, the superiority of aminosilane-coated IONPs against dextran-coated IONPs in MHT following intratumoral injection was reported due to the higher tumor uptake of the former in pre-clinical studies. The aminosilane-coated IONPs (with 6–10 °C temperature rise) provided 1.7–4.5-fold prolongation in survival time of RG-2 glioma-bearing rats

due to their homogeneous and intratumoral distribution, while no significant effect on survival of rats receiving dextran-coated IONPs (with a temperature rise of 2 °C) was observed [211].

In the first clinical trial, feasibility and tolerability of MHT with intratumorally injected NanoTherm® and subsequent heating of the nanoparticles in an AMF was evaluated on 14 GBM patients. They received 4–10 thermotherapy sessions (AMF strength of 3.8–13.5 kA/m) and single fractions (2 Gy) of radiotherapy (a median dose of 30 Gy, 16–70 Gy). The MHT was well tolerated by all patients with minor or no side effects, and the tumor temperature reached 44.6 °C (42.4–49.5 °C) during the treatment. Although five patients received radiation at the doses less than 60 Gy (that is the recommended dose for GBM patients), and only five patients received chemotherapy, the median survival was reported 14.5 months [209] that is comparable with the median survival of 14.6 months for patients receiving the current standard of care (radiotherapy at dose of 60 Gy plus temozolomide) [5].

In a follow-up phase II clinical study, 66 GBM patients (59 with recurrent GBM) received an intratumoral injection of NanoTherm® followed by MHT in combination with fractionated radiotherapy (a median dose of 30 Gy). The overall survival after primary tumor diagnosis (OS-1), increased to 23.2 months [207], which significantly exceeded the median 14.6 months in the reference group [5]. In addition, overall survival following diagnosis of first tumor recurrence (OS-2) was reported to be 13.4 months *vis à vis* 6.2 months in another study with a similar population. The clinical outcomes of this study suggested a remarkable augmentation in the overall survival of GBM patients through the combination of thermotherapy with a lower radiotherapy dosage of 30 Gy [207].

In a more recent preliminary study on 6 recurrent GBM patients, NanoTherm® was coated on the wall of the cavity after tumor resection, using a hydroxycellulose mesh and fibrin

glue, termed as NanoPaste<sup>®</sup> (Fig. 1.7a), followed by six 1-h hyperthermia sessions and concurrent fractionated radiotherapy at a dose of 39.6 Gy. The patients treated at first recurrence showed a median OS of 23.9 months, while at second recurrence or later the median OS was found to be 7.1 months. Moreover, the surrounding tissue exhibited an upregulation of Caspase-3 and heat shock protein 70, and a significant increase in CD3+, CD8+ T-cells as well as CD68+ macrophages upon the intracavitary thermotherapy (Fig. 1.7b,c). The NanoPaste is currently proceeding to a phase-I study on patients at first recurrence GBM who are eligible for re-surgery [212]. Therefore, intracavitary thermotherapy with IONPs combined with radiotherapy can be a promising therapeutic modality in GBM patients at first recurrence, warranting further clinical studies.

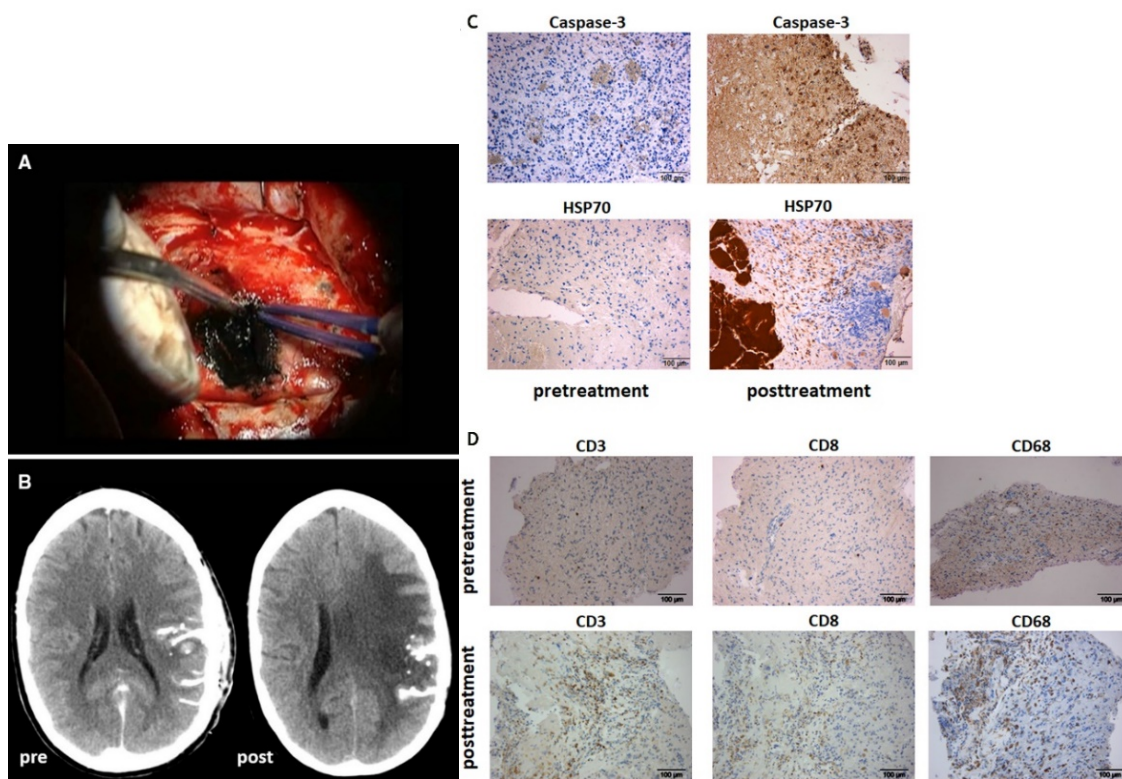


Fig. 1.7. (A) intraoperative picture of NanoPaste application onto the resection cavity wall. (B) representative CT scans of a patient prior (left side) and post-thermotherapy (right side) with remarkable edema around nanoparticle deposits. (C) Representative pictures from a patient demonstrating enhanced Caspase-3 and HSP70 expression after treatment. (D) Representative pictures of immunohistochemical staining. They demonstrate a significant infiltration of CD3+, CD8+ and CD68+ cells after intracavitary thermotherapy, while the pre-treatment samples do not exhibit T-cell immune cell infiltrates (magnification  $\times 200$ ). Reproduced with permission from Ref [212].

Still, many attempts are being made to further improve the functionality of IONPs in MHT of glioma, in pre-clinical studies. In one of the recent studies, biologically synthesized iron oxide nanoparticles, called magnetosomes were prepared using MSR-1 magnetotactic bacteria. The magnetosomes were reported to show improved magnetic properties owing to a high level of crystallinity and fewer aggregation thanks to the chain arrangement, leading to homogenous tumor temperature distribution [213,214]. The magnetosome mineral core was purified to remove most organic material and endotoxins (endotoxin level of 10–100 EU mL<sup>-1</sup> mg<sup>-1</sup>) and coated with poly-L-lysine (M-PLL). Thence, the antitumor efficacy of the coated magnetosomes was studied in intracranial U87-Luc tumor bearing-mice upon their intratumoral administration and followed magnetic sessions (AMF of strength 27 mT and frequency 202 kHz., 23-27 magnetic sessions each lasting 30 min). In 100% of treated mice, the tumor was fully disappeared within 68 days post-implantation, confirmed by the absence of tumor cells through histological analysis, and they survived whole of the experiment (350 days). However, in the control group with commercial IONPs, tumor disappearance was only observed in 20% of the treated mice [213]. In a similar work by the same group, magnetosomes with controlled endotoxin release (endotoxin level of 1400–8400 EU mL<sup>-1</sup> mg<sup>-1</sup>) were prepared demonstrating superior antitumor activity compared to commercial IONPs that can be attributed to both larger production of heat and endotoxin release under AMF application, which can potentially be replaced by nonpyrogenic substance such as M-PLA. Of note, magnetosomes occupied only 10% of the whole tumor volume when exhibited tumor destruction in the animals. This means that an indirect mechanism such as an immune reaction might be involved in the tumor regression [215].

The prolonged retention time of IONPs localized within tumor enables successful multiple MHT upon a single injection of the nanoparticles [216,217]. To impart long-term nanoparticle

retention within the tumor, PEG-based magnetic hydrogel was fabricated by incorporating IONPs, showing the potential capability of implantation after surgical resection of the GBM tumor or injection *in situ* [194]. Later, an injectable solution of thermosensitive poly(organophosphazene) (PPZ) nanocapsules embedded with SPIONs in the core ( $D_H$ : 177 nm) was prepared. The resulting solution could be transformed into hydrogel form at body temperature *via* the hydrophobic interaction. The SPION-loaded nanocapsule hydrogels (SPION-NHs) could extend the SPIONs retention within tumors after a single intratumoral injection by more than three weeks leading to increase tumor temperature to 45°C for multiple MHT, while in the case of intratumorally injected PEG-SPIONs solution as the control, the tumor temperature reduced from 44 °C after the first MHT to 38 °C after the fourth MHT *ipso facto* their fast dissipation. Correspondingly, the tumor was significantly eradicated by four cycles of MHT in subcutaneously U-87 MG tumor-bearing nude mice treated with SPION-NHs, while in the cohort treated with PEG-SPIONs, no significant reduction in tumor size was observed [216].

#### 1.4.6.2. Magnetic Hyperthermia to Trigger Drug Release from IONPs

Magnetic hyperthermia also can be utilized as a drug-releasing trigger providing a controlled site-specific drug release upon heating the IONP-based formulations [218]. In fact, the heat generated by the magnetic IONPs under AMF is recruited as a trigger for on-demand drug release from the IONPs at the tumor site [219]. To develop a magnetic hyperthermia-responsive drug delivery system, Hayashi et al., [219] synthesized DOX-containing carboxylic polypyrrole nanoparticles with glass-transition temperature ( $T_g$ ) of 44°C, and IONPs were incorporated into the nanoparticles. During exposure to the AMF, the IONPs produced heat above the  $T_g$  resulting in the softening of the polymer phase that allows the release of DOX (~60% of the DOX content was released by 20-min exposure to AMF). Magnetic field-responsive iron oxide-loaded hollow

mesoporous silica nanocapsules containing DOX were also synthesized by Lu et al., [220]. Exposing to an AMF markedly enhanced the release of DOX by 2.6-fold compared to the non-AMF-stimulated nanocapsules. This accelerated drug release could be attributed to the temperature gradient that generates between the core versus the outside environment of the nanocapsules that consequently stimulates the drug diffusion to the surrounding media.

In another study, positively charged tumor necrosis factor-related apoptosis-inducing ligand (TRAIL) and hydrophobic SPIONs were complexed with negatively charged PPZ *via* ionic and hydrophobic interactions, respectively, to form thermosensitive and injectable TRAIL/SPION nanocomplex hydrogels providing an MHT-mediated release of TRAIL through hydrogel dissolution. Thanks to the synergistic anti-tumor effects of MHT and TRAIL, significant tumor reduction was observed after 2 cycles of mild MHT at 43 °C (tumor's  $V/V_{\text{initial}}$  of 15.3, *ca.* 15.5, 13.6, and 1.3 for untreated, MHT alone, TRAIL-SPION-NHs alone, and TRAIL-SPION-NHs with MHT, respectively) [217].

#### 1.4.7. Concluding Remarks and Future Prospects

Engineered IONPs due to their biocompatibility, biodegradability and tunable magnetic properties have extensively studied in imaging, drug delivery and magnetic hyperthermia therapy in glioma models. Generally, engineered IONPs not only can be employed as T1 and T2 MRI contrast agents, but also can be functionalized with other imaging probes allowing multi-modal imaging techniques (e.g. PET, NIRF) in one system. IONPs also can be utilized as efficacious drug delivery systems to enhance transportation of the chemotherapeutics across the BBB, improve their pharmacokinetics, overcome the MDR and efflux transporters of cancer cells, and provide a ligand-mediated as well as site-specific magnetic targeting for glioma therapy. Moreover, IONPs

can be exploited to induce localized magnetic hyperthermia under an alternating magnetic field, demonstrating synergistic anti-tumor effects with radiotherapy in glioma models. Taken together, IONPs as efficacious theranostic tools, can amalgamate multiple diagnosis and therapeutic regimens to provide complementary information for early diagnosis, surgical resection, and therapeutic follow-up, while showing synergistic therapeutic effects of multiple drugs/regimens, in one system.

Currently, Ferumoxytol is the only FDA-approved IONP-based formulation, recommended for treatment of iron deficiency anemia in adult patients which is also under clinical investigations for MRI imaging in brain tumors. Moreover, with respect to the application of IONPs in MHT, NanoTherm® in combination with fractionated radiotherapy has shown some improvements in the overall survival of GBM patients in the early clinical studies, necessitating further investigations. Hitherto, in spite of some promising results in animal models, no IONP-based drug delivery systems have yet entered clinical studies, highlighting the importance of extensive pre-clinical studies to develop more efficacious formulations.

The IONP-based formulations that have yet been developed for clinical trials mostly rely on passive targeting through the EPR effect. While the EPR effect has found applicable in pre-clinical studies, the EPR effect alone may not be sufficient in clinical trials for all patients. Moreover, the EPR strongly depends on size and progression of the tumor while for early stage of the brain tumors, the EPR effect does not play an important role. In addition, the EPR effect in humans is impacted by tumor heterogeneity as well as interpatient variability. These hurdles highlight the importance of developing IONP-based formulations with the capability of ligand-mediated active targeting and/or transient BBB disruption approaches for clinical applications. Moreover, magnetic targeting can simultaneously be applied using an external magnetic field to

regulate IONP systemic biodistribution and enhance tumor exposure to the nanoparticles and their payloads by holding them at the desired site of action.

The non-invasive transient disruption of the BBB through either osmotic solutions, cadherin peptides or physical approaches like FUS have also been successfully applied in pre-clinical studies to enhance penetration of therapeutic agents into the tumor site of the brain. The applications of both mannitol (egs. NCT02861898, NCT01269853) and FUS (eg. NCT02343991) for BBB opening in patients with brain tumors are still under clinical investigations. Moreover, cadherin peptides have shown significant enhanced paracellular diffusion of various marker molecules through the BBB into the brain *in vivo* via inhibition of the cell-adhesion protein interactions at the intercellular junctions [169].

In comparison to the systematically osmotic disruption of the BBB, the FUS provides the advantages of the local BBB disruption through a physical approach. This local disruption will be more important when used in combination with magnetic targeting to draw IONPs to the site of action, then augment their penetration into the brain by applying the FUS. Therefore, this local approach not only can enhance the tumor exposure to the IONPs, but also reduces systemic BBB opening and correspondingly diminish the risk of CNS toxicity or extensive entering various substances into the brain. However, as discussed in section 1.5, intensity of the FUS beam decreases along gradients extending out from the center point of the beam [187]. This may lead to a non-uniform opening of the BBB, while the drug concentration gradient is the only driving force to deliver the drug to the invading and metastatic tumor cells at the therapeutic levels. Besides, this gradient of the drug concentration may lead to rapid propagation of the drug, reducing the concentration of the drug to below the therapeutic level at the tumor site.

Alternatively, using cadherin peptides has potentially the advantages of uniform enhanced permeability of the BBB leading to the homogenous and sufficient delivery of the drugs into the tumor and metastatic sites. Moreover, cadherin peptides have shown a fast time frame for BBB disruption (3-6 min) with acceptable recovery time for re-establishment of the BBB integrity (60 min) *in vivo*. This acceptable recovery time of the BBB integrity can reduce the risk of an uncontrolled influx of low and high molecular weight substances from the blood into the brain and consequently decreases the risk of neurological toxicity that might be caused by the conventional hyperosmotic disruption method using mannitol.

Intratumoral administration of IONPs (NanoTherm<sup>®</sup>, or NanoPaste<sup>®</sup>) has also successfully been employed in clinical practice for MHT to bypass the BBB and provide high doses of IONPs at the tumor site, which might have the potential to be utilized in drug delivery. Still, the intratumoral injection of IONPs mainly relies on the tumor detection by the MRI. However, the MRI is likely not to show most peripheral portions of the tumor where the invading tumor cells infiltrate healthy brain parenchyma without an extensive BBB disruption and neoangiogenesis [18,19]. In other words, the normal permeability of the BBB does not allow the gadolinium to leak out into the interstitial tissues, leading to no or minimal contrast enhancement of the peripheral tumor cells [19].

Taken together, it is envisaged that systemic administration of IONPs in combination with magnetic targeting and the non-invasive transient disrupting methods of the BBB, in particular the cadherin peptides can effectively address the current limitations of applying nanoparticles and will offer more efficacious theranostic platforms for patients suffering from brain tumors. In this context, systematically drug delivery with IONPs concomitant with transient disruption of the

BBB can potentially overcome the clinical shortcomings of the current approaches that merely rely on the EPR effect or active targeting.

## 1.4.8. References

- 1 Grauwet, K. and Chiocca, E.A. (2016) Glioma and microglia, a double entendre. *Nature immunology* 17 (11), 1240
- 2 Weller, M. et al. (2015) Glioma. *Nature reviews Disease primers* 1, 15017
- 3 Ferrer, V.P. et al. (2018) Glioma infiltration and extracellular matrix: key players and modulators. *Glia* 66 (8), 1542-1565
- 4 Paw, I. et al. (2015) Mechanisms regulating glioma invasion. *Cancer letters* 362 (1), 1-7
- 5 Stupp, R. et al. (2005) Radiotherapy plus concomitant and adjuvant temozolomide for glioblastoma. *New England Journal of Medicine* 352 (10), 987-996
- 6 Ankri, R. et al. (2016) Gold nanorods based air scanning electron microscopy and diffusion reflection imaging for mapping tumor margins in squamous cell carcinoma. *ACS nano* 10 (2), 2349-2356
- 7 Kircher, M.F. et al. (2012) A brain tumor molecular imaging strategy using a new triple-modality MRI-photoacoustic-Raman nanoparticle. *Nature medicine* 18 (5), 829
- 8 Norouzi, M. et al. (2018) Salinomycin-loaded Nanofibers for Glioblastoma Therapy. *Scientific reports* 8 (1), 9377
- 9 Norouzi, M. (2018) Recent advances in brain tumor therapy: application of electrospun nanofibers. *Drug discovery today*
- 10 Norouzi, M. et al. (2017) Electrospun-based systems in cancer therapy. In *Electrospun Materials for Tissue Engineering and Biomedical Applications*, pp. 337-356, Elsevier
- 11 Karabeber, H. et al. (2014) Guiding brain tumor resection using surface-enhanced Raman scattering nanoparticles and a hand-held Raman scanner. *Acs Nano* 8 (10), 9755-9766
- 12 Cheng, Y. et al. (2014) Blood-brain barrier permeable gold nanoparticles: an efficient delivery platform for enhanced malignant glioma therapy and imaging. *Small* 10 (24), 5137-5150
- 13 Norouzi, M. et al. (2016) Injectable hydrogel-based drug delivery systems for local cancer therapy. *Drug discovery today*
- 14 Di Marco, L.Y. et al. (2015) Vascular dysfunction in the pathogenesis of Alzheimer's disease—a review of endothelium-mediated mechanisms and ensuing vicious circles. *Neurobiology of disease* 82, 593-606
- 15 Tavazoie, M. et al. (2008) A specialized vascular niche for adult neural stem cells. *Cell stem cell* 3 (3), 279-288
- 16 Hola, K. et al. (2015) Tailored functionalization of iron oxide nanoparticles for MRI, drug delivery, magnetic separation and immobilization of biosubstances. *Biotechnology Advances* 33 (6), 1162-1176
- 17 Verger, A. and Langen, K.-J. (2017) PET Imaging in glioblastoma: use in clinical practice. In *Glioblastoma [Internet]*, Codon Publications
- 18 Meola, A. et al. (2018) Gold nanoparticles for brain tumor imaging: a systematic review. *Frontiers in neurology* 9
- 19 Villanueva-Meyer, J.E. et al. (2017) Current clinical brain tumor imaging. *Neurosurgery* 81 (3), 397-415
- 20 Liu, H. et al. (2016) Application of iron oxide nanoparticles in glioma imaging and therapy: from bench to bedside. *Nanoscale* 8 (15), 7808-7826
- 21 Huang, J. et al. (2016) Magnetic nanoparticle facilitated drug delivery for cancer therapy with targeted and image-guided approaches. *Advanced functional materials* 26 (22), 3818-3836
- 22 Daglioglu, C. (2017) Enhancing tumor cell response to multidrug resistance with pH-sensitive quercetin and doxorubicin conjugated multifunctional nanoparticles. *Colloids and Surfaces B: Biointerfaces* 156, 175-185
- 23 Sharma, R. et al. (2017) Theranostic nanomedicine; a next generation platform for cancer diagnosis and therapy. *Mini reviews in medicinal chemistry* 17 (18), 1746-1757

- 24 Laurent, S. et al. (2014) Superparamagnetic iron oxide nanoparticles for delivery of therapeutic agents: opportunities and challenges. *Expert opinion on drug delivery* 11 (9), 1449-1470
- 25 Abenojar, E.C. et al. (2016) Structural effects on the magnetic hyperthermia properties of iron oxide nanoparticles. *Progress in Natural Science: Materials International* 26 (5), 440-448
- 26 Bernd, H. et al. (2009) Safety and tolerability of ultrasmall superparamagnetic iron oxide contrast agent: comprehensive analysis of a clinical development program. *Investigative radiology* 44 (6), 336-342
- 27 McCormack, P.L. (2012) Ferumoxytol. *Drugs* 72 (15), 2013-2022
- 28 Schiller, B. et al. (2014) Safety and effectiveness of ferumoxytol in hemodialysis patients at 3 dialysis chains in the United States over a 12-month period. *Clinical therapeutics* 36 (1), 70-83
- 29 Muehe, A.M. et al. (2016) Safety report of ferumoxytol for magnetic resonance imaging in children and young adults. *Investigative radiology* 51 (4), 221
- 30 Dadfar, S.M. et al. (2019) Iron oxide nanoparticles: Diagnostic, therapeutic and theranostic applications. *Advanced drug delivery reviews* 138, 302-325
- 31 El-Boubbou, K. (2018) Magnetic iron oxide nanoparticles as drug carriers: clinical relevance. *Nanomedicine* 13 (8), 953-971
- 32 Xu, H.-L. et al. (2016) Glioma-targeted superparamagnetic iron oxide nanoparticles as drug-carrying vehicles for theranostic effects. *Nanoscale* 8 (29), 14222-14236
- 33 Chertok, B. et al. (2008) Iron oxide nanoparticles as a drug delivery vehicle for MRI monitored magnetic targeting of brain tumors. *Biomaterials* 29 (4), 487-496
- 34 Feng, Q. et al. (2018) Uptake, distribution, clearance, and toxicity of iron oxide nanoparticles with different sizes and coatings. *Scientific reports* 8 (1), 2082
- 35 Mou, X. et al. (2015) Applications of magnetic nanoparticles in targeted drug delivery system. *Journal of nanoscience and nanotechnology* 15 (1), 54-62
- 36 Ghoreishian, S.M. et al. (2018)  $\gamma$ -radiolysis as a highly efficient green approach to the synthesis of metal nanoclusters: a review of mechanisms and applications. *Chemical Engineering Journal*
- 37 Grenier, P. et al. (2018) Anti-polyethylene glycol antibodies alter the protein corona deposited on nanoparticles and the physiological pathways regulating their fate in vivo. *Journal of controlled release* 287, 121-131
- 38 Jiang, W. et al. (2017) Designing nanomedicine for immuno-oncology. *Nature Biomedical Engineering* 1 (2), 0029
- 39 Rajkumar, S. and Prabakaran, M. (2018) Multi-functional nanocarriers based on iron oxide nanoparticles conjugated with doxorubicin, poly (ethylene glycol) and folic acid as theranostics for cancer therapy. *Colloids and Surfaces B: Biointerfaces* 170, 529-537
- 40 Khandhar, A. et al. (2017) Evaluation of PEG-coated iron oxide nanoparticles as blood pool tracers for preclinical magnetic particle imaging. *Nanoscale* 9 (3), 1299-1306
- 41 Abdollah, M.R. et al. (2018) Fucoidan prolongs the circulation time of dextran-coated iron oxide nanoparticles. *ACS nano* 12 (2), 1156-1169
- 42 Remya, N. et al. (2016) Toxicity, toxicokinetics and biodistribution of dextran stabilized iron oxide nanoparticles for biomedical applications. *International journal of pharmaceuticals* 511 (1), 586-598
- 43 Soares, P.I. et al. (2016) Thermal and magnetic properties of chitosan-iron oxide nanoparticles. *Carbohydrate polymers* 149, 382-390
- 44 Saikia, C. et al. (2016) Effect of crosslinker on drug delivery properties of curcumin loaded starch coated iron oxide nanoparticles. *International journal of biological macromolecules* 93, 1121-1132
- 45 Arami, H. et al. (2015) In vivo delivery, pharmacokinetics, biodistribution and toxicity of iron oxide nanoparticles. *Chemical Society Reviews* 44 (23), 8576-8607
- 46 Cole, A.J. et al. (2011) Polyethylene glycol modified, cross-linked starch-coated iron oxide nanoparticles for enhanced magnetic tumor targeting. *Biomaterials* 32 (8), 2183-2193
- 47 Cole, A.J. et al. (2011) Magnetic brain tumor targeting and biodistribution of long-circulating PEG-modified, cross-linked starch-coated iron oxide nanoparticles. *Biomaterials* 32 (26), 6291-6301

- 48 Maurizi, L. et al. (2015) Influence of surface charge and polymer coating on internalization and biodistribution of polyethylene glycol-modified iron oxide nanoparticles. *Journal of biomedical nanotechnology* 11 (1), 126-136
- 49 Sun, C. et al. (2008) Magnetic nanoparticles in MR imaging and drug delivery. *Advanced drug delivery reviews* 60 (11), 1252-1265
- 50 Sun, Z. et al. (2013) Characterization of cellular uptake and toxicity of aminosilane-coated iron oxide nanoparticles with different charges in central nervous system-relevant cell culture models. *International journal of nanomedicine* 8, 961
- 51 Chertok, B. et al. (2010) Polyethyleneimine-modified iron oxide nanoparticles for brain tumor drug delivery using magnetic targeting and intra-carotid administration. *Biomaterials* 31 (24), 6317-6324
- 52 Janát-Amsbury, M.M. et al. (2011) Geometry and surface characteristics of gold nanoparticles influence their biodistribution and uptake by macrophages. *European Journal of Pharmaceutics and Biopharmaceutics* 77 (3), 417-423
- 53 Liu, Y. et al. (2017) Suppressing Nanoparticle-Mononuclear Phagocyte System Interactions of Two-Dimensional Gold Nanorings for Improved Tumor Accumulation and Photothermal Ablation of Tumors. *ACS nano* 11 (10), 10539-10548
- 54 Niikura, K. et al. (2013) Gold nanoparticles as a vaccine platform: influence of size and shape on immunological responses in vitro and in vivo. *ACS nano* 7 (5), 3926-3938
- 55 Salatin, S. et al. (2015) Effect of the surface modification, size, and shape on cellular uptake of nanoparticles. *Cell biology international* 39 (8), 881-890
- 56 Black, K.C.L. et al. (2014) Radioactive <sup>198</sup>Au-doped nanostructures with different shapes for in vivo analyses of their biodistribution, tumor uptake, and intratumoral distribution. *ACS nano* 8 (5), 4385-4394
- 57 Huang, X. et al. (2011) The shape effect of mesoporous silica nanoparticles on biodistribution, clearance, and biocompatibility in vivo. *ACS nano* 5 (7), 5390-5399
- 58 Sun, Z. et al. (2016) Differential internalization of brick shaped iron oxide nanoparticles by endothelial cells. *Journal of Materials Chemistry B* 4 (35), 5913-5920
- 59 Lee, J.H. et al. (2014) Rod-shaped iron oxide nanoparticles are more toxic than sphere-shaped nanoparticles to murine macrophage cells. *Environmental toxicology and chemistry* 33 (12), 2759-2766
- 60 Roohi, F. et al. (2012) Studying the effect of particle size and coating type on the blood kinetics of superparamagnetic iron oxide nanoparticles. *International journal of nanomedicine* 7, 4447
- 61 In, G.K. and Nieva, J. (2015) Emerging chemotherapy agents in lung cancer: nanoparticles therapeutics for non-small cell lung cancer. *Translational Cancer Research* 4 (4), 340-355
- 62 Shubayev, V.I. et al. (2009) Magnetic nanoparticles for theragnostics. *Advanced drug delivery reviews* 61 (6), 467-477
- 63 Longmire, M. et al. (2008) Clearance properties of nano-sized particles and molecules as imaging agents: considerations and caveats.
- 64 Kievit, F.M. and Zhang, M. (2011) Surface engineering of iron oxide nanoparticles for targeted cancer therapy. *Accounts of chemical research* 44 (10), 853-862
- 65 Gupta, A.K. and Gupta, M. (2005) Synthesis and surface engineering of iron oxide nanoparticles for biomedical applications. *biomaterials* 26 (18), 3995-4021
- 66 Perrault, S.D. et al. (2009) Mediating tumor targeting efficiency of nanoparticles through design. *Nano letters* 9 (5), 1909-1915
- 67 Jiang, W. et al. (2015) Remodeling tumor vasculature to enhance delivery of intermediate-sized nanoparticles. *Acs Nano* 9 (9), 8689-8696
- 68 Huang, K. et al. (2012) Size-dependent localization and penetration of ultrasmall gold nanoparticles in cancer cells, multicellular spheroids, and tumors in vivo. *ACS nano* 6 (5), 4483-4493
- 69 Sun, Z. (2016) Characterization of iron oxide nanoparticles (IONPs) for brain targeted delivery.

- 70 Serlin, Y. et al. (2015) Anatomy and physiology of the blood–brain barrier. In *Seminars in cell & developmental biology* (Vol. 38), pp. 2-6, Elsevier
- 71 Daina, A. and Zoete, V. (2016) A boiled-egg to predict gastrointestinal absorption and brain penetration of small molecules. *ChemMedChem* 11 (11), 1117-1121
- 72 Löscher, W. and Potschka, H. (2005) Blood-brain barrier active efflux transporters: ATP-binding cassette gene family. *NeuroRx* 2 (1), 86-98
- 73 Kreuter, J. (2013) Mechanism of polymeric nanoparticle-based drug transport across the blood-brain barrier (BBB). *Journal of microencapsulation* 30 (1), 49-54
- 74 Zhang, T.-T. et al. (2016) Strategies for transporting nanoparticles across the blood–brain barrier. *Biomaterials science* 4 (2), 219-229
- 75 Schleich, N. et al. (2015) Iron oxide-loaded nanotheranostics: major obstacles to in vivo studies and clinical translation. *Journal of Controlled Release* 198, 35-54
- 76 Meyers, J.D. et al. (2013) Nanoparticles for imaging and treating brain cancer. *Nanomedicine* 8 (1), 123-143
- 77 Danhier, F. (2016) To exploit the tumor microenvironment: Since the EPR effect fails in the clinic, what is the future of nanomedicine? *Journal of Controlled Release* 244, 108-121
- 78 Golombek, S.K. et al. (2018) Tumor targeting via EPR: Strategies to enhance patient responses. *Advanced drug delivery reviews*
- 79 Jain, R.K. et al. (2014) The role of mechanical forces in tumor growth and therapy. *Annual review of biomedical engineering* 16, 321-346
- 80 Liu, Y. and Lu, W. (2012) Recent advances in brain tumor-targeted nano-drug delivery systems. *Expert opinion on drug delivery* 9 (6), 671-686
- 81 Wadajkar, A.S. et al. (2017) Tumor-targeted nanotherapeutics: overcoming treatment barriers for glioblastoma. *Wiley Interdisciplinary Reviews: Nanomedicine and Nanobiotechnology* 9 (4)
- 82 Wang, Z. et al. (2017) Active targeting theranostic iron oxide nanoparticles for MRI and magnetic resonance-guided focused ultrasound ablation of lung cancer. *Biomaterials* 127, 25-35
- 83 Bakhtiary, Z. et al. (2016) Targeted superparamagnetic iron oxide nanoparticles for early detection of cancer: Possibilities and challenges. *Nanomedicine: Nanotechnology, Biology and Medicine* 12 (2), 287-307
- 84 Yang, J. et al. (2015) Conjugation of iron oxide nanoparticles with RGD-modified dendrimers for targeted tumor MR imaging. *ACS applied materials & interfaces* 7 (9), 5420-5428
- 85 Luo, Y. et al. (2015) RGD-functionalized ultrasmall iron oxide nanoparticles for targeted T 1-weighted MR imaging of gliomas. *Nanoscale* 7 (34), 14538-14546
- 86 Shevtsov, M.A. et al. (2014) Superparamagnetic iron oxide nanoparticles conjugated with epidermal growth factor (SPION–EGF) for targeting brain tumors. *International journal of nanomedicine* 9, 273
- 87 Bouras, A. et al. (2015) Radiosensitivity enhancement of radioresistant glioblastoma by epidermal growth factor receptor antibody-conjugated iron-oxide nanoparticles. *Journal of neuro-oncology* 124 (1), 13-22
- 88 Hadjipanayis, C.G. et al. (2010) EGFRvIII antibody–conjugated iron oxide nanoparticles for magnetic resonance imaging–guided convection-enhanced delivery and targeted therapy of glioblastoma. *Cancer research*, 0008-5472. CAN-0010-1022
- 89 Jiang, W. et al. (2012) Conjugation of functionalized SPIONs with transferrin for targeting and imaging brain glial tumors in rat model. *PloS one* 7 (5), e37376
- 90 Abakumov, M.A. et al. (2015) VEGF-targeted magnetic nanoparticles for MRI visualization of brain tumor. *Nanomedicine: Nanotechnology, Biology and Medicine* 11 (4), 825-833
- 91 Chen, G.-J. et al. (2014) Angiopep-pluronic F127-conjugated superparamagnetic iron oxide nanoparticles as nanotheranostic agents for BBB targeting. *Journal of Materials Chemistry B* 2 (34), 5666-5675
- 92 Ding, H. et al. (2014) Enhanced blood–brain barrier transmigration using a novel transferrin embedded fluorescent magneto-liposome nanoformulation. *Nanotechnology* 25 (5), 055101

- 93 Kievit, F.M. et al. (2010) Chlorotoxin labeled magnetic nanovectors for targeted gene delivery to glioma. *Acs Nano* 4 (8), 4587-4594
- 94 Veiseh, O. et al. (2009) Inhibition of tumor-cell invasion with chlorotoxin-bound superparamagnetic nanoparticles. *Small* 5 (2), 256-264
- 95 Fang, J.H. et al. (2014) Magnetic Core-Shell Nanocapsules with Dual-Targeting Capabilities and Co-Delivery of Multiple Drugs to Treat Brain Gliomas. *Advanced healthcare materials* 3 (8), 1250-1260
- 96 Xie, H. et al. (2011) Lactoferrin-conjugated superparamagnetic iron oxide nanoparticles as a specific MRI contrast agent for detection of brain glioma in vivo. *Biomaterials* 32 (2), 495-502
- 97 Ledford, H. (2016) Bankruptcy of nanomedicine firm worries drug developers: financial troubles of leading biotech firm highlight challenges of making innovative drugs. *Nature* 533 (7603), 304-306
- 98 Von Hoff, D.D. et al. (2016) Phase I study of PSMA-targeted docetaxel-containing nanoparticle BIND-014 in patients with advanced solid tumors. *Clinical Cancer Research* 22 (13), 3157-3163
- 99 Rosenblum, D. et al. (2018) Progress and challenges towards targeted delivery of cancer therapeutics. *Nature communications* 9 (1), 1410
- 100 Shi, J. et al. (2017) Cancer nanomedicine: progress, challenges and opportunities. *Nature Reviews Cancer* 17 (1), 20
- 101 Natfji, A.A. et al. (2017) Parameters affecting the enhanced permeability and retention effect: the need for patient selection. *Journal of pharmaceutical sciences* 106 (11), 3179-3187
- 102 Revia, R.A. and Zhang, M. (2016) Magnetite nanoparticles for cancer diagnosis, treatment, and treatment monitoring: recent advances. *Materials Today* 19 (3), 157-168
- 103 Guo, X. et al. (2017) External magnetic field-enhanced chemo-photothermal combination tumor therapy via iron oxide nanoparticles. *ACS applied materials & interfaces* 9 (19), 16581-16593
- 104 Alexiou, C. et al. (2000) Locoregional cancer treatment with magnetic drug targeting. *Cancer research* 60 (23), 6641-6648
- 105 Puttick, S. et al. (2015) PET, MRI, and simultaneous PET/MRI in the development of diagnostic and therapeutic strategies for glioma. *Drug discovery today* 20 (3), 306-317
- 106 Alexiou, G.A. et al. (2009) Glioma recurrence versus radiation necrosis: accuracy of current imaging modalities. *Journal of neuro-oncology* 95 (1), 1-11
- 107 Karunanithi, S. et al. (2013) Comparative diagnostic accuracy of contrast-enhanced MRI and 18 F-FDOPA PET-CT in recurrent glioma. *European radiology* 23 (9), 2628-2635
- 108 Pawelski, H. et al. (2014) SPECT-and PET-based approaches for noninvasive diagnosis of acute renal allograft rejection. *BioMed research international* 2014
- 109 Göttler, J. et al. (2017) Intra-lesional spatial correlation of static and dynamic FET-PET parameters with MRI-based cerebral blood volume in patients with untreated glioma. *European journal of nuclear medicine and molecular imaging* 44 (3), 392-397
- 110 Sánchez-Cabezas, S. et al. (2019) Combining magnetic hyperthermia and dual T1/T2 MR imaging using highly versatile iron oxide nanoparticles. *Dalton Transactions*
- 111 Penfield, J.G. and Reilly Jr, R.F. (2007) What nephrologists need to know about gadolinium. *Nature Reviews Nephrology* 3 (12), 654
- 112 Rogosnitzky, M. and Branch, S. (2016) Gadolinium-based contrast agent toxicity: a review of known and proposed mechanisms. *Biometals* 29 (3), 365-376
- 113 Kanda, T. et al. (2015) Gadolinium-based contrast agent accumulates in the brain even in subjects without severe renal dysfunction: evaluation of autopsy brain specimens with inductively coupled plasma mass spectroscopy. *Radiology* 276 (1), 228-232
- 114 McDonald, R.J. et al. (2015) Intracranial gadolinium deposition after contrast-enhanced MR imaging. *Radiology* 275 (3), 772-782
- 115 Darrah, T.H. et al. (2009) Incorporation of excess gadolinium into human bone from medical contrast agents. *Metallomics* 1 (6), 479-488

- 116 (2015) FDA Drug Safety Communication: FDA evaluating the risk of brain deposits with repeated use of gadolinium-based contrast agents for magnetic resonance imaging (MRI). (Vol. 2019)
- 117 Alcantara, D. et al. (2016) Iron oxide nanoparticles as magnetic relaxation switching (MRSw) sensors: Current applications in nanomedicine. *Nanomedicine: Nanotechnology, Biology and Medicine* 12 (5), 1253-1262
- 118 Hamilton, B.E. et al. (2011) Comparative analysis of ferumoxytol and gadoteridol enhancement using T1-and T2-weighted MRI in neuroimaging. *American Journal of Roentgenology* 197 (4), 981-988
- 119 Toth, G.B. et al. (2017) Current and potential imaging applications of ferumoxytol for magnetic resonance imaging. *Kidney international* 92 (1), 47-66
- 120 Liu, H. et al. (2016) Recombinant epidermal growth factor-like domain-1 from coagulation factor vii functionalized iron oxide nanoparticles for targeted glioma magnetic resonance imaging. *International journal of nanomedicine* 11, 5099
- 121 Shah, A. and Dobrovolskaia, M.A. (2018) Immunological effects of iron oxide nanoparticles and iron-based complex drug formulations: therapeutic benefits, toxicity, mechanistic insights, and translational considerations. *Nanomedicine: Nanotechnology, Biology and Medicine* 14 (3), 977-990
- 122 Anselmo, A.C. and Mitragotri, S. (2016) Nanoparticles in the clinic. *Bioengineering & translational medicine* 1 (1), 10-29
- 123 Shen, B. et al. (2016) Smart multifunctional magnetic nanoparticle-based drug delivery system for cancer thermo-chemotherapy and intracellular imaging. *ACS applied materials & interfaces* 8 (37), 24502-24508
- 124 Wang, Y.-X.J. (2015) Current status of superparamagnetic iron oxide contrast agents for liver magnetic resonance imaging. *World journal of gastroenterology* 21 (47), 13400
- 125 Gkagkanasiou, M. et al. (2016) USPIO-Enhanced MRI Neuroimaging: A Review. *Journal of Neuroimaging* 26 (2), 161-168
- 126 Oliveira, I.S. et al. (2016) Blood pool contrast agents for venous magnetic resonance imaging. *Cardiovascular diagnosis and therapy* 6 (6), 508
- 127 Barajas Jr, R.F. et al. (2018) Combined iron oxide nanoparticle ferumoxytol and gadolinium contrast enhanced MRI define glioblastoma pseudoprogression. *Neuro-oncology* 21 (4), 517-526
- 128 Choi, Y.J. et al. (2013) Pseudoprogression in patients with glioblastoma: added value of arterial spin labeling to dynamic susceptibility contrast perfusion MR imaging. *Acta Radiologica* 54 (4), 448-454
- 129 Thomas, A.A. et al. (2015) Dynamic contrast enhanced T1 MRI perfusion differentiates pseudoprogression from recurrent glioblastoma. *Journal of neuro-oncology* 125 (1), 183-190
- 130 Neuwelt, E.A. et al. (2007) The potential of ferumoxytol nanoparticle magnetic resonance imaging, perfusion, and angiography in central nervous system malignancy: a pilot study. *Neurosurgery* 60 (4), 601-612
- 131 Zhou, Z. et al. (2012) A synergistically enhanced T1–T2 dual-modal contrast agent. *Advanced materials* 24 (46), 6223-6228
- 132 Xiao, N. et al. (2014) T1–T2 dual-modal MRI of brain gliomas using PEGylated Gd-doped iron oxide nanoparticles. *Journal of colloid and interface science* 417, 159-165
- 133 Chen, K. et al. (2009) Triblock copolymer coated iron oxide nanoparticle conjugate for tumor integrin targeting. *Biomaterials* 30 (36), 6912-6919
- 134 Shi, X. and Shen, L. (2018) Integrin  $\alpha\beta3$  receptor targeting PET/MRI dual-modal imaging probe based on the  $^{64}\text{Cu}$  labeled manganese ferrite nanoparticles. *Journal of inorganic biochemistry* 186, 257-263
- 135 Jiang, L. et al. (2013) pH/temperature sensitive magnetic nanogels conjugated with Cy5. 5-labeled lactoferrin for MR and fluorescence imaging of glioma in rats. *Biomaterials* 34 (30), 7418-7428

- 136 Shevtsov, M.A. et al. (2015) Brain tumor magnetic targeting and biodistribution of superparamagnetic iron oxide nanoparticles linked with 70-kDa heat shock protein study by nonlinear longitudinal response. *Journal of Magnetism and Magnetic Materials* 388, 123-134
- 137 Lee, H.-Y. et al. (2008) PET/MRI dual-modality tumor imaging using arginine-glycine-aspartic (RGD)-conjugated radiolabeled iron oxide nanoparticles. *Journal of Nuclear Medicine* 49 (8), 1371-1379
- 138 Thomas, R. et al. (2013) Magnetic iron oxide nanoparticles for multimodal imaging and therapy of cancer. *International journal of molecular sciences* 14 (8), 15910-15930
- 139 Xie, J. et al. (2010) PET/NIRF/MRI triple functional iron oxide nanoparticles. *Biomaterials* 31 (11), 3016-3022
- 140 Desgrosellier, J.S. and Cheresch, D.A. (2010) Integrins in cancer: biological implications and therapeutic opportunities. *Nature Reviews Cancer* 10 (1), 9
- 141 Li, D. et al. (2018) First-in-human study of PET and optical dual-modality image-guided surgery in glioblastoma using <sup>68</sup>Ga-IRDye800CW-BBN. *Theranostics* 8 (9), 2508
- 142 Lee, C. et al. (2018) In vivo delineation of glioblastoma by targeting tumor-associated macrophages with near-infrared fluorescent silica coated iron oxide nanoparticles in orthotopic xenografts for surgical guidance. *Scientific reports* 8
- 143 Carril, M. (2017) Activatable probes for diagnosis and biomarker detection by MRI. *Journal of Materials Chemistry B* 5 (23), 4332-4347
- 144 Wang, Y. and Kohane, D.S. (2017) External triggering and triggered targeting strategies for drug delivery. *Nature Reviews Materials* 2 (6), 17020
- 145 Du, J. et al. (2015) Stimuli-responsive nanoparticles for targeting the tumor microenvironment. *Journal of Controlled Release* 219, 205-214
- 146 Joniec, A. et al. (2016) Magnetoliposomes as potential carriers of doxorubicin to tumours. *Chemistry—A European Journal* 22 (49), 17715-17724
- 147 German, S. et al. (2015) Liposomes loaded with hydrophilic magnetite nanoparticles: preparation and application as contrast agents for magnetic resonance imaging. *Colloids and Surfaces B: Biointerfaces* 135, 109-115
- 148 Ying, X.-Y. et al. (2011) Magnetic lipid nanoparticles loading doxorubicin for intracellular delivery: Preparation and characteristics. *Journal of Magnetism and Magnetic Materials* 323 (8), 1088-1093
- 149 Rostami, E. et al. (2014) Drug targeting using solid lipid nanoparticles. *Chemistry and physics of lipids* 181, 56-61
- 150 Kulkarni, J.A. et al. (2017) Rapid synthesis of lipid nanoparticles containing hydrophobic inorganic nanoparticles. *Nanoscale* 9 (36), 13600-13609
- 151 Allen, T.M. and Cullis, P.R. (2013) Liposomal drug delivery systems: from concept to clinical applications. *Advanced drug delivery reviews* 65 (1), 36-48
- 152 Frascione, D. et al. (2012) Ultrasmall superparamagnetic iron oxide (USPIO)-based liposomes as magnetic resonance imaging probes. *International journal of nanomedicine* 7, 2349
- 153 Amstad, E. et al. (2011) Triggered release from liposomes through magnetic actuation of iron oxide nanoparticle containing membranes. *Nano letters* 11 (4), 1664-1670
- 154 Ling, Y. et al. (2012) Temozolomide loaded PLGA-based superparamagnetic nanoparticles for magnetic resonance imaging and treatment of malignant glioma. *International journal of pharmaceutics* 430 (1-2), 266-275
- 155 Prabhu, S. et al. (2017) A polymeric temozolomide nanocomposite against orthotopic glioblastoma xenograft: tumor-specific homing directed by nestin. *Nanoscale* 9 (30), 10919-10932
- 156 Kievit, F.M. et al. (2011) Doxorubicin loaded iron oxide nanoparticles overcome multidrug resistance in cancer in vitro. *Journal of controlled release* 152 (1), 76-83
- 157 Shen, C. et al. (2019) Doxorubicin and indocyanine green loaded superparamagnetic iron oxide nanoparticles with Pegylated phospholipid coating for magnetic resonance with fluorescence imaging and chemotherapy of glioma. *International journal of nanomedicine* 14, 101

- 158 Mu, Q. et al. (2015) Stable and efficient Paclitaxel nanoparticles for targeted glioblastoma therapy. *Advanced healthcare materials* 4 (8), 1236-1245
- 159 Mu, Q. et al. (2016) Gemcitabine and chlorotoxin conjugated iron oxide nanoparticles for glioblastoma therapy. *Journal of Materials Chemistry B* 4 (1), 32-36
- 160 Kaluzova, M. et al. (2015) Targeted therapy of glioblastoma stem-like cells and tumor non-stem cells using cetuximab-conjugated iron-oxide nanoparticles. *Oncotarget* 6 (11), 8788
- 161 Freeman, A.C. et al. (2018) Convection-enhanced delivery of cetuximab conjugated iron-oxide nanoparticles for treatment of spontaneous canine intracranial gliomas. *Journal of neuro-oncology*, 1-11
- 162 Park, S. et al. (2010) Cellular uptake pathway and drug release characteristics of drug-encapsulated glycol chitosan nanoparticles in live cells. *Microscopy research and technique* 73 (9), 857-865
- 163 Kumar, M. et al. (2018) Beyond the Blood–Brain Barrier: Facing New Challenges and Prospects of Nanotechnology-Mediated Targeted Delivery to the Brain. In *Nanotechnology-Based Targeted Drug Delivery Systems for Brain Tumors*, pp. 397-437, Elsevier
- 164 ROSSMEISL, J. (2017) 21 Maximizing Local Access to Therapeutic Deliveries in Glioblastoma. Part V: Clinically Relevant Model for Testing New Therapeutic Approaches.
- 165 Saucier-Sawyer, J.K. et al. (2016) Distribution of polymer nanoparticles by convection-enhanced delivery to brain tumors. *Journal of Controlled Release* 232, 103-112
- 166 Elenes, E.Y. and Rylander, C.G. (2017) Maximizing Local Access to Therapeutic Deliveries in Glioblastoma. Part II: Arborizing Catheter for Convection-Enhanced Delivery in Tissue Phantoms. In *Glioblastoma [Internet]*, Codon Publications
- 167 Bernal, G.M. et al. (2014) Convection-enhanced delivery and in vivo imaging of polymeric nanoparticles for the treatment of malignant glioma. *Nanomedicine: Nanotechnology, Biology and Medicine* 10 (1), 149-157
- 168 Crawford, L. et al. (2016) Concepts, technologies, and practices for drug delivery past the blood–brain barrier to the central nervous system. *Journal of Controlled Release* 240, 251-266
- 169 Laksitorini, M.D. et al. (2015) Modulation of intercellular junctions by cyclic-ADT peptides as a method to reversibly increase blood–brain barrier permeability. *Journal of pharmaceutical sciences* 104 (3), 1065-1075
- 170 Zwiewka, M. et al. (2015) Osmotic stress modulates the balance between exocytosis and clathrin-mediated endocytosis in *Arabidopsis thaliana*. *Molecular plant* 8 (8), 1175-1187
- 171 MIYAGAMI, M. et al. (1990) Intra-arterial ACNU chemotherapy employing 20% mannitol osmotic blood-brain barrier disruption for malignant brain tumors. *Neurologia medico-chirurgica* 30 (8), 582-590
- 172 Iwadate, Y. et al. (1993) Intra-arterial mannitol infusion in the chemotherapy for malignant brain tumors. *Journal of neuro-oncology* 15 (2), 185-193
- 173 Boockvar, J.A. et al. (2011) Safety and maximum tolerated dose of superselective intraarterial cerebral infusion of bevacizumab after osmotic blood-brain barrier disruption for recurrent malignant glioma. *Journal of neurosurgery* 114 (3), 624-632
- 174 Sun, Z. et al. (2014) Magnetic field enhanced convective diffusion of iron oxide nanoparticles in an osmotically disrupted cell culture model of the blood–brain barrier. *International journal of nanomedicine* 9, 3013
- 175 Yang, J. et al. (2011) Detection of amyloid plaques targeted by USPIO-A $\beta$ 1–42 in Alzheimer's disease transgenic mice using magnetic resonance microimaging. *Neuroimage* 55 (4), 1600-1609
- 176 Wadghiri, Y.Z. et al. (2003) Detection of Alzheimer's amyloid in transgenic mice using magnetic resonance microimaging. *Magnetic Resonance in Medicine: An Official Journal of the International Society for Magnetic Resonance in Medicine* 50 (2), 293-302
- 177 McCarty, D. et al. (2009) Mannitol-facilitated CNS entry of rAAV2 vector significantly delayed the neurological disease progression in MPS IIIB mice. *Gene therapy* 16 (11), 1340
- 178 Chen, K.-B. et al. (2013) Intravenous mannitol does not increase blood–brain barrier permeability to inert dyes in the adult rat forebrain. *Neuroreport* 24 (6), 303-307

- 179 On, N.H. et al. (2014) Modulation of blood–brain barrier permeability in mice using synthetic E-cadherin peptide. *Molecular pharmaceutics* 11 (3), 974-981
- 180 Siegal, T. et al. (2000) In vivo assessment of the window of barrier opening after osmotic blood–brain barrier disruption in humans. *Journal of neurosurgery* 92 (4), 599-605
- 181 Sawyer, A.J. et al. (2006) New methods for direct delivery of chemotherapy for treating brain tumors. *The Yale journal of biology and medicine* 79 (3-4), 141-152
- 182 Liu, H.-L. et al. (2010) Blood-brain barrier disruption with focused ultrasound enhances delivery of chemotherapeutic drugs for glioblastoma treatment. *Radiology* 255 (2), 415-425
- 183 Liu, H.-L. et al. (2010) Magnetic resonance monitoring of focused ultrasound/magnetic nanoparticle targeting delivery of therapeutic agents to the brain. *Proceedings of the National Academy of Sciences* 107 (34), 15205-15210
- 184 Sattiraju, A. et al. (2017) Maximizing Local Access to Therapeutic Deliveries in Glioblastoma. Part IV: Image-Guided, Remote-Controlled Opening of the Blood–Brain Barrier for Systemic Brain Tumor Therapy.
- 185 Etame, A.B. et al. (2012) Enhanced delivery of gold nanoparticles with therapeutic potential into the brain using MRI-guided focused ultrasound. *Nanomedicine: Nanotechnology, Biology and Medicine* 8 (7), 1133-1142
- 186 Fan, C.-H. et al. (2013) SPIO-conjugated, doxorubicin-loaded microbubbles for concurrent MRI and focused-ultrasound enhanced brain-tumor drug delivery. *Biomaterials* 34 (14), 3706-3715
- 187 Mesiwala, A.H. et al. (2002) High-intensity focused ultrasound selectively disrupts the blood-brain barrier in vivo. *Ultrasound in medicine & biology* 28 (3), 389-400
- 188 Zheng, K. et al. (2006) Structure and function of the intercellular junctions: barrier of paracellular drug delivery. *Current pharmaceutical design* 12 (22), 2813-2824
- 189 He, Q. et al. (2018) Towards improvements for penetrating the blood–brain barrier—recent progress from a material and pharmaceutical perspective. *Cells* 7 (4), 24
- 190 Cui, Y. et al. (2016) Dual-targeting magnetic PLGA nanoparticles for codelivery of paclitaxel and curcumin for brain tumor therapy. *ACS applied materials & interfaces* 8 (47), 32159-32169
- 191 Calzolari, A. et al. (2010) Transferrin receptor 2 is frequently and highly expressed in glioblastomas. *Translational oncology* 3 (2), 123-134
- 192 Kreuter, J. et al. (2002) Apolipoprotein-mediated transport of nanoparticle-bound drugs across the blood-brain barrier. *Journal of drug targeting* 10 (4), 317-325
- 193 Sun, W. et al. (2004) Specific role of polysorbate 80 coating on the targeting of nanoparticles to the brain. *Biomaterials* 25 (15), 3065-3071
- 194 Meenach, S.A. et al. (2010) Poly (ethylene glycol)-based magnetic hydrogel nanocomposites for hyperthermia cancer therapy. *Acta Biomaterialia* 6 (3), 1039-1046
- 195 Negut, I. et al. (2017) Progress of nanoparticles research in cancer therapy and diagnosis. In *Nanostructures for Cancer Therapy*, pp. 159-176, Elsevier
- 196 Lin, J.C. et al. (1998) Enhancement of anticancer drug delivery to the brain by microwave induced hyperthermia. *Bioelectrochemistry and Bioenergetics* 47 (2), 259-264
- 197 Mahmoudi, K. et al. (2018) Magnetic hyperthermia therapy for the treatment of glioblastoma: a review of the therapy's history, efficacy and application in humans. *International Journal of Hyperthermia* 34 (8), 1316-1328
- 198 Chiu-Lam, A. and Rinaldi, C. (2016) Nanoscale thermal phenomena in the vicinity of magnetic nanoparticles in alternating magnetic fields. *Advanced functional materials* 26 (22), 3933-3941
- 199 Silva, A.C. et al. (2011) Application of hyperthermia induced by superparamagnetic iron oxide nanoparticles in glioma treatment. *International journal of nanomedicine* 6, 591
- 200 Johannsen, M. et al. (2010) Magnetic nanoparticle hyperthermia for prostate cancer. *International Journal of Hyperthermia* 26 (8), 790-795
- 201 Kossatz, S. et al. (2015) Efficient treatment of breast cancer xenografts with multifunctionalized iron oxide nanoparticles combining magnetic hyperthermia and anti-cancer drug delivery. *Breast Cancer Research* 17 (1), 66

- 202 Sadhukha, T. et al. (2013) Inhalable magnetic nanoparticles for targeted hyperthermia in lung cancer therapy. *Biomaterials* 34 (21), 5163-5171
- 203 Xu, H. et al. (2017) Evaluation of nano-magnetic fluid on malignant glioma cells. *Oncology letters* 13 (2), 677-680
- 204 Neshastehriz, A. et al. (2018) Gold-coated iron oxide nanoparticles trigger apoptosis in the process of thermo-radiotherapy of U87-MG human glioma cells. *Radiation and environmental biophysics* 57 (4), 405-418
- 205 Yin, P.T. et al. (2014) Combined magnetic nanoparticle-based microRNA and hyperthermia therapy to enhance apoptosis in brain cancer cells. *Small* 10 (20), 4106-4112
- 206 Yanase, M. et al. (1998) Antitumor immunity induction by intracellular hyperthermia using magnetite cationic liposomes. *Japanese Journal of cancer research* 89 (7), 775-782
- 207 Maier-Hauff, K. et al. (2011) Efficacy and safety of intratumoral thermotherapy using magnetic iron-oxide nanoparticles combined with external beam radiotherapy on patients with recurrent glioblastoma multiforme. *Journal of neuro-oncology* 103 (2), 317-324
- 208 Johannsen, M. et al. (2005) Clinical hyperthermia of prostate cancer using magnetic nanoparticles: presentation of a new interstitial technique. *International journal of hyperthermia* 21 (7), 637-647
- 209 Maier-Hauff, K. et al. (2007) Intracranial thermotherapy using magnetic nanoparticles combined with external beam radiotherapy: results of a feasibility study on patients with glioblastoma multiforme. *Journal of neuro-oncology* 81 (1), 53-60
- 210 Tomitaka, A. et al. (2019) Surface-engineered multimodal magnetic nanoparticles to manage CNS diseases. *Drug discovery today*
- 211 Jordan, A. et al. (2006) The effect of thermotherapy using magnetic nanoparticles on rat malignant glioma. *Journal of neuro-oncology* 78 (1), 7-14
- 212 Grauer, O. et al. (2019) Combined intracavitary thermotherapy with iron oxide nanoparticles and radiotherapy as local treatment modality in recurrent glioblastoma patients. *Journal of neuro-oncology* 141 (1), 83-94
- 213 Alphandéry, E. et al. (2017) Development of non-pyrogenic magnetosome minerals coated with poly-l-lysine leading to full disappearance of intracranial U87-Luc glioblastoma in 100% of treated mice using magnetic hyperthermia. *Biomaterials* 141, 210-222
- 214 Le Fèvre, R. et al. (2017) Enhanced antitumor efficacy of biocompatible magnetosomes for the magnetic hyperthermia treatment of glioblastoma. *Theranostics* 7 (18), 4618
- 215 Alphandéry, E. et al. (2017) Chains of magnetosomes with controlled endotoxin release and partial tumor occupation induce full destruction of intracranial U87-Luc glioma in mice under the application of an alternating magnetic field. *Journal of controlled release* 262, 259-272
- 216 Zhang, Z.-Q. and Song, S.-C. (2016) Thermosensitive/superparamagnetic iron oxide nanoparticle-loaded nanocapsule hydrogels for multiple cancer hyperthermia. *Biomaterials* 106, 13-23
- 217 Zhang, Z.-Q. and Song, S.-C. (2017) Multiple hyperthermia-mediated release of TRAIL/SPION nanocomplex from thermosensitive polymeric hydrogels for combination cancer therapy. *Biomaterials* 132, 16-27
- 218 Hu, S.H. et al. (2012) Core-shell nanocapsules stabilized by single-component polymer and nanoparticles for magneto-chemotherapy/hyperthermia with multiple drugs. *Advanced materials* 24 (27), 3627-3632
- 219 Hayashi, K. et al. (2014) Magnetically responsive smart nanoparticles for cancer treatment with a combination of magnetic hyperthermia and remote-control drug release. *Theranostics* 4 (8), 834
- 220 Lu, F. et al. (2013) Iron oxide-loaded hollow mesoporous silica nanocapsules for controlled drug release and hyperthermia. *Chemical Communications* 49 (97), 11436-11438

## **Chapter 2**

# **Doxorubicin-loaded Iron Oxide Nanoparticles for Glioblastoma Therapy**

# Doxorubicin-loaded Iron Oxide Nanoparticles for Glioblastoma Therapy

## ABSTRACT

Although doxorubicin (DOX) is an effective anti-cancer drug with cytotoxicity in a variety of different tumors, its effectiveness in treating glioblastoma multiforme (GBM) is constrained by insufficient penetration across the blood-brain barrier (BBB). In this study, biocompatible magnetic iron oxide nanoparticles (IONPs) stabilized with trimethoxysilylpropyl-ethylenediamine triacetic acid (EDT) were developed as a DOX's carrier for GBM chemotherapy. The loaded DOX was entirely released within 4 days with the capability of an accelerated release in acidic microenvironments. The DOX-loaded EDT-IONPs (DOX-EDT-IONPs) demonstrated an efficient uptake in mouse brain-derived microvessel endothelial, bEnd.3, Madin–Darby canine kidney transfected with multi-drug resistant protein 1 (MDCK-MDR), and human U251 GBM cells. The DOX-EDT-IONPs could augment DOX's uptake in U251 cells by 2.8-fold and significantly inhibited U251 cell proliferation, while the loaded DOX was entirely released within 4 days with the capability of an accelerated release in acidic microenvironments. Moreover, the DOX-EDT-IONPs were found to be effective in apoptotic-induced GBM cell death over 90% within 48 hours of treatment. Gene expression studies revealed a significant downregulation of TOP II and Ku70, crucial enzymes for DNA repair and replication, as well as MiR-155 oncogene, concomitant with an upregulation of caspase 3 and tumor suppressors i.e., p53, MEG3 and GAS5, in U251 cells upon treatment with DOX-EDT-IONPs. An *in vitro* MDCK-MDR-GBM co-culture model was used to assess the BBB permeability and resulting tumor activity of the DOX-EDT-IONPs and DOX treatments. The DOX-EDT-IONP showed improved permeability compared to DOX alone, however cytotoxicity was similar in both treatment groups. Using a cadherin binding peptide (ADTC5) to transiently open tight junctions further enhanced DOX-EDT-IONP permeability. Combining transient modulation of tight junctions with application of an external magnetic field was most effective in enhancing permeability and cytotoxicity in

the MDCK-MDR-GBM co-culture model. Therefore, the combination of the magnetic enhanced convective diffusion and the cadherin binding peptide for transiently opening the BBB tight junctions are expected to enhance the efficacy of GBM chemotherapy using the DOX-EDT-IONPs. In general, the developed approach enables the chemotherapeutic to overcome both BBB and multidrug resistance (MDR) glioma cells while providing a site-specific magnetic targeting.

**Keywords:** Iron oxide nanoparticles; Doxorubicin; Glioblastoma; Drug delivery; Blood-brain barrier; Magnetic field.

## 2.1. Introduction

Glioblastoma multiforme (GBM) is the most common and aggressive form of malignant gliomas whose current standard of care involves surgical resection followed by chemotherapy and radiotherapy [1,2]. Nevertheless, the median survival of GBM patients who receive the current standard of care is 14.6 months post-diagnosis, with a 5-year survival rate of 9.8% [3,4]. The extensive infiltration of GBM tumors in addition to the presence of the blood–brain barrier (BBB) limits therapeutic options. The BBB is made of tight junctions between endothelial cells and surrounding astrocyte foot processes, controlling the passage of substances from the bloodstream into the brain [5,6]. Besides the tight junctions that restrict the paracellular passage of drugs, brain endothelial cells also express a number of efflux transporters such as P-glycoprotein (P-gp) and breast cancer resistance protein (BCRP), thus limiting drug penetration into the brain [7]. In this respect, a majority of the current chemotherapeutics available to treat GBM have BBB liabilities that impedes their therapeutic efficacy. As a result, the chemotherapeutic options are limited and those drugs that are used often require high doses that pose severe systemic toxicity to the normal tissues [6,8,9].

To address these issues, numerous engineered nanoparticles (e.g. iron oxide nanoparticles, gold nanoparticles, nanoliposomes) have been used as drug delivery systems capable of penetrating the BBB and delivering therapeutic agents to the GBM cells [10-12]. Iron oxide nanoparticles (IONPs, magnetite ( $\text{Fe}_3\text{O}_4$ ) or maghemite ( $\gamma\text{-Fe}_2\text{O}_3$ )), *inter alia*, have found extensive applications in cancer theranostics by virtue of their tunable size-dependent magnetic properties. Moreover, IONPs are biocompatible and biodegradable, which can be incorporated into the body's iron cycle upon degradation [6,13,14]. The surface of IONPs can be further modified in order to (i) improve their biocompatibility and aqueous dispersibility, (ii) prolong their

circulating time in blood through minimizing nonspecific phagocytosis by the reticuloendothelial system (RES) and also, (iii) provide plenty of active sites for drug loading [11,15]. To this end, a variety of biopolymers such as poly(ethylene glycol) (PEG) [16], poly(ethylene imine) (PEI) [17], dextran [18] and chitosan [19] have been employed for surface modification of IONPs.

Generally, the inherent magnetic properties of the IONPs make them a promising option for both magnetic resonance imaging (MRI) as a contrast agent, and for site-specific magnetic targeting using an external magnetic field [13,14]. Several types of IONPs have been developed, hitherto, as MRI contrast agents in clinical trials such as Ferumoxide (Feridex®), Ferumoxylol (Feraheme®), Ferucarbotran (Resovist®) and ferumoxtran-10 (Combidex®), thanks to their effective reduction of T1, T2, and T2\* relaxation times [11,20]. Moreover, several IONPs have been fabricated as an efficacious nanocarrier for anti-cancer drugs such as DOX [21,22], paclitaxel [23] and 5-fluorouracil [24], albeit none of these have progressed to clinical trials yet in the U.S.

Doxorubicin (DOX) is an anthracycline antibiotic with potent antitumor activity in a variety of cancer cells [25]. Generally, DOX intercalates base pairs of the DNA strands, thus inhibiting the synthesis of DNA as well as RNA through blocking the replication and transcription processes. In addition, DOX inhibits topoisomerase II (TOP2), an enzyme regulating DNA under- and over-winding, further preventing DNA replication, transcription and repair. Generation of free radicals is another mechanism of DOX activity that induces oxidative damage resulting in cleavage or degradation of DNA [25,26]. DOX is considered as one of the most effective chemotherapeutics and is currently indicated by the FDA for a variety of neoplastic conditions such as leukemia, neuroblastoma, soft tissue and bone sarcoma, breast carcinoma, ovarian carcinoma, bladder carcinoma, thyroid carcinoma, gastric carcinoma, Hodgkin's disease, malignant lymphoma and bronchogenic carcinoma [25]. Intravenous (i.v.) administration of DOX, however, exhibits several

adverse effects including dose-limiting cardiotoxicity and myelosuppression [25,27]. The underlying mechanisms of cardiotoxicity are mainly attributed to the overproduction of reactive oxygen species (ROS) and inhibition of topoisomerase II $\beta$  (Top2 $\beta$ )[28]. Whilst DOX is one of the most effective chemotherapeutics *in vitro* against cell lines derived from malignant gliomas (IC50 of is DOX 0.5  $\mu$ M vs temozolomide, as the standard agent in glioma chemotherapy, with an IC50 of 35  $\mu$ M on U251 GBM cell line)[29,30], its inadequate penetration into the BBB severely constrains i.v. administration of DOX in GBM patients. However, the therapeutic efficacy of either pegylated liposomal DOX [31] or its intratumoral administration [32] in patients with malignant gliomas has been corroborated.

Taken together, development of drug delivery systems for DOX with a capability of site-specific drug release and improved BBB penetration would represent a significant improvement for treatment of GBM. Thus far, several nanotechnology-based DOX formulations have been developed. Doxil $\text{\textcircled{R}}$  is a pegylated liposomal formulation of doxorubicin approved by the FDA for administration in a variety of human cancers [33,34]. In addition, other nanotechnology-based DOX formulations such as NK-911 $\text{\textcircled{R}}$  (DOX-conjugated poly-aspartic acid/polyethylene glycol micelles, phase II, metastatic pancreatic cancer) and Livatag $\text{\textcircled{R}}$  (DOX-loaded polyalkylcyanoacrylate nanoparticles, phase III, primary liver cancer) are under clinical trials [25].

In this study, EDT-coated IONPs were developed as the delivery system for DOX and the anti-cancer effects of the formulation were investigated *in vitro* on GBM cells. In this study, cadherin binding peptide was utilized for the first time as a transient disruption agent to enhance the permeability of IONPs across the BBB. Therefore, this combinational approach of using a cadherin binding peptide and an external magnetic field together not only enhanced the penetration

of the nanoparticles but also augmented therapeutic response and induced more apoptosis in GBM cells.

## 2.2. Materials and methods

### 2.2.1. Materials

The chemical reagents were acquired from Sigma Aldrich (St. Louis, MO), and the cell culture and biochemical reagents were purchased from Thermo Fisher Scientific Inc, USA, unless otherwise specified.

### 2.2.2. Synthesis and characterization of EDT-IONPs

Iron oxide nanoparticles were fabricated under mild conditions at room temperature as previously described [35]. Briefly,  $\text{Fe}(\text{acac})_3$  (2.83 g, 8 mmol) was dissolved in ethanol/DI water (6:4) and purged with nitrogen for 1 h, followed by adding  $\text{NaBH}_4$  (3.03 g, 80.0 mmol) in deoxygenated DI water under stirring (1000 rpm). When the color of the reaction mixture changed from red to black, it indicates the formation of IONPs (approximately 20 min). For coating, (Trimethoxysilylpropyl)-ethylenediamine triacetic acid (EDT, 16 mL) was added, and the reaction mixture was stirred overnight at room temperature. The blackish brown solution was filtered, and the solvent was evaporated at 50°C under low pressure. The obtained viscous mixture was dissolved in 200 mL of cold ethanol and left until excess  $\text{NaBH}_4$  became crystallized, which was removed by filtration. Finally, ethanol was completely removed, the product was dissolved in 50 mL DI water and dialyzed against DI water to remove the unreacted EDT, followed by centrifugation at 4000 rpm for 30 min [35]. The dark reddish-brown supernatant was collected and stored for further use.

The size distribution of EDT-IONP in DI water was measured by dynamic light scattering (DLS) using a Photocor Complex system. The FTIR spectrum was taken using a Thermo Nicolet iS10 FTIR spectrometer. Transmission electron microscopy (TEM) images of the EDT-IONPs were obtained using a Philips CM 10 electron microscope (FEI, Hillsboro, USA).

### 2.2.3. Drug loading on EDT-IONPs

To load DOX on the EDT-IONPs, EDT-IONPs (20  $\mu\text{g}$ ) and DOX (20  $\mu\text{g}$ ) in 200  $\mu\text{L}$  phosphate-buffered saline (PBS, pH 6) was combined and incubated overnight under ambient conditions. Afterwards, the mixture was centrifuged at 12,000 rpm for 10 min and the solution was completely withdrawn. Then, the nanoparticles were washed with PBS (pH 7.4) twice to remove free DOX and the nanoparticles were centrifuged again to collect the DOX-loaded EDT-IONPs (DOX-EDT-IONPs).

### 2.2.4. Biocompatibility assessment of EDT-IONPs

To assess the biocompatibility of the synthesized EDT-IONPs, a mouse brain-derived microvessel endothelial cell line, bEnd.3 (American type tissue culture collection, Manassas, VA) was employed as a cell culture model for the BBB. The Madin–Darby canine kidney (MDCK) transfected with multi-drug resistant protein 1 (MDR) was also used. MDCK is an epithelial cell line originally derived from the normal dog kidney and transfected with MDR, expressing P-gp and tight junction proteins. Therefore, the MDCK-MDR has been reported as a model for the BBB permeability [36,37]. Furthermore, an authenticated human U251 GBM cell line was used for biocompatibility evaluation of EDT-IONPs. The bEnd.3, MDCK-MDR and U251 cells (cells at passage number 20–30) were cultured at a density of  $2 \times 10^4$  (bEnd.3, MDCK-MDR) and  $1 \times 10^4$  (U251) cell/ $\text{cm}^2$  in 96-well plates, and incubated overnight at 37 °C allowing the cells to attach. Next day, the cells were treated with EDT-IONPs (0.25 to 50  $\mu\text{g}/\text{mL}$ ) suspended in the cell culture

medium for 48 h. Thereafter, the culture medium was removed, and the cells were washed with PBS followed by incubation with fresh medium containing 0.5 mg/mL of 3-(4,5-dimethylthiazol-2-yl)-2,5-diphenyltetrazoliumbromide (MTT, 0.5 mg/mL) reagent at 37 °C. After 3 hours, the medium was withdrawn, and blue crystals were dissolved in pure DMSO [38-40]. The absorbance of the solutions was measured using a Synergy HT plate reader (BioTek, Winooski, VT) at the wavelength of 570 nm and the relative cell viability was calculated as  $[\text{OD}]_{\text{test}}/[\text{OD}]_{\text{control}}$ , upon five measurements.

#### 2.2.5. Drug release from EDT-IONPs

The release of DOX from the EDT-IONPs was measured in PBS (pH 7.4 mimicking physiological pH, and 4.5 mimicking pH of acidic intracellular compartments such as endosomes) at 37 °C. For this purpose, the DOX-EDT-IONPs were suspended in 1 mL PBS in Eppendorf tubes and at various time points, the tubes were centrifuged at 12,000 rpm for 10 min to pellet the nanoparticles and the solution was completely collected followed by re-suspension of the nanoparticles in 1 mL of fresh PBS. The concentration of the released DOX in the solution was determined by fluorescence measurement (excitation and emission wavelengths of 485 nm and 590 nm, respectively) using a Synergy HT plate reader. The concentration of the released DOX from DOX-EDT-IONPs was calculated using a serial dilution of a DOX standard solution.

#### 2.2.6. Cellular uptake of EDT-IONPs and DOX

To study the cellular uptake of DOX-EDT-IONPs; bEnd.3, MDCK-MDR, and U251 cells were grown in 24-well culture plates to reach a confluent monolayer and then they were treated with cell culture medium containing either EDT-IONPs or DOX-EDT-IONPs (10 and 20  $\mu\text{g}/\text{mL}$ ) for 4 h at 37 °C with and without a static magnetic field (rare-earth circular magnets, diameter: 20 mm, Lee Valley, Winnipeg, CA). Then the cells were washed with cold PBS to remove non-

adhered nanoparticles, and lysed with 0.1% triton solution in PBS overnight at -20 °C. The content of IONPs was determined based upon the Ferrozine assay as previously reported [41]. Briefly, HCl (500  $\mu$ L of 12 M) was added to wells, and were incubated at room temperature for 1 h with gentle shaking to digest the IONPs, followed by neutralization with NaOH (500  $\mu$ L of 12 M). Then, hydroxylamine hydrochloride (120  $\mu$ L of 2.8 M) in 4 M HCl was added, and the samples were incubated for 1 h at room temperature with gentle shaking. Afterwards, ammonium acetate solution (50  $\mu$ L of 10 M, pH 9.5) and ferrozine (300  $\mu$ L of 10 mM) in 0.1 M ammonium acetate solution were added sequentially to each well, and the absorbance of the solutions was determined at 562 nm by a Synergy HT plate reader. The concentration of EDT-IONPs was quantified based upon an iron chloride standard solution. The protein content of the lysed cells was also measured using a BCA protein assay kit.

The localization of EDT-IONPs in the cell organelles was also studied using TEM as previously described [42,43]. For this purpose, U251 cells were treated with either EDT-IONPs or DOX-EDT-IONPs in accordance with the uptake study, and after washing with PBS, the cells were disassociated using a 0.25% trypsin EDTA solution (Hyclone, Logan, UT). After centrifugation of the collected cells (5 minutes at 1500 g), the cell pellet was resuspended in 3% glutaraldehyde in 0.1 M phosphate buffer (pH 7.3) for 3 hours at room temperature. Then the samples were fixed for 2 h at room temperature in 1% osmium tetroxide in 0.1 M phosphate buffer, dehydrated in ascending concentrations of ethanol and embedded in Epon resin. Thin sections were stained with uranyl acetate and lead citrate, and photographed by TEM.

To measure the cellular uptake of DOX, U251 cells were grown in 6-well plates as described earlier and treated with cell culture media supplemented with an equal drug concentration of either DOX or DOX-EDT-IONPs to initiate the cellular drug accumulation. After

2 h, the cells were washed with cold PBS three times and lysed with 0.1% triton solution in PBS as described somewhere else [44]. The concentration of DOX in the cell lysates was measured as delineated in section *Drug release from EDT-IONPs* and normalized with the protein content of the lysed cells.

### 2.2.7. Cytotoxicity of DOX-EDT-IONPs in GB cell line

The cytotoxicity of DOX-EDT-IONPs against U251 cells was studied using MTT and flow cytometry analyses. For MTT assay, the cells were cultured as described in section 2.2.4. Next day, the medium was changed with fresh medium (negative control), medium containing free DOX with equivalent concentrations corresponding to DOX released from EDT-IONPs at the same period of time (positive control), EDT-IONPs and DOX-EDT-IONPs. After a 48-h treatment, viability of the cells was determined by MTT assay as described in section *Biocompatibility assessment of EDT-IONPs*.

Moreover, cell apoptosis/necrosis was investigated using Annexin V-FITC/PI apoptosis Kit. For this study, the cells were treated with either EDT-IONPs, free DOX or DOX-EDT-IONPs over a 48-h period, followed by incubation in fresh cell culture media without any treatment for 24 h. Afterwards, the cells were stained with Annexin V-FITC and PI in accordance with the manufacturer's protocol, and consequently were analyzed using flow cytometry (BD FACSCanto II Flow Cytometer instrument (BD Bioscience)). In addition, to study the effect of various treatments on cell proliferation, U251 cells were stained with a fluorescent carboxyfluorescein succinimidyl ester dye (CFSE, 50 mM), for 20 min at 37°C. Thereafter, the medium was removed, and the cells were washed and treated with either free DOX, EDT-IONPs, or DOX-EDT-IONPs for 48 h followed by changing the media and leaving the cells without further treatment for 24 h. Then, the fluorescence intensity of the cells was determined using flow cytometry. In fact, during

each cell division, the cellular content of CFSE decreases that results in a sequential halving of the cellular fluorescent intensity with each mitotic event [45].

To observe any changes in morphology, the U251 cells were treated for 48 h as mentioned above, followed by washing with PBS, fixating with paraformaldehyde (4% v/v) for 20 min at room temperature and permeabilization with Triton X-100 (0.2% v/v) for 10 min. The specimens were then blocked with BSA solution (3% w/v) for 1 h at room temperature, washed with PBS, and the cells incubated with primary phospho-H2AX antibody solution (1:500 in 3% BSA, 0.3% Triton X-100 in PBS) at 4°C overnight. Afterwards, the primary antibody was withdrawn, and a goat anti-rabbit secondary antibody labeled with Alexa 488 dye (1:500 in the same buffer as the primary antibody) was added to each well and incubated at room temperature for 1 h. Then, the cells were washed with PBS and the actin cytoskeleton was stained with ActinRed for 30 min followed by the nucleus staining with DAPI solution (100 nM) for 5 min at 37 °C. Finally, the samples were washed with PBS and visualized by a fluorescence microscope (Zeiss Axio observer Z1, Germany).

#### 2.2.8. Reactive oxygen species measurement

The extent to which the various treatments resulted in ROS generation in the U251 cells was evaluated via the peroxide-dependent oxidation of the non-fluorescent 2',7'-dichlorofluorescein diacetate (DCFDA). In this cell-based assay, DCFDA freely diffuses into the cells. Once inside, the DCFDA is transformed to the highly fluorescent and cell impermeable 2',7'-dichlorofluorescein (DCF) through ROS mediated metabolism [46]. For this study, the cells were cultured in black 96 well plates at a density of 5000 cell/cm<sup>2</sup>. Next day, the cells were washed with PBS and exposed to 50 µM DCFHDA in PBS for 45 min at 37 °C. Afterwards, the DCFHDA solution was removed, and the cells were washed and treated with either EDT-IONPs, DOX or

DOX-EDT-IONPs in cell culture media over 72 h. At various time points, cellular accumulation of ROS in response to the treatments was calculated by measuring the oxidation of DCFDA to the fluorescent DCF using a Synergy HT fluorescent plate reader at Ex/Em 485/590 nm.

### 2.2.9. Quantitative RT-PCR

The gene studies were conducted on U251 cells upon a 48-h treatment with either EDT-IONPs, DOX or DOX-EDT-IONPs. To this end, total RNA of the cells was extracted using TRIZOL reagent (Invitrogen, USA) according to the manufacturer's protocol. Then, the purity and concentration of the extracted RNA were determined by UV-VIS spectrophotometry (NanoDrop, Thermo Fisher Scientific Inc, USA). Afterwards, the level of mRNA encoding Top II, Ku70, p53, Caspase 3, Wnt 1, MEG3, GAS5, and MIR155 was determined by quantitative reverse-transcript polymerase chain reaction (qRT-PCR). The RT-PCR was implemented using iTaq Universal SYBR Green Supermix kit (Bio-Rad, USA) in an Applied Biosystems 7300 Real-Time PCR system and  $\beta$ -actin was employed as the housekeeping gene. The following thermal cycles were designed for the reactions: 1 cycle of 10 min at 50 °C for the reverse transcription reaction, 1 cycle of 1 min at 95 °C for polymerase activation, 40 cycles consisting of 15 sec at 95 °C for denaturation and 1 min at 60 °C for annealing. The expression of the target genes was normalized to the  $\beta$ -actin expression and relative gene fold changes were calculated using the comparative  $C_t$  method ( $2^{-\Delta\Delta C_t}$ ) as mentioned previously [38]. The primer sequences are shown in Table 2.1.

Table 2.1. Sequences of human primers

	Forward	Reverse
<b>TOP2</b>	ATTCCCAAACCTCGATGATGC	CCCCATATTTGTCTCTCCCA
<b>Ku70</b>	CTGTCCAAGTTGGTCGCTTC	CTGCCCTTAAACTGGTCAA
<b>p53</b>	TCTGAGTCAGGCCCTTCTGT	GTTCCGAGAGCTGAATGAGG
<b>Caspase 3</b>	CTCTGGTTTTTCGGTGGGTGT	CGCTTCCATGTATGATCTTTGGTT
<b>Wnt1</b>	CAACAGCAGTGGCCGATGGTGG	CGGCCTGCCTCGTTGTTGTGAAG
<b>GAS5</b>	TGGTTCTGCTCCTGGTAACG	AGGATAACAGGTCTGCCTGC
<b>MEG3</b>	GCTGAAGAACTGCGGATGGA	CATTCGAGGTCCCTTCCCAC
<b>MIR 155</b>	AATCGTGATAGGGGTTTTTGCC	ATGTAGGAGTCAGTTGGAGGC
<b><math>\beta</math>-actin</b>	AATGCCAGGTACATGGTGG	AGGAAGGAAGGCTGGAAGAGTG

### 2.2.10. *In vitro* BBB-GBM model

Nanoparticles as a drug carrier for brain tumor therapy need to first overcome the limited permeability of the BBB as well as the efflux transporters such as P-gp expressed on the brain endothelial cells, which are responsible for low drug permeation into the brain. The Madin–Darby canine kidney epithelial cell line stably transfected with human multi-drug resistant protein 1 (MDCK-MDR) cells overexpress P-gp, and have reduced paracellular diffusion due to the complex tight junction proteins. Together these properties make MDCK-MDR cells a reproducible and accurate *in vitro* cell culture model for examining and predicting the penetration of drugs and solutes across the BBB [36,37]. In the present study, MDCK-MDR cells (passage number 20-30, cell density 100,000 cell/cm<sup>2</sup>) were plated on the apical side of a porous polycarbonate Transwell<sup>TM</sup> membrane inserts (4.6 cm<sup>2</sup>, pore size: 3.0  $\mu$ m, Corning Inc., USA). Once a confluent MDCK-MDR monolayer was obtained (typically in 6 days), U251 cells were cultured in the basolateral side of the well plates. Free DOX (1  $\mu$ g/mL) or DOX-EDT-IONPs was added to the

apical media compartment of the insert along with an IRdye 800CW PEG as a permeability marker. In addition, a cyclic ADTC5 peptide (Cyclo(1,7)Ac-CDTPPVC-NH<sub>2</sub>), which was synthesized as previously reported [47] was added to the apical media compartment of the insert to block the cadherin–cadherin interactions and thus enhancing drug delivery through the MDCK-MDR monolayer. The cells were then incubated at 37°C for 4 h in both the presence and absence of a static magnetic field (rare-earth circular magnet, diameter: 30 mm, Lee Valley, Winnipeg, CA). Afterwards, the apical media and the inserts were removed and the GBM cells with the basolateral cell culture media were incubated for an additional 48-h after which the basolateral media was collected to determine IONP (Ferrozine assay) and IR dye permeability as well as the cell viability (MTT assay).

#### 2.2.11. Statistical analysis

The studies were conducted in triplicate and the results were reported as the mean  $\pm$  standard deviation (SD). Statistical analysis was conducted in GraphPad Prism using one or mixed two-way ANOVA (each applicable), with multiple post-hoc analysis of Tukey and with an adjusted p-value. The hypotheses were based on H<sub>0</sub>: All groups should have the same mean measurement values, and H<sub>1</sub>: All groups do not have the same mean measurement values. The adjusted p-value < 0.05 (adjusted based on the entire family of comparisons) was considered as the significant level to reject the null hypothesis, as previously reported [48-50].

## 2.3. Results and discussion

### 2.3.1. Characterization of EDT-IONPs

Photographs of the EDT-IONP and DOX-EDT-IONP suspensions were shown in Fig. 2.1a. Both suspensions were stable and the reddish of the DOX-EDT-IONP is attributed to the presence of DOX. The TEM image illustrates EDT-IONPs (Fig. 2.1b) and DOX-EDT-IONPs (Fig. 2.1c) with a quasi-spherical morphology and a core size of  $4.76\pm 0.7$  nm (Fig. 2.1d). The hydrodynamic diameter ( $D_H$ ) and zeta potential ( $\zeta$ ) of the EDT-IONPs were measured to be  $51.8\pm 1.3$  nm, and  $-27.3\pm 1.0$  mV, respectively. The FTIR spectrum of the EDT-IONPs is shown in Fig. 2.1e. The Fe-O-Fe stretching of the core was observed at  $594\text{ cm}^{-1}$  and the Si-O-Si stretching band of the aminosilane shell was found at  $991\text{ cm}^{-1}$ . The carbonyl stretching band of EDT coating and the C-H stretching (of propyl group) bands were observed at  $1600\text{ cm}^{-1}$  and  $2927\text{ cm}^{-1}$ , respectively. EDT is generally a biocompatible coating that provides many negative charged sites on the surface of the nanoparticles [43,51], which can be utilized for ionic interaction with positively charged DOX molecules. Also, we previously reported the biocompatibility of the EDT-IONPs in Female Balb/c healthy mice [43]. Magnetic and further physicochemical characterizations of the IONPs were previously reported elsewhere [35,52].

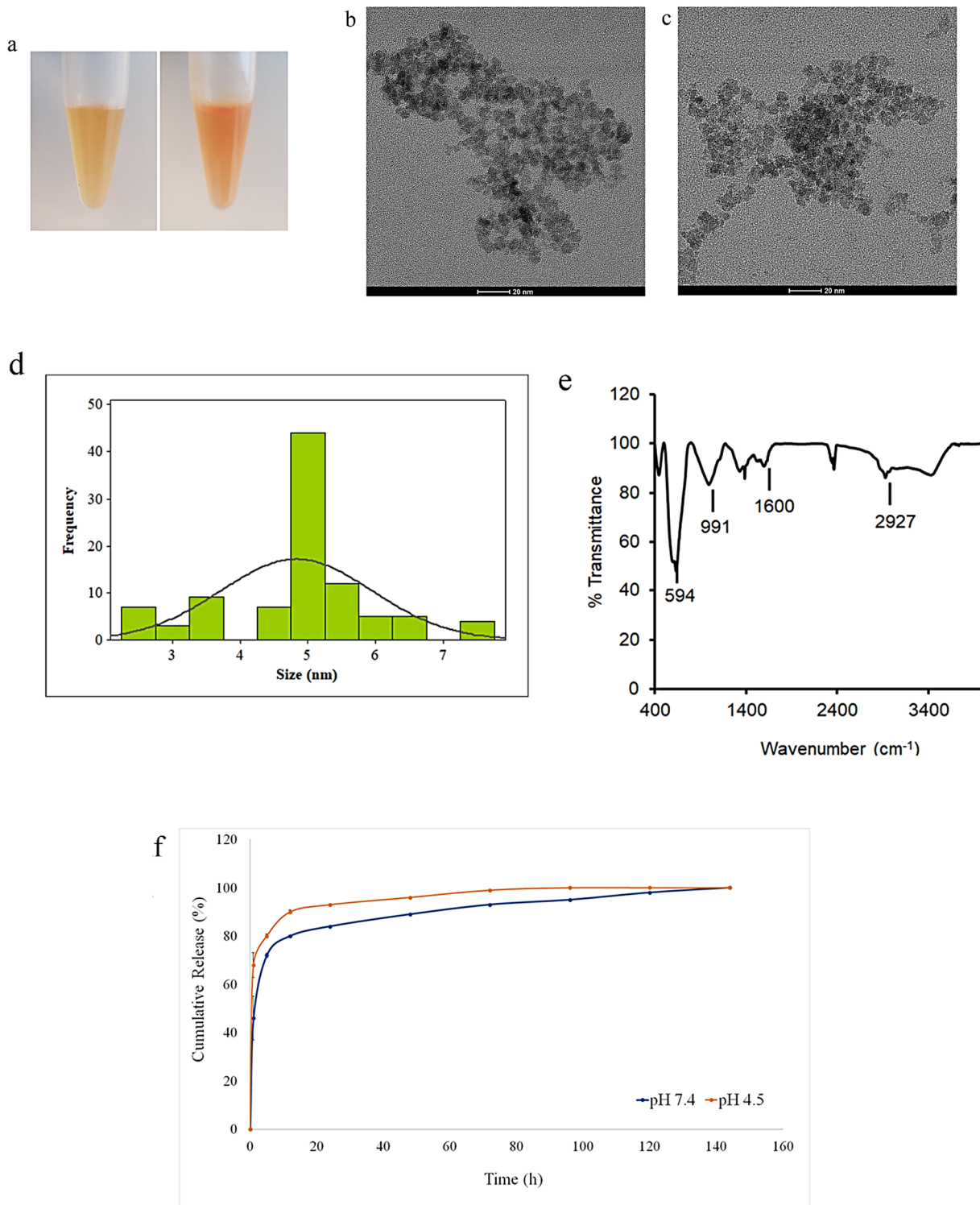


Fig. 2.1. characterization of nanoparticles: (a) photographs of EDT-IONP (left) and DOX- EDT-IONP (right) solutions in PBS; TEM images of (b) EDT-IONPs, and (c) DOX- EDT-IONPs; (d) histogram of EDT-IONP size distribution from 100 measurements; (e) FTIR spectrum of EDT-IONP, (f) release of DOX from the DOX-EDT-IONPs in pH 7.4 and 4.5.

### 2.3.2. Characterization of DOX-IONPs

The DOX loading efficiency on the EDT-IONPs was calculated to be  $5\pm 0.5\%$ . Loading of DOX increased  $\zeta$  of the negative EDT-IONPs from  $-27.3\pm 1.0$  mV to  $0.0\pm 0.02$  mV for DOX-EDT-IONPs. This change in surface charge of the nanoparticles upon drug loading can be attributed to the electrostatic interactions between the amine groups of DOX and carboxylic acid groups of EDT coating. Moreover, upon release of the loaded-DOX from nanoparticles within 4 days, the surface charge of the nanoparticles became negative again and returned to  $-25.69\pm 2.8$  mV. In addition, the  $D_H$  of the EDT-IONPs increased from  $51.8 \pm 1.3$  nm (polydispersity index: PDI 0.14) to  $75.5\pm 3.2$  nm (PDI 0.27) upon DOX loading. The release profile of DOX from the nanoparticles is depicted in Fig. 2.1f. The nanoparticles demonstrated a burst release of  $42\pm 5\%$  within the initial 3 hours, while the remaining coated DOX gradually released within a 4-day period. However, since the recovery time for re-establishment of the BBB integrity was reported to be within 60 min post-injection of the cadherin binding peptide *in vivo* [53], the DOX-EDT-IONPs are expected to enter the brain within an hour, while carrying over 60% of initial concentration of the loaded DOX. Moreover, the rapid release of DOX (within an hour) from the DOX-EDT-IONPs that magnetically has been drawn to the target site, can increase the chance of DOX entering the brain through the transiently open tight junctions of the BBB to provide higher concentration of the drug within the brain.

Release studies performed at pH 4.5 also showed an accelerated initial release of DOX from the nanoparticles with up to  $64\pm 4\%$  within the initial hours. The enhanced release at pH 4.5 was due to the reduced electrostatic interactions between DOX and IONPs [11], reminiscent of the DOX-IONP's capability of an accelerated DOX release upon entering the acidic tumor

microenvironment or acidic cellular compartments such as endosomes [54-56]. The release of DOX from the IONPs observed in the present study was similar to previous reports with polymer-based nanoparticles. In one study, iron oxide nanoparticles and DOX were loaded in poly-L-arginine/chitosan nanoparticles, in which ca. 40% and ca. 65% of the loaded DOX was released within 2 h at pHs 7 and 5, respectively [57]. Although covalent bonding of DOX to the surface of the nanoparticles can result in increased loading and reduced initial burst release, these advantages are countered by potential reductions in the total release of the drug from the nanoparticles. For instance, when DOX was covalently conjugated to iron oxide nanoparticles via a pH-sensitive hydrazone linkage, there was a 29% burst release within 2 h. However, only 4% of the loaded DOX was further released within 24 h and the cumulative release was only around 35% in acidic pH conditions [58].

### 2.3.3. Biocompatibility of EDT-IONPs

Biocompatibility of the EDT-IONPs on U251, bEnd.3 and MDCK-MDR cells was studied. No cytotoxicity was observed in these three cell lines treated with EDT-IONPs at a concentration ranging from 0.25 to 30  $\mu\text{g}/\text{mL}$  (Fig. 2.2). Although treatment with either DOX-EDT-IONPs or free DOX (1  $\mu\text{g}/\text{mL}$ ) exhibited an approximately 40% reduction in the bEnd.3 cell viability, no significant cytotoxicity was observed in MDCK-MDR. This is likely attributed to the presence of P-gp efflux transporter that restricts uptake of DOX by MDCK-MDR cells [59]. The cytotoxicity of DOX-EDT-IONPs on U251 will be discussed in 2.5.

In order to deliver an effective concentration of both DOX and EDT-IONPs to GBM cells in our studies, the concentration of 20  $\mu\text{g}/\text{mL}$  of EDT-IONPs was selected for use in the remaining studies. This concentration, which was well tolerated in various cell lines, enables delivering enough DOX to observe cytotoxicity on the tumor cells. We previously reported biocompatibility

of IONPs on endothelial, astrocyte and neuron cells at a concentration up to 100  $\mu\text{g/mL}$  [41]. Moreover, iron oxide nanoparticles clinically demonstrate acceptable biocompatibility and they are captured by the reticuloendothelial system (RES), by which the iron is incorporated into the body's iron cycle [6,60]. In practice, iron oxide nanoparticles are coated with biocompatible and hydrophilic materials, diminishing the non-specific protein adsorption on the nanoparticle surface and decreasing their recognition and clearance by the RES, thereby their circulation time, as well as accumulation in the brain tumor can be augmented [61,62].

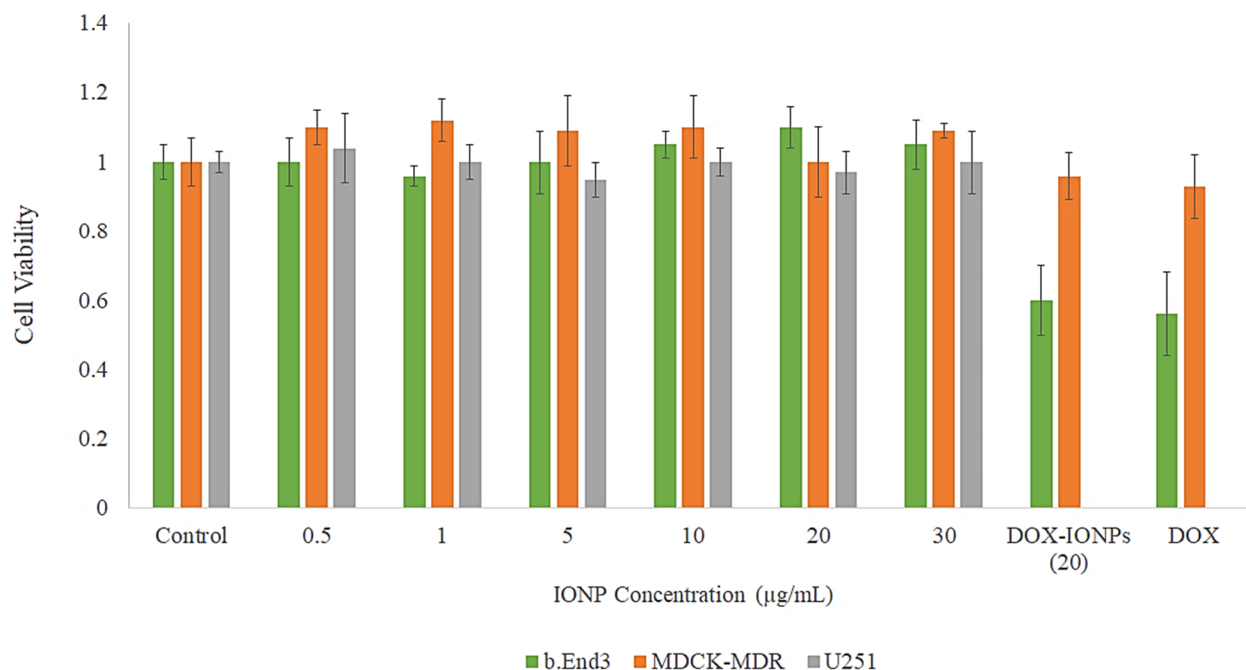


Fig. 2.2. Biocompatibility of EDT-IONPs on b.End3, MDCK-MDR and U251 cell lines after 48 hour treatment using MTT assay (n=5). The Y-axis represents cell viability compared to the control.

#### 2.3.4. Cellular uptake of the EDT-IONPs and DOX

The uptakes of EDT-IONPs and DOX-EDT-IONPs in bEnd.3 (Fig. 2.3a), U251 (Fig. 2.3b) and MDCK-MDR (Fig. 2. 3c) were evaluated. The uptake of both EDT-IONP and DOX-EDT-IONP was concentration-dependent, and the uptake of drug-loaded IONP was generally greater

than that of the EDT-IONPs (Fig. 2.3). Moreover, the cellular uptake of the nanoparticles was augmented in the presence of a magnetic field. The bEnd.3 and MDCK-MDR demonstrated a greater uptake of the nanoparticles than that of U251. Generally, highly efficient uptake of the nanoparticles by endothelial cells is essentially required for their efficacious transportation into the brain through the endocytosis [63]. Moreover, the higher uptake of DOX-EDT-IONPs than that of EDT-IONPs could be attributed to the neutral surface charge of the former, favoring cellular uptake of the drug-loaded nanoparticles. Similarly, greater uptake of IONP based on positive surface charge has been observed for a number of cells including the bEnd.3 brain endothelial cells [41].

To further evaluate the uptake of the EDT-IONPs and DOX-EDT-IONPs in U251 cells, TEM images were taken which illustrate the formation of nanoparticle-contained intracellular vesicles (i.e., endosomes/lysosomes) indicating an endocytosis pathway for uptake of the nanoparticles (Fig. 2.4). This finding is consistent with our previous studies reporting IONP uptake in the cells through a likely interaction with caveolae localized in lipid rafts within the plasma membrane [42].

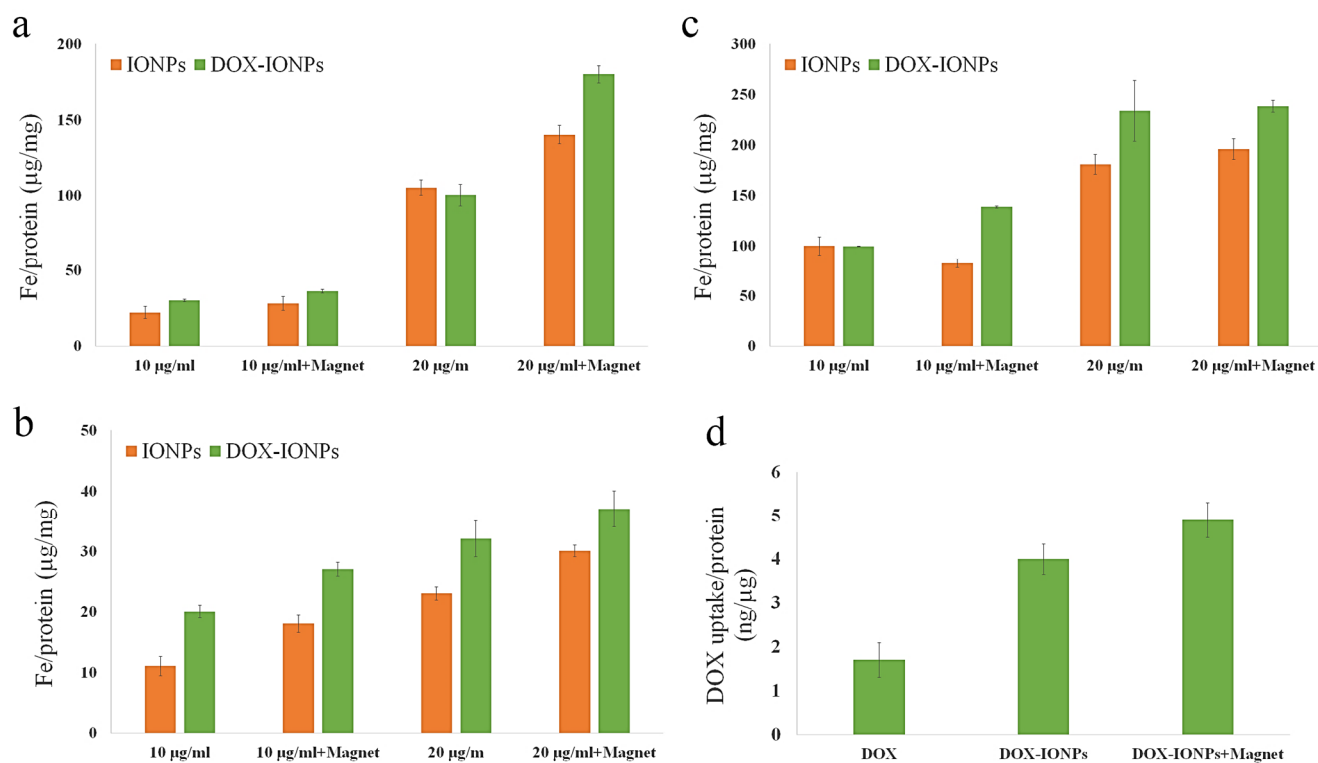


Fig. 2.3. Uptake of EDT-IONPs and DOX-EDT-IONPs by (a) b.End 3, (b) U251, and (c) MDCK-MDR after 4-h treatment. (d) uptake of DOX by U251 cells treated with either DOX, DOX-EDT-IONPs, or DOX-EDT-IONPs + Magnet after 2 h. \* indicates a significant difference compared to DOX at  $p < 0.05$ . Data is presented as mean  $\pm$  S.D, and  $n = 3$  (three replications). IONPs and DOX-IONPs represent for EDT-IONPs and DOX-EDT-IONPs.

In terms of drug accumulation in U251 GBM cells, treatment with DOX-EDT-IONPs, was more effective than DOX alone. In the present study, the DOX-EDT-IONP resulted in approximately 2-fold greater uptake compared to an equal concentration of DOX in solution (Fig. 2.3d). In addition, application of an external magnetic field further enhanced the DOX accumulation in the U251 cells ( $2.8 \pm 0.5$ -fold, Fig. 2.3c). In practice, the efficacy of chemotherapy with DOX is limited by the multiple drug resistance (MDR) mechanisms due to the overexpression of ATP-binding cassette (ABC) and P-gp efflux transporter in cancer cells. The expression of both P-gp and MDR1 in U251 has also been previously reported [64]. In this regard, Wang *et al.*, [64] reported that co-administration of  $\beta$ -asarone and TMZ could decrease P-gp and MDR1 expression

in U251, thus promoting TMZ's entry into the GBM cells. Therefore, in this study, the DOX loaded on the nanoparticles could bypass the P-gp efflux system, leading to higher DOX's uptake in the GBM cells [6,58,65]. Similarly, higher uptake of DOX upon treatment of C6 glioma cells with DOX-loaded-polysorbate 80-SPIONs in comparison to that of free DOX was reported through endocytosis of the nanoparticles [11].

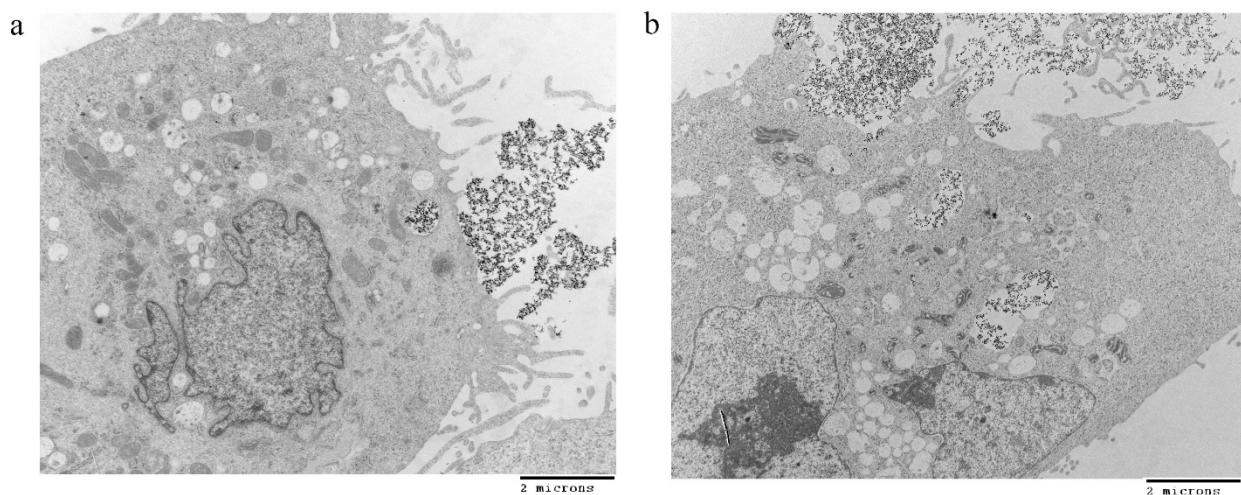


Fig. 2.4. TEM images of nanoparticles uptake by U251 cells cell after 4 h of the treatment, (a) EDT-IONPs and (b) DOX-EDT-IONPs.

### 2.3.5. Cytotoxicity of DOX-EDT-IONPs on cancer cell

The cytotoxicity of DOX-EDT-IONPs against U251 was studied in comparison to free DOX at different concentrations (0.25, 0.5 and 0.1  $\mu\text{g/mL}$ ). Based on the MTT assay, the cell viability upon a 48 h-treatment with DOX and DOX-EDT-IONPs (at concentration of 1  $\mu\text{g/mL}$  of DOX) decreased to  $25\% \pm 1.1\%$  and more significantly to  $17\% \pm 1.9\%$  ( $p < 0.05$ ), whilst the EDT-IONPs did not show cytotoxic effects on GBM cells (Fig. 2.5). It is also noteworthy to mention that the  $\text{IC}_{50}$  of DOX was found to be ca. 300  $\mu\text{g/mL}$  (supplementary materials: Fig. S 2.1), and the selected concentration (0.5 and 1  $\mu\text{g/mL}$ ) were above that. The concentration of 1  $\mu\text{g/mL}$  of

DOX was selected for the subsequent studies. Similar cytotoxic effects of DOX released from DOX-loaded-chitosan-modified Fe<sub>3</sub>O<sub>4</sub> nanoparticles [15], and core-shell nanocarriers (ZnO-polyacrylamide-DOX) [66] against GBM cell lines have previously been reported. In addition to the modest improvement in cytotoxicity of DOX when administered as DOX-EDT-IONPs on GBM cells, the capability of DOX-EDT-IONPs to improve DOX's delivery across the biological barriers is also of importance in determining overall improvements with the IONP formulation. Moreover, the DOX-EDT-IONPs potentially provide the capability of site-specific magnetic targeting to diminish DOX's systemic side effects [11,15]. For example, Xu *et al.*, [11] reported that IONPs could enhance DOX uptake by C6 glioma cells in rats bearing intracranial tumors particularly in the presence of an external magnetic field, while DOX-associated toxicity was prevented. Correspondingly, animal survival was prolonged from 32 days and 38.5 days for mice treated with DOX and DOX-IONPs, respectively to 79.2 days for mice treated with DOX-IONPs in the presence of an external magnetic field.

Induction of apoptosis through DNA damage via intercalation into DNA and inhibition of topoisomerase-II is a *de facto* mechanism of DOX's cytotoxicity [67]. In this study, both DOX and DOX-EDT-IONPs were found to be effective in inducing apoptosis in U251 cells after 72 h, leading to ca. 93% late apoptotic cell death, and no considerable cell viability (Fig. 2.6). In late apoptosis, the cellular membrane integrity is lost, thus cells demonstrate both annexin V-FITC (+)/PI (+) [68]. Likewise, treatments with both DOX and DOX-EDT-IONPs significantly inhibited GBM cell proliferation by over 90% (Fig. 2.7). Similarly, the anti-proliferative effects of DOX loaded in cationic solid lipid nanoparticles (CASLNs) [69] and DOX-polyglycerol-nanodiamond composites [70] were reported on U87 GBM cell line. For example, Kuo *et al.*, [69]

reported a greater anti-proliferative effect of DOX-CASLNs than that of free DOX due to the higher DOX uptake in GBM cells by the carrier-mediated pathway.

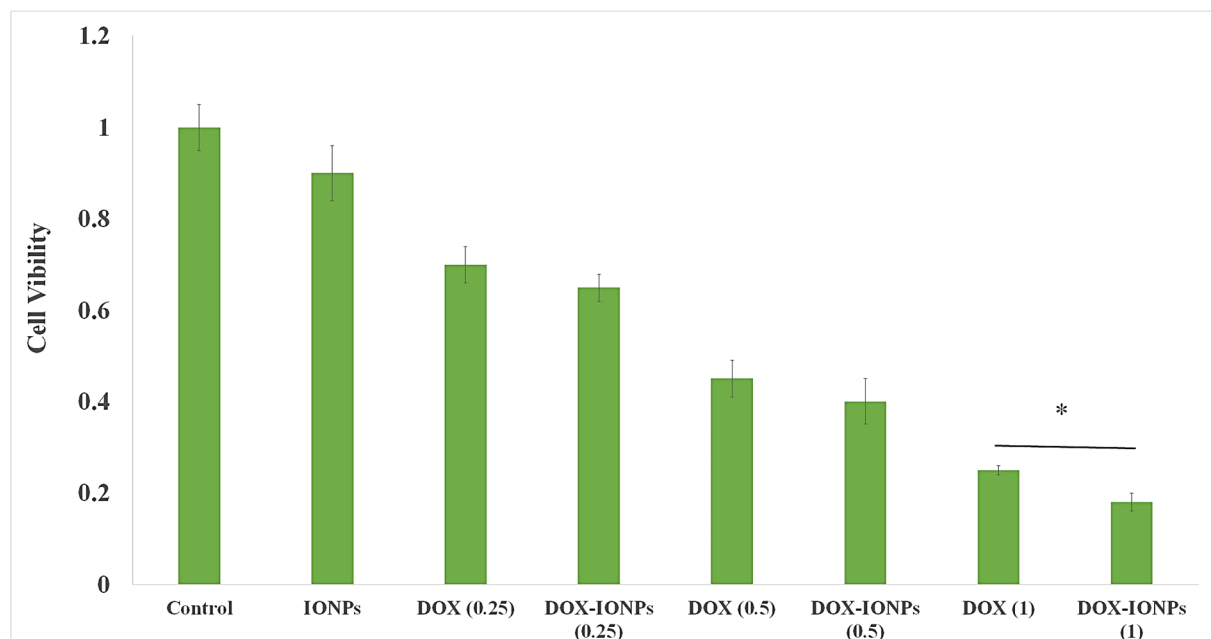


Fig. 2.5. Cytotoxicity assessment of various concentrations of DOX and DOX-EDT-IONPs (0.25, 0.5 and 0.1  $\mu\text{g}/\text{mL}$ ) on U251 after 48 h treatment. \* indicates a significant difference at  $p < 0.05$ . Data is presented as mean  $\pm$  S.D, and  $n=6$ . The Y-axis represents cell viability compared to the control. IONPs and DOX-IONPs represent for EDT-IONPs and DOX-EDT-IONPs.

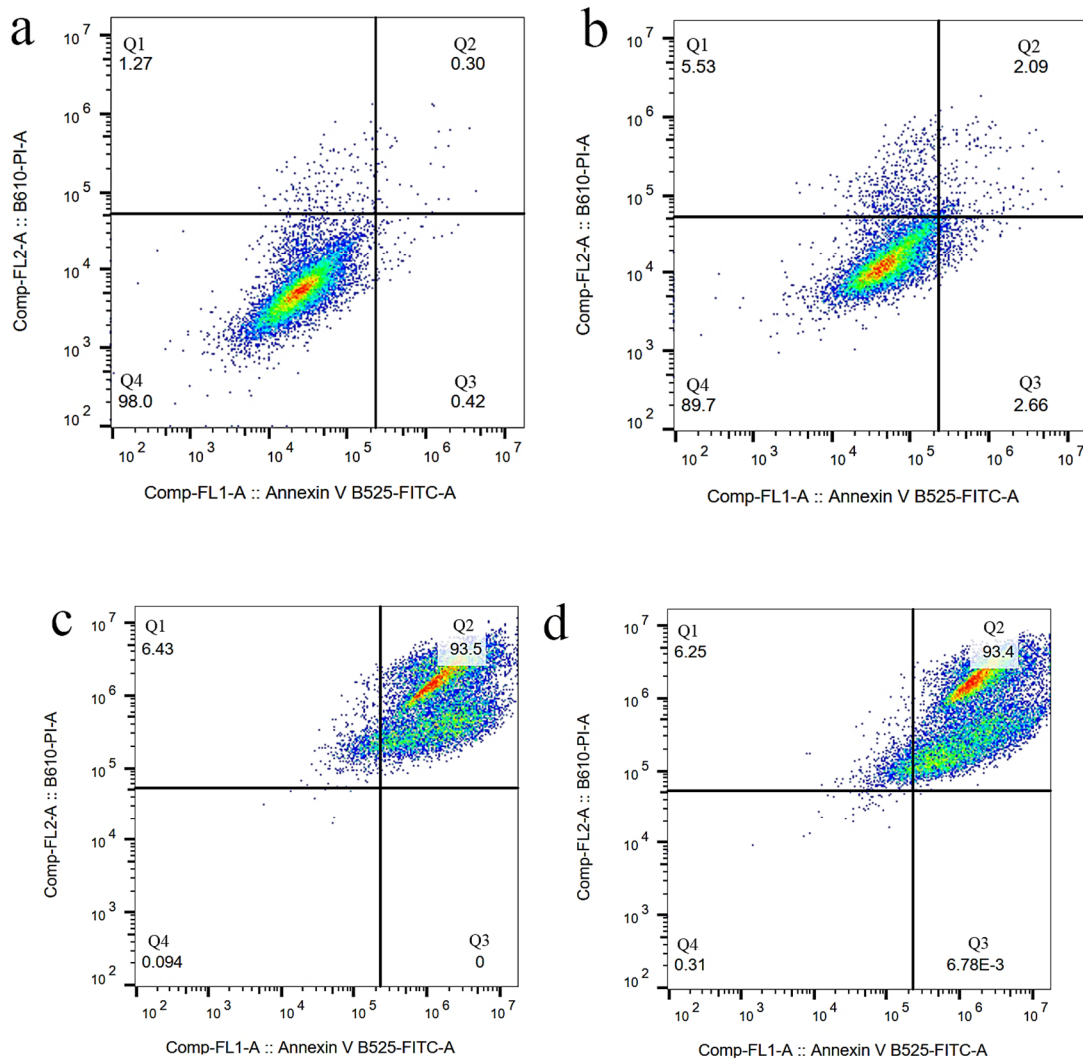


Fig. 2.6. Flow cytometer analysis for cell apoptosis/necrosis of U251 upon 48-hour treatment, stained with Annexin V-FITC and PI. (a) Control, (b) EDT-IONPs (c) DOX, and (d) DOX-EDT-IONPs. (Q4) demonstrates Live, (Q3) early apoptotic, (Q2) late apoptotic and (Q1) necrotic cells.

The studies of cell morphology indicated that in addition to a significant reduction in the cell population, both DOX and DOX-EDT-IONPs treatments induced notable morphological changes from a cuboidal morphology of normal U251 to a shrunken and spindle-like structure of actin cytoskeleton and a disrupted nucleus (Fig. 2.8). The effect of DOX in induction of remodeling

in actin cytoskeleton and disruption of central stress fibers leading to impaired cell adhesion and increased cell detachment has been reported previously [71]. Moreover, phosphorylated H2AX ( $\gamma$ -H2AX), mediating DNA double-strand break, is an early and sensitive biomarker in DNA double-strand break response [72]. In Fig. 2.8,  $\gamma$ -H2AX can be visualized as foci by immunofluorescence in U251 treated with either DOX or DOX-EDT-IONPs. Such findings indicate DNA damage following DOX treatment in GBM cells. This is in accordance with previous findings of DOX-induced DNA damage and appearance of  $\gamma$ -H2AX in breast [72] and lung [73] cancer cells.

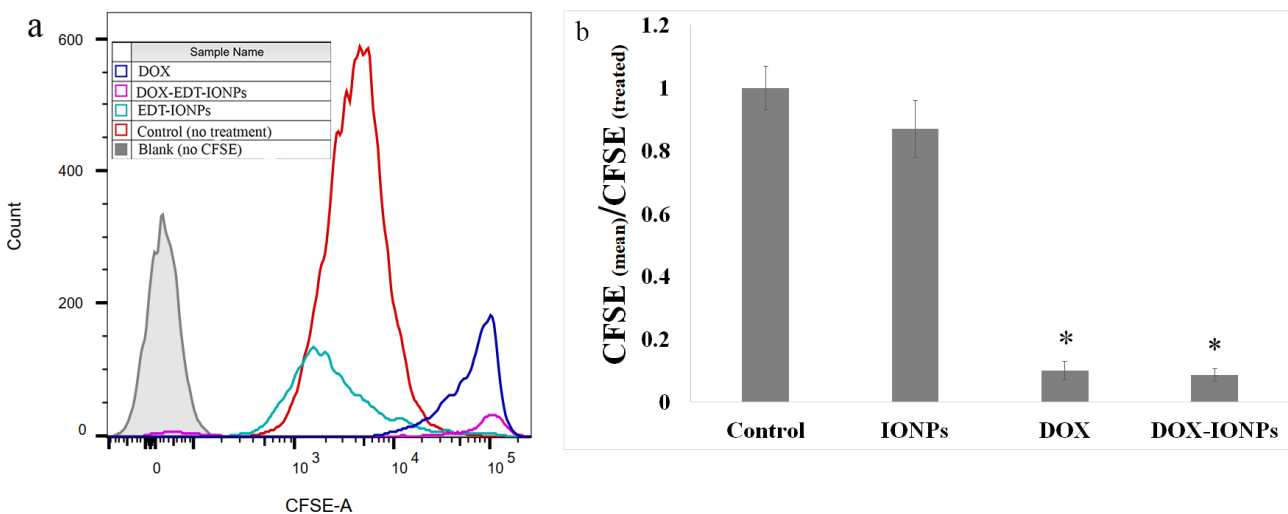


Fig. 2.7. Flow cytometer analysis for cell proliferation assay of carboxyfluorescein succinimidyl ester (CFSE)-labelled U251 upon treatment with EDT-IONPs, DOX and DOX-EDT-IONPs. (a) CFSE flow cytometry graph, and (b) the relative cell proliferation inhibition calculated by (mean CFSE control/mean CFSE treated). \* shows a significant difference compared to the control group at  $p < 0.05$ . IONPs and DOX-IONPs represent for EDT-IONPs and DOX-EDT-IONPs.

The studies of cell morphology indicated that in addition to a significant reduction in the cell population, both DOX and DOX-EDT-IONPs treatments induced notable morphological changes from a cuboidal morphology of normal U251 to a shrunken and spindle-like structure of actin cytoskeleton and a disrupted nucleus (Fig. 2.8). The effect of DOX in induction of remodeling in actin cytoskeleton and disruption of central stress fibers leading to impaired cell adhesion and

increased cell detachment has been reported previously [71]. Moreover, phosphorylated H2AX ( $\gamma$ -H2AX), mediating DNA double-strand break, is an early and sensitive biomarker in DNA double-strand break response [72]. In Fig. 2.8,  $\gamma$ -H2AX can be visualized as foci by immunofluorescence in U251 treated with either DOX or DOX-EDT-IONPs. Such findings indicate DNA damage following DOX treatment in GBM cells. This is in accordance with previous findings of DOX-induced DNA damage and appearance of  $\gamma$ -H2AX in breast [72] and lung [73] cancer cells.

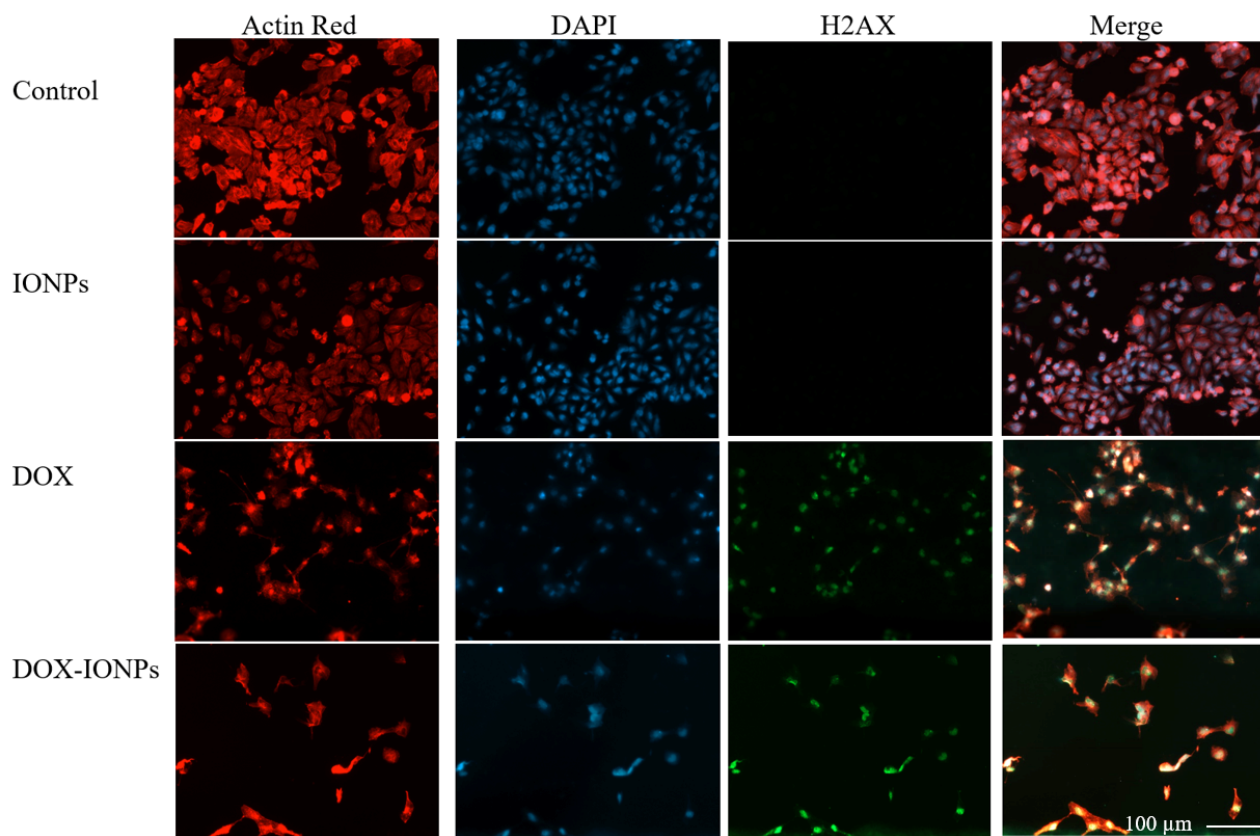


Fig. 2.8. Fluorescence microscopy images of U251 with or without treatment after 48 h. Red, blue and green fluorescence colours represent Alexa Fluor@ 488 phalloidin-stained F-actin, DAPI-stained cell nuclei, and  $\gamma$ -H2AX, a marker of DNA double-strand breaks, respectively. IONPs and DOX-IONPs represent for EDT-IONPs and DOX-EDT-IONPs.

### 2.3.6. ROS generation

ROS generation is a well-known mechanism of DOX to induce apoptotic death in various cancer cells such as human osteosarcoma Saos-2 [74], and human ovarian cancer cells [75]. Treatment of U251 with either DOX or DOX-EDT-IONPs increased the formation of ROS by  $1.9\pm 0.11$  and  $2.2\pm 0.18$  fold, respectively within 72 h, while only DOX-EDT-IONPs showed a ROS-inducing effect at 48 h (Fig. 2.9). Similarly, the effect of DOX on ROS induction and apoptosis in U87 GBM cell line has been reported [76]. It is also noteworthy to mention that ROS-induction is one of cytotoxicities associated with IONPs and over 800% enhancement in the intracellular ROS was reported into porcine endothelial cells (3 h exposure, 0.5 mg/mL of IONPs)[77]. Nonetheless, our finding proves that the synthesized EDT-IONPs were biocompatible and did not induce intracellular ROS *per se*. Taken together, triggered ROS-mediated DNA damage is suggested as one of the potential mechanisms of DOX-induced cell apoptosis in human GBM cells.

### 2.3.7. Quantitative RT-PCR

To demonstrate the anti-cancer effect and mechanism of DOX and DOX-EDT-IONPs treatments on U251, a series of gene studies was conducted (Fig. 2.10). Topoisomerase II $\alpha$  (Top II) is a key enzyme in DNA replication, that is considered as a prominent molecular target of several anti-cancer drugs such as DOX and etoposide [78,79]. DOX inhibits topoisomerase II (TOP2), by which the DNA replication, transcription and repair are interrupted [26]. Ku70, a DNA-dependent protein kinase, is another factor involved in the repair of DNA double-strand breaks and known as a survival factor in some cancer cells [80,81]. Treatment of U251 with DOX-

EDT-IONPs reduced markedly the expression of both Ku70 and Top II, which would further reduce DNA repair and replication in the GBM cells.

Caspases are essential mediators of programmed cell death and they are triggered sequentially, in which activation of Caspase 12 leads to the activation of Caspase 9 and the subsequent ‘effector’ Caspase 3 [82]. Both DOX and DOX-EDT-IONPs treatments upregulated the Caspase 3 gene expression, which is consistent with its upregulation in C6 glioma [11], leukemia HL-60 [83], and MCF-7 breast cancer [84] cells upon DOX treatments. p53 is a tumor suppressor protein whose mutation is the most prevalent genetic alteration in human cancers [85]. In fact, the p53 protein can inhibit DNA synthesis and regulates cell apoptosis through competition with the DNA repair mechanisms [26]. The U251 cells treated with DOX and DOX-EDT-IONPs exhibited an upregulated expression of p53.

Maternally Expressed Gene 3 (MEG3) is an imprinted non-coding RNA that acts as a tumor suppressor through both p53-dependent and p53-independent pathways [86]. Furthermore, it has been found that MEG3 expression markedly is diminished in glioma tumors, whereas whose expression can inhibit cell proliferation and promoted cell apoptosis in U251 and U87 GBM cell lines [87]. lncRNA-growth arrest-specific 5 (Gas5) is another tumor-suppressor gene that is downregulated in glioma cells [88,89]. Suppressing the GBM tumor malignancy has been observed through introduction of Gas 5 and consequently downregulation of miR-222 [90]. Here, both DOX and DOX-EDT-IONPs treatments were found to be effective in upregulation of both tumor suppressors, i.e. MEG3 and Gas5, which potentially leads to GBM cell apoptosis.

MiR-155 is an important oncogenic microRNA that is overexpressed in various malignant tumors including GBM, whose mechanism of action is associated with a blockade of Caspase-3 activity and regulation of multiple genes involved in cancer cell proliferation, and invasiveness

[91,92]. The expression of MiR-155 in U251 was downregulated upon treatment with either DOX (0.457±0.24 fold) or more significantly with DOX-EDT-IONPs (0.28±0.03-fold, p<0.05). It also has been reported that downregulation of MiR-155 can enhance the chemosensitivity of U251 cells to Taxol by interrupting the activity of EAG1 pathways and inducing apoptosis [92].

In addition, the Wnt signaling pathway plays an important role in malignant transformation and tumor progression in gliomas [93], and the capacity of intracranial tumor formation has been found to be reduced upon Wnt silencing, *in vivo* [94,95]. Here, U251 demonstrated a significant downregulation of Wnt1 upon the treatments with either DOX (0.21±0.04 fold) or DOX-EDT-IONPs (0.17±0.03 fold).

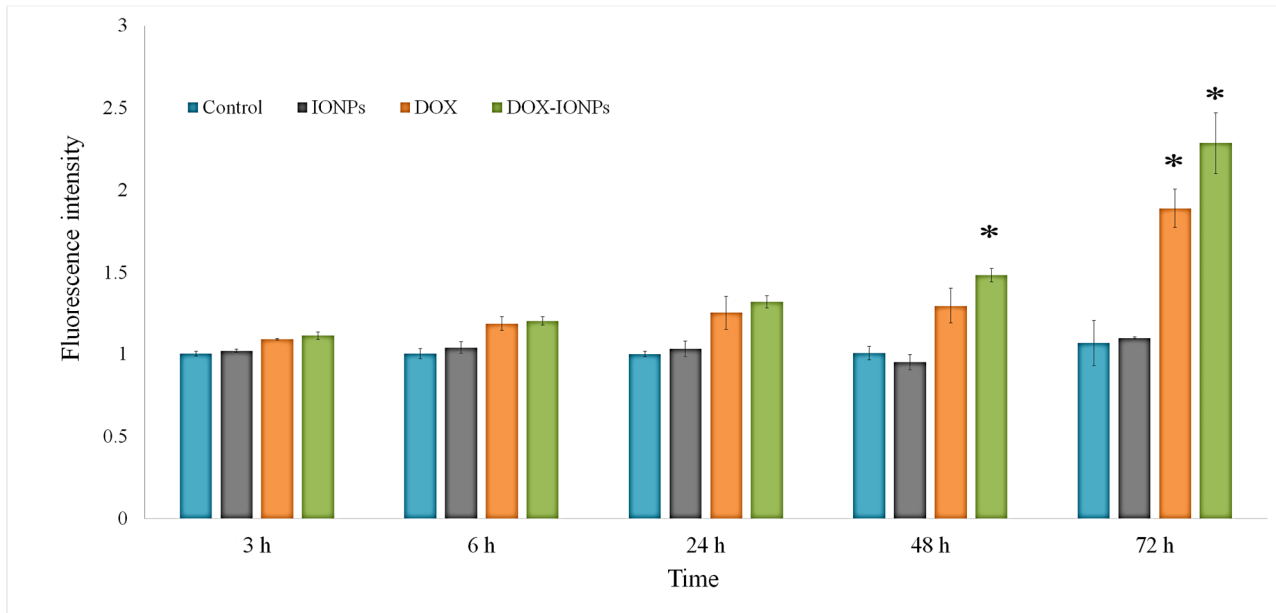


Fig. 2.9. ROS induction by EDT-IONPs, DOX or DOX-EDT-IONPs in U251 at different time-points. \* indicates a significant difference compared to the control group at p <0.05. Data is presented as mean ±S.D, and n = 5. IONPs and DOX-IONPs represent for EDT-IONPs and DOX-EDT-IONPs.

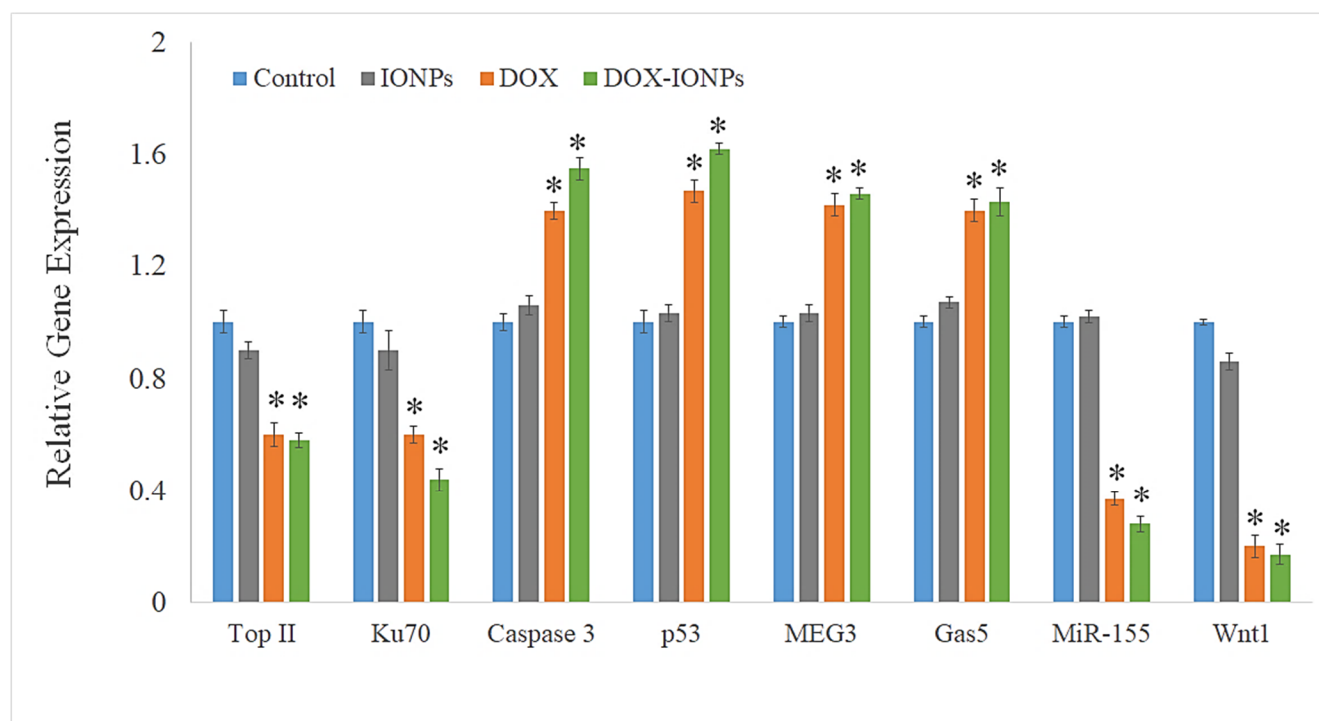


Fig. 2.10. Relative gene expression of U251 cell upon treatment with either EDT-IONPs, DOX or DOX-EDT-IONPs for 48 h. \* indicates a significance difference compared to the control group, and \*\* compared to DOX-treated cells at  $p < 0.05$ . Data is presented as mean  $\pm$  S.D, and  $n=5$ . IONPs and DOX-IONPs represent for EDT-IONPs and DOX-EDT-IONPs.

### 2.3.8. Anti-cancer effect of DOX-EDT-IONPs (*in vitro* GBM model)

Due to the inability of DOX to cross the BBB and penetrate into the tumor site, it demonstrates little effectiveness in treating GBM when administered systemically [96]. Having considered that, development of an efficient drug delivery system enabling penetration of DOX across the BBB and enhancing its bioavailability is a matter of significant importance in GBM chemotherapy. Since most of the brain endothelial cell lines have been reported that do not form a restrictive paracellular barrier required for screening the passage of small molecules [97], in the present study MDCK-MDR monolayer was used to assess the BBB permeability of DOX and DOX-EDT-IONPs. The MDCK-MDR cells overexpress P-gp and have reduced paracellular

diffusion due to the complex tight junction proteins. Therefore, these properties make MDCK-MDR cells a reproducible and accurate *in vitro* cell culture model for examining and predicting the permeability of drugs and solutes across the BBB [36,37]. In addition, a good correlation between bi-directional transport across MDCK-MDR cell monolayer and *in vivo* CNS was reported for 28 compounds [37]. Moreover, since the penetration of DOX across the BBB is mainly restricted by the P-gp expression under normal physiological conditions[98], the MDCK-MDR cells overexpressing P-gp can be an accurate *in vitro* cell culture model to predict the BBB permeability for DOX.

The limited BBB penetration of DOX was apparent in the BBB-GBM co-culture model (Fig. 2.11a). Evidence for this is the cytotoxicity of DOX (1 µg/mL) in the U251 monocultures compared to the BBB-GBM co-culture model. This is likely attributed to the P-gp drug efflux transporter liabilities of DOX. The DOX-EDT-IONP formulation showed a significant increase (ca. 1.5-fold) in penetration of DOX compared to DOX alone in the BBB-GBM co-culture model (Fig. 2.11a). As DOX is a substrate of P-gp efflux transporter that highly restricts its penetration into the brain [98,99], the improvement in DOX permeability observed in the present study is attributed the DOX-loaded nanoparticles circumventing the P-gp efflux transporter in the MDCK-MDR monolayers. However, despite the increase in permeability observed with DOX-EDT-IONP in the *in vitro* BBB model, the resulting cytotoxicity was not significantly higher than that of DOX alone (Fig. 2.11b). This suggests that improvement in DOX permeability with the IONP formulation alone was not sufficient to produce an enhanced cytotoxic response and additional measures were necessary to impact both permeability and response in the BBB-GBM co-culture model.

Transient disruption of the BBB with hyperosmotic solutions like mannitol has been reported to enhance the delivery of therapeutic molecules as well as IONPs into the brain [100-102]. In this regard, mannitol has extensively been used in combination with anti-tumor agents in clinical trials of glioma therapy over the last three decades [103,104]. Similarly, Sun *et al.*, [105] reported a significant increase in permeability of both EDT-IONPs and aminosilane-coated (AmS)-IONPs across brain endothelial cell monolayers when tight junctions were disrupted using mannitol. However, the extensive opening of the BBB by mannitol and the long recovery time for re-establishment of the BBB integrity can cause a gross and uncontrolled influx of low and high molecular weight substances from the blood into the brain that can result in neurological toxicity, jeopardizing patient safety [106]. In this study, using ADTC5 showed the advantage of not producing an extensive change in permeability of large molecules compared to the mannitol as evidenced by the IRDye permeability ( $2.7\pm 0.4\%$  and  $3.1\pm 0.3\%$  without and with ADTC5, respectively, compared to  $15.6\pm 0.6\%$  with mannitol). Moreover, as mentioned before, the recovery time for re-establishment of the BBB integrity was reported to be within 60 min post-injection of the cadherin binding peptide *in vivo* [53]. This means that using the cadherin peptide allowed the MDCK-MDR monolayers to maintain barrier properties to large IRDye macromolecule marker, while allowing enhanced penetration to the IONPs, especially in the presence of an external magnetic field. We have named this approach magnetic enhanced convective diffusion (MECD) as the IONPs diffuse across the transiently disrupted cell barrier in a bulk flow manner that is accelerated by the presence of an external magnetic field.

By transiently opening the MDCK-MDR monolayer tight junctions using ADTC5 and in combination with an external magnetic field, the GBM cell viability significantly decreased upon treatment with DOX-EDT-IONPs compared to the GBM cells treated with free DOX (cell viability

66±3.3% and 45±3.7% for GBM cells treated with free DOX and DOX-EDT-IONPs, respectively) (Fig. 2.11b). This result was consistent with the higher DOX-EDT-IONP permeability through the MDCK-MDR monolayer when both ADTC5 and external magnetic fields were applied.

The capability of DOX-EDT-IONPs to pass through the BBB was also examined using the MDCK-MDR-GBM co-culture model. Under normal conditions, DOX-EDT-IONPs showed 5.2±0.4% penetration across the MDCK-MDR monolayer over 4 hours of the treatment. The diffusion of DOX-EDT-IONPs could be increased by either enhancing the MDCK-MDR monolayer permeability with ADTC5 (6.2±0.45%) or by application of an external magnetic field (7.4±0.5%) (Fig. 2.11c). Using both ADTC5 and external magnetic field also could significantly augment DOX-EDT-IONP penetration by 8.5±0.36%. The greater penetration of DOX-EDT-IONP than that of IRdye could be attributed to the endocytosis and intracellular transport of the nanoparticles across the MDCK-MDR cells [107,108]. To the best of our knowledge, this is the first report on the combinational effect of cadherin binding peptide and external magnetic field as an effective approach to enhance the permeability of drug delivery systems across the BBB.

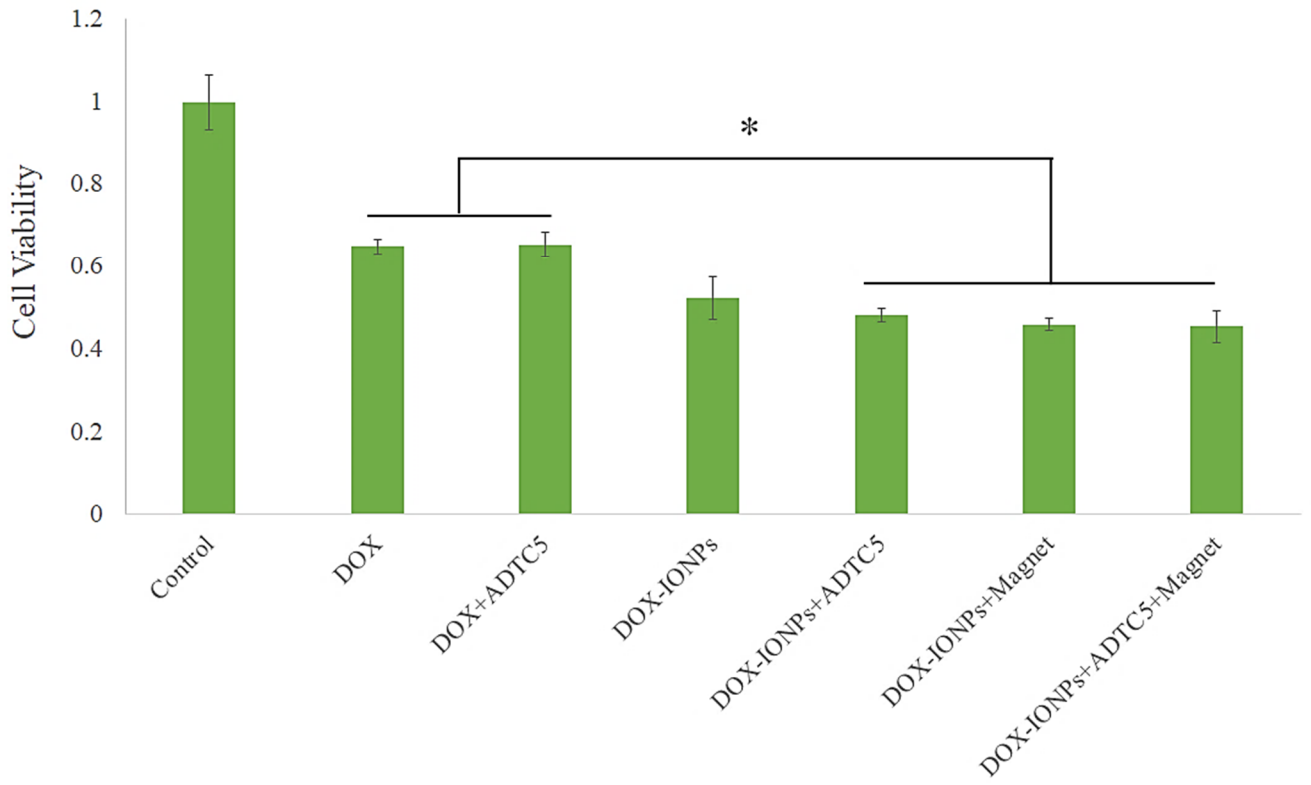
As mentioned earlier, IONPs uniquely provide a site-specific magnetic targeting utilizing an external magnetic field to draw the nanoparticles to the site of action and enhancing their bioavailability [109]. For instance, by applying an external magnetic field, overall tumor exposure to magnetic nanoparticles was enhanced by 5-fold compared to non-targeted tumors [110]. Moreover, ADTC5 has shown an enhanced delivery of various marker molecules (e.g., <sup>14</sup>C-mannitol, Gd-DTPA) across the MDCK monolayer *in vitro*, and the BBB *in vivo* through binding to the EC1 domain of E-cadherin, blocking the cadherin–cadherin interactions and thus enhancing the delivery of molecules into the brain via the paracellular pathway of the BBB [111].

Therefore, the developed DOX-EDT-IONPs in combination with the magnetic enhanced convective diffusion and the cadherin binding peptide for transiently opening the BBB tight junctions were found effective to enhance DOX's bioavailability and anti-cancer effect in GBM cells by virtue of overcoming the MDR and enhancing the permeability of DOX through a BBB model *in vitro*.

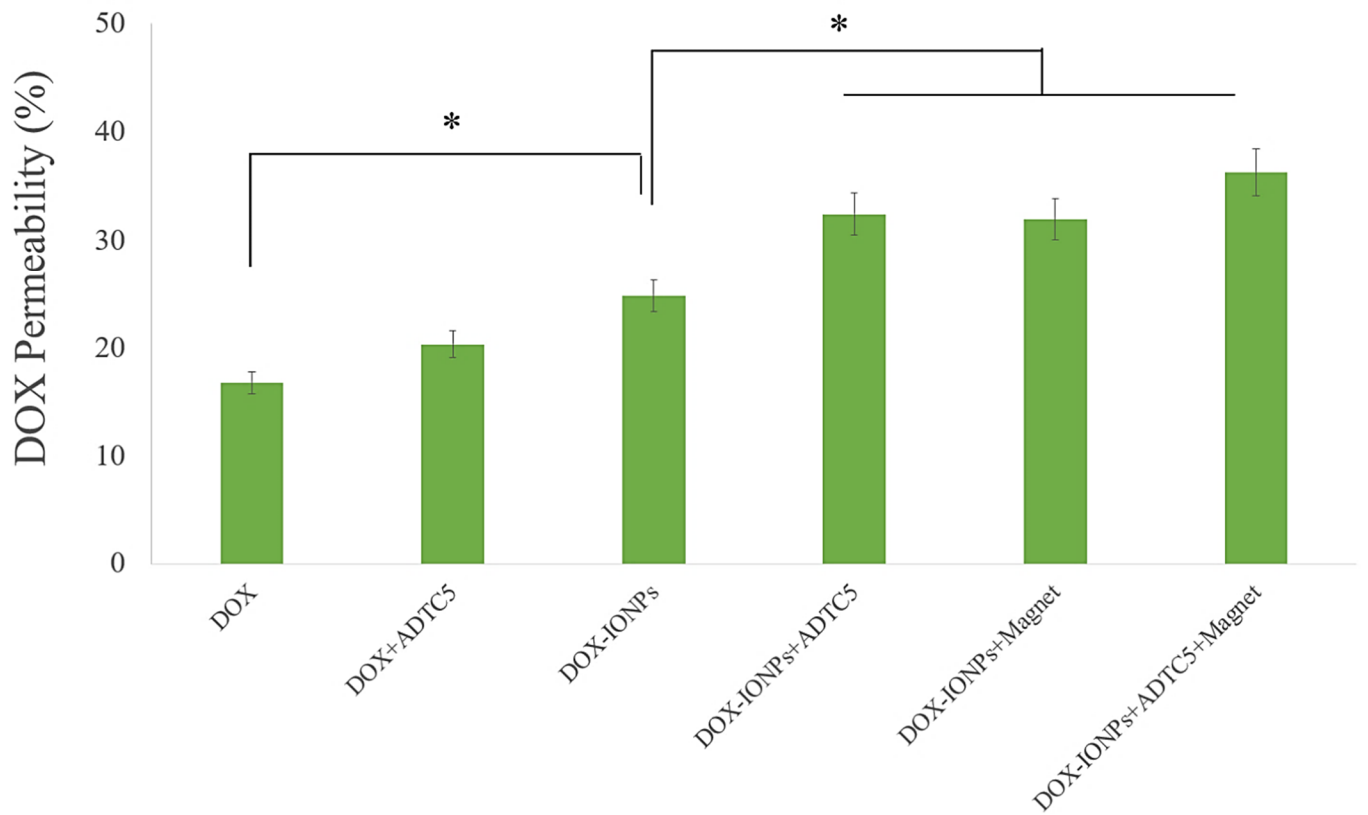
This combinational approach can potentially be an efficacious alternative for the passive targeting through the enhance permeability and retention (EPR) effect, or ligand-based active targeting of the IONPs in clinical practice. In fact, the EPR effect in humans has been found not as prominent as in animal models [112]. Moreover, for early stage of brain tumors, the EPR effect cannot play an important role inasmuch as the BBB is still intact, and leakiness is observed at the stages when tumor volume is high and difficult to treat [113]. In addition, the infiltrating tumor cells are mostly associated with the intact BBB that would impede passive targeting of nanoparticles [114]. On the other hand, the clinical outcomes of active targeting have still not been promising in trials that can be attributed to the expression of target receptors in some types of tumors, the tumor heterogeneity and the interpatient variability [115,116]. BIND-014 and MM-302 are two examples of active targeting nanomedicines that failed in clinical studies[115]. Having considered that, this novel combinational approach of using cadherin binding peptide for transiently opening the BBB tight junctions in juxtaposition with magnetic enhanced convective diffusion can be an alternative and effective approach for the passive targeting and ligand-based active targeting of drug-loaded IONPs in clinical practice. This combinational approach can provide a site-specific magnetic targeting to reduce systemic distribution of the drug-loaded IONPs, a transiently opening of the BBB tight junctions using a cadherin binding peptide, and an enhanced convective diffusion of the magnetic nanoparticles into the brain. These together can

reduce the systemic toxicity of chemotherapy, enhance the permeability of the drug-loaded nanoparticles into the brain and ameliorate the efficacy of GBM chemotherapy by providing a therapeutic concentration of the effective anti-cancer drugs like DOX that are intrinsically impermeable to the BBB.

a



b



c

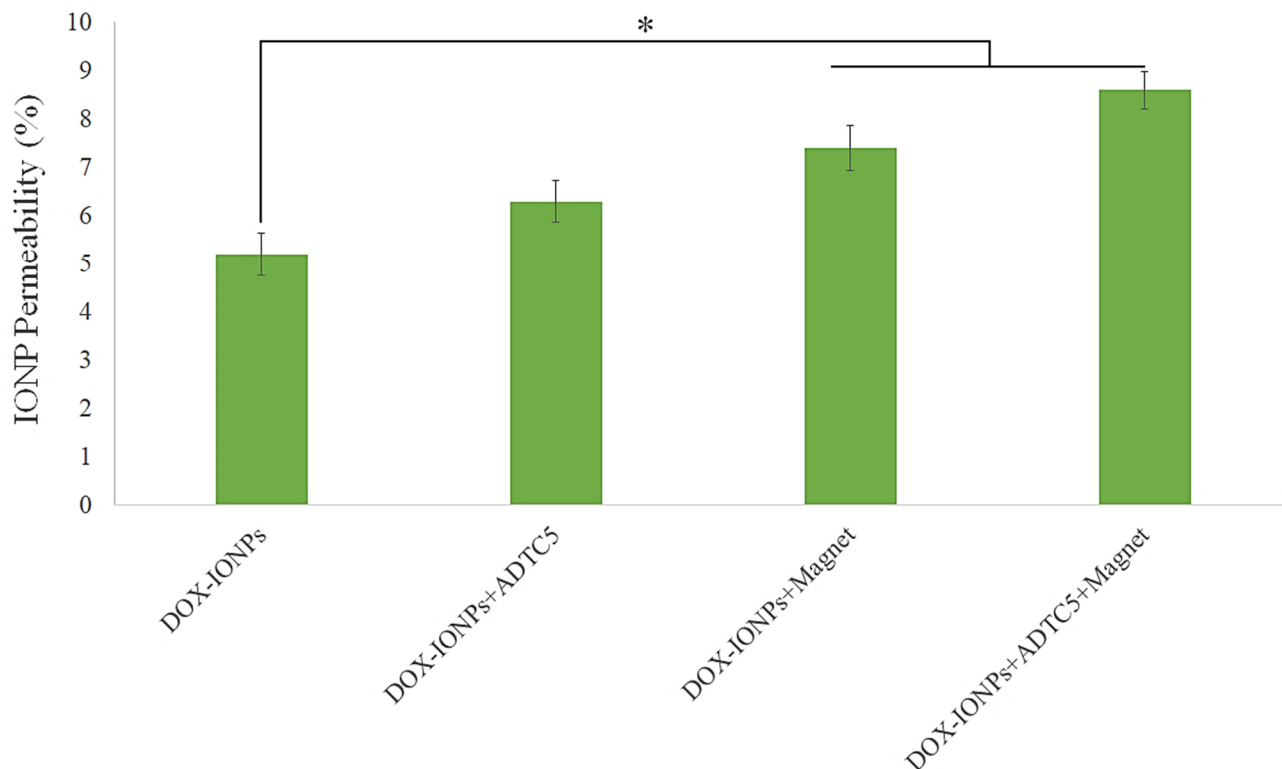


Fig. 2.11. Anti-cancer efficacy of DOX-EDT-IONPs compared to the free DOX on an MDCK-MDR-GBM model *in vitro*. (a) DOX permeability across the MDCK-MDR monolayer with or without IONPs in the presence or absence of magnet and ADTC5 (b) cytotoxicity of each formulation on U251 cells after penetrating the monolayer. (c) DOX-IONPs permeability across the MDCK-MDR monolayer with or without magnet and ADTC5. \* indicates a significant difference at  $p < 0.05$  with the other treated groups. Data is presented as mean  $\pm$  S.D, and  $n=3$ . IONPs and DOX-IONPs represent for EDT-IONPs and DOX-EDT-IONPs.

## 2.4. Conclusion

In this study, DOX-EDT-IONPs were developed to facilitate drug delivery to GBM tumor cells. The DOX was entirely released from the DOX-EDT-IONPs within 4 days, while the nanoparticles could augment the DOX's uptake in U251 cells by 2.8-fold. The DOX-EDT-IONPs was found to be effective in apoptosis-induced cell death, proliferation inhibition, and ROS-induction in U251 cells. Moreover, DOX-EDT-IONPs treatment could downregulate TOP II and

Ku70, essential enzymes for DNA repair and replication, as well as MiR-155 oncogene, while concomitantly upregulated Caspase 3, a key mediator of apoptosis, and tumor suppressors i.e., p53, MEG3 and GAS5, in U251 cells. Furthermore, recruiting an *in vitro* MDCK-MDR-GBM co-culture model, the EDT-IONPs could enhance DOX penetration through the MDCK-MDR monolayer over 2-fold and provided significantly higher anti-cancer effect than free DOX in GBM cells in the presence of an external magnetic field and ADTC5. In addition, the DOX-EDT-IONPs demonstrated  $5.2 \pm 0.4\%$  permeability through the MDCK-MDR monolayer that significantly increased in the presence of an external magnetic field to  $7.4 \pm 0.5\%$ , indicating the magnetically driven enhanced diffusion of DOX-EDT-IONPs across the MDCK-MDR monolayer. In addition, using a cyclic ADT peptide as a transient disruption agent in combination with an external magnetic field could augment the permeability of DOX-EDT-IONPs across the monolayer to  $8.5 \pm 0.36\%$ . Therefore, using an external magnetic field, not only the developed DOX-EDT-IONPs can potentially be drawn to the target site, but also their penetration into the brain can be enhanced. Moreover, the combination of an external magnetic field and a cadherin binding peptide can further augment the penetration of the DOX-EDT-IONPs, while do not extensively disrupt the BBB as compared to other techniques like hyperosmotic treatment. Therefore, the BBB remains relatively intact to large macromolecules, which correspondingly diminishes the risk of neurological toxicity. In conclusion, the developed DOX-EDT-IONPs in combination with the magnetic enhanced convective diffusion and the ADTC5 for transiently opening the BBB tight junctions can potentially provide an efficacious formulation of DOX in GBM chemotherapy by virtue of enhancing DOX's penetration into the brain, overcoming the MDR cancer cells, providing a site-specific magnetic targeting and diminishing the systemic toxicity.

## 2.5. References

- 1 Hu, S. et al. (2018) Real-Time Imaging of Brain Tumor for Image-Guided Surgery. *Advanced healthcare materials*, 1800066
- 2 Grauwet, K. and Chiocca, E.A. (2016) Glioma and microglia, a double entendre. *Nature immunology* 17 (11), 1240
- 3 Stupp, R. et al. (2009) Effects of radiotherapy with concomitant and adjuvant temozolomide versus radiotherapy alone on survival in glioblastoma in a randomised phase III study: 5-year analysis of the EORTC-NCIC trial. *The lancet oncology* 10 (5), 459-466
- 4 Heffernan, J.M. et al. (2017) PNIPAAm-co-Jeffamine®(PNJ) scaffolds as in vitro models for niche enrichment of glioblastoma stem-like cells. *Biomaterials* 143, 149-158
- 5 Hong, C.S. et al. (2016) Characterization of the blood brain barrier in pediatric central nervous system neoplasms. *Journal of interdisciplinary histopathology* 4 (2), 29
- 6 Liu, H. et al. (2016) Application of iron oxide nanoparticles in glioma imaging and therapy: from bench to bedside. *Nanoscale* 8 (15), 7808-7826
- 7 Kulczar, C. et al. (2017) Development of a direct contact astrocyte-human cerebral microvessel endothelial cells blood-brain barrier coculture model. *Journal of Pharmacy and Pharmacology* 69 (12), 1684-1696
- 8 Cheng, Y. et al. (2014) Blood-brain barrier permeable gold nanoparticles: an efficient delivery platform for enhanced malignant glioma therapy and imaging. *Small* 10 (24), 5137-5150
- 9 Norouzi, M. et al. (2017) Electrospun-based systems in cancer therapy. In *Electrospun Materials for Tissue Engineering and Biomedical Applications*, pp. 337-356, Elsevier
- 10 Gao, H. (2016) Progress and perspectives on targeting nanoparticles for brain drug delivery. *Acta Pharmaceutica Sinica B* 6 (4), 268-286
- 11 Xu, H.-L. et al. (2016) Glioma-targeted superparamagnetic iron oxide nanoparticles as drug-carrying vehicles for theranostic effects. *Nanoscale* 8 (29), 14222-14236
- 12 Mujokoro, B. et al. (2016) Nano-structures mediated co-delivery of therapeutic agents for glioblastoma treatment: A review. *Materials Science and Engineering: C* 69, 1092-1102
- 13 Hola, K. et al. (2015) Tailored functionalization of iron oxide nanoparticles for MRI, drug delivery, magnetic separation and immobilization of biosubstances. *Biotechnology Advances* 33 (6), 1162-1176
- 14 Lee, N. et al. (2015) Iron oxide based nanoparticles for multimodal imaging and magnetoresponsive therapy. *Chemical Reviews* 115 (19), 10637-10689
- 15 Wang, X. et al. (2014) Construction of doxorubicin-loading magnetic nanocarriers for assaying apoptosis of glioblastoma cells. *Journal of colloid and interface science* 436, 267-275
- 16 Quinto, C.A. et al. (2015) Multifunctional superparamagnetic iron oxide nanoparticles for combined chemotherapy and hyperthermia cancer treatment. *Nanoscale* 7 (29), 12728-12736
- 17 Chertok, B. et al. (2010) Polyethyleneimine-modified iron oxide nanoparticles for brain tumor drug delivery using magnetic targeting and intra-carotid administration. *Biomaterials* 31 (24), 6317-6324
- 18 Peng, M. et al. (2015) Dextran-coated superparamagnetic nanoparticles as potential cancer drug carriers in vivo. *Nanoscale* 7 (25), 11155-11162
- 19 Lin, J. et al. (2015) Drug/dye-loaded, multifunctional PEG-chitosan-iron oxide nanocomposites for methotrexate synergistically self-targeted cancer therapy and dual model imaging. *ACS applied materials & interfaces* 7 (22), 11908-11920
- 20 Wang, Y.-X.J. (2015) Current status of superparamagnetic iron oxide contrast agents for liver magnetic resonance imaging. *World journal of gastroenterology* 21 (47), 13400
- 21 Fan, C.-H. et al. (2013) SPIO-conjugated, doxorubicin-loaded microbubbles for concurrent MRI and focused-ultrasound enhanced brain-tumor drug delivery. *Biomaterials* 34 (14), 3706-3715

- 22 Zhu, L. et al. (2013) Multifunctional pH-sensitive superparamagnetic iron-oxide nanocomposites for targeted drug delivery and MR imaging. *Journal of controlled release* 169 (3), 228-238
- 23 Chang, Y. et al. (2013) Dendrimer functionalized water soluble magnetic iron oxide conjugates as dual imaging probe for tumor targeting and drug delivery. *Polymer Chemistry* 4 (3), 789-794
- 24 Shen, B. et al. (2016) Smart multifunctional magnetic nanoparticle-based drug delivery system for cancer thermo-chemotherapy and intracellular imaging. *ACS applied materials & interfaces* 8 (37), 24502-24508
- 25 Cagel, M. et al. (2017) Doxorubicin: nanotechnological overviews from bench to bedside. *Drug discovery today* 22 (2), 270-281
- 26 Meredith, A.M. and Dass, C.R. (2016) Increasing role of the cancer chemotherapeutic doxorubicin in cellular metabolism. *Journal of Pharmacy and Pharmacology* 68 (6), 729-741
- 27 Akin, S. et al. (2018) Ifosfamide and doxorubicin in the treatment of advanced leiomyosarcoma. *Current problems in cancer* 42 (3), 344-349
- 28 Damiani, R.M. et al. (2018) Influence of PARP-1 inhibition in the cardiotoxicity of the topoisomerase 2 inhibitors doxorubicin and mitoxantrone. *Toxicology in Vitro*
- 29 Cibi, R. and Nair, A.J. (2016) Evaluation of the Efficacy of the Compound Actinomycin D in Tumor Cell Lines. *Int. J. Curr. Microbiol. App. Sci* 5 (7), 405-411
- 30 Jhaveri, N. et al. (2011) Noscapine inhibits tumor growth in TMZ-resistant gliomas. *Cancer letters* 312 (2), 245-252
- 31 Hau, P. et al. (2004) Pegylated liposomal doxorubicin—efficacy in patients with recurrent high-grade glioma. *Cancer: Interdisciplinary International Journal of the American Cancer Society* 100 (6), 1199-1207
- 32 Voulgaris, S. et al. (2002) Intratumoral doxorubicin in patients with malignant brain gliomas. *American journal of clinical oncology* 25 (1), 60-64
- 33 Du, Y. et al. (2018) Synthesis and Evaluation of Doxorubicin-Loaded Gold Nanoparticles for Tumor-Targeted Drug Delivery. *Bioconjugate chemistry* 29 (2), 420-430
- 34 Barenholz, Y.C. (2012) Doxil®—the first FDA-approved nano-drug: lessons learned. *Journal of controlled release* 160 (2), 117-134
- 35 Yathindranath, V. et al. (2013) One-pot synthesis of iron oxide nanoparticles with functional silane shells: a versatile general precursor for conjugations and biomedical applications. *Langmuir* 29 (34), 10850-10858
- 36 Madgula, V.L. et al. (2007) Transport of decursin and decursinol angelate across Caco-2 and MDR-MDCK cell monolayers: in vitro models for intestinal and blood-brain barrier permeability. *Planta medica* 73 (04), 330-335
- 37 Wang, Q. et al. (2005) Evaluation of the MDR-MDCK cell line as a permeability screen for the blood–brain barrier. *International journal of pharmaceutics* 288 (2), 349-359
- 38 Norouzi, M. et al. (2018) Salinomycin-loaded Nanofibers for Glioblastoma Therapy. *Scientific reports* 8 (1), 9377
- 39 Vakilian, S. et al. (2018) L. inermis-loaded nanofibrous scaffolds for wound dressing applications. *Tissue and Cell*
- 40 Norouzi, M. et al. (2015) PLGA/gelatin hybrid nanofibrous scaffolds encapsulating EGF for skin regeneration. *Journal of biomedical materials research Part A* 103 (7), 2225-2235
- 41 Sun, Z. et al. (2013) Characterization of cellular uptake and toxicity of aminosilane-coated iron oxide nanoparticles with different charges in central nervous system-relevant cell culture models. *International journal of nanomedicine* 8, 961
- 42 Sun, Z. et al. (2016) Differential internalization of brick shaped iron oxide nanoparticles by endothelial cells. *Journal of Materials Chemistry B* 4 (35), 5913-5920
- 43 Sun, Z. et al. (2016) Biodistribution of negatively charged iron oxide nanoparticles (IONPs) in mice and enhanced brain delivery using lysophosphatidic acid (LPA). *Nanomedicine: Nanotechnology, Biology and Medicine* 12 (7), 1775-1784

- 44 Wong, H.L. et al. (2006) A mechanistic study of enhanced doxorubicin uptake and retention in multidrug resistant breast cancer cells using a polymer-lipid hybrid nanoparticle system. *Journal of Pharmacology and Experimental Therapeutics* 317 (3), 1372-1381
- 45 Kaech, S.M. and Ahmed, R. (2001) Memory CD8+ T cell differentiation: initial antigen encounter triggers a developmental program in naive cells. *Nature immunology* 2 (5), 415
- 46 Eruslanov, E. and Kusmartsev, S. (2010) Identification of ROS using oxidized DCFDA and flow-cytometry. In *Advanced protocols in oxidative stress II*, pp. 57-72, Springer
- 47 Sinaga, E. et al. (2002) Increasing paracellular porosity by E-cadherin peptides: discovery of bulge and groove regions in the EC1-domain of E-cadherin. *Pharmaceutical research* 19 (8), 1170-1179
- 48 Lee, J.-Y. et al. (2017) Chemosensitizing indomethacin-conjugated chitosan oligosaccharide nanoparticles for tumor-targeted drug delivery. *Acta biomaterialia* 57, 262-273
- 49 Huang, P. et al. (2016) Zwitterionic nanoparticles constructed from bio-reducible RAFT-ROP double head agent for shell shedding triggered intracellular drug delivery. *Acta biomaterialia* 40, 263-272
- 50 Zhang, T. et al. (2019) Multitargeted Nanoparticles Deliver Synergistic Drugs across the Blood-Brain Barrier to Brain Metastases of Triple Negative Breast Cancer Cells and Tumor-Associated Macrophages. *Advanced healthcare materials*, 1900543
- 51 Sun, Z. et al. (2014) Magnetic field enhanced convective diffusion of iron oxide nanoparticles in an osmotically disrupted cell culture model of the blood-brain barrier. *International journal of nanomedicine* 9, 3013
- 52 Yathindranath, V. et al. (2011) A Versatile Method for the Reductive, One-Pot Synthesis of Bare, Hydrophilic and Hydrophobic Magnetite Nanoparticles. *Advanced Functional Materials* 21 (8), 1457-1464
- 53 On, N.H. et al. (2014) Modulation of blood-brain barrier permeability in mice using synthetic E-cadherin peptide. *Molecular pharmaceuticals* 11 (3), 974-981
- 54 Mu, Q. et al. (2015) Anti-HER2/neu peptide-conjugated iron oxide nanoparticles for targeted delivery of paclitaxel to breast cancer cells. *Nanoscale* 7 (43), 18010-18014
- 55 Norouzi, M. et al. (2016) Injectable hydrogel-based drug delivery systems for local cancer therapy. *Drug discovery today*
- 56 Norouzi, M. (2018) Recent advances in brain tumor therapy: application of electrospun nanofibers. *Drug discovery today*
- 57 Weissleder, R. et al. (1989) Superparamagnetic iron oxide: pharmacokinetics and toxicity. *AJR. American journal of roentgenology* 152 (1), 167-173
- 58 Kievit, F.M. et al. (2011) Doxorubicin loaded iron oxide nanoparticles overcome multidrug resistance in cancer in vitro. *Journal of controlled release* 152 (1), 76-83
- 59 Hellinger, É. et al. (2012) Comparison of brain capillary endothelial cell-based and epithelial (MDCK-MDR1, Caco-2, and VB-Caco-2) cell-based surrogate blood-brain barrier penetration models. *European Journal of Pharmaceutics and Biopharmaceutics* 82 (2), 340-351
- 60 Corot, C. et al. (2006) Recent advances in iron oxide nanocrystal technology for medical imaging. *Advanced drug delivery reviews* 58 (14), 1471-1504
- 61 Chen, J. et al. (2010) Gold nanocages as photothermal transducers for cancer treatment. *Small* 6 (7), 811-817
- 62 Melamed, J.R. et al. (2016) Using gold nanoparticles to disrupt the tumor microenvironment: an emerging therapeutic strategy. *ACS nano* 10 (12), 10631-10635
- 63 Saraiva, C. et al. (2016) Nanoparticle-mediated brain drug delivery: overcoming blood-brain barrier to treat neurodegenerative diseases. *Journal of Controlled Release* 235, 34-47
- 64 Wang, N. et al. (2017)  $\beta$ -Asarone promotes Temozolomide's entry into glioma cells and decreases the expression of P-glycoprotein and MDR1. *Biomedicine & Pharmacotherapy* 90, 368-374
- 65 Gautier, J. et al. (2013) Recent advances in theranostic nanocarriers of doxorubicin based on iron oxide and gold nanoparticles. *Journal of Controlled Release* 169 (1), 48-61

- 66 Zhang, Z.Y. et al. (2013) Biodegradable ZnO@ polymer core-shell nanocarriers: pH-triggered release of doxorubicin in vitro. *Angewandte Chemie International Edition* 52 (15), 4127-4131
- 67 Li, T.-F. et al. (2019) Doxorubicin-polyglycerol-nanodiamond composites stimulate glioblastoma cell immunogenicity through activation of autophagy. *Acta biomaterialia*
- 68 Ye, N. et al. (2007) Characterizing doxorubicin-induced apoptosis in HepG2 cells using an integrated microfluidic device. *Electrophoresis* 28 (7), 1146-1153
- 69 Kuo, Y.-C. and Liang, C.-T. (2011) Catanionic solid lipid nanoparticles carrying doxorubicin for inhibiting the growth of U87MG cells. *Colloids and Surfaces B: Biointerfaces* 85 (2), 131-137
- 70 Li, T.-F. et al. (2018) Dendritic cell-mediated delivery of doxorubicin-polyglycerol-nanodiamond composites elicits enhanced anti-cancer immune response in glioblastoma. *Biomaterials* 181, 35-52
- 71 Wei, L. et al. (2015) Dissecting the mechanisms of doxorubicin and oxidative stress-induced cytotoxicity: the involvement of actin cytoskeleton and ROCK1. *PLoS One* 10 (7), e0131763
- 72 Deng, Y. et al. (2018) Triptolide sensitizes breast cancer cells to Doxorubicin through the DNA damage response inhibition. *Molecular carcinogenesis* 57 (6), 807-814
- 73 El-Awady, R.A. et al. (2016) Modulation of DNA damage response and induction of apoptosis mediates synergism between doxorubicin and a new imidazopyridine derivative in breast and lung cancer cells. *DNA repair* 37, 1-11
- 74 Tsang, W. et al. (2003) Reactive oxygen species mediate doxorubicin induced p53-independent apoptosis. *Life sciences* 73 (16), 2047-2058
- 75 Rogalska, A. et al. (2011) The role of reactive oxygen species in WP 631-induced death of human ovarian cancer cells: a comparison with the effect of doxorubicin. *Toxicology in Vitro* 25 (8), 1712-1720
- 76 Sharma, V. et al. (2007) Kaempferol induces apoptosis in glioblastoma cells through oxidative stress. *Molecular cancer therapeutics* 6 (9), 2544-2553
- 77 Buyukhatipoglu, K. and Clyne, A.M. (2011) Superparamagnetic iron oxide nanoparticles change endothelial cell morphology and mechanics via reactive oxygen species formation. *Journal of biomedical materials research Part A* 96 (1), 186-195
- 78 Järvinen, T.A. et al. (2000) Amplification and deletion of topoisomerase II $\alpha$  associate with ErbB-2 amplification and affect sensitivity to topoisomerase II inhibitor doxorubicin in breast cancer. *The American journal of pathology* 156 (3), 839-847
- 79 Nitiss, J.L. (2009) Targeting DNA topoisomerase II in cancer chemotherapy. *Nature Reviews Cancer* 9 (5), 338
- 80 Ma, J. et al. (2017) Ku70 inhibits gemcitabine-induced DNA damage and pancreatic cancer cell apoptosis. *Biochemical and biophysical research communications* 484 (4), 746-752
- 81 Hada, M. et al. (2016) Cytosolic Ku70 regulates Bax-mediated cell death. *Tumor Biology* 37 (10), 13903-13914
- 82 Boehmerle, W. and Endres, M. (2011) Salinomycin induces calpain and cytochrome c-mediated neuronal cell death. *Cell death & disease* 2, e168
- 83 Rozalski, M. et al. (2005) Induction of caspase 3 activity, bcl-2 bax and p65 gene expression modulation in human acute promyelocytic leukemia HL-60 cells by doxorubicin with amifostine. *Pharmacol Rep* 57 (3), 360-366
- 84 Feng, L. et al. (2018) Targeted multifunctional redox-sensitive micelle co-delivery of DNA and doxorubicin for the treatment of breast cancer. *Journal of Materials Chemistry B* 6 (20), 3372-3386
- 85 Joerger, A. and Fersht, A. (2007) Structure-function-rescue: the diverse nature of common p53 cancer mutants. *Oncogene* 26 (15), 2226
- 86 Zhou, Y. et al. (2007) Activation of p53 by MEG3 non-coding RNA. *Journal of Biological Chemistry* 282 (34), 24731-24742
- 87 Wang, P. et al. (2012) Overexpression of the long non-coding RNA MEG3 impairs in vitro glioma cell proliferation. *Journal of cellular biochemistry* 113 (6), 1868-1874

- 88 Yin, D. et al. (2014) Long noncoding RNA GAS5 affects cell proliferation and predicts a poor prognosis in patients with colorectal cancer. *Medical oncology* 31 (11), 253
- 89 Ma, C. et al. (2016) The growth arrest-specific transcript 5 (GAS5): a pivotal tumor suppressor long noncoding RNA in human cancers. *Tumor Biology* 37 (2), 1437-1444
- 90 Zhao, X. et al. (2015) Gas5 exerts tumor-suppressive functions in human glioma cells by targeting miR-222. *Molecular Therapy* 23 (12), 1899-1911
- 91 Faraoni, I. et al. (2009) miR-155 gene: a typical multifunctional microRNA. *Biochimica et Biophysica Acta (BBA)-Molecular Basis of Disease* 1792 (6), 497-505
- 92 Meng, W. et al. (2012) Anti-miR-155 oligonucleotide enhances chemosensitivity of U251 cell to taxol by inducing apoptosis. *Cell biology international* 36 (7), 653-659
- 93 Reya, T. and Clevers, H. (2005) Wnt signalling in stem cells and cancer. *Nature* 434 (7035), 843
- 94 Kaur, N. et al. (2013) Wnt3a mediated activation of Wnt/ $\beta$ -catenin signaling promotes tumor progression in glioblastoma. *Molecular and Cellular Neuroscience* 54, 44-57
- 95 Rampazzo, E. et al. (2013) Wnt activation promotes neuronal differentiation of glioblastoma. *Cell death & disease* 4, e500
- 96 Meng, Y. et al. (2018) Low-intensity MR-guided focused ultrasound mediated disruption of the blood-brain barrier for intracranial metastatic diseases. *Frontiers in oncology* 8
- 97 Yang, S. et al. (2017) Identification of two immortalized cell lines, ECV304 and bEnd3, for in vitro permeability studies of blood-brain barrier. *PloS one* 12 (10), e0187017
- 98 Tilloy, S. et al. (2006) Methylated  $\beta$ -cyclodextrin as P-gp modulators for deliverance of doxorubicin across an in vitro model of blood-brain barrier. *Bioorganic & medicinal chemistry letters* 16 (8), 2154-2157
- 99 Ohnishi, T. et al. (1995) In vivo and in vitro evidence for ATP-dependency of P-glycoprotein-mediated efflux of doxorubicin at the blood-brain barrier. *Biochemical pharmacology* 49 (10), 1541-1544
- 100 Yang, J. et al. (2011) Detection of amyloid plaques targeted by USPIO-A $\beta$ 1-42 in Alzheimer's disease transgenic mice using magnetic resonance microimaging. *Neuroimage* 55 (4), 1600-1609
- 101 Wadghiri, Y.Z. et al. (2003) Detection of Alzheimer's amyloid in transgenic mice using magnetic resonance microimaging. *Magnetic Resonance in Medicine: An Official Journal of the International Society for Magnetic Resonance in Medicine* 50 (2), 293-302
- 102 Boockvar, J.A. et al. (2011) Safety and maximum tolerated dose of superselective intraarterial cerebral infusion of bevacizumab after osmotic blood-brain barrier disruption for recurrent malignant glioma. *Journal of neurosurgery* 114 (3), 624-632
- 103 MIYAGAMI, M. et al. (1990) Intra-arterial ACNU chemotherapy employing 20% mannitol osmotic blood-brain barrier disruption for malignant brain tumors. *Neurologia medico-chirurgica* 30 (8), 582-590
- 104 Iwadate, Y. et al. (1993) Intra-arterial mannitol infusion in the chemotherapy for malignant brain tumors. *Journal of neuro-oncology* 15 (2), 185-193
- 105 Sun, Z. et al. (2014) Magnetic field enhanced convective diffusion of iron oxide nanoparticles in an osmotically disrupted cell culture model of the blood-brain barrier. *International journal of nanomedicine* 9, 3013-3026
- 106 He, Q. et al. (2018) Towards improvements for penetrating the blood-brain barrier—recent progress from a material and pharmaceutical perspective. *Cells* 7 (4), 24
- 107 Harush-Frenkel, O. et al. (2008) Surface charge of nanoparticles determines their endocytic and transcytotic pathway in polarized MDCK cells. *Biomacromolecules* 9 (2), 435-443
- 108 He, B. et al. (2013) The transport pathways of polymer nanoparticles in MDCK epithelial cells. *Biomaterials* 34 (17), 4309-4326
- 109 Revia, R.A. and Zhang, M. (2016) Magnetite nanoparticles for cancer diagnosis, treatment, and treatment monitoring: recent advances. *Materials Today* 19 (3), 157-168
- 110 Chertok, B. et al. (2008) Iron oxide nanoparticles as a drug delivery vehicle for MRI monitored magnetic targeting of brain tumors. *Biomaterials* 29 (4), 487-496

- 111** Laksitorini, M.D. et al. (2015) Modulation of intercellular junctions by cyclic-ADT peptides as a method to reversibly increase blood–brain barrier permeability. *Journal of pharmaceutical sciences* 104 (3), 1065-1075
- 112** Danhier, F. (2016) To exploit the tumor microenvironment: Since the EPR effect fails in the clinic, what is the future of nanomedicine? *Journal of Controlled Release* 244, 108-121
- 113** Liu, Y. and Lu, W. (2012) Recent advances in brain tumor-targeted nano-drug delivery systems. *Expert opinion on drug delivery* 9 (6), 671-686
- 114** Wang, Z. et al. (2017) Active targeting theranostic iron oxide nanoparticles for MRI and magnetic resonance-guided focused ultrasound ablation of lung cancer. *Biomaterials* 127, 25-35
- 115** Shi, J. et al. (2017) Cancer nanomedicine: progress, challenges and opportunities. *Nature Reviews Cancer* 17 (1), 20
- 116** Rodallec, A. et al. (2018) Pharmacokinetics variability: Why nanoparticles are not just magic-bullets in oncology. *Critical reviews in oncology/hematology*

## Supplementary Materials

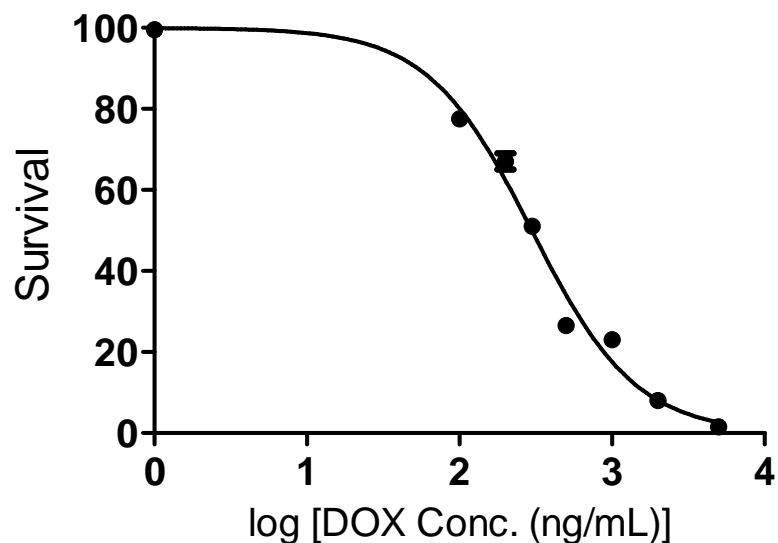


Fig. S 2.1. IC<sub>50</sub> curve of DOX on U251 cells. The cells were treated with DOX solution in cell culture media for 48 h and the MTT assay was then conducted. The IC<sub>50</sub> of DOX was found to be ca. 300 ng/mL.

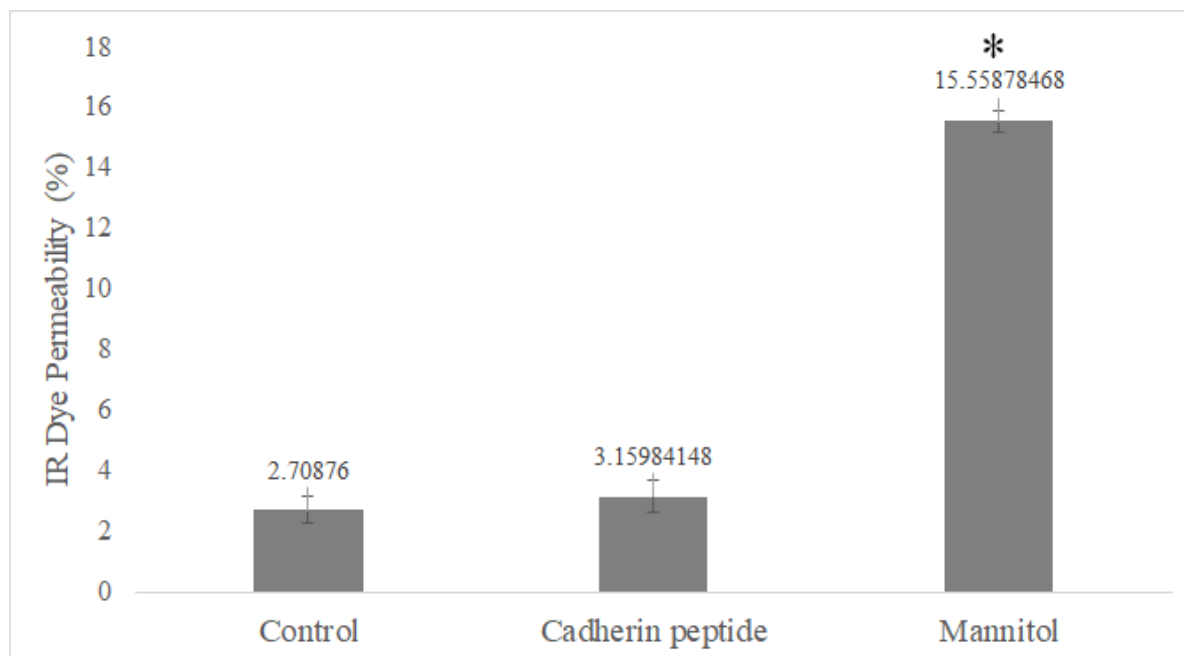


Fig. S 2.2. IRDye permeability across the MDCK-MDR monolayer upon 4-h treatment with peptide or mannitol within the uptake study. \* indicates a significance difference compared to the control (no disrupting agent) and cadherin peptide groups ( $p < 0.01$ ).

## Chapter 3

# **Salinomycin-loaded Iron Oxide Nanoparticles for Glioblastoma Therapy**

# Salinomycin-loaded Iron Oxide Nanoparticles for Glioblastoma Therapy

## ABSTRACT

Salinomycin is an antibiotic introduced recently as a new and effective anti-cancer drug. In this study, magnetic iron oxide nanoparticles (IONPs) were utilized as a drug carrier for salinomycin for potential use in glioblastoma (GBM) chemotherapy. The biocompatible polyethylenimine (PEI)-polyethylene glycol (PEG)-IONPs exhibited an efficient uptake in both mouse brain-derived microvessel endothelial (bEnd.3) and human U251 GBM cell lines. The salinomycin-loaded PEI-PEG-IONPs (Sali-IONPs) released salinomycin over 4 days with an initial release of  $44\pm 3\%$  that increased to  $66\pm 5\%$  in acidic pH. The Sali-IONPs inhibited U251 cell proliferation and decreased viability (by ca. 70% within 48 hours), and they were found to be effective in ROS-mediated GBM cell death. Gene studies revealed significant activation of caspases in U251 cells upon treatment with Sali-IONPs. Furthermore, the upregulation of tumor suppressors i.e. p53, Rbl2, Gas5 was observed, while TopII, Ku70, CyclinD1, and Wnt1 were concomitantly downregulated. When examined in an *in vitro* BBB-GBM co-culture model, Sali-IONPs had limited penetration ( $1.0\pm 0.08\%$ ) through the bEnd.3 monolayer and resulted in a 60% viability of U251 cells. However, hyperosmotic disruption coupled with applied external magnetic field significantly enhanced permeability of Sali-IONPs across bEnd.3 monolayers ( $3.2\pm 0.1\%$ ) and reduced viability of U251 cells to 38%. These findings suggest that Sali-IONPs combined with penetration enhancers, such as hyperosmotic mannitol and external magnetic fields, can potentially provide an effective and site-specific magnetic targeting for GBM chemotherapy.

**Keywords:** Iron oxide nanoparticles; Salinomycin, GBM; Drug delivery, Blood-brain barrier, Magnetic field.

### 3.1. Introduction

Glioblastoma multiforme (GBM) is the most prevalent and aggressive form of primary brain tumors in adults, whose current standard of care includes surgical resection followed by radio- and chemo-therapy [1-3]. However, the extensive infiltrative nature of GBM tumors makes complete surgical resection difficult. Furthermore, the presence of the blood-brain barrier (BBB) limits the penetration of many chemotherapeutics into the brain and poses a significant obstacle in effective treatment of GBM [4-6]. The BBB is composed of a continuous endothelium surrounded by astrocytic foot processes, and pericytes, that together regulate the passage of substances from the bloodstream into the brain [7]. In addition to the tight junctions, brain endothelial cells also express a number of efflux transporters such as P-glycoprotein (P-gp) and breast cancer resistance protein (BCRP), which limits drug penetration into the brain [8]. In this regard, most of the current chemotherapeutics suffer from an inability to penetrate the BBB effectively, resulting in limited therapeutic effects. Furthermore, simply increasing the dose of chemotherapeutic administered to achieve the desired therapeutic concentration at the tumor site is not possible due to systemic adverse side effects [7,9].

To circumvent this hurdle, a variety of engineered nanoparticles (e.g. gold nanoparticles, nanoliposomes) have been developed as drug delivery systems with the capability of transporting therapeutic agents across the BBB and targeting GBM cells [10-13]. Amidst the broad range of engineered nanoparticles, iron oxide nanoparticles (IONPs, magnetite ( $\text{Fe}_3\text{O}_4$ ) or maghemite ( $\gamma\text{-Fe}_2\text{O}_3$ )) offer many advantages in cancer theranostics by virtue of their tunable size-dependent

magnetic properties [7,14]. The inherent magnetic properties of the IONPs not only make them an ideal candidate as a contrast agent for magnetic resonance imaging (MRI), but also for a site-specific magnetic targeting utilizing an external magnetic field. In addition, among various metal oxide nanoparticles, IONPs have a good safety profile, with the components being shuttled into the body's iron cycle upon degradation [7,14,15]. For these reasons, IONPs have emerged as potential nanocarriers for site-specific magnetic targeting of anti-cancer drugs, antibodies, peptides, and siRNAs [7,14,16,17].

Thus far, IONPs have been developed as an efficacious nanocarrier for a variety of anti-cancer drugs including doxorubicin [18], paclitaxel [19], gemcitabine [20], cetuximab [21] and EGFRvIIIAb [22] in glioma therapy. Moreover, several IONPs have been developed as MRI contrast agents in clinical trials such as Ferumoxide (Feridex®), Ferumoxitol (Feraheme®), Ferucarbotran (Resovist®) and ferumoxtran-10 (Combidex®), owing to their effective reduction of T1, T2, and T2\* relaxation times [23,24]. Although IONPs as drug carriers have not entered clinical trials yet, their utility in site-specific and enhanced drug delivery of chemotherapeutics have widely been reported in pre-clinical studies for treatment of malignant gliomas [11,25].

Salinomycin is an antibacterial and ionophore anticoccidial therapeutic drug whose anti-cancer effect has recently been identified [26,27]. As a chemotherapeutic, salinomycin was reported to be 100-fold more effective than paclitaxel in inducing apoptosis in breast cancer stem-like cells [28]. More recent studies have authenticated the anti-cancer effects of salinomycin on gastrointestinal sarcoma, osteosarcoma, and colorectal cancer [29]. Whereas the molecular mechanisms of salinomycin toxicity have not been fully described, the release of cytochrome c, and the activation of Caspases are believed to be implicated in salinomycin's anti-cancer mechanisms [29]. In addition, salinomycin can target cancer stem cells and prevent the Wnt/ $\beta$ -

catenin pathway, which is crucial for stem cell self-renewal [27]. Furthermore, salinomycin may cause strong and time-dependent ATP-depletion in cancer cells [29], and interferes with potassium channels, promoting the efflux of potassium ions from mitochondria and cytoplasm, thus promoting cell apoptosis [30].

The anti-cancer effect of salinomycin-loaded poly(lactic-co-glycolic acid) (PLGA) nanofibers [31], as implantable drug carriers at the tumor cavity after surgical resection, has previously been reported on GBM cells, suggesting a potential application in local treatment of brain tumors. However, systemically administered salinomycin is not able to penetrate the BBB, and has reduced oral absorption because of the multidrug efflux transporter P-glycoprotein (P-gp) [32]. Therefore, development of intravenous (i.v.) drug delivery systems for salinomycin with the capability of crossing the BBB and entering the brain is of significant clinical importance.

In this study, surface-modified IONPs were synthesized and characterized as a potential delivery system for salinomycin. For this purpose, salinomycin-loaded polyethylenimine (PEI)-polyethylene glycol (PEG)-IONP was fabricated and its anti-cancer effects on GBM cells were investigated. The results revealed that Sali-PEI-PEG-IONPs inhibited U251 cell proliferation and effectively decreased U251 cell viability. Moreover, the permeability of the nanoparticle formulation across an *in vitro* model of the BBB was examined. Our results showed that while Sali-PEI-PEG-IONP permeability was low, when combined with an external magnetic field and a transient disruption method, a significant improvement in penetration of the nanoparticles was observed. Further studies using a BBB-GBM co-culture model demonstrated that transient disruption when combined with an external magnetic field could also improve salinomycin therapeutic effect with more induced apoptosis in GBM cells.

## 3.2. Materials and methods

### 3.2.1. Materials

All chemical reagents were purchased from Sigma Aldrich (St. Louis, MO), and all cell culture and biochemical reagents were obtained from Thermo Fisher Scientific Inc, USA, unless otherwise specified.

### 3.2.2. Synthesis and characterization of IONPs

IONPs were synthesized as previously reported by our group [33]. Briefly, to synthesise IONP-Sil(NH<sub>2</sub>), Fe(acac)<sub>3</sub> (2.83 g, 8 mmol) was dissolved in 6:4 ethanol to DI water and purged with nitrogen for 1 h, followed by adding NaBH<sub>4</sub> (3.03 g, 80.0 mmol) in deoxygenated DI water under stirring (1000 rpm). After 20 min, the color of the reaction mixture changed from red to black, evincing the formation of IONPs. After 1 hour, (3-aminopropyl) triethoxysilane (APTES, 16 mL) was added, and the reaction mixture was stirred overnight at room temperature. The blackish brown solution was filtered, and the solvent was removed at 50°C under low pressure. The obtained viscous mixture was dissolved in 200 mL of cold ethanol and left until excess NaBH<sub>4</sub> became crystallized, which was removed by filtration. This step was repeated until no further crystal was observed. Then, ethanol was completely removed, the product was dissolved in 50 mL DI water and dialyzed against DI water to remove the unreacted APTES, followed by centrifugation at 4000 rpm for 30 min. The dark reddish-brown supernatant was collected and stored for further use.

For the synthesis of PEI-PEG-IONPs, PEG diacid 600 (2.0 g, 3.3 mmol), EDC (0.19 g, 1 mmol) and NHS (0.21 g, 1 mmol) were dissolved in DI water and stirred for 15 min. Then, IONP-Sil(NH<sub>2</sub>) solution (~42.0 mg of aminosilane, ~0.3 mmol) was added to the mixture and stirred for

an additional 3 h. The product was dialyzed against DI water followed by centrifugation at 4000 rpm. The obtained supernatant was collected and stored for further use. To accomplish the PEI coating,  $\text{Na}_2\text{CO}_3$ ,  $\text{NaHCO}_3$  ( $\text{Na}_2\text{CO}_3 = 0.21198\text{g}$ ,  $\text{NaHCO}_3 = 1.512\text{g}$ ), EDC (0.19 g, 1 mmol) and NHS (0.21 g, 1 mmol) and IONP-PEG(COOH) were dissolved in 20 mL DI water under stirring. After 15 minutes, PEI2K (2mg/mL) in 30 mL of DI water was added rapidly to the reaction mixture and mixed overnight. The following day, the obtained crude product was washed with DI water and dialyzed against DI water to yield PEI-PEG-IONPs.

Initial characterization of the PEI-PEG-IONP intermediates for physico-chemical and magnetic properties have been previously reported[33]. For confirmation of the size and polydispersity of the PEI-PEG-IONPs, the IONP size distribution in DI water was determined by dynamic light scattering (DLS) measurements using a Photocor Complex system. The FTIR spectrum was taken using a Thermo Nicolet iS10 FTIR spectrometer. TEM images of the nanoparticles were acquired using a Philips CM 10 electron microscope (FEI, Hillsboro, USA).

### 3.2.3. Drug loading on IONPs

To load salinomycin on the synthesized PEI-PEG-IONPs, equal concentrations (30  $\mu\text{g/mL}$ ) of PEI-PEG-IONPs and salinomycin were mixed in phosphate-buffered saline (PBS, pH 6) and the reaction mixture was incubated overnight. The resulting mixture was then centrifuged at 12,000 rpm for 10 min and the aqueous supernatant was carefully removed. Subsequently, the salinomycin-loaded PEI-PEG-IONPs (Sali-PEI-PEG-IONPs) were re-suspended, washed twice with PBS (pH 7.4) and separated by centrifugation as described above to remove any non-adherent salinomycin.

### 3.2.4. Biocompatibility evaluation of IONPs

To evaluate the biocompatibility of the synthesized PEI-PEG-IONPs, a mouse brain-derived microvessel endothelial cell line, bEnd.3 (American type tissue culture collection, Manassas, VA) was used as a cell culture model for the BBB, in addition to the authenticated human U251 GBM cell line. The bEnd.3 cells (passage number 20–30) were cultured in DMEM (Gibco, UK) supplemented with 10% fetal bovine serum (FBS, Hyclone, Logan, UT), 1% mL penicillin and streptomycin Invitrogen, USA). The U251 cells (passage number 20–30) were cultured in DMEM/F12 (Gibco, UK), supplemented with 10% FBS and 1% penicillin-streptomycin. To assess the effect of PEI-PEG-IONPs on cell viability, the bEnd.3 and U251 cells were seeded at a density of  $2 \times 10^4$  and  $1 \times 10^4$  cell/cm<sup>2</sup>, respectively in 96-well plates, and incubated overnight at 37 °C to allow them to attach. Then, the cells were treated with PEI-PEG-IONPs at the concentrations of 0.25 to 50 µg/mL suspended in the cell culture media, for 48 h. Afterward, the culture media was removed, and the cells were washed with PBS and incubated in medium supplemented with 0.5 mg/mL 3-(4,5-dimethylthiazol-2-yl)-2,5-diphenyltetrazoliumbromide (MTT) reagent for 3 h at 37 °C. Then, the media was removed and the cells were solubilized in DMSO [31]. Absorbance of the solubilized cells was determined using a Synergy HT plate reader (BioTek, Winooski, VT) at the wavelength of 570 nm. The relative cell viability was calculated as  $[\text{OD}]_{\text{test}}/[\text{OD}]_{\text{control}}$ , and the average value was obtained from five measurements.

### 3.2.5. Drug release from IONPs

The release kinetics of salinomycin from the PEI-PEG-IONPs was determined at 37 °C in PBS (pH 7.4 to mimic pH of the blood and extracellular fluid, and pH 4.5 to mimic acidic tumor micro-environment and endosomal compartments). To this end, the Sali-PEI-PEG-IONPs were suspended in 1 mL PBS and at various time points, the tubes were centrifuged at 12,000 rpm for

10 min to pellet the nanoparticles and the solution was entirely collected and replaced with 1 mL of fresh PBS. The concentration of the released salinomycin was measured using an Ionophore ELISA kit (Europroxima, The Netherlands), in compliance with manufacturer's protocol. Quantitative determinations of salinomycin released from the IONP as a function of incubation time were determined based on standard curves performed with each analysis.

### 3.2.6. Cellular uptake of IONPs

Confluent monolayers of bEnd.3 and U251 cells were grown in 24-well culture plates and treated with culture media containing either PEI-PEG-IONPs or Sali-PEI-PEG-IONPs (30  $\mu\text{g}/\text{mL}$ ) for 4 h at 37 °C in both presence and absence of a static external magnetic field. Afterward, the cell monolayers were washed 3 times with cold PBS to remove unbound nanoparticles, followed by lysing the cells with 0.1% Triton solution in PBS overnight at -20 °C. The IONP content was determined based on the Ferrozine assay as previously reported [34]. Briefly, 500  $\mu\text{L}$  of 12 M HCl was added to each well and incubated for 1 h at room temperature with gentle shaking to solubilize the nanoparticles. The samples were then neutralized with 500  $\mu\text{L}$  of 12 M NaOH, followed by the addition of 120  $\mu\text{L}$  of hydroxylamine hydrochloride (2.8 M) in 4 M HCl and incubation at room temperature with gentle shaking for 1 h. Thereafter, 50  $\mu\text{L}$  of 10 M ammonium acetate solution (pH 9.5) and 300  $\mu\text{L}$  of 10 mM ferrozine in 0.1 M ammonium acetate solution were added consecutively to each sample, and the absorbance was measured at 562 nm using a Synergy HT plate reader. Quantitative determination of IONP concentration was fulfilled based on a standard curve prepared using various dilutions of an iron chloride atomic absorption standard (Fisher Scientific, Ottawa, ON). The protein content of the lysed cells was determined using a BCA protein assay kit (Pierce™ BCA protein assay kit, ThermoFisher Scientific, USA).

The cellular localization of the PEI-PEG-IONPs was also examined using transmission electron microscopy (TEM). For this study, U251 cells were treated with the nanoparticles as described above. After 4 h, the media was removed and the cells were washed with PBS, and disassociated using a 0.25% trypsin EDTA solution (Hyclone, Logan, UT). The collected cells were then centrifuged (5 minutes at 1500 g) and the cell pellet was resuspended in 3% glutaraldehyde in 0.1 M phosphate buffer (pH 7.3) at room temperature for 3 hours. This was followed by post-fixation for 2 h at room temperature in 1% osmium tetroxide in 0.1 M phosphate buffer, dehydration in ascending concentrations of ethanol and embedding in Epon resin. Thin sections were stained with uranyl acetate and lead citrate, visualized and photographed by TEM.

### 3.2.7. Cytotoxicity of Sali- IONPs in GB cell line

The cytotoxicity of Sali-PEI-PEG-IONPs against U251 cells was evaluated using MTT assay. For this purpose, the cells were cultured as described previously. After a 24-h period, the media were changed with fresh media (negative control), media containing an equivalent amount of salinomycin corresponding to salinomycin released from Sali-PEI-PEG-IONPs over the same time (positive control, 1  $\mu\text{g}/\text{mL}$ ), PEI-PEG-IONPs and Sali-PEI-PEG-IONPs. Following a 48-h treatment, viability of the cells was determined by MTT assay as described in section 2.4.

Moreover, to observe the effects of the treatments on the cell proliferation, the cells were labeled with the fluorescent dye carboxyfluorescein succinimidyl ester (CFSE), 50  $\mu\text{M}$  for 20 min at 37°C. The cellular content of CFSE is reduced during each cell division resulting in a sequential halving of the cellular fluorescent intensity with each mitototic event [35]. Following the loading of CFSE into the cells, the media was changed, and the cells were washed and treated with either PEI-PEG-IONPs, salinomycin (1  $\mu\text{g}/\text{mL}$ ) or Sali-PEI-PEG-IONPs (equivalent to 1  $\mu\text{g}/\text{mL}$  of salinomycin) for an additional 48 h. Following the 48-h exposure, the media was changed, and

the cells were left for 24 h without any further treatment. Thereafter, the fluorescence intensity of the cells was measured using flow cytometry (BD FACSCanto II Flow Cytometer instrument (BD Bioscience)). In addition, cell apoptosis was determined using Annexin V-FITC/PI apoptosis Kit (Thermo Fisher Scientific, USA). For this purpose, the cells were treated similarly either with PEI-PEG-IONPs, salinomycin or Sali-PEI-PEG-IONPs for 48 h, followed by 24 h incubation without any further treatment. Thereafter, the cells were stained with Annexin V-FITC and PI according to the manufacturer's protocol, and subsequently were analyzed using flow cytometry.

Morphology of the U251 cells after 48 h treatment was also studied using a fluorescence microscope (Zeiss Axio observer Z1, Germany). To this end, the treated cells were washed with PBS and fixed with 4% paraformaldehyde for 20 min at room temperature, followed by permeabilization with 0.2% Triton X-100 for 5 min. Then, actin cytoskeleton was stained with ActinRed for 30 min and the nucleus was stained with DAPI solution (100 nM) for 5 min at 37 °C. Afterwards, the samples were washed with PBS and visualized by the microscope.

### 3.2.8. Reactive oxygen species determination

Intracellular ROS was measured based on the peroxide-dependent oxidation of the non-fluorescent 2',7'-dichlorofluorescein diacetate (DCFDA). Upon entering the cells, acetate groups of the DCFDA get cleaved by intracellular esterases, being transformed to the highly fluorescent and cell impermeable 2',7'-dichlorofluorescein (DCF) [36]. For this study, U251 cells were seeded in black 96 well plates at a density of 5000 cell/cm<sup>2</sup> and cultured overnight. After washing the cells with PBS, they were stained with 50 µM DCFH-DA in PBS for 45 min at 37 °C. Then, the DCFDA solution was removed and the washed cells were treated with either PEI-PEG-IONPs, salinomycin or Sali-PEI-PEG-IONPs in cell culture media for up to 72 h. The cellular accumulation of ROS in

response to the treatments was calculated by measuring the oxidation of DCFDA to the fluorescent DCF using a Synergy HT fluorescent plate reader at Ex/ Em=485/535 nm.

### 3.2.9. Quantitative RT-PCR

The U251 cells were treated with either PEI-PEG-IONPs, salinomycin and Sali-PEI-PEG-IONPs for 48 hours. After washing the cells with PBS, the total RNA was extracted utilizing TRIZOL reagent (Invitrogen, USA) in accordance with the manufacturer's protocol. The RNA's purity and concentration were measured by UV-VIS spectrophotometry (NanoDrop, Thermo Fisher Scientific Inc, USA). Thenceforth, the expression level of mRNA encoding Top II, Ku70, p53, Caspase 9, Caspase 3, cyclin D, Wnt 1, Rbl2, GAS5, and MIR155 was determined by quantitative reverse-transcript polymerase chain reaction (qRT-PCR). The RT-PCR was carried out using iTaq Universal SYBR Green supermix kit (Bio-Rad, USA) and  $\beta$ -actin was considered as the housekeeping gene. The reactions were conducted in an Applied Biosystems 7300 Real-Time PCR system with the following cycles: 1 cycle of 10 min at 50 °C for the reverse transcription reaction, 1 cycle of 1 min at 95 °C for polymerase activation, 40 cycles consisting of 15 sec at 95 °C for denaturation and 1 min at 60 °C for annealing. The changes in relative gene fold were calculated by the comparative  $C_t$  method ( $2^{-\Delta\Delta C_t}$ ) and the target genes' expression was normalized to the  $\beta$ -actin. The sequences of the primers have been listed in Table 3.1.

Table 3.1. Sequences of human primers.

	Forward	Reverse
<b>TOP2</b>	ATTCCCAAACCTCGATGATGC	CCCCATATTTGTCTCTCCCA
<b>Ku70</b>	CTGTCCAAGTTGGTCGCTTC	CTGCCCTTAAACTGGTCAA
<b>p53</b>	TCTGAGTCAGGCCCTTCTGT	GTTCCGAGAGCTGAATGAGG
<b>Caspase 9</b>	CACGGCAGAAGTTCACATTG	AACAGGCAAGCAGCAAAGTT
<b>Caspase 3</b>	CTCTGGTTTTTCGGTGGGTGT	CGCTTCCATGTATGATCTTTGGTT
<b>Cyclin D</b>	GTCCCACTCCTACGATACGC	CAGGGCCGTTGGGTAGAAAA
<b>Wnt1</b>	CAACAGCAGTGGCCGATGGTGG	CGGCCTGCCTCGTTGTTGTGAAG
<b>Rbl2</b>	GGTTCCTCACTGAGTGATTACTGT	AGAAGCCTCCTATGCTCACG
<b>GAS5</b>	TGGTTCTGCTCCTGGTAACG	AGGATAACAGGTCTGCCTGC
<b>MIR 155</b>	AATCGTGATAGGGGTTTTTGCC	ATGTAGGAGTCAGTTGGAGGC
<b>β-actin</b>	AATGCCAGGGTACATGGTGG	AGGAAGGAAGGCTGGAAGAGTG

### 3.2.10. *In vitro* BBB-GBM model

As the IONPs for GBM therapy would be required to first pass the BBB, a brain endothelial cell–GBM cell co-culture model was established to assess permeability and anti-cancer effect of the IONP formulations. For this study, bEnd.3 cells were plated on the apical side of a porous polyethylene terephthalate (PET) membrane (cell culture inserts, pore size: 3.0 μm, BD Bioscience, USA). Once confluent bEnd.3 monolayers were obtained (typically in 7 days), the culture inserts were transferred to 6-well plates containing U251 cells (cell density  $2 \times 10^5$  cell/well) to assess both permeability and pharmacological responses. Free salinomycin (1 μg/mL) or Sali-PEI-PEG-IONPs was added to the apical media compartment of the insert along with a 70 kDa

Fluorescein isothiocyanate-dextran (FDX70000) permeability marker. The cells were then incubated at 37°C for 6 hours in both the presence and absence of a static magnetic field. Thereafter, the apical media and the inserts were withdrawn and the U251 cells with the basolateral cell culture media were incubated for an additional 24-h after which the basolateral media was collected to determine IONP (Ferrozine assay) and the cell viability (MTT assay) was examined. To assess permeability following transient disruption of the bEnd.3 monolayer through the hyperosmotic condition, the bEnd.3 monolayers were pre-treated with DMEM containing 1.4 M mannitol for 2 hours, after which the monolayers were washed with PBS and then placed in 6-well plates containing U251 cells for permeability and cytotoxicity studies as described above.

### 3.2.11. Statistical analysis

The studies were conducted in triplicate and the results were reported as the mean  $\pm$  standard deviation (SD). Statistical analysis was conducted in GraphPad Prism using one or mixed two-way ANOVA (each applicable), with multiple post-hoc analysis of Tukey and with an adjusted p-value. The hypotheses were based on  $H_0$ : All groups should have the same mean measurement values, and  $H_1$ : All groups do not have the same mean measurement values. The adjusted p-value  $< 0.05$  (adjusted based on the entire family of comparisons) was considered as the significant level to reject the null hypothesis, as previously reported [37-39].

## 3.3. Results and discussion

### 3.3.1. Characterization of IONPs

The TEM image of the PEI-PEG-IONPs indicates the nanoparticles have a quasi-spherical morphology and a core size of  $4.76 \pm 0.7$  nm (Fig. 3.1a,b). In addition, the observed hydrodynamic diameter ( $D_H$ ) and zeta potential ( $\zeta$ ) of the PEI-PEG-IONPs were  $84.1 \pm 14$  nm, and  $+27.14$  mV,

respectively. The FTIR spectrum of the nanoparticles is depicted in Fig. 3.1c. The siloxane shell was characterized by the Si-O-Si stretching band at  $991\text{ cm}^{-1}$ . Symmetric and asymmetric C-H stretching (of propyl group) bands, as well as N-H bending (from free amine groups) were observed at  $2821$ ,  $2887$ , and  $1587\text{ cm}^{-1}$ , respectively. The strong peak at  $1112\text{ cm}^{-1}$  corresponds to the C-O-C stretching band of the conjugated PEG. The carbonyl stretching band from the amide linkage was also observed at  $1649\text{ cm}^{-1}$  and the Fe-O-Fe stretching of the core was found at  $588\text{ cm}^{-1}$ .

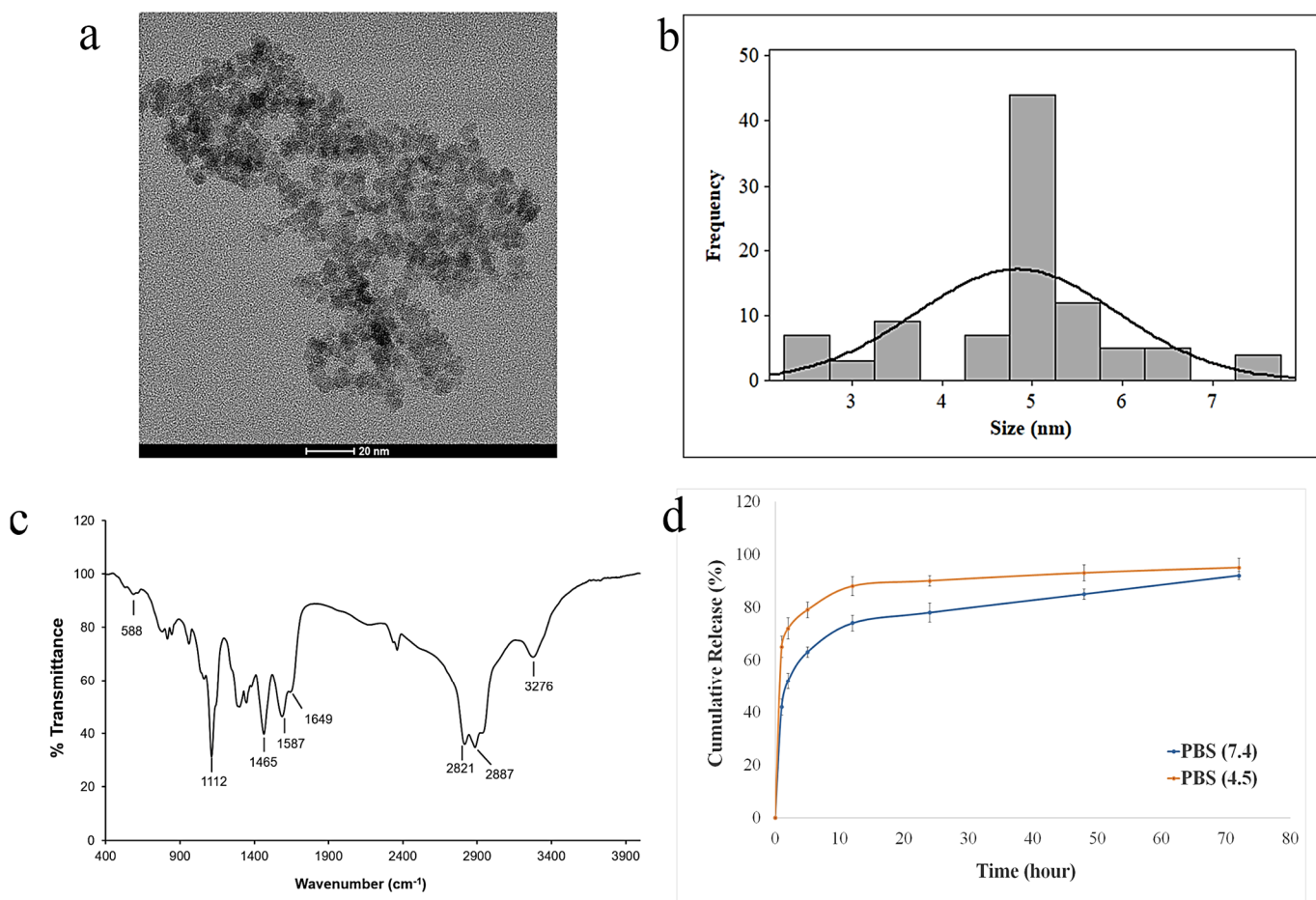


Fig. 3.1. PEI-PEG-IONPs characterization: (a) TEM images, (b) size distribution histogram, (c) FTIR spectrum, (d) release of salinomycin from the nanoparticles in pHs 7.4 (physiological pH), and 4.5 (pH of acidic intracellular compartments such as endosomes).

### 3.3.2. Characterization of the Sali-IONPs

The efficiency of salinomycin loading on the PEI-PEG-IONPs was calculated to be  $3.4\pm 0.4\%$ . Loading of salinomycin decreased the  $\zeta$  of the PEI-PEG-IONPs from  $+27.14$  mV to  $+0.8$  mV, indicative of an electrostatic interaction between the amine groups of PEI and the carboxyl groups of salinomycin. The release profile of salinomycin from the nanoparticles is illustrated in Fig. 3.1d. The nanoparticles showed a burst release of salinomycin with  $44\pm 3\%$  release within the initial hours, followed by a more sustained release over 72 hours for the remaining coated drug. In addition, the acidic microenvironment accelerated the release of salinomycin from the nanoparticles up to  $66\pm 5\%$  within the initial hours, indicating the capability of an accelerated drug release once the nanoparticles enter the acidic tumor microenvironment or acidic intracellular compartments such as endosomes [40,41]. The initial burst release of the salinomycin can be related to adsorption of the drug on the exterior regions of the polymer coating on the IONPs [42,43], and the weak electrostatic forces between the drug and the coating polymer. This study is the first to report the application of metal oxide nanoparticles for delivery of salinomycin and their potential applications for GBM chemotherapy. However, the salinomycin release profile obtained in the present study using IONPs is similar to those previously reported with polymer-based nanoparticle systems of salinomycin. For example, Chen et al., [44] developed lipid-polymer nanoparticles as drug carrier of salinomycin for osteosarcoma treatment, with an initial burst release of  $\sim 60\%$ , and a cumulative drug release of  $\sim 80\%$  in 72 h. Similarly, salinomycin-loaded PEGylated poly(lactic-co-glycolic acid) nanoparticles demonstrated a fast release of salinomycin (ca. 50%) in the initial 24 h, reaching the cumulative release of  $\sim 65\%$  in the following 48 h [45].

Transient disruption of the BBB has been suggested as an effective approach to enhance the delivery of therapeutics across the BBB and treat malignant gliomas in clinical studies [46-48]. In this context, it is noteworthy to mention that the maximum disruption of the BBB after administration of mannitol, the most common hyperosmotic transient disruption agent, has been reported to occur within 5 min and lasts around 20-30 min, in animal studies [49] and substantially longer, up to 8 hours in humans [50]. Therefore, the initial burst release of salinomycin from the nanoparticles, which already have been drawn to the target site using an external magnet field, can increase the chance of the drug entering the brain within the optimum time frame of the BBB disruption. Moreover, the drug-loaded IONPs are expected to enter the brain within this time frame using both transient disruption of the BBB and magnetic targeting. Thus, a therapeutic concentration of the drug can be delivered to the tumor cells via the nanoparticles, even with an initial burst release of salinomycin. Chertok et al., [25] also reported that IONPs entered the brain within 1 h post-injection using magnetic targeting without transient disruption of the BBB that can be attributed to the EPR effect.

### 3.3.3. Biocompatibility of the IONPs

The biocompatibility of the PEI-PEG-IONPs on U251 and bEnd.3 was evaluated. The PEI-PEG-IONPs at a concentration ranging from 0.25 to 50  $\mu\text{g}/\text{mL}$  did not show any cytotoxicity, *per se*, on U251 (Fig. 3.2b). In addition, their biocompatibility up to 320  $\mu\text{g}/\text{mL}$  on HepG2 was previously reported [33]. Likewise, the PEI-PEG-IONPs at a concentration of 0.25 to 30  $\mu\text{g}/\text{mL}$  did not show cytotoxicity on bEnd.3, albeit a minor reduction in cell viability was observed at the concentration of 50  $\mu\text{g}/\text{mL}$  (Fig. 3.2a). Therefore, the concentration of 30  $\mu\text{g}/\text{mL}$  of PEI-PEG-IONPs opted for the next steps of this study. The Sali-PEI-PEG-IONPs and free salinomycin were also found fairly biocompatible on bEnd.3 with an approximately 20% diminution in the cell

viability upon 48 h treatment. In clinical practice, iron oxide nanoparticles generally exhibit desired biocompatibility profile and they are mainly captured by the reticuloendothelial system (RES), hereby the iron is incorporated into the body's iron cycle [7,51]. Coating the iron oxide nanoparticles with hydrophilic macromolecules such PEG reduces the non-specific protein adsorption on the nanoparticles and avoids their recognition and clearance by the RES, which ultimately leads to an extended circulation time of the nanoparticles as well as enhanced accumulation in the brain tumor [52,53].

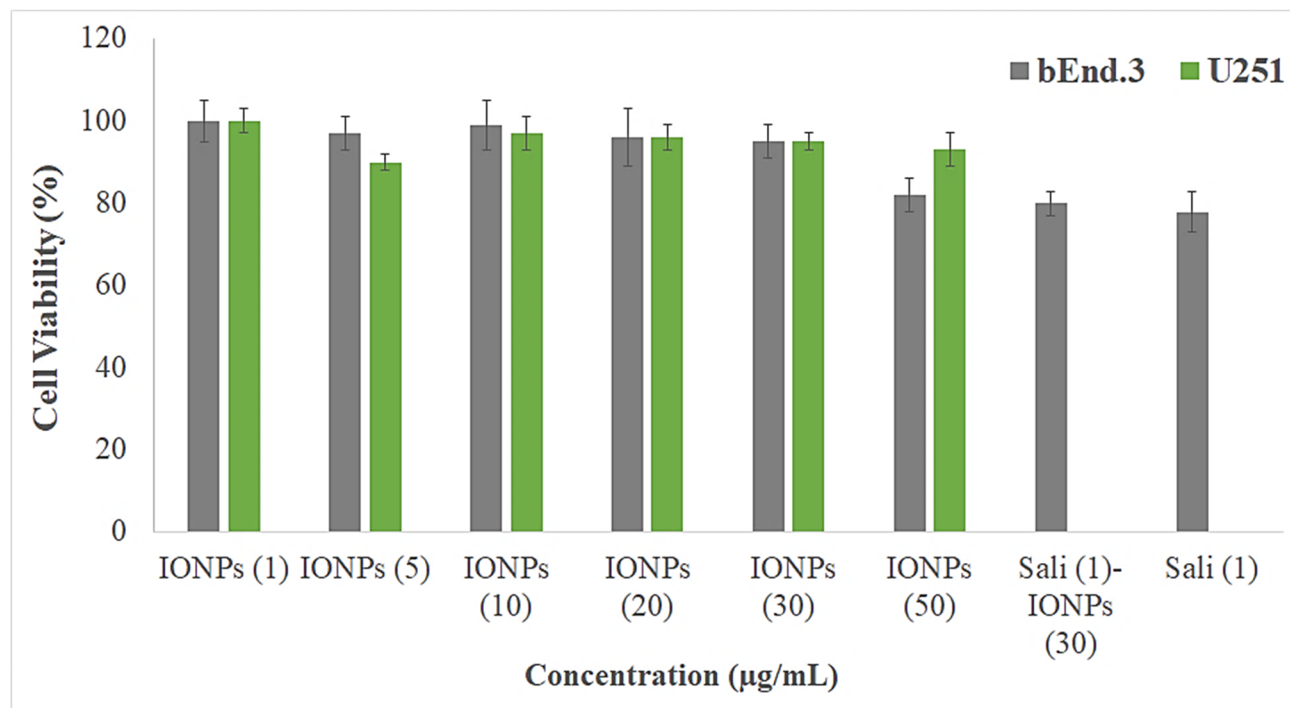
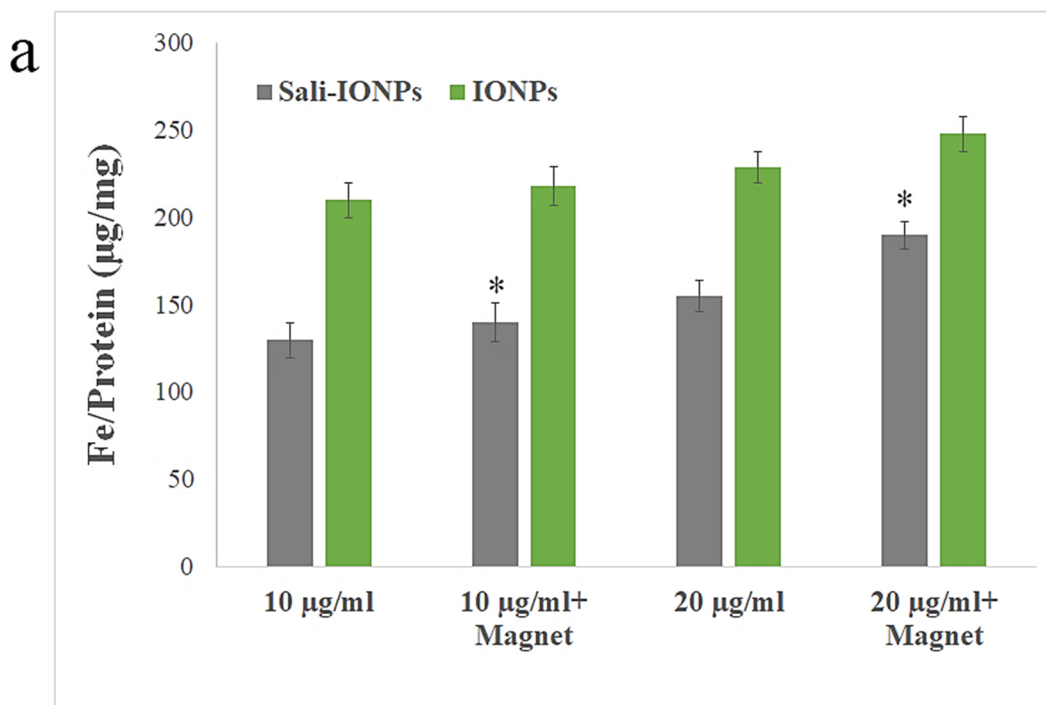


Fig. 3.2. Biocompatibility of different concentrations of PEI-PEG-IONPs on (a) bEnd.3 and (b) U251 cell lines after 48 h treatment using MTT assay (n=5). The Y-axis represents cell viability compared to the control.

### 3.3.4. Cellular uptake of the IONPs

The uptake of both PEI-PEG-IONPs and Sali-PEI-PEG-IONPs in bEnd.3 (Fig. 3.3a) and U251 (Fig. 3.3b) were examined. The nanoparticle uptake in the cells was concentration-

dependent, while application of an external magnetic field resulted in slight increases in IONP uptake, regardless of the formulation (i.e. PEI-PEG-IONPs or Sali-PEI-PEG-IONPs). Generally, the bEnd.3 had greater uptake of the nanoparticles than that of U251, and the higher uptake of PEI-PEG-IONPs can be attributed to the more positive charge on the bare nanoparticles compared to the Sali-PEI-PEG-IONPs. This finding is consistent with our previous studies reporting a higher uptake of positively charged IONPs in bEnd.3 cells, astrocytes and neurons compared to negatively charged IONPs, owing to the electrostatic interactions between positively charged nanoparticles and the negatively charged plasma membrane of the cells [34]. Likewise, higher cellular uptake of positively charged iron oxide nanoparticles was reported in various mammalian cell lines in comparison to the negatively charged and neutral formulations [54]. Furthermore, the uptake of the nanoparticles appeared to be primarily through endocytosis as TEM images clearly showed the distribution of the nanoparticles to be along the outside plasma membrane and within intracellular vesicles (ie. endosomes/lysosomes) (Fig. 3.4a,b).



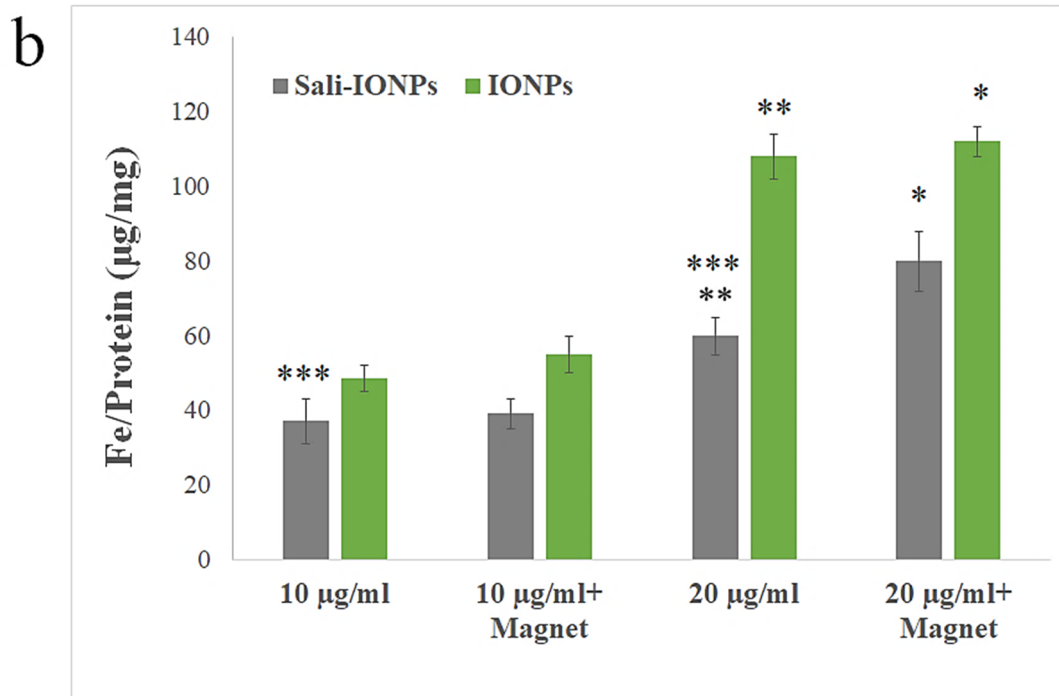


Fig. 3.3. Uptake of IONPs and Sali-IONPs by (a) b.End 3 and (b) U251 after 4 h treatment. \* indicates a significant difference at  $p < 0.05$  between the specified groups. Data was presented as mean  $\pm$  S.D, and  $n = 3$ .

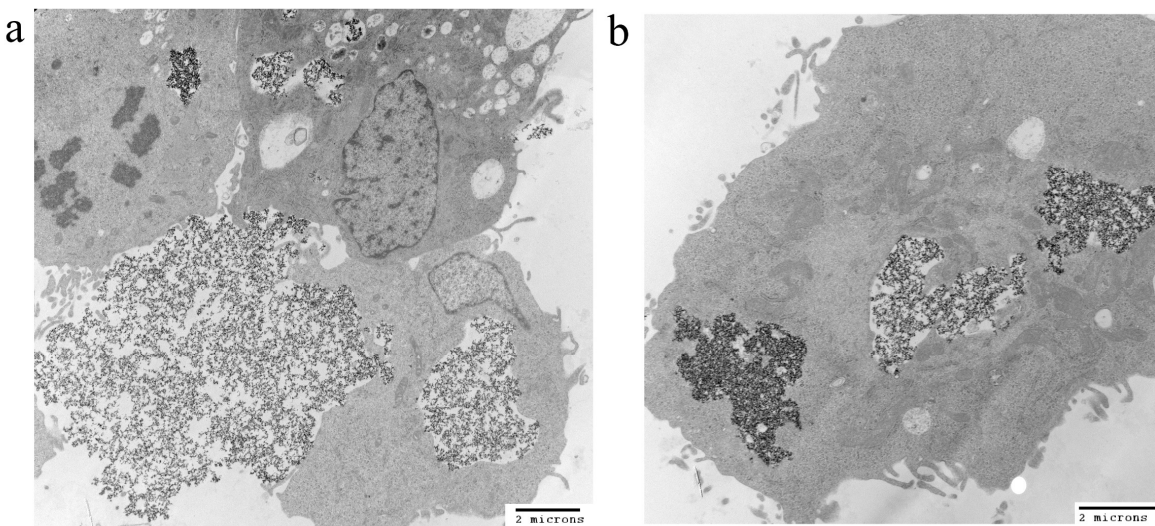


Fig. 3.4. TEM images of a) IONPs and b) Sali-IONPs uptake by U251 cell after 4 h of the treatment.

### 3.3.5. Cytotoxicity of Sali-IONPs on cancer cell

We previously studied the cytotoxicity effects of salinomycin on U251 human glioblastoma cell line [31]. Herein, the cytotoxicity of the Sali-PEI-PEG-IONPs on U251 was investigated in comparison to that of free salinomycin. Based on the MTT viability studies (Fig. 5), while the PEI-PEG-IONPs themselves did not show cytotoxic effects on U251, both treatments with free salinomycin and Sali-PEI-PEG-IONPs (1  $\mu\text{g}/\text{mL}$  of salinomycin) could significantly decrease the cell viability to  $45\pm 2.2\%$  and  $36\pm 3.5\%$ , respectively. Correspondingly, both salinomycin and Sali-PEI-PEG-IONPs were found to be equally effective in inducing apoptosis and necrosis in treated U251 cells, and a diminution of the cell viability to ca. 36% and 23%, respectively was observed (Fig. 3.6). Moreover, salinomycin and Sali-PEI-PEG-IONP treatments could significantly inhibit U251 cell proliferation (Fig. 3.7). A similar cytotoxic and anti-proliferative response to salinomycin has been reported in other types of cancer cells such as pancreatic [55], leukemia [56], prostate [57], lung [58] and ovarian [59] cancer cells.

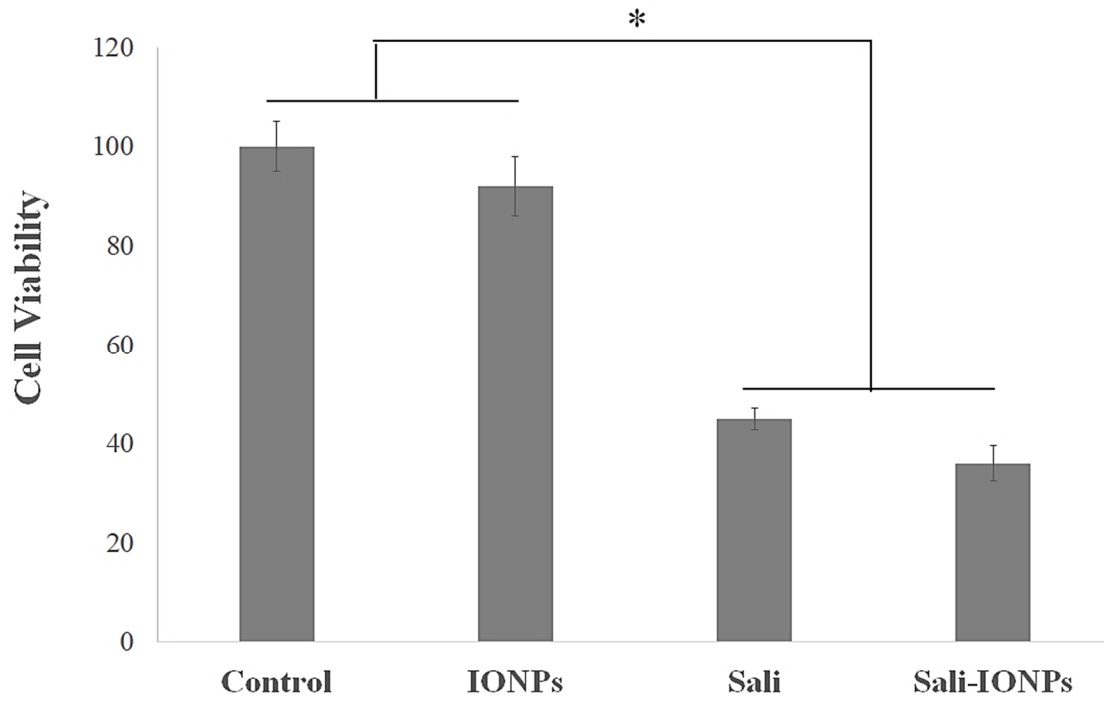
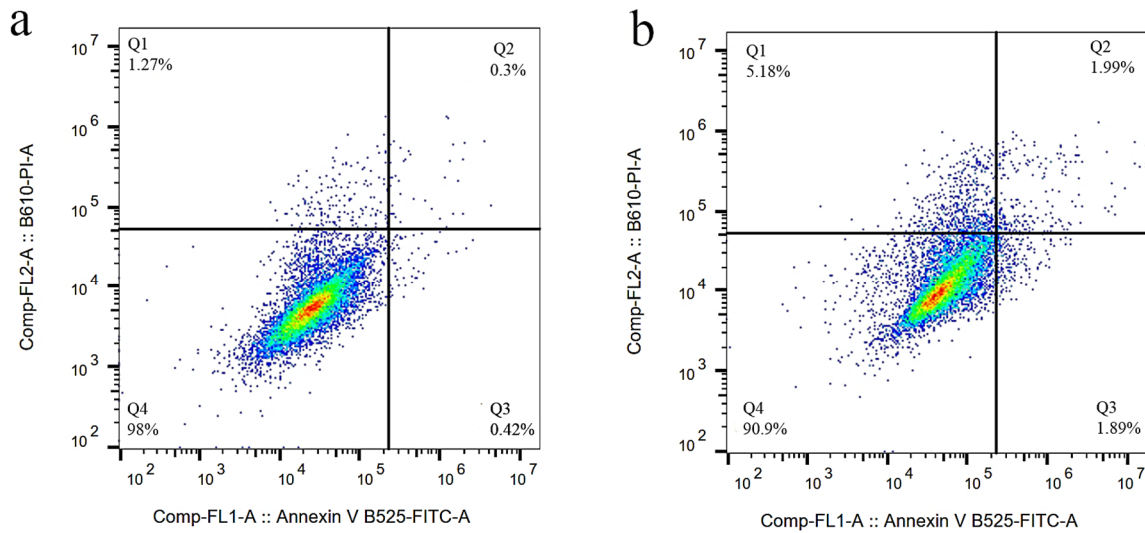


Fig. 3.5. Cytotoxicity evaluation of salinomycin and Sali-IONPs on U251 after 48 h treatment. \* indicates a significant difference compared to the control group at  $p < 0.05$ . Data was presented as mean  $\pm$  S.D, and  $n = 6$ .



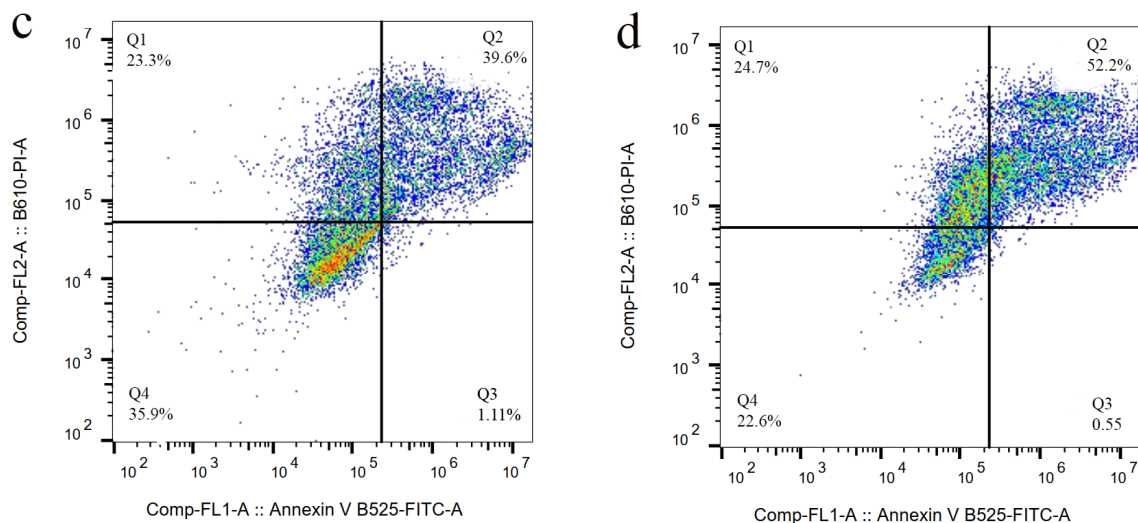


Fig. 3.6. Cell apoptosis/necrosis of U251 upon treatment, stained with Annexin V-FITC and PI. (a) Control, (b) IONPs (c) salinomycin, and (d) Sali-IONPs. (Q4) shows live, (Q3) early apoptotic, (Q2) late apoptotic and (Q1) necrotic cells.

The cell morphology was also examined by fluorescence microscopy as shown in Fig. 3.8. In addition to decreasing the cell number, both salinomycin and Sali-PEI-PEG-IONPs induced notable morphological changes in U251 cells following exposure. While the normal cells demonstrated a typical cuboidal morphology of U251, the actin cytoskeleton was changed to a shrunken and spindle-like structure upon treatment with either salinomycin or Sali-PEI-PEG-IONPs. Since the dynamic remodeling of the actin cytoskeleton is essential for cell migration, salinomycin can inhibit cell migration through a notable loss of actin stress fibers. Such responses to salinomycin have been reported in both pancreatic and liver cancer cells [55].

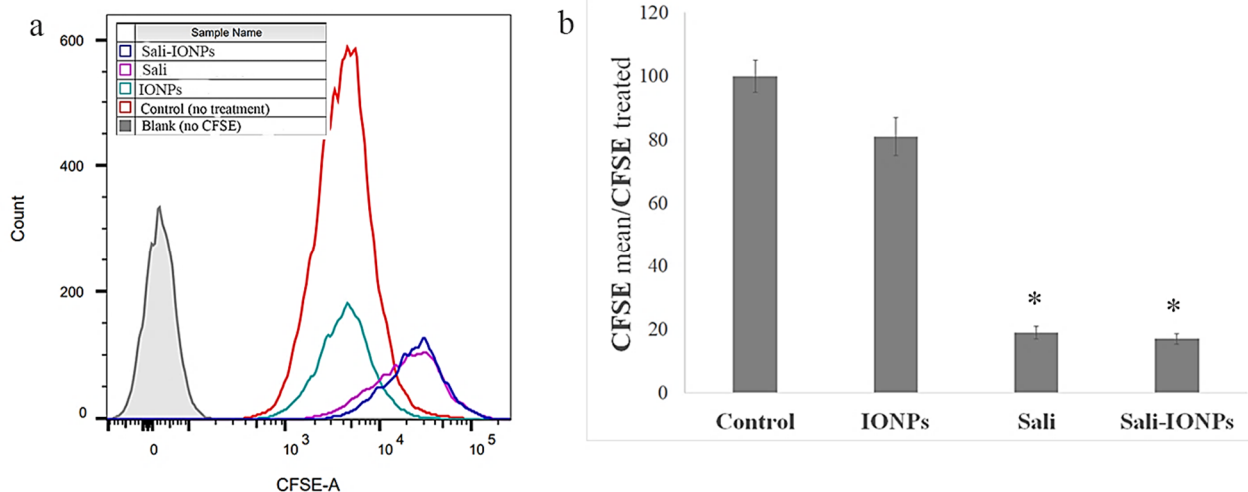


Fig. 3.7. Cell proliferation analysis of CFSE-labelled U251 upon treatment with IONPs, salinomycin and Sali-IONPs. (a) CFSE flow cytometry graph, and (b) the relative cell proliferation inhibition by (mean CFSE control/mean CFSE treated). \* indicates a significant difference compared to the control group at  $p < 0.05$ .

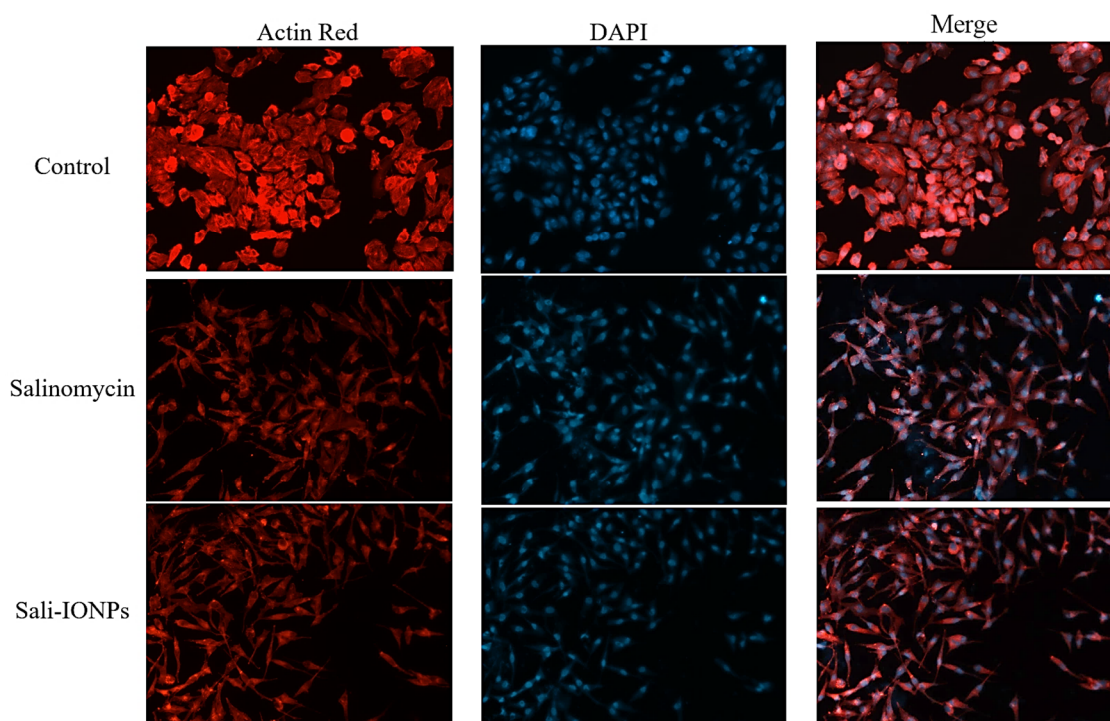


Fig. 3.8. Fluorescence microscopy images of U251 treated with either salinomycin or Sali-IONPs after 48 h of the treatment. Red and blue fluorescence colours represent Alexa Fluor@ 488 phalloidin-stained F-actin and DAPI-stained cell nuclei, respectively.

### 3.3.6. ROS generation

Salinomycin-mediated ROS generation is known as a determining event committing the cancer cells to apoptotic death [57]. Increased formation of ROS was observed in the present study following exposure of U251 cells to salinomycin or Sali-PEI-PEG-IONPs (Fig. 3.9). Both salinomycin and Sali-PEI-PEG-IONPs were effective in ROS generation in U251 cells upon 48 and 72 hours of the treatment, while Sali-PEI-PEG-IONPs induced significantly higher ROS at 72 h, indicating the capability of inducing ROS-mediated apoptotic cell death. In this context, triggered ROS-mediated DNA damage has been suggested as a *de facto* mechanism of salinomycin-induced cell growth inhibition in human glioma cells [60]. Xipell et al., [61] also reported that salinomycin could trigger ROS generation in various glioma cell lines.

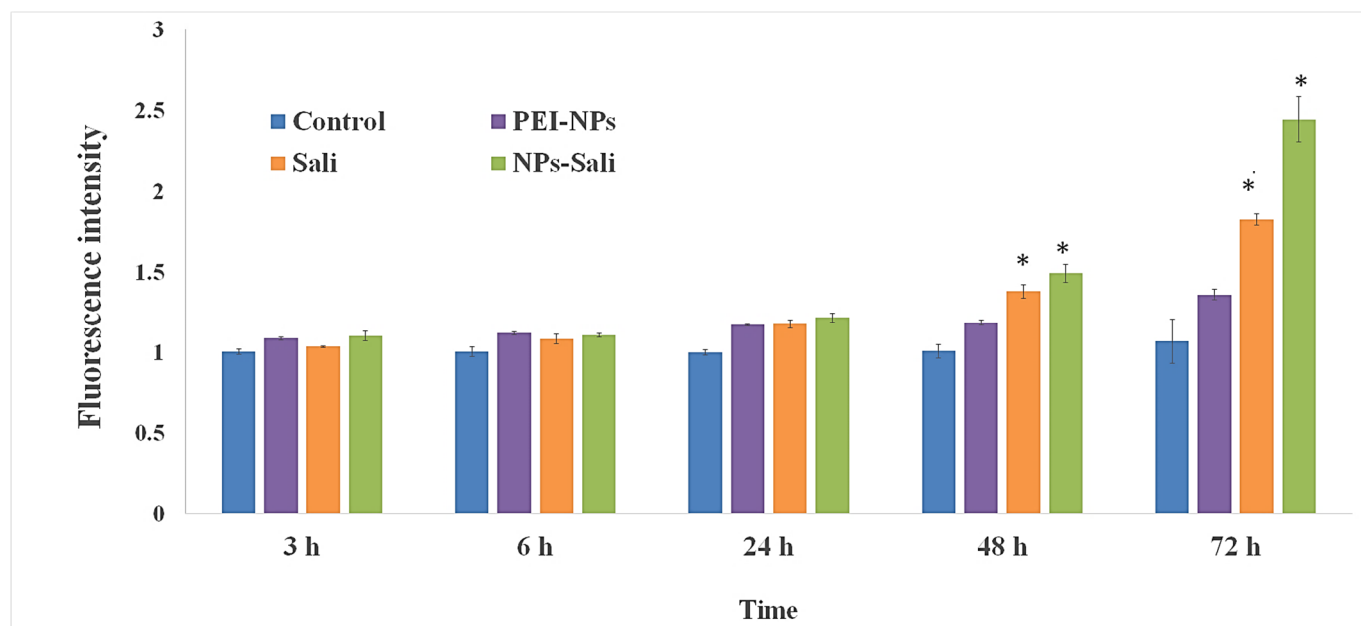


Fig. 3.9. ROS generation in U251 treated with either IONPs, salinomycin or Sali-IONPs at different time-points. \* indicates a significant difference compared to the control group at  $p < 0.05$ . Data was presented as mean  $\pm$ S.D, and  $n = 5$ .

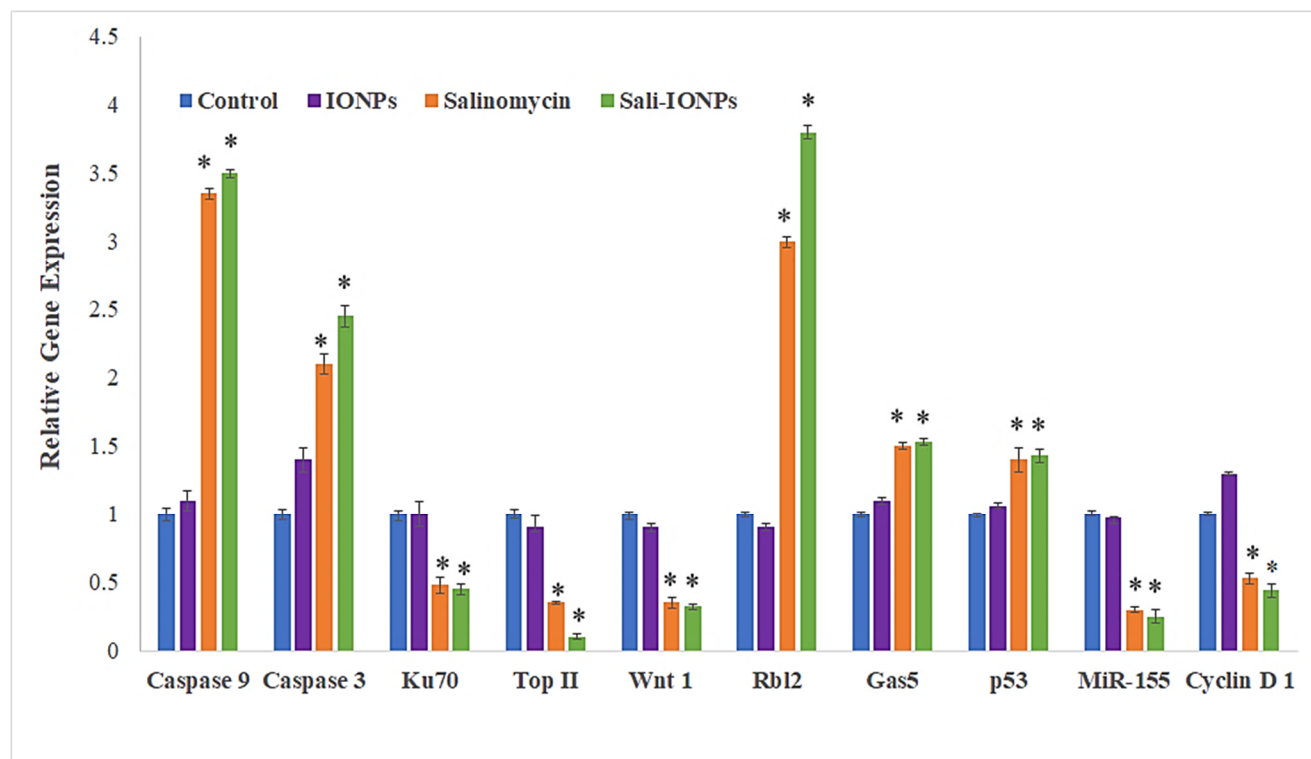


Fig. 3.10. Relative gene expression of U251 cell treated with either IONPs, salinomycin or Sali-IONPs after 48 h of the treatment. \* and \*\* indicate a significant difference compared to the control and salinomycin groups, respectively at  $p < 0.05$ . Data was presented as mean  $\pm$  S.D, and  $n=5$ .

### 3.3.7. Quantitative RT-PCR

To elucidate the anti-cancer mechanisms of salinomycin and Sali-PEI-PEG-IONP treatments on U251, a series of genes was selected for investigation based on our previous *in vitro* studies (Fig. 3.10). Activation of Caspases and release of cytochrome c have been reported to be involved in salinomycin's anti-cancer mechanisms [29]. Generally, Caspases are triggered in a sequential manner, in which, the activation of Caspase 12 triggers activation of Caspase 9 and the subsequent 'effector' Caspase 3 [62]. The cell treatment with Sali-PEI-PEG-IONPs elevated Caspase 9 and Caspase 3 expression by  $3.5 \pm 0.2$  and  $2.5 \pm 0.3$  fold, respectively. Salinomycin's effect on triggering Caspase-dependent apoptosis by elevating the intracellular ROS level in prostate cancer cells has also been reported [57].

Ku70, a DNA-dependent protein kinase, is involved in the repair of DNA double-strand breaks and it has been known as a survival factor in some cancer cells [63,64]. Sali-PEI-PEG-IONPs treatment could significantly reduce Ku70 expression by  $0.48\pm 0.4\%$ . Ku70 has been introduced as a primary resistance factor, whose knockdown could significantly chemo-sensitize gemcitabine-induced cell death and inhibit cell proliferation in pancreatic cancer cells [63]. Topoisomerase II $\alpha$  (Top II) is another nuclear key enzyme in DNA replication, considered as the molecular target for some anti-cancer drugs (Top II inhibitors) like etoposide and doxorubicin [65]. We found that both salinomycin and Sali-PEI-PEG-IONPs treatments could notably reduce Top II expression in GBM cells, while Top II expression has been found to be associated with high proliferation of cancer cells [66].

The Wnt signaling pathway is important in regulating stem cell self-renewal, and has been implicated in the pathogenesis of various cancers [67]. Furthermore, the Wnt signaling plays a critical role in malignant transformation and tumor progression in gliomas, while the therapeutic strategies aimed at silencing Wnt expression in glioma cells have shown a decreased capacity for intracranial tumor formation *in vivo* [68,69]. In this study, Wnt1 expression in U251 was significantly attenuated upon treatment with either salinomycin or Sali-PEI-PEG-IONPs. Inhibitory effects of salinomycin on Wnt signaling and apoptosis induction in lymphocytic leukemia cells [69], breast cancer cells [70] and gastric cancer stem cells [71] have previously been reported.

Rbl2 belongs to the retinoblastoma (Rb) family that are considered as tumor suppressors. The Rb can inhibit cell cycle progression through disabling the E2F family of cell cycle-promoting transcription factors [72]. Treatment with salinomycin and Sali-PEI-PEG-IONPs augmented Rbl2 expression by  $2.7\pm 0.08$  and  $3.8\pm 0.1$ -fold, respectively, that can result in inhibition of the cell cycle

progression. The long non-coding RNA (lncRNA)-growth arrest-specific 5 (Gas5) is another tumor-suppressor gene that is downregulated in several cancers such as glioma, gastric, pancreatic, breast, prostate, lung and colorectal [73,74]. Introduction of Gas5 has been found to suppress tumor malignancy by downregulating miR-222 in GBM cell lines [75]. In the present study, salinomycin (both free salinomycin and Sali-PEI-PEG-IONPs formulations) significantly upregulated Gas5 expression in U251 cells. To the best of our knowledge, this is the first report of such changes in Gas5 with salinomycin exposure.

Treatment of U251 cells with salinomycin and Sali-PEI-PEG-IONPs upregulated p53 expression in U251 GBM cells. The tumor suppressor protein p53 is the most common genetic alteration in human cancers, affecting about 50% of all tumor types [76]. Qin et al, [77] found that salinomycin could induce programmed necrosis via ROS-p53-cyclophilin-D signaling in U87 GBM cells. In this context, increased ROS caused unphosphorylated p53 to migrate into the mitochondrial matrix where it bound to cyclophilin D (Cyp-D) forming a p53-CypD complex. It was reported this complex can stimulate the opening of mitochondrial permeability transition pores, leading to a loss in the mitochondrial membrane potential and the release of cytochrome c which ultimately leads to necrosis [78].

MiR-155 is a prominent oncogenic microRNA that regulates genes involved in immunity and cancer-related pathways. MiR-155 is overexpressed in a variety of malignant tumors whose mechanism of effect is accredited to a blockade of Caspase-3 activity [79]. In this study, we reported for the first time that both salinomycin and Sali-PEI-PEG-IONPs could significantly attenuate MiR-155 expression in GBM cells.

Cyclin D1 is a key regulator protein for the G1-S cell cycle phase transition and cell proliferation whose overexpression is predominantly associated with human tumorigenesis and

cellular metastases in a variety of cancers including GBM [80-82]. Salinomycin and Sali-PEI-PEG-IONP-treated cells demonstrated a downregulation of Cyclin D1 that is consistent with salinomycin's effect in downregulating cyclin D1 in ovarian [83], prostate and breast [84] cancer cells.

### 3.3.8. Evaluation of Sali-IONPs in BBB-GBM co-culture model

As the potential treatments of GBM must be able to reach therapeutically relevant levels in the brain, the Sali-PEI-PEG-IONPs were examined using an *in vitro* BBB-GBM co-culture model. For this study, bEnd.3 cell monolayers were grown on Transwell inserts and placed in 6-well plates containing U251 cells for the study of permeability and anti-cancer efficacy of the Sali-PEI-PEG-IONPs. Under normal conditions, Sali-PEI-PEG-IONPs had limited penetration across the bEnd.3 monolayers ( $1.0 \pm 0.1\%$  over 6 hours). Permeability of the Sali-PEI-PEG-IONPs could be increased by either application of an external magnetic field ( $1.9 \pm 0.3\%$ ), or by altering bEnd.3 monolayer integrity with hyperosmotic mannitol solution ( $2.1 \pm 0.1\%$ ) (Fig. 3.11a). Similarly, the FDX permeability marker showed permeability of  $6.2 \pm 0.4\%$ , due to the smaller size than that of IONPs, that was increased to  $11.6 \pm 0.3\%$  with the administration of mannitol. While either the application of an external magnetic field to intact endothelial monolayers or application of a transient disruption agent increased the permeability of Sali-PEI-PEG-IONPs, the resulting effect on cytotoxicity to U251 cells was similar to that of salinomycin alone (Fig. 3.11b). However, combining an external magnetic field with transient disruption of the endothelial monolayer resulted in even greater increases in Sali-PEI-PEG-IONPs permeability ( $3.2 \pm 0.1\%$ ) and as a result, improved cytotoxicity in U251 cells (cell viability  $62 \pm 4\%$  for free salinomycin vs  $38 \pm 0.7\%$  for Sali-PEI-PEG-IONPs +magnet+mannitol). With the enhanced permeability following application

of mannitol and an external magnetic field, the cytotoxic responses in the BBB-GBM model were similar in magnitude to our initial cytotoxicity assessments in the U251 monocultures.

Generally, the physio-chemical properties of salinomycin suggest its limited BBB permeability and brain accumulation under normal conditions. Furthermore, the role of drug efflux transporters in restriction of the brain penetration of salinomycin has been reported *in vivo* [32]. In this study, the Sali-PEI-PEG-IONPs exhibited limited permeability under normal conditions. However, in the presence of an external magnetic field and transient disruption of the endothelial monolayer, significant increases in Sali-PEI-PEG-IONP permeability were observed. It is noteworthy to mention that utilizing an external magnetic field not only can enhance the passage of magnetic IONPs as a drug delivery system for chemotherapeutics across the BBB, but also can provide a site-specific magnetic targeting to draw the nanoparticles to the site of action, regulating their systemic biodistribution and decreasing their systemic toxicity *in vivo* [25,85]. Taken together, it is suggested that utilizing transient disruption of the BBB in combination with an external magnetic field can potentially enhance the uptake of drug-loaded IONPs and augment the efficacy of GBM chemotherapy. The advantage of this approach over approaches that target receptor-mediated endocytosis across the BBB [86], is the ability to reserve the ligand vectors on the IONP for cancer cell targeting within the brain.

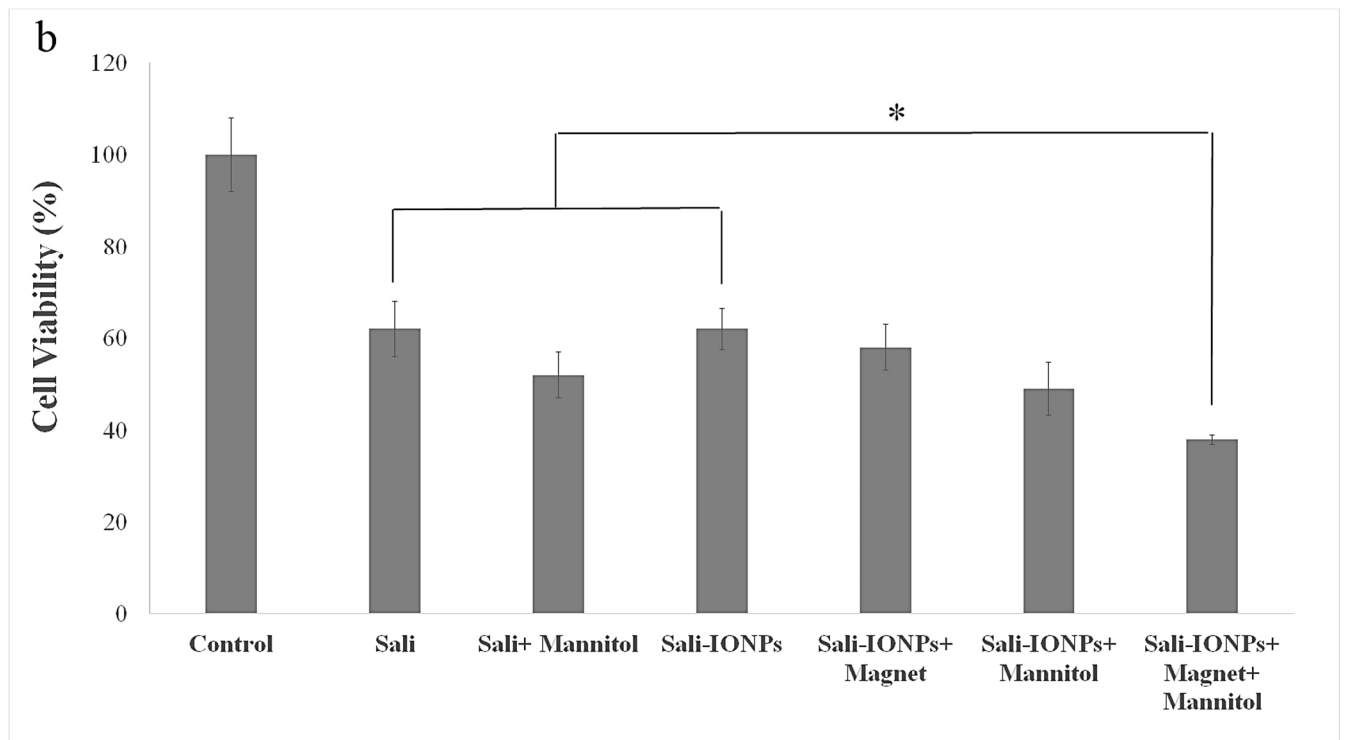
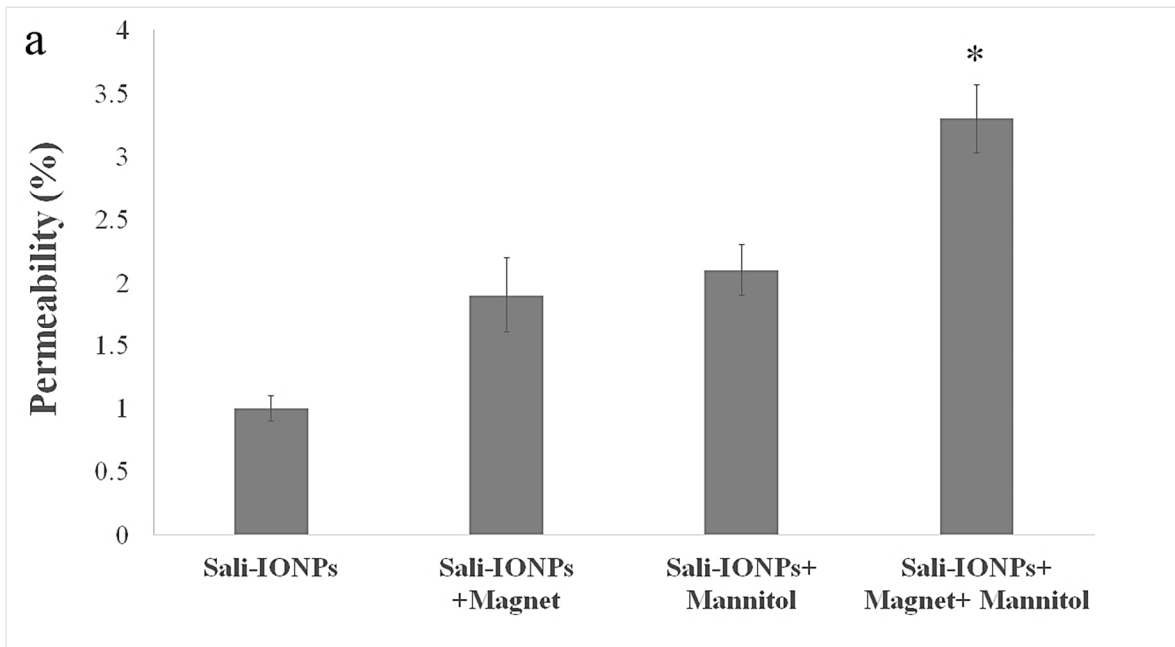


Fig. 3.11. Evaluation of anti-cancer efficacy of Sali-IONPs compared to the free salinomycin on a BBB-brain tumor model *in vitro*. (a) Sali-IONPs permeability across the bEnd.3 monolayer with or without magnet and mannitol (b) cytotoxicity of each formulation on U251 cells after penetrating the bEnd.3 monolayer. \* indicates a significant difference at  $p < 0.05$  with the other treated groups. Data was presented as mean  $\pm$ S.D, and  $n=3$ .

### 3.4. Conclusion

In this study, Sali-PEI-PEG-IONPs were fabricated to facilitate salinomycin delivery to GBM tumor cells. Salinomycin was released from the PEI-PEG-IONPs over 4 days with the capability of an accelerated initial release in the acidic microenvironments. The PEI-PEG-IONPs were found to be biocompatible in bEnd.3 and U251 cells, while both cell lines could efficiently uptake the nanoparticles. Moreover, the Sali-PEI-PEG-IONPs significantly induced ROS generation and apoptosis in U251 cells and inhibited their proliferation. The cell treatment with Sali-PEI-PEG-IONPs could efficaciously activate Caspase cascade, and upregulated the tumor suppressors i.e. p53, Rb12, Gas5. Concomitantly, TopII, Ku70, CyclinD1, and Wnt1 were downregulated in the treated cells. In addition, it was perceived that salinomycin can be recruited as an up-regulator of Gas5 and down-regulator of Top II and MiR-155 in glioma cancer cells. Of note, in an *in vitro* BBB-GBM co-culture model, the Sali-PEI-PEG-IONPs could augment salinomycin penetration through the bEnd.3 layer and provided more anti-cancer effects on U251 cells than that of free salinomycin in the presence of a magnetic field and mannitol. Therefore, the Sali-PEI-PEG-IONPs in combination with an external magnetic field and transient disruption of the BBB can be utilized as a new therapeutic platform to enhance salinomycin's penetration into the brain and provide a site-specific magnetic targeting for GBM chemotherapy. This approach not only can increase salinomycin's therapeutic efficiency, but also potentially diminishes the off-target exposure and toxicity.

### 3.5. References

- 1 Hathout, L. et al. (2016) Modeling the efficacy of the extent of surgical resection in the setting of radiation therapy for glioblastoma. *Cancer science* 107 (8), 1110-1116
- 2 Shi, W. et al. (2018) Investigating the Effect of Reirradiation or Systemic Therapy in Patients With Glioblastoma After Tumor Progression: A Secondary Analysis of NRG Oncology/Radiation Therapy Oncology Group Trial 0525. *International Journal of Radiation Oncology\* Biology\* Physics* 100 (1), 38-44
- 3 Grauwet, K. and Chiocca, E.A. (2016) Glioma and microglia, a double entendre. *Nature immunology* 17 (11), 1240
- 4 Kenny, G.D. et al. (2013) Multifunctional receptor-targeted nanocomplexes for the delivery of therapeutic nucleic acids to the brain. *Biomaterials* 34 (36), 9190-9200
- 5 Norouzi, M. (2018) Recent advances in brain tumor therapy: application of electrospun nanofibers. *Drug discovery today*
- 6 Norouzi, M. et al. (2016) Injectable hydrogel-based drug delivery systems for local cancer therapy. *Drug discovery today*
- 7 Liu, H. et al. (2016) Application of iron oxide nanoparticles in glioma imaging and therapy: from bench to bedside. *Nanoscale* 8 (15), 7808-7826
- 8 Kulczar, C. et al. (2017) Development of a direct contact astrocyte-human cerebral microvessel endothelial cells blood-brain barrier coculture model. *Journal of Pharmacy and Pharmacology* 69 (12), 1684-1696
- 9 Cheng, Y. et al. (2014) Blood-brain barrier permeable gold nanoparticles: an efficient delivery platform for enhanced malignant glioma therapy and imaging. *Small* 10 (24), 5137-5150
- 10 Gao, H. (2016) Progress and perspectives on targeting nanoparticles for brain drug delivery. *Acta Pharmaceutica Sinica B* 6 (4), 268-286
- 11 Xu, H.-L. et al. (2016) Glioma-targeted superparamagnetic iron oxide nanoparticles as drug-carrying vehicles for theranostic effects. *Nanoscale* 8 (29), 14222-14236
- 12 Mujokoro, B. et al. (2016) Nano-structures mediated co-delivery of therapeutic agents for glioblastoma treatment: A review. *Materials Science and Engineering: C* 69, 1092-1102
- 13 Norouzi, M. et al. (2017) Electrospun-based systems in cancer therapy. In *Electrospun Materials for Tissue Engineering and Biomedical Applications*, pp. 337-356, Elsevier
- 14 Hola, K. et al. (2015) Tailored functionalization of iron oxide nanoparticles for MRI, drug delivery, magnetic separation and immobilization of biosubstances. *Biotechnology Advances* 33 (6), 1162-1176
- 15 Wu, W. et al. (2015) Recent progress on magnetic iron oxide nanoparticles: synthesis, surface functional strategies and biomedical applications. *Science and technology of advanced materials* 16 (2), 023501
- 16 Lee, N. et al. (2015) Iron oxide based nanoparticles for multimodal imaging and magnetoresponsive therapy. *Chemical Reviews* 115 (19), 10637-10689
- 17 Arami, H. et al. (2015) In vivo delivery, pharmacokinetics, biodistribution and toxicity of iron oxide nanoparticles. *Chemical Society Reviews* 44 (23), 8576-8607
- 18 Kievit, F.M. et al. (2011) Doxorubicin loaded iron oxide nanoparticles overcome multidrug resistance in cancer in vitro. *Journal of controlled release* 152 (1), 76-83
- 19 Mu, Q. et al. (2015) Stable and efficient Paclitaxel nanoparticles for targeted glioblastoma therapy. *Advanced healthcare materials* 4 (8), 1236-1245
- 20 Mu, Q. et al. (2016) Gemcitabine and chlorotoxin conjugated iron oxide nanoparticles for glioblastoma therapy. *Journal of Materials Chemistry B* 4 (1), 32-36
- 21 Kaluzova, M. et al. (2015) Targeted therapy of glioblastoma stem-like cells and tumor non-stem cells using cetuximab-conjugated iron-oxide nanoparticles. *Oncotarget* 6 (11), 8788

- 22 Hadjipanayis, C.G. et al. (2010) EGFRvIII antibody-conjugated iron oxide nanoparticles for magnetic resonance imaging-guided convection-enhanced delivery and targeted therapy of glioblastoma. *Cancer research*, 0008-5472. CAN-0010-1022
- 23 Jin, R. et al. (2014) Superparamagnetic iron oxide nanoparticles for MR imaging and therapy: design considerations and clinical applications. *Current opinion in pharmacology* 18, 18-27
- 24 Wang, Y.-X.J. (2015) Current status of superparamagnetic iron oxide contrast agents for liver magnetic resonance imaging. *World journal of gastroenterology* 21 (47), 13400
- 25 Chertok, B. et al. (2008) Iron oxide nanoparticles as a drug delivery vehicle for MRI monitored magnetic targeting of brain tumors. *Biomaterials* 29 (4), 487-496
- 26 Naujokat, C. and Steinhart, R. (2012) Salinomycin as a drug for targeting human cancer stem cells. *BioMed Research International* 2012
- 27 Huczynski, A. (2012) Salinomycin—a new cancer drug candidate. *Chemical biology & drug design* 79 (3), 235-238
- 28 Gupta, P.B. et al. (2009) Identification of selective inhibitors of cancer stem cells by high-throughput screening. *Cell* 138 (4), 645-659
- 29 Jangamreddy, J.R. et al. (2013) Salinomycin induces activation of autophagy, mitophagy and affects mitochondrial polarity: differences between primary and cancer cells. *Biochimica et Biophysica Acta (BBA)-Molecular Cell Research* 1833 (9), 2057-2069
- 30 Managò, A. et al. (2015) Early effects of the antineoplastic agent salinomycin on mitochondrial function. *Cell death & disease* 6 (10), e1930
- 31 Norouzi, M. et al. (2018) Salinomycin-loaded Nanofibers for Glioblastoma Therapy. *Scientific reports* 8 (1), 9377
- 32 Lagas, J.S. et al. (2008) P-glycoprotein limits oral availability, brain penetration, and toxicity of an anionic drug, the antibiotic salinomycin. *Antimicrobial agents and chemotherapy* 52 (3), 1034-1039
- 33 Yathindranath, V. et al. (2013) One-pot synthesis of iron oxide nanoparticles with functional silane shells: a versatile general precursor for conjugations and biomedical applications. *Langmuir* 29 (34), 10850-10858
- 34 Sun, Z. et al. (2013) Characterization of cellular uptake and toxicity of aminosilane-coated iron oxide nanoparticles with different charges in central nervous system-relevant cell culture models. *International journal of nanomedicine* 8, 961
- 35 Kaech, S.M. and Ahmed, R. (2001) Memory CD8+ T cell differentiation: initial antigen encounter triggers a developmental program in naive cells. *Nature immunology* 2 (5), 415
- 36 Eruslanov, E. and Kusmartsev, S. (2010) Identification of ROS using oxidized DCFDA and flow-cytometry. In *Advanced protocols in oxidative stress II*, pp. 57-72, Springer
- 37 Lee, J.-Y. et al. (2017) Chemosensitizing indomethacin-conjugated chitosan oligosaccharide nanoparticles for tumor-targeted drug delivery. *Acta biomaterialia* 57, 262-273
- 38 Huang, P. et al. (2016) Zwitterionic nanoparticles constructed from bioreducible RAFT-ROP double head agent for shell shedding triggered intracellular drug delivery. *Acta biomaterialia* 40, 263-272
- 39 Zhang, T. et al. (2019) Multitargeted Nanoparticles Deliver Synergistic Drugs across the Blood-Brain Barrier to Brain Metastases of Triple Negative Breast Cancer Cells and Tumor-Associated Macrophages. *Advanced healthcare materials*, 1900543
- 40 Mu, Q. et al. (2015) Anti-HER2/neu peptide-conjugated iron oxide nanoparticles for targeted delivery of paclitaxel to breast cancer cells. *Nanoscale* 7 (43), 18010-18014
- 41 Norouzi, M. et al. (2015) Advances in Skin Regeneration: Application of Electrospun Scaffolds. *Advanced Healthcare Materials* 4 (8), 1114-1133
- 42 Tran, T.T.-D. et al. (2015) Design of iron oxide nanoparticles decorated oleic acid and bovine serum albumin for drug delivery. *Chemical Engineering Research and Design* 94, 112-118

- 43 Hervault, A. et al. (2016) Doxorubicin loaded dual pH-and thermo-responsive magnetic nanocarrier for combined magnetic hyperthermia and targeted controlled drug delivery applications. *Nanoscale* 8 (24), 12152-12161
- 44 Chen, F. et al. (2018) Targeted salinomycin delivery with EGFR and CD133 aptamers based dual-ligand lipid-polymer nanoparticles to both osteosarcoma cells and cancer stem cells. *Nanomedicine: Nanotechnology, Biology and Medicine*
- 45 Ni, M. et al. (2015) Poly (lactic-co-glycolic acid) nanoparticles conjugated with CD133 aptamers for targeted salinomycin delivery to CD133+ osteosarcoma cancer stem cells. *International journal of nanomedicine* 10, 2537
- 46 Sun, Z. et al. (2014) Magnetic field enhanced convective diffusion of iron oxide nanoparticles in an osmotically disrupted cell culture model of the blood-brain barrier. *International journal of nanomedicine* 9, 3013-3026
- 47 Iwadate, Y. et al. (1993) Intra-arterial mannitol infusion in the chemotherapy for malignant brain tumors. *Journal of neuro-oncology* 15 (2), 185-193
- 48 Choi, C. et al. (2018) Additional increased effects of mannitol-temozolomide combined treatment on blood-brain barrier permeability. *Biochemical and biophysical research communications* 497 (2), 769-775
- 49 McCarty, D. et al. (2009) Mannitol-facilitated CNS entry of rAAV2 vector significantly delayed the neurological disease progression in MPS IIIB mice. *Gene therapy* 16 (11), 1340
- 50 Siegal, T. et al. (2000) In vivo assessment of the window of barrier opening after osmotic blood—brain barrier disruption in humans. *Journal of neurosurgery* 92 (4), 599-605
- 51 Corot, C. et al. (2006) Recent advances in iron oxide nanocrystal technology for medical imaging. *Advanced drug delivery reviews* 58 (14), 1471-1504
- 52 Chen, J. et al. (2010) Gold nanocages as photothermal transducers for cancer treatment. *Small* 6 (7), 811-817
- 53 Melamed, J.R. et al. (2016) Using gold nanoparticles to disrupt the tumor microenvironment: an emerging therapeutic strategy. *ACS nano* 10 (12), 10631-10635
- 54 Zhu, X.-M. et al. (2012) Enhanced cellular uptake of aminosilane-coated superparamagnetic iron oxide nanoparticles in mammalian cell lines. *International journal of nanomedicine* 7, 953
- 55 Schenk, M. et al. (2015) Salinomycin inhibits growth of pancreatic cancer and cancer cell migration by disruption of actin stress fiber integrity. *Cancer letters* 358 (2), 161-169
- 56 Urbaniak, A. et al. (2018) Salinomycin derivatives exhibit activity against primary acute lymphoblastic leukemia (ALL) cells in vitro. *Biomedicine & Pharmacotherapy* 99, 384-390
- 57 Kim, K.-Y. et al. (2011) Salinomycin-induced apoptosis of human prostate cancer cells due to accumulated reactive oxygen species and mitochondrial membrane depolarization. *Biochemical and biophysical research communications* 413 (1), 80-86
- 58 Tung, C.-L. et al. (2017) Salinomycin acts through reducing AKT-dependent thymidylate synthase expression to enhance erlotinib-induced cytotoxicity in human lung cancer cells. *Experimental cell research* 357 (1), 59-66
- 59 Kaplan, F. and Teksen, F. (2016) Apoptotic effects of salinomycin on human ovarian cancer cell line (OVCAR-3). *Tumor Biology* 37 (3), 3897-3903
- 60 Zhao, S.-J. et al. (2017) Induction of G1 Cell Cycle Arrest in Human Glioma Cells by Salinomycin Through Triggering ROS-Mediated DNA Damage In Vitro and In Vivo. *Neurochemical research* 42 (4), 997-1005
- 61 Xipell, E. et al. (2016) Salinomycin induced ROS results in abortive autophagy and leads to regulated necrosis in glioblastoma. *Oncotarget* 7 (21), 30626-30641
- 62 Boehmerle, W. and Endres, M. (2011) Salinomycin induces calpain and cytochrome c-mediated neuronal cell death. *Cell death & disease* 2, e168
- 63 Ma, J. et al. (2017) Ku70 inhibits gemcitabine-induced DNA damage and pancreatic cancer cell apoptosis. *Biochemical and biophysical research communications* 484 (4), 746-752

- 64 Hada, M. et al. (2016) Cytosolic Ku70 regulates Bax-mediated cell death. *Tumor Biology* 37 (10), 13903-13914
- 65 Järvinen, T.A. et al. (2000) Amplification and deletion of topoisomerase II $\alpha$  associate with ErbB-2 amplification and affect sensitivity to topoisomerase II inhibitor doxorubicin in breast cancer. *The American journal of pathology* 156 (3), 839-847
- 66 Romero, A. et al. (2011) Assessment of topoisomerase II  $\alpha$  status in breast cancer by quantitative PCR, gene expression microarrays, immunohistochemistry, and fluorescence in situ hybridization. *The American journal of pathology* 178 (4), 1453-1460
- 67 Reya, T. and Clevers, H. (2005) Wnt signalling in stem cells and cancer. *Nature* 434 (7035), 843
- 68 Kaur, N. et al. (2013) Wnt3a mediated activation of Wnt/ $\beta$ -catenin signaling promotes tumor progression in glioblastoma. *Molecular and Cellular Neuroscience* 54, 44-57
- 69 Rampazzo, E. et al. (2013) Wnt activation promotes neuronal differentiation of glioblastoma. *Cell death & disease* 4, e500
- 70 King, T.D. et al. (2012) The wnt/ $\beta$ -catenin signaling pathway: A potential therapeutic target in the treatment of triple negative breast cancer. *Journal of cellular biochemistry* 113 (1), 13-18
- 71 Mao, J. et al. (2014) Roles of Wnt/beta-catenin signaling in the gastric cancer stem cells proliferation and salinomycin treatment. *Cell death & disease* 5, e1039
- 72 Reynolds, M.R. et al. (2014) Control of glutamine metabolism by the tumor suppressor Rb. *Oncogene* 33 (5), 556-566
- 73 Yin, D. et al. (2014) Long noncoding RNA GAS5 affects cell proliferation and predicts a poor prognosis in patients with colorectal cancer. *Medical oncology* 31 (11), 253
- 74 Ma, C. et al. (2016) The growth arrest-specific transcript 5 (GAS5): a pivotal tumor suppressor long noncoding RNA in human cancers. *Tumor Biology* 37 (2), 1437-1444
- 75 Zhao, X. et al. (2015) Gas5 exerts tumor-suppressive functions in human glioma cells by targeting miR-222. *Molecular Therapy* 23 (12), 1899-1911
- 76 Joerger, A. and Fersht, A. (2007) Structure–function–rescue: the diverse nature of common p53 cancer mutants. *Oncogene* 26 (15), 2226
- 77 Qin, L.-s. et al. (2015) ROS-p53-cyclophilin-D signaling mediates salinomycin-induced glioma cell necrosis. *Journal of Experimental & Clinical Cancer Research* 34 (1), 57
- 78 Magrath, J.W. and Kim, Y. (2017) Salinomycin's potential to eliminate glioblastoma stem cells and treat glioblastoma multiforme. *International journal of oncology* 51 (3), 753-759
- 79 Faraoni, I. et al. (2009) miR-155 gene: a typical multifunctional microRNA. *Biochimica et Biophysica Acta (BBA)-Molecular Basis of Disease* 1792 (6), 497-505
- 80 Marampon, F. et al. (2016) Cyclin D1 silencing suppresses tumorigenicity, impairs DNA double strand break repair and thus radiosensitizes androgen-independent prostate cancer cells to DNA damage. *Oncotarget* 7 (5), 5383
- 81 Bachmann, K. et al. (2015) Cyclin D1 is a strong prognostic factor for survival in pancreatic cancer: analysis of CD G870A polymorphism, FISH and immunohistochemistry. *Journal of surgical oncology* 111 (3), 316-323
- 82 Arato-Ohshima, T. and Sawa, H. (1999) Over-expression of cyclin D1 induces glioma invasion by increasing matrix metalloproteinase activity and cell motility. *International journal of cancer* 83 (3), 387-392
- 83 Koo, K. et al. (2013) Salinomycin induces cell death via inactivation of Stat3 and downregulation of Skp2. *Cell death & disease* 4 (6), e693
- 84 Lu, W. and Li, Y. (2014) Salinomycin Suppresses LRP6 Expression and Inhibits Both Wnt/ $\beta$ -catenin and mTORC1 Signaling in Breast and Prostate Cancer Cells. *Journal of cellular biochemistry* 115 (10), 1799-1807
- 85 Cole, A.J. et al. (2011) Magnetic brain tumor targeting and biodistribution of long-circulating PEG-modified, cross-linked starch-coated iron oxide nanoparticles. *Biomaterials* 32 (26), 6291-6301
- 86 Ulbrich, K. et al. (2011) Targeting the insulin receptor: nanoparticles for drug delivery across the blood–brain barrier (BBB). *Journal of drug targeting* 19 (2), 125-132

## **Chapter 4**

# **Salinomycin-loaded Injectable Thermosensitive Hydrogels for Glioblastoma Therapy**

# Salinomycin-loaded Injectable Thermosensitive Hydrogels for Glioblastoma Therapy

## ABSTRACT

Local drug delivery approaches for treating brain tumors not only diminish the toxicity of systemic chemotherapy, but also circumvent the blood-brain barrier (BBB) which restricts the passage of most chemotherapeutics to the brain. Recently, salinomycin has attracted much attention as a potential chemotherapeutic agent in a variety of cancers. In this study, poly (ethylene oxide)/poly (propylene oxide)/poly (ethylene oxide) (PEO-PPO-PEO, Pluronic F127) and poly (dl-lactide-co-glycolide-b-ethylene glycol-b-dl-lactide-co-glycolide) (PLGA-PEG-PLGA), the two most common thermosensitive copolymers, were utilized as local delivery systems for salinomycin in the treatment of glioblastoma. The Pluronic and PLGA-PEG-PLGA hydrogels released 100% and 36% of the encapsulated salinomycin over a one-week period, respectively. While both hydrogels were found to be effective at inhibiting glioblastoma cell proliferation, inducing apoptosis and generating intracellular reactive oxygen species, the Pluronic formulation showed better biocompatibility, a superior drug release profile and an ability to further enhance the cytotoxicity of salinomycin, compared to the PLGA-PEG-PLGA hydrogel formulation. Animal studies in subcutaneous U251 xenografted nude mice also revealed that Pluronic+salinomycin hydrogel reduced tumor growth compared to free salinomycin- and PBS-treated mice by 4-fold and 5-fold, respectively within 12 days. Therefore, it is envisaged that salinomycin-loaded Pluronic can be utilized as an injectable thermosensitive hydrogel platform for local treatment of glioblastoma,

providing a sustained release of salinomycin at the tumor site and potentially bypassing the BBB for drug delivery to the brain.

**Keywords:** Salinomycin; Glioblastoma; Thermosensitive injectable hydrogels; Pluronic; PLGA-PEG-PLGA

## 4.1. Introduction

Glioblastoma multiforme (GBM) is the most commonly occurring malignant brain tumor in adults, and the median survival time for patients who are diagnosed with GBM is 14.6 months [1-3]. Chemotherapeutic options for treating GBM are limited due to the blood–brain barrier (BBB) that restricts the passage of many drugs into the brain and prevents achieving therapeutic levels at the tumor site [4-6]. To overcome the limited BBB permeability of many chemotherapeutics, local drug delivery approaches providing sustained release of drugs at the brain tumor site are of increasing interest. In addition to circumventing the BBB, local drug delivery can minimize the systemic toxicity of the chemotherapeutics while providing a high concentration of the drugs at the tumor site [5,7,8].

A variety of local drug delivery systems have been investigated such as hydrogels, wafers, nanofibers, rods and films [9-11]. Amongst these, hydrogels have attracted much attention as they can be injected less-invasively in and around the tumor site providing a controlled delivery/release of chemotherapeutics. Injectable hydrogels that exhibit a sol–gel phase transition following injection in response to an external stimulus such as temperature, pH, and light provide improved methods for controlled drug release at the desired site of action [12,13]. Generally, injectable hydrogels can be formed *in situ* through either physical or chemical crosslinking methods. Of these two methods, the physical-crosslinked-hydrogels show some distinct advantages as they do not need photoirradiation, organic solvents or crosslinking catalysts [14]. Thermosensitive hydrogels are the most common class of stimuli-sensitive hydrogels having the ability to be injected into the body in a liquid state, and then undergoing a phase transition to gelation state at the physiological temperatures within the body [15,16].

A variety of chemotherapeutics such as doxorubicin [17,18], paclitaxel [19-21] and 5-fluorouracil [22,23] have been incorporated into thermosensitive hydrogel drug delivery systems to treat various types of cancer. Poly(ethylene oxide)-poly(propylene oxide)-poly(ethylene oxide) (PEO<sub>100</sub>-PPO<sub>69</sub>-PEO<sub>100</sub>) triblock copolymer, known as Pluronic®, approved by the Food and Drug Administration (FDA) and poly(lactide-co-glycolide)-b-poly(ethylene glycol)-b-poly(lactide-co-glycolide) (PLGA-PEG-PLGA) triblock copolymer, whose PEG and PLGA meet FDA's approval for clinical applications, are the most common injectable thermosensitive hydrogels utilized for local drug delivery [7]. Until now, Gliadel® is the only local drug delivery system approved by the FDA for high-grade gliomas as an adjunct to surgery and radiation. Gliadel® is a biodegradable wafer of poly(carboxyphenoxy-propane/sebacic acid) releasing carmustine (BCNU); that is implanted into the tumor cavity after surgical resection of the glioma tumors [5]. Clinical findings have revealed that the median survival from surgery to death in GBM patients significantly improved from 39.9 weeks (for the placebo group) to 53.3 weeks for the group receiving Gliadel® [24].

Salinomycin is an antibacterial and ionophore anticoccidial agent, that shows cytotoxic effects on a variety of cancer cells such as gastrointestinal sarcoma, osteosarcoma, and colorectal [25]. Although a unifying molecular mechanism of salinomycin toxicity has not been definitively identified, activation of cytochrome C and Caspase, increasing mitochondrial membrane potential and time-dependent ATP-depletion in cancer cells are all considered as potential pathways contributing to the salinomycin-induced cytotoxicity reported [26]. Salinomycin has also been reported to be more effective in killing cancer stem cells that initiate tumor formation. Studies by Gupta et al., [27] found salinomycin to be 100-time more effective than paclitaxel at killing breast

cancer stem-like cells. In addition, the Wnt/ $\beta$ -catenin pathway, essential for brain cancer stem cell self-renewal, can also be blocked by salinomycin [28].

In this study, salinomycin-loaded injectable hydrogels were examined as potential local drug delivery systems for the treatment of GBM. To this end, we examined two types of the most common thermosensitive hydrogels i.e. Pluronic F127 and PLGA-PEG-PLGA, comparing their characteristics as local drug delivery systems, and their synergistic effects with salinomycin in an established human GBM cell line. As the physical-chemical properties of salinomycin, together with its drug efflux transporter liabilities, limits both its oral absorption and BBB penetration [29,30], development of local drug delivery systems for salinomycin with the capability of bypassing the BBB and entering the brain directly is of significant clinical importance. To the best of our knowledge, this is the first study to develop an injectable local drug delivery system for salinomycin. Based on the findings of this study, the Pluronic+salinomycin can potentially be utilized as an effective therapeutic platform for local drug delivery and treatment of GBM and other solid tumors.

## 4.2. Materials and methods

### 4.2.1. Materials

PLGA-PEG-PLGA (1700-1500-1700Da, LA:GA 15:1) was purchased from PolySciTech, USA. PEO<sub>98</sub>-PPO<sub>67</sub>-PEO<sub>98</sub> (Pluronic F-127, MW~12600), salinomycin monosodium salt, 3-(4,5-dimethylthiazol-2-yl)-2,5-diphenyltetrazoliumbromide (MTT), 4',6-diamidino-2-phenylindole dihydrochloride (DAPI), and 2',7'-dichlorofluorescein diacetate (DCFDA) were all obtained from Sigma Aldrich (St. Louis, MO, USA). Dulbecco's Modified Eagle Medium: Nutrient Mixture F-12 (DMEM/F12), fetal bovine serum (FBS), trypsin, penicillin and streptomycin were purchased

from Gibco (Grand Island, NY, USA USA). ActinRed™ 555 was purchased from Invitrogen Life Technologies.

#### 4.2.2. In vitro degradation

To measure the degradation rate of the hydrogels, 0.5 mL of each hydrogel (20 wt% in D.I. water) was injected into Eppendorf tubes and incubated at 37 °C for 10 min, allowing gel formation. Once the gel was formed, 2 mL phosphate-buffered saline (PBS, pH 7.4) was added and the samples were incubated at 37 °C. At various times (up to 30 days), the PBS was removed, and the hydrogel samples dried at room temperature and weighed. The degradation profile of the hydrogels was obtained by plotting the weight of the hydrogels against the time of incubation.

#### 4.2.3. In vitro drug release

The release kinetics of salinomycin from the hydrogels were studied at 37°C in PBS (pH 7.4). 20 wt% solutions of Pluronic and PLGA-PEG-PLGA were solubilized in D.I. water for 2 hours and overnight, respectively in an iced-water bath. Salinomycin was added to the polymer solutions (with a final concentration of 1 µg/mL of polymer) and mixed well to make a homogenous polymer-drug solution. For the drug release study, the drug-loaded hydrogels (0.5 mg, 20 wt%) were incubated in 2 mL PBS, and at various time points, the solution was removed and replenished with fresh PBS. The concentration of salinomycin in the PBS was measured using an Ionophore ELISA kit (Europroxima, The Netherlands), based on the manufacturer's instruction. The accumulative release of salinomycin from the hydrogels was calculated as a function of incubation time.

The drug release mechanism was also investigated using the semi-empirical equation developed by Korsmeyer–Peppas:

$$\frac{M_t}{M_\infty} = kt^n$$

Where  $M_t$  and  $M_\infty$  are cumulative concentrations of the released drug at time  $t$  and infinite time, respectively. The  $k$  is the drug release rate constant, and  $n$  is the release exponent [31,32]. Determination of the mechanism of drug release is based on the value of  $n$ . A Fickian diffusion mechanism is followed when  $n=0.5$ , values of  $0.5 < n < 1$  and  $n=1$  indicate anomalous transport and case II transport mechanism (zero-order release), respectively [32].

#### 4.2.4. In vitro cytotoxicity study

The human GBM cell line (U251, passage number 20-25), and ANA-1 murine macrophages (passage number 26-32) were used to evaluate the cytotoxicity of the hydrogels. The U251, and ANA-1 cells were cultured in DMEM/F12, and DMEM, respectively, supplemented with 10% fetal bovine serum and 1% penicillin-streptomycin. The cells were passed using a 0.25% trypsin EDTA solution upon confluency.

The cytotoxicity of salinomycin-loaded hydrogels against U251 cells was assessed using the MTT assay. Briefly, the GBM cells were seeded in 24-well plates at a density of 10,000 cells/cm<sup>2</sup> and incubated overnight at 37°C. Afterwards, the media was removed and replaced with either fresh media (control), culture media containing salinomycin (either 0.5 or 1 µg/mL), or media containing salinomycin-loaded PLGA-PEG-PLGA and Pluronic hydrogels. To add the hydrogels to cell culture media, the salinomycin-loaded polymers at liquid state were prepared at 4°C and pre-cooled syringes and needles were used in order to prevent gelation. When the polymer solution was exposed to the cell culture media at a temperature of 37 °C, gelation occurred. After

48 hours, the culture media was removed, the cells washed with PBS, then fresh culture media containing 0.5 mg/mL of MTT reagent was added. Following a 3-h incubation period at 37 °C, the media was removed and replaced with pure DMSO to dissolve formazone crystals. The absorbance of the resulting cell lysis solutions was read using Synergy HT microplate reader (Biotek, USA) at a wavelength of 570 nm. The relative cell viability was calculated as  $[\text{OD}]_{\text{test}}/[\text{OD}]_{\text{control}}$ . To evaluate potential synergistic interactions of salinomycin and the hydrogels, a coefficient of drug interaction (CDI) analysis was used [33]. The CDI was calculated as follows:  $\text{CDI} = \text{AB}/(\text{A} \times \text{B})$ , where AB is the absorbance ratio of the drug-hydrogel combination group to the control (PBS-treated) group, while A and B is the absorbance ratio of drug alone (A) and hydrogel alone (B) to control at 570 nm. Those CDI values  $< 1$  indicate synergism, while CDI values  $< 0.7$  indicate a significant synergistic effect, CDI values equal to 1 represent additive effects and  $\text{CDI} > 1$  indicate antagonist effects [33].

In addition, cell apoptosis was studied using Annexin V-FITC/PI apoptosis kit (Thermo Fisher Scientific, USA). To this end, the U251 cells were treated either with free drug, or drug-loaded hydrogels for 48 h, followed by staining with Annexin V-FITC and PI in accordance with the manufacturer's protocol and the cells were sorted with flow cytometry (BD FACSCanto II Flow Cytometer instrument (BD Bioscience)). To study the effects of the various treatments on cell proliferation, cells were labeled with the fluorescent dye carboxyfluorescein succinimidyl ester (CFSE, 50 mM) for 20 min at 37°C. Afterwards, the solution was removed and the cells were treated with free salinomycin, or salinomycin-loaded hydrogels for 48 h. Fluorescent intensity of the cells was measured using flow cytometry. As the cellular content of CFSE is reduced during each cell division, the cellular fluorescent intensity is inversely proportional to proliferation [34].

The morphology of the U251 cells was also examined using a fluorescence microscope (Zeiss Axio observer Z1, Germany). Cells were washed with PBS and fixed with 4% paraformaldehyde for 20 min at room temperature and rinsed with PBS. To permeabilize the cells, they were treated with 0.2% Triton X-100 for 5 min and washed with PBS four times. Subsequently, the actin cytoskeleton and nucleus of the cells were stained with ActinRed and DAPI (100 nM), respectively at 37° C.

#### 4.2.5. Reactive oxygen species (ROS) determination

Intracellular ROS was measured based on the intracellular peroxide-dependent oxidation of 2',7'-dichlorofluorescein diacetate (DCFDA). The DCFDA is a non-fluorescent dye, that upon oxidation within the mitochondria of the cell is transformed to the highly fluorescent 2',7'-dichlorofluorescein (DCF) [35]. For this study, the cells were cultured in black 96 well plates at a density of 10000 cell/cm<sup>2</sup>. After 24 h, the cells were washed and stained with 50 µM DCFDA in PBS for 45 min at 37 °C. Subsequently, the solution was removed, and the cells were treated with salinomycin and salinomycin-loaded hydrogels in PBS for 30 min to 3 h. At the predetermined time points, the fluorescence intensity was measured using a microplate reader at Ex/Em= 485/535 nm.

#### 4.2.6. Quantitative RT-PCR

For gene studies, the GBM cells were treated with free salinomycin, hydrogels, and salinomycin-loaded hydrogels for 48 hours. The remaining viable cells were washed with PBS and their total RNA was extracted utilizing TRIZOL reagent (Invitrogen, USA) according to the manufacturer's protocol. Afterwards, the level of mRNA encoding Caspase-3, Bax, Rbl1, Rbl2 and Wnt1 was studied by quantitative reverse-transcript polymerase chain reaction (qRT-PCR) and β-actin was used as the housekeeping gene. The qRT-PCR was administrated using iTaq

Universal SYBR Green Supermix kit (Bio-Rad, USA). The reaction was performed in an Applied Biosystems 7300 PCR system with the following cycles: 1 cycle of 10 min at 50°C for the reverse transcription reaction, 1 cycle of 1 min at 95 °C for polymerase activation, 40 cycles consisting of 15 sec at 95°C for denaturation and 1 min at 60°C for annealing. Comparative C<sub>t</sub> method ( $2^{-\Delta\Delta C_t}$ ) was utilized to calculate the relative expression of the target genes which was normalized to the  $\beta$ -actin. The sequences of the primers are listed in Table 4.1.

Table 4.1. Sequences of human primers

	<b>Forward</b>	<b>Reverse</b>
<b><math>\beta</math>-actin</b>	AATGCCAGGGTACATGGTGG	AGGAAGGAAGGCTGGAAGAGTG
<b>RBL1</b>	CCGGAAGCAGAGGAGGATTC	GGGCACATAATCGCATTGGC
<b>RBL2</b>	GGTTCCCACTGAGTGATTACTGT	AGAAGCCTCCTATGCTCACG
<b>Caspase 3</b>	CTCTGGTTTTTCGGTGGGTGT	CGCTTCCATGTATGATCTTTGGTT
<b>Wnt1</b>	CAACAGCAGTGGCCGATGGTGG	CGGCCTGCCTCGTTGTTGTGAAG
<b>Bax</b>	CAAACCTGGTGCTCAAGGCC	GAGACAGGGACATCAGTCGC

#### 4.2.7. Anti-tumor study on GBM xenograft models

To evaluate the antitumor effect of salinomycin, and Pluronic+salinomycin *in vivo*, subcutaneous GBM tumors were generated in female BALB/c nude mice. All animal procedures were approved by the Royan Institutional Review Board and Institutional Ethics Committee (approved protocol ID of J/90/1397). For this purpose, U251 human GBM cells were transplanted via subcutaneous injection of  $5 \times 10^6$  cells into the flank of each mice. Ten days post-transplantation, the mice were intratumorally injected with either PBS (placebo), Pluronic, salinomycin (20  $\mu$ g/kg) in PBS, or Pluronic+salinomycin (equivalent to 20  $\mu$ g/kg of salinomycin) (n=3 in each group). A second follow up intratumoral injection was performed 7 days later. Tumor size and mouse body weight were measured daily and mice were sacrificed at 21-days post tumor

cell injection. The dissected tumor tissues were fixed in 10% formalin, and embedded in paraffin. The tissues were then sectioned, deparaffinized and stained with hematoxylin and eosin (H&E) for histological analysis.

#### 4.2.8. Statistical analysis

The studies were conducted in triplicate and the results were reported as the mean  $\pm$  standard deviation (SD). Statistical analysis was conducted in GraphPad Prism using one or mixed two-way ANOVA (each applicable), with multiple post-hoc analysis of Tukey and with an adjusted p-value. The hypotheses were based on  $H_0$ : All groups should have the same mean measurement values, and  $H_1$ : All groups do not have the same mean measurement values. The adjusted p-value  $< 0.05$  (adjusted based on the entire family of comparisons) was considered as the significant level to reject the null hypothesis, as previously reported [36-38].

### 4.3. Result and Discussion

#### 4.3.1. Characterization of the hydrogels

PEO-PPO-PEO (Pluronic F127) and PLGA-PEG-PLGA are thermosensitive polymers exhibiting reversible thermo-gelation properties at unique sol-gel transition temperatures. At temperatures below the transition point, the hydrogels are fluid, while above the transition temperature the hydrogels become semi-solid [7] (Fig. 4.1a). For the 20% wt Pluronic and PLGA-PEG-PLGA hydrogels, the thermo-gelation occurred at temperatures above 10 and 30 °C, respectively. The thermo-gelation phenomenon is explained by the interactions between different segments of the copolymers. For Pluronic, at concentrations above the critical micellar concentration (CMC, ca.  $4 \times 10^{-3}$  g/mL [39]), increases in temperature cause copolymer molecules to aggregate into micelles resulting in dehydration of the hydrophobic PO blocks. Thereafter, the

spherical micelles with the dehydrated PPO cores and hydrated swollen PEO chains in the outer shells, are formed. The result of this ordered packing of micelles is gelation. The micelles are released from the matrix during the process of gel erosion [40,41]. Similarly, for PLGA-PEG-PLGA (CMC, ca.  $2.82 \times 10^{-5}$  g/mL [42]), the block copolymers are first assembled into micelles, in which the hydrophobic PLGA blocks constitute the cores of the micelles, and the hydrophilic PEG blocks form the coronas; then the micelles are further aggregated to form the gel as the temperature increases [43-45].

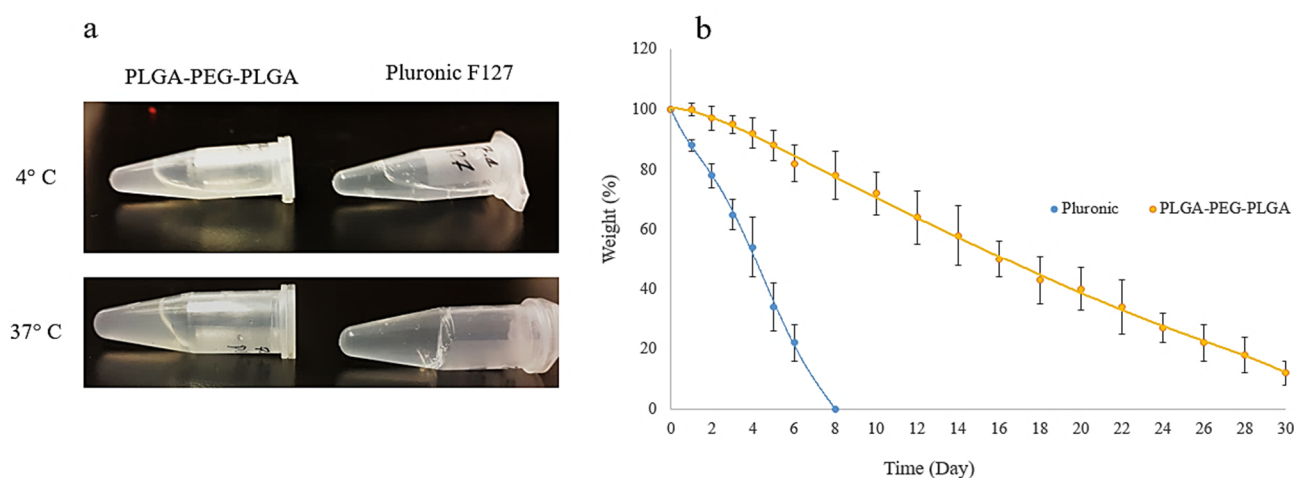


Fig. 4.1. (a) hydrogel appearances at 4°C and 37°C (20 %wt solution in D.I water); (b) *in vitro* degradation profile as a function of incubation time in PBS (pH 7.4, 37°C).

The *in vitro* degradation patterns of the Pluronic and PLGA-PEG-PLGA hydrogels are shown in Fig. 4.1b. Pluronic hydrogel was totally degraded within a week, while PLGA-PEG-PLGA gel required one month (Fig. 4.1b). The release of salinomycin from the hydrogels was correlated with the gel degradation pattern. The Pluronic released all the encapsulated salinomycin within a week compared to  $36 \pm 4\%$  of the total drug that was released in the same period of time from the PLGA-PEG-PLGA hydrogel (Fig. 4.2). In terms of drug release kinetics, the calculated exponent  $n$  is consistent with an anomalous transport involving both Fickian diffusion and polymer chain relaxation for Pluronic, and also for PLGA-PEG-PLGA after 4 days (Table 4.2).

Generally, the lower degradation rate of PLGA-PEG-PLGA can be attributed to the intrinsically stronger intermolecular forces between the ester group in the core, compared to the ether group in the core of Pluronic [46]. In addition, it has been proposed that the PEG chains in the corona of the PLGA-PEG-PLGA micelles allow for a more condensed packing within the gel matrix and reduced dissolution of gel in aqueous media [44].

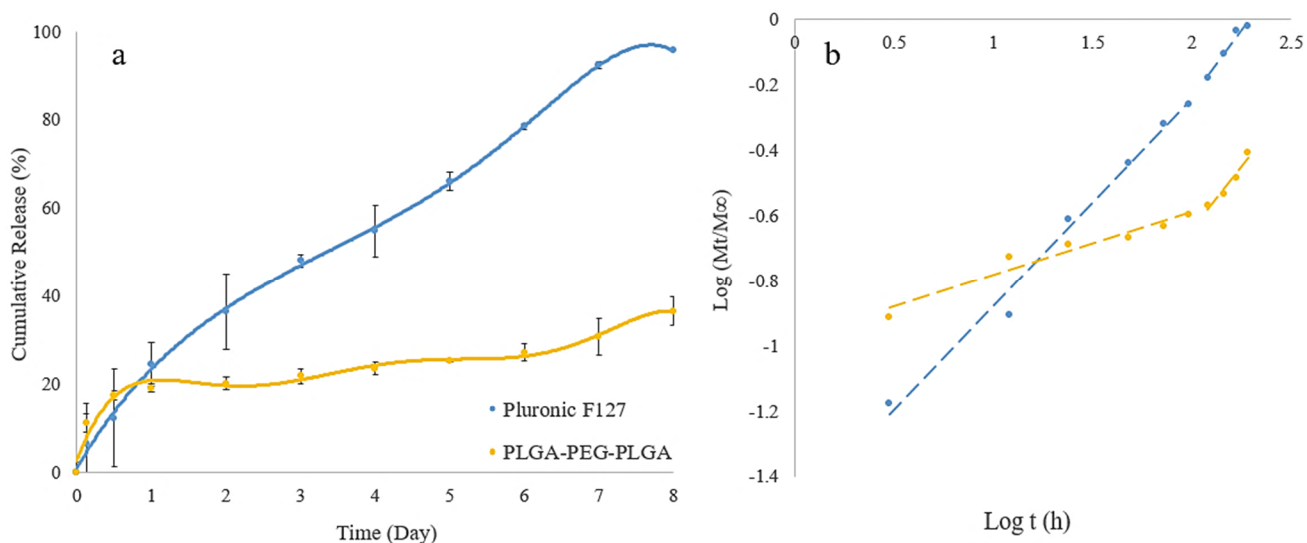


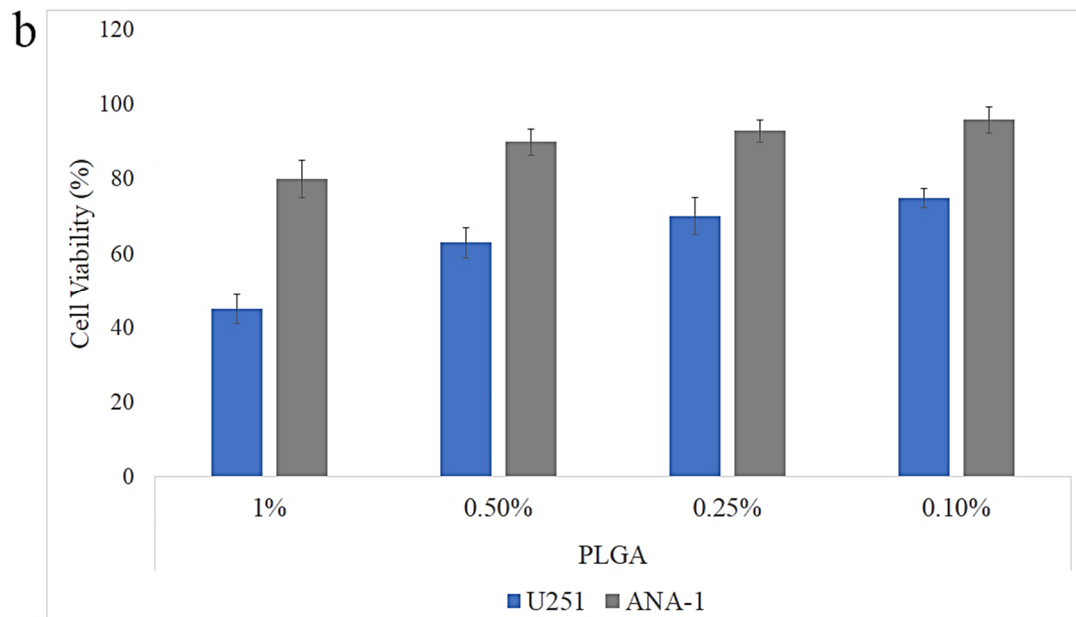
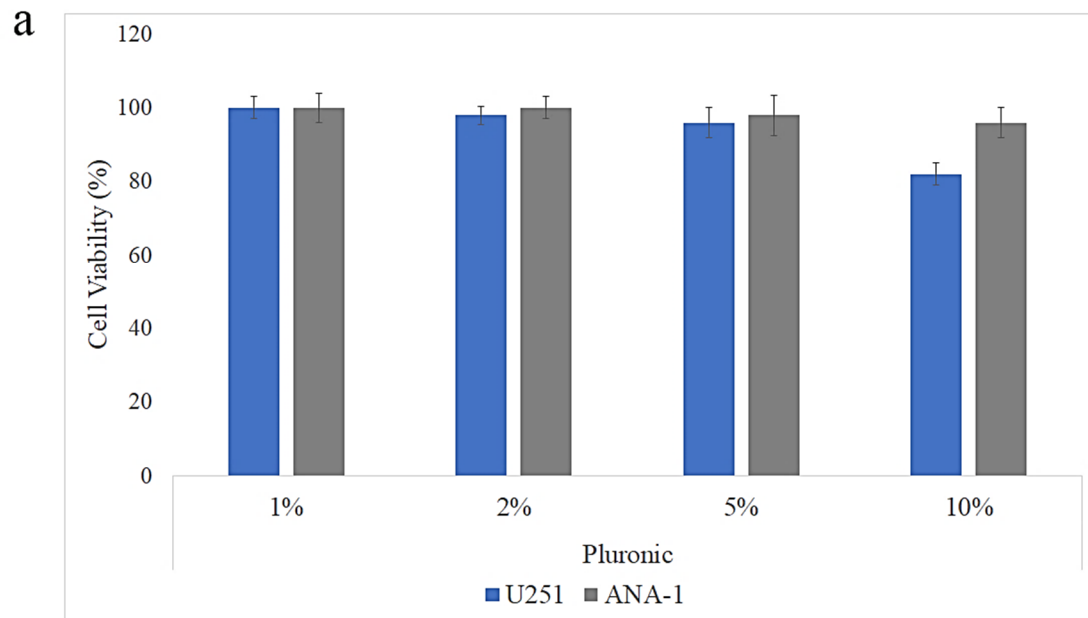
Fig. 4.2. (a) *in vitro* release profile of salinomycin from Pluronic and PLGA-PEG-PLGA at pH 7.4; (b) mechanistic analysis of salinomycin release according to Korsmeyer–Peppas equation.

Table 4.2. *n* and *k* values for salinomycin release from the hydrogels

	Time (day)	<i>n</i>	<i>k</i>	<i>R</i> <sup>2</sup>
<b>Pluronic</b>	0-4	0.63	0.03	0.99
	4-8	0.82	0.01	0.96
<b>PLGA-PEG-PLGA</b>	0-4	0.19	0.1	0.94
	4-8	0.77	0.006	0.94

### 4.3.2. Cytotoxicity of the drug-loaded hydrogels on GBM cells

Various concentrations of both hydrogels (prepared from 20 wt% hydrogels in D.I. water) were tested on both U251 GBM cells and ANA-1 macrophages to find the optimum concentrations without significant cytotoxicity (Fig. 4.3a,b). Although PLGA-PEG-PLGA showed some cytotoxicity in U251 cells (Fig. 4.3c), no cytotoxicity was observed with ANA-1 macrophages and therefore a final polymer concentration of 0.1% w/v was selected for examining salinomycin-hydrogel responses in GBM cells. Pluronic did not show any cytotoxicity alone in either ANA-1 or U251 cell lines and a final polymer concentration of 2% w/v was selected. The resulting cytotoxicity of the drug delivery systems and salinomycin on U251 cells are shown in Fig. 4.3. The salinomycin concentrations were chosen based on our previous study on GBM cells [47]. Salinomycin alone (1  $\mu\text{g}/\text{mL}$ ) reduced cell viability to  $42\pm 3\%$  while PLGA-PEG-PLGA and Pluronic containing the same concentration of salinomycin resulted in cell viabilities of  $16\pm 2\%$  and  $8\pm 4\%$ , respectively. Also, the CDI values for PLGA-PEG-PLGA and Pluronic containing salinomycin were calculated to be 0.52 and 0.20, respectively, indicative of a significant synergistic effect between salinomycin and both hydrogels. Likewise, in the apoptosis study, the cell viability decreased from 55% (24% late apoptosis, 12% necrosis) for free salinomycin to 9% (42% late apoptosis, 45% necrosis) for salinomycin-loaded Pluronic (Fig. 4.4). In addition, both salinomycin and the salinomycin-loaded hydrogels were found to be effective in reducing U251 cell proliferation by over 80% (Fig. 4.5). Similarly, the inhibitory effect of salinomycin on proliferation of various cancer cells such as hepatocellular carcinoma cells [48] and gastric cancer stem cells [49] has been reported.



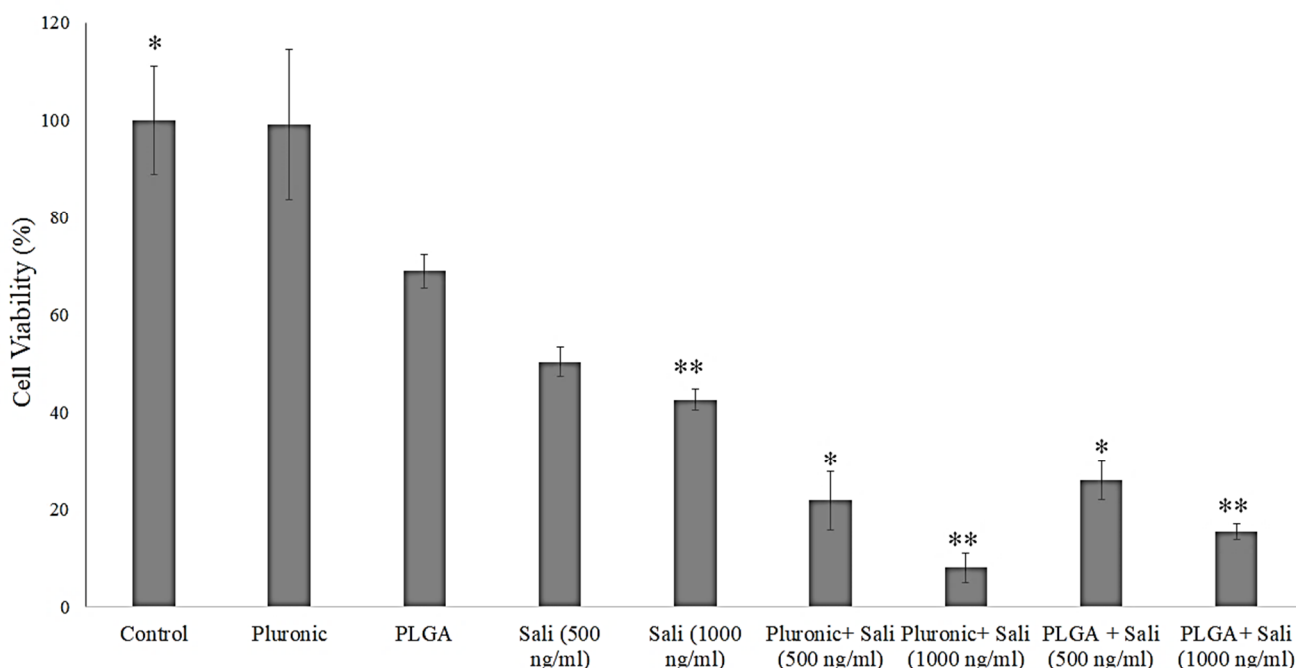
**c**

Fig. 4.3. Biocompatibility of Pluronic (a) and PLGA-PEG-PLGA (b) on U251 GBM, and ANA-1 macrophage cell lines. (c) cytotoxicity of salinomycin and hydrogels containing salinomycin on U251 cells after 48 h. Sali: salinomycin and PLGA: PLGA-PEG-PLGA; significant differences were shown by \* (compared to control) and \*\* (compared to salinomycin 1  $\mu\text{g}/\text{mL}$ ) at  $p < 0.05$ . Sali represents salinomycin.

The enhanced cytotoxicity of salinomycin following formulation with Pluronic block copolymers observed in the current study is similar to the previous findings with other chemotherapeutic agents [50-52]. For example, enhanced cellular uptake and anti-cancer effect of doxorubicin with Pluronic has been reported both *in vitro* and *in vivo* [53-55], that can be attributed to the improved pharmacokinetic/biodistribution and enhanced drug uptake into the cell through either endocytosis of the drug-polymer micelle complex [55,56], or inhibition of drug efflux in cancer cells. On the other hand, upon dissociation of the micelles, the hydrophobic PPO chain of Pluronic incorporates into the plasma membrane resulting in decreased microviscosity and increased membrane fluidization that can increase toxicity to the drug [55,57]. Furthermore,

various Pluronic formulations have been reported to attenuate drug sequestration in cytoplasmic vesicles, thus favorably altering drug bioavailability within the cancer cells [55,58]. Similarly, PLGA-PEG-PLGA enhanced cytotoxicity of salinomycin in this study, which can be related to the enhanced stability of salinomycin. Such a phenomenon has previously been reported with topotecan where the fraction of the active lactone form of topotecan was found to increase by ca. 40% in the PLGA-PEG-PLGA hydrogel matrix, compared to that of the free drug in PBS [59].

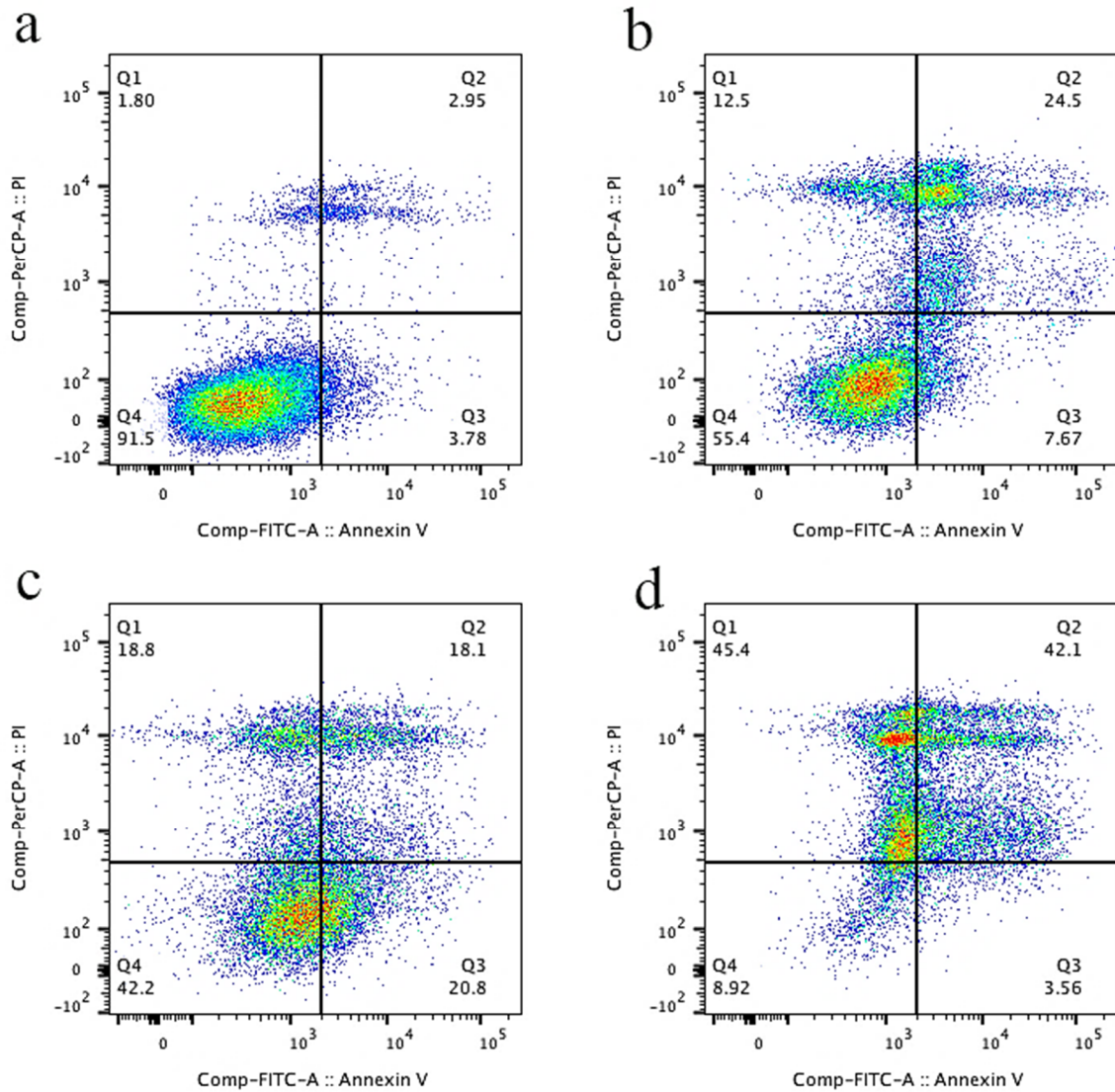


Fig. 4.4. Cell apoptosis/necrosis of treated U251 after 48 h, stained with Annexin V-FITC and PI. (a) Control, (b) salinomycin (c) PLGA-PEG-PLGA+salinomycin, and (d) Pluronic-salinomycin. Cell populations were sorted based on live (Q4), early apoptotic (Q3), late apoptotic (Q2) and necrotic cells (Q1).

Morphology of the cell was also studied by fluorescence microscopy as illustrated in Fig. 4.6. Untreated cells and cells treated with the hydrogel alone showed the typical cuboidal morphology of U251. However, salinomycin-treated cells displayed apoptotic morphological changes including cellular shrinkage and cytoskeletal damage [60]. In fact, the treated cells

exhibited shrunken morphology and spindle-like structure with notable changes in proliferation compared to control. A similar altered morphology has been reported with salinomycin in pancreatic and liver cancer cells where such changes were associated with mitochondria-dependent apoptosis [61-64].

#### 4.3.3. ROS generation

Salinomycin-mediated ROS generation is well-known as an important event leading to the apoptotic death of cancer cells [63]. Similarly, salinomycin's ability to trigger ROS generation in GBM cells in a concentration-dependent fashion has been reported [65]. In the present study, enhanced ROS following exposure to both free drug and salinomycin in hydrogel formulations was examined in the U251 glioblastoma cell line (Fig. 4.7). Consistent with the synergistic effect on cytotoxicity observed with Pluronic+salinomycin and PLGA-PEG-PLGA+salinomycin, both salinomycin hydrogel treatment groups were found to be more effective than free salinomycin in ROS generation in U251 cells. As ROS-mediated DNA damage was proposed as a *de facto* mechanism of salinomycin-induced cell growth inhibition in human glioma cells [66], the synergistic effects on ROS formation with the hydrogels could have therapeutic advantages.

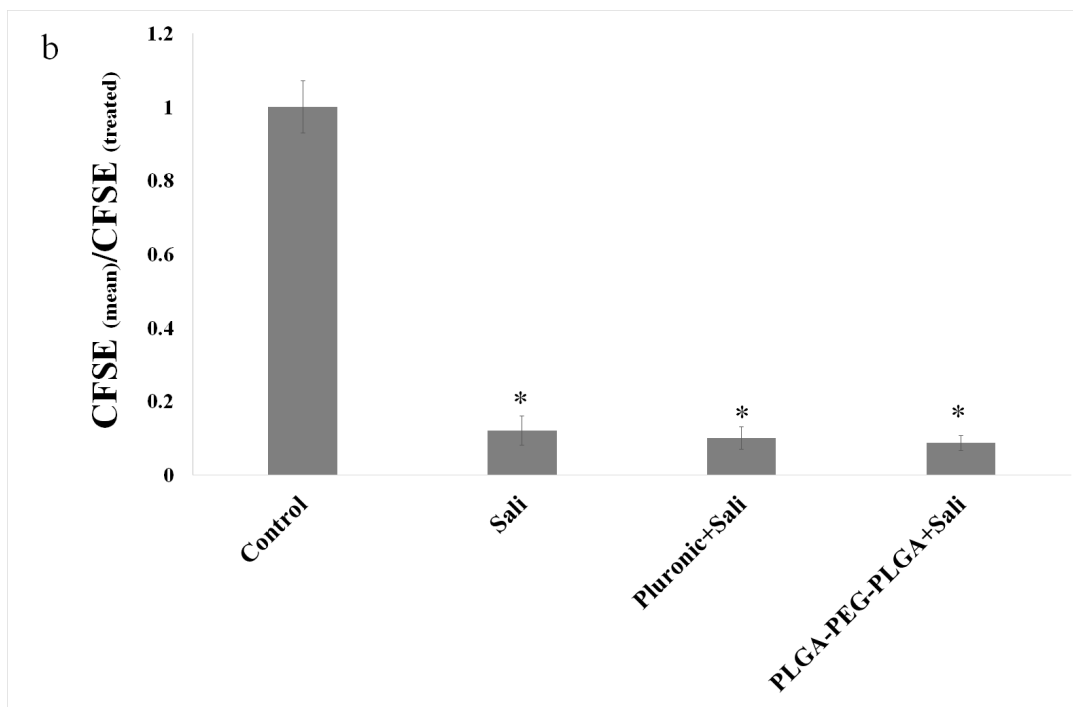
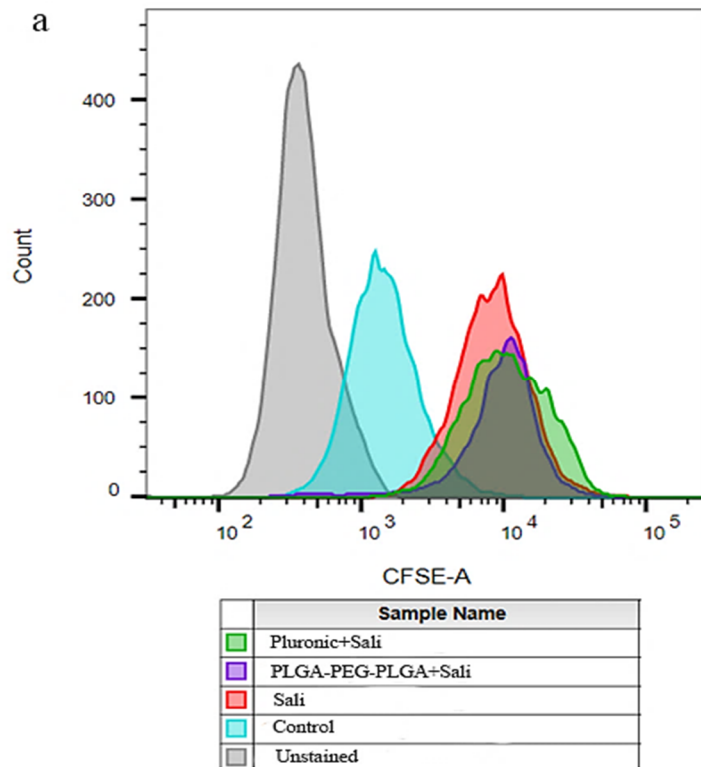


Fig. 4.5. Cell proliferation assay of CFSE-labelled U251 after 48 h treatment. (a) CFSE flow cytometry graph, and (b) the relative cell proliferation as calculated by the mean  $CFSE_{control}/mean CFSE_{treated}$ . \* indicates a significant difference compared to the control group at  $p < 0.05$ . Sali represents salinomycin.

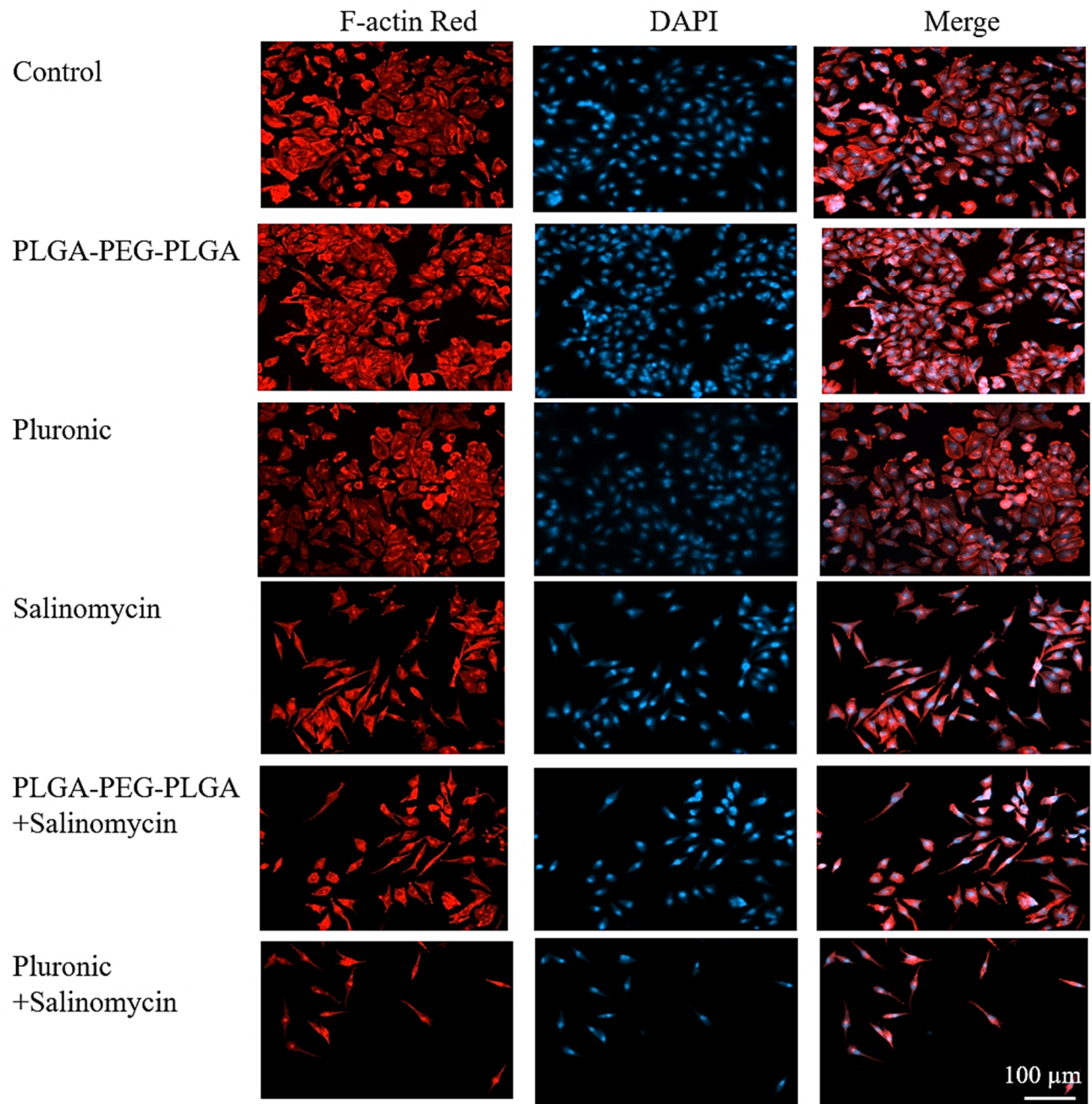


Fig. 4.6. Fluorescence microscopy images of U251 treated with salinomycin and the hydrogels containing salinomycin after 48 h. Red and blue fluorescence represents Alexa Fluor@ 488 phalloidin-stained F-actin and DAPI-stained cell nuclei, respectively.

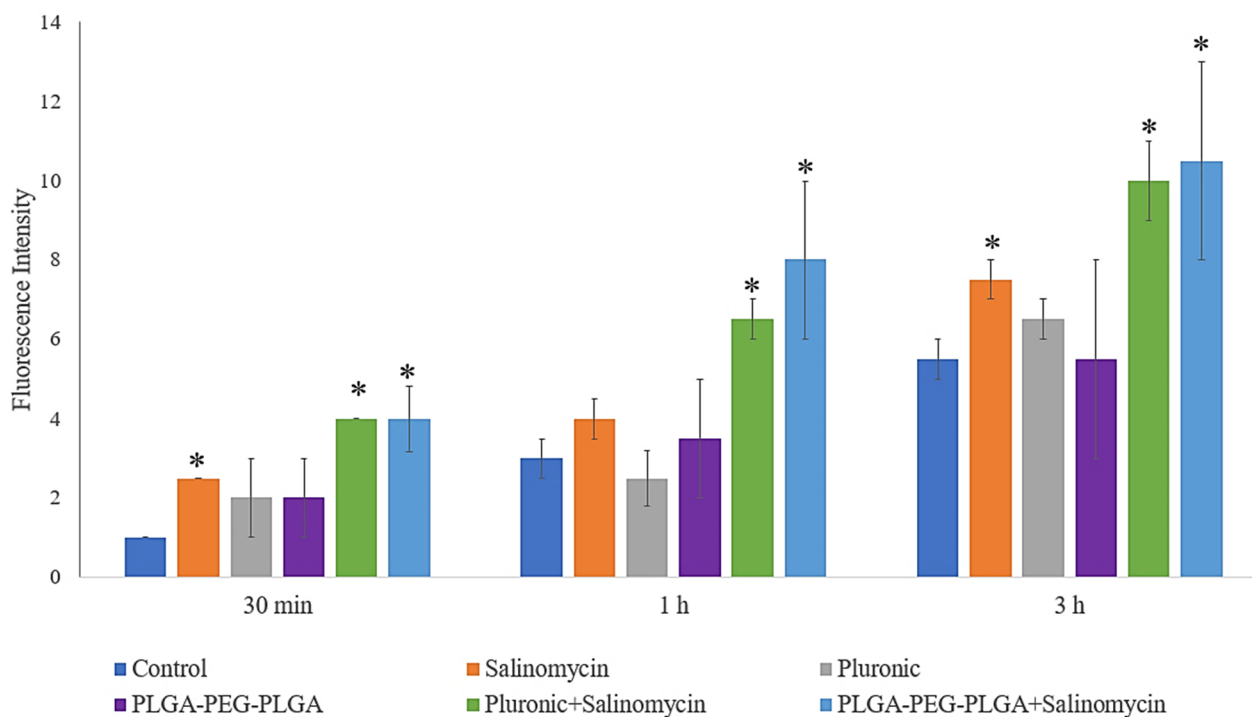


Fig. 4.7. ROS level in U251 treated with salinomycin and the hydrogels containing salinomycin at different timepoints. \* indicates significant compared to the control group at  $p < 0.05$ .

#### 4.3.4. Gene expression studies

To investigate the anti-cancer mechanisms of salinomycin and salinomycin-loaded hydrogels on U251, a series of genes was selected based on our previous *in vitro* studies [47] (Fig. 4.8). Apoptosis is a programmed cell death process involving the activation and release of selected regulatory molecules and cysteine-aspartic proteases, known collectively as caspases. The caspases are activated in a sequential manner, in which Caspase-1 and -9 are triggered first, followed by Caspase-3 which is critical in the apoptotic process [67,68]. Treatment of U251 cells with salinomycin, Pluronic+salinomycin and PLGA-PEG-PLGA+salinomycin upregulated Caspase-3 by 4-fold. The upregulation of Caspase-3 together with elevated intracellular ROS could account for the caspase-dependent apoptosis observed in U251 cells following salinomycin

treatment. A similar response to salinomycin has been reported previously with prostate cancer cells [69].

Bax is an apoptosis-promoting member of the Bcl-2 protein family, whose elevation can trigger mitochondrial-mediated apoptosis pathways as well as activation of Caspase-3 [70]. The results of the present study show that Pluronic+salinomycin significantly ( $p < 0.05$ ) increased the expression level of the pro-apoptotic protein Bax in U251. Interestingly neither salinomycin nor Pluronic alone produced significant changes in the Bax expression. However, the effect of salinomycin on upregulation of Bax in some cancer cells such as prostate [69], colorectal [71] and ovarian [72] cancer cells has been reported. Moreover, Minko et al., [50] reported that addition of Pluronic to doxorubicin could further upregulate Bax expression compared to doxorubicin alone in multidrug-resistant human breast cancer cells.

The retinoblastoma (Rb) family (Rb-1, Rb1, and Rb12), known as the tumor suppressors, are typically dysregulated in a variety of human cancer cells. The retinoblastoma family can inhibit cell cycle progression through disabling the E2F family of cell cycle-promoting transcription factors and suppress glutamine metabolism contributing to the tumor suppressor activity [73]. In this study, salinomycin-treatment significantly upregulated the gene expression of both Rb1 (by 2-fold), and Rb12 (by 13-fold). The highest Rb upregulation was observed in Pluronic+salinomycin treatment. However, as the gene study was conducted on the cells that survived from the 48-h treatment (i.e. approximately 50% and 8% of the total cell population that survived from free salinomycin and Pluronic+salinomycin treatments), no significant difference was observed in expression of Rb genes between the free salinomycin and the Pluronic+salinomycin treatments.

Wnt signaling plays an important role in malignant transformation and tumor progression in gliomas. In addition, silencing of Wnt expression in glioma cells leads to a decreased capacity for intracranial tumor formation *in vivo* [74,75]. As the results show, salinomycin-treatment reduced the expression of Wnt1 in human GBM cells. Reductions in Wnt signaling has been reported in leukemia cells [76], breast cancer cells [77] and gastric cancer stem cells [49].

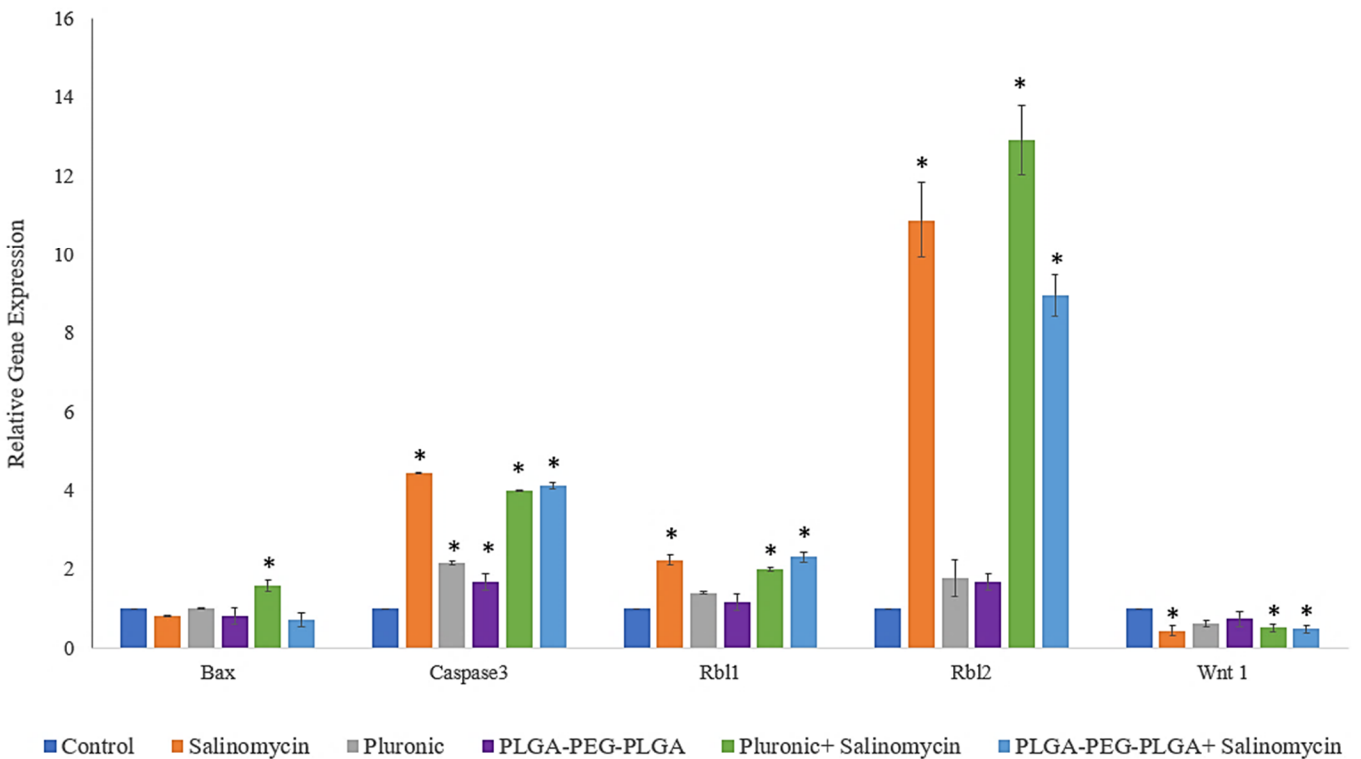


Fig. 4.8. Relative gene expression of U251 cell treated with salinomycin and the hydrogels containing salinomycin after 48 h. \* indicates a significant difference compared to the control group at  $p < 0.05$ .

#### 4.3.5. Tumor growth inhibition in GBM xenograft model

Based on the extent of salinomycin release from the Pluronic hydrogel, the higher biocompatibility of Pluronic *per se* on various cell lines and the robust synergistic anti-cancer effect observed with salinomycin in U251 glioblastoma cells, the Pluronic+salinomycin hydrogels were selected for further study in subcutaneous U251 tumor-bearing nude mice. Subcutaneous tumor models have been commonly used to assess local drug delivery systems and provide initial proof-of-concept for the intended clinical applications [78,79]. Tumor volume increased rapidly during the 12-day treatment period in the control (PBS) group, with over 6-fold increase in size observed over the time of treatment (Fig. 4.9a). A similar rapid growth of tumor was observed in the Pluronic treatment group. Mice receiving salinomycin alone showed only a minor reduction in tumor growth rate compared to the control group (Fig. 4.9a). In contrast, the Pluronic+salinomycin hydrogel treatment group showed significant reductions in tumor growth compared to both the PBS (5-fold at day 12,  $p < 0.05$ ) and salinomycin (ca. 4-fold at day 12,  $p < 0.05$ ) groups (Fig. 4.9a). It also should be noted that none of the treatments caused significant changes in body weight (Fig. 4.9b). The images of the H&E stained tumor tissues also showed few lymphocytes and the absence of eosinophils & neutrophils (Fig. 4.10), suggesting inflammation from the drug and/or the hydrogel treatments were minimal. Moreover, pathological assessment of the tumor tissue showed reduced mitosis in the Pluronic+salinomycin treated mice compared to the other treatment groups (Fig. 4.10).

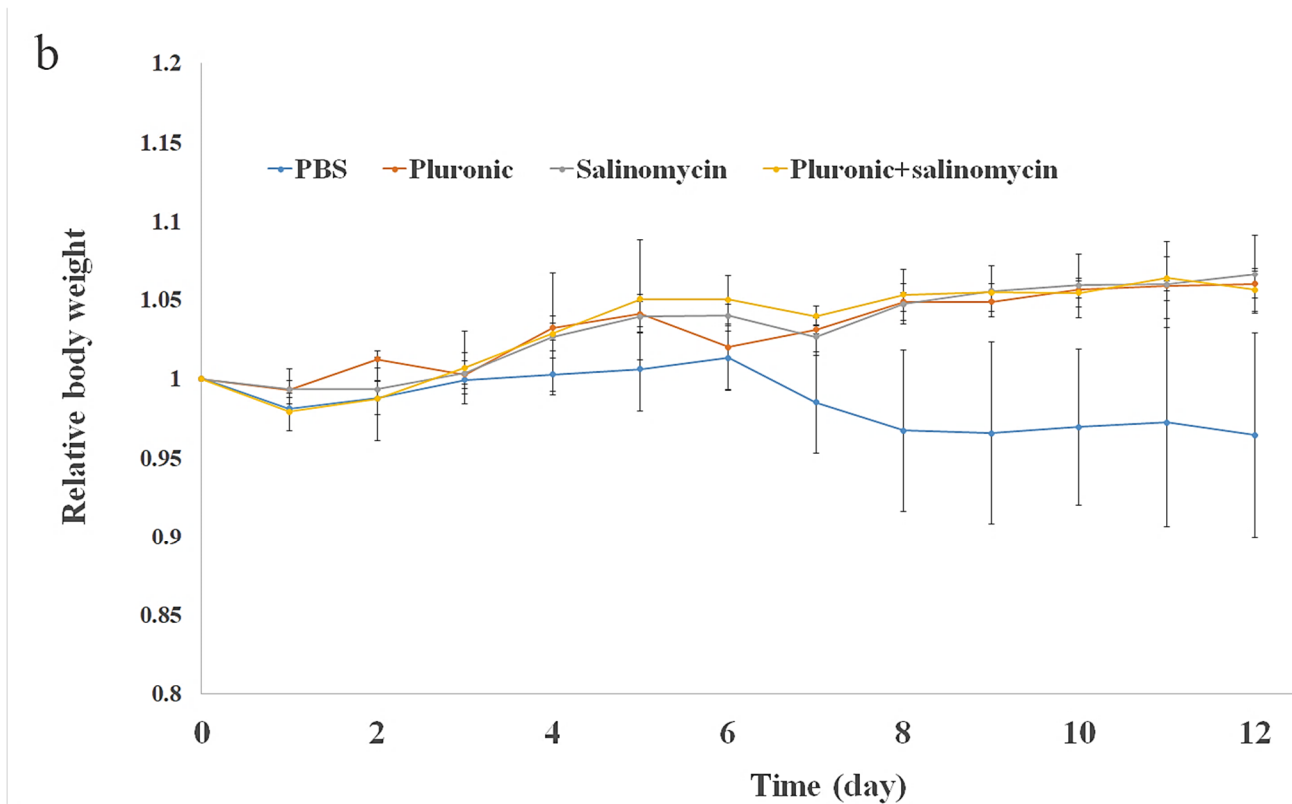
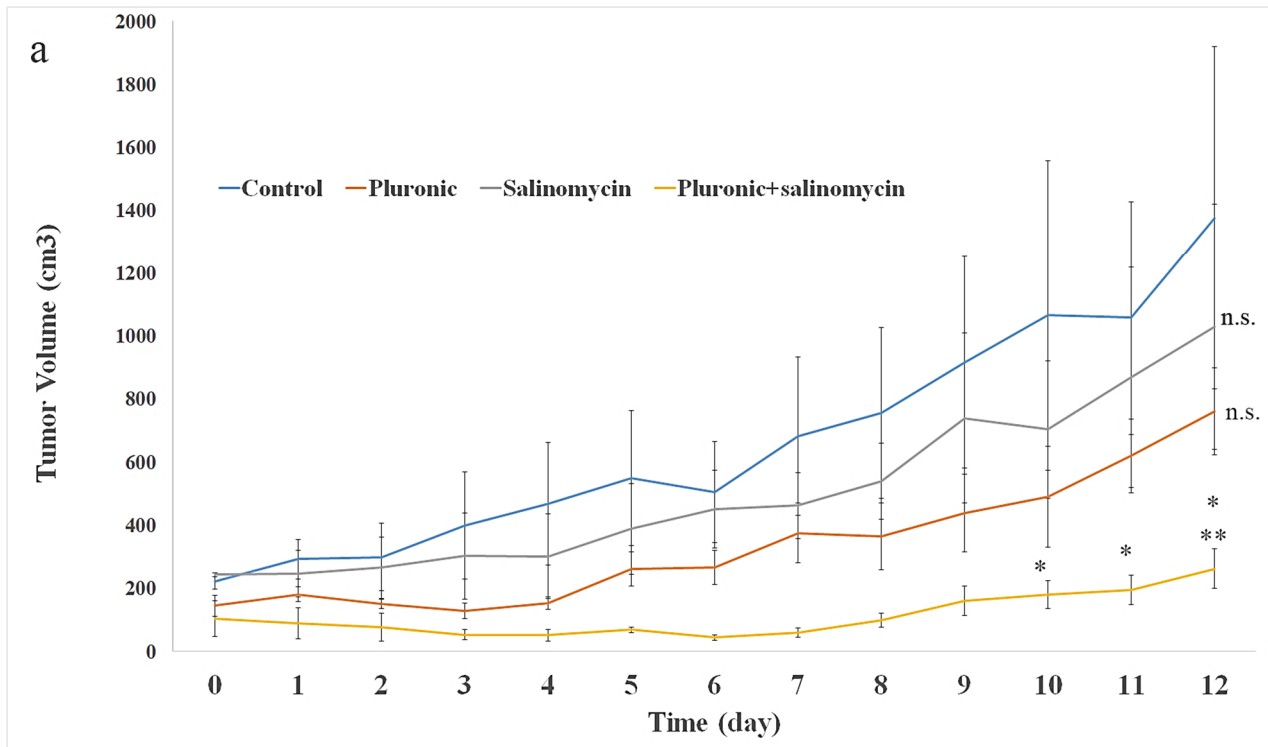


Fig. 4.9. (a) Tumor volumes of subcutaneous U251 xenografted nude mice treated with PBS, Pluronic, salinomycin, and Pluronic+salinomycin for 12 days. \* and \*\* indicate a significant difference compared to the control and salinomycin groups, respectively at  $p < 0.05$ , and n.s. means not significant compared to control. The data were reported as the mean $\pm$ standard error. (b) relative body weight of mice received different treatments.

Given the dose (20  $\mu$ g/kg) of salinomycin selected for these studies and the anticipated short residence time for the drug at the tumor site, substantial reductions in tumor growth following treatment with drug alone were not expected. Indeed, previous studies examining the effects of intraperitoneal (i.p.) injections of salinomycin in mice bearing U251 subcutaneous tumors reported much higher systemic doses of the drug were required to reduce tumor growth [80,81]. Studies by Clazolari and colleagues [80], reported no improvement in U251 tumor progression following i.p. injections of 200 ng/kg salinomycin every three days. However, daily i.p. injections of salinomycin (5 mg/kg), were reported to cause significant shrinkage of U251 subcutaneous tumors [81]. These studies highlight the challenges facing the use of salinomycin systemically that requires exposure to high doses of the drug and potentially adverse systemic effects.

In this study, while the drug alone was not effective in reducing tumor growth, the Pluronic+salinomycin treatment group had a dramatic inhibitory impact on tumor progression. The significant reduction in the tumor size can be ascribed to the sustained release of salinomycin from the Pluronic hydrogel and the resulting enhanced exposure to the drug within the tumor site. Given the synergistic effects of Pluronic and salinomycin observed *in vitro*, there may also be pharmacodynamic as well as pharmacokinetic advantages in the Pluronic hydrogel formulations. The findings of the current study suggest an injectable Pluronic+salinomycin hydrogel could have potential applications in the treatment of GBM. The advantages include providing for sustained release of therapeutically relevant concentrations of salinomycin within the tumor site, while

overcoming the BBB limitations for effective drug delivery into the brain. While subsequent intracranial tumor studies of the Pluronic+salinomycin hydrogel are required, the present study provides important proof-of-concept for the use of salinomycin and Pluronic hydrogels for local treatment of brain tumors.

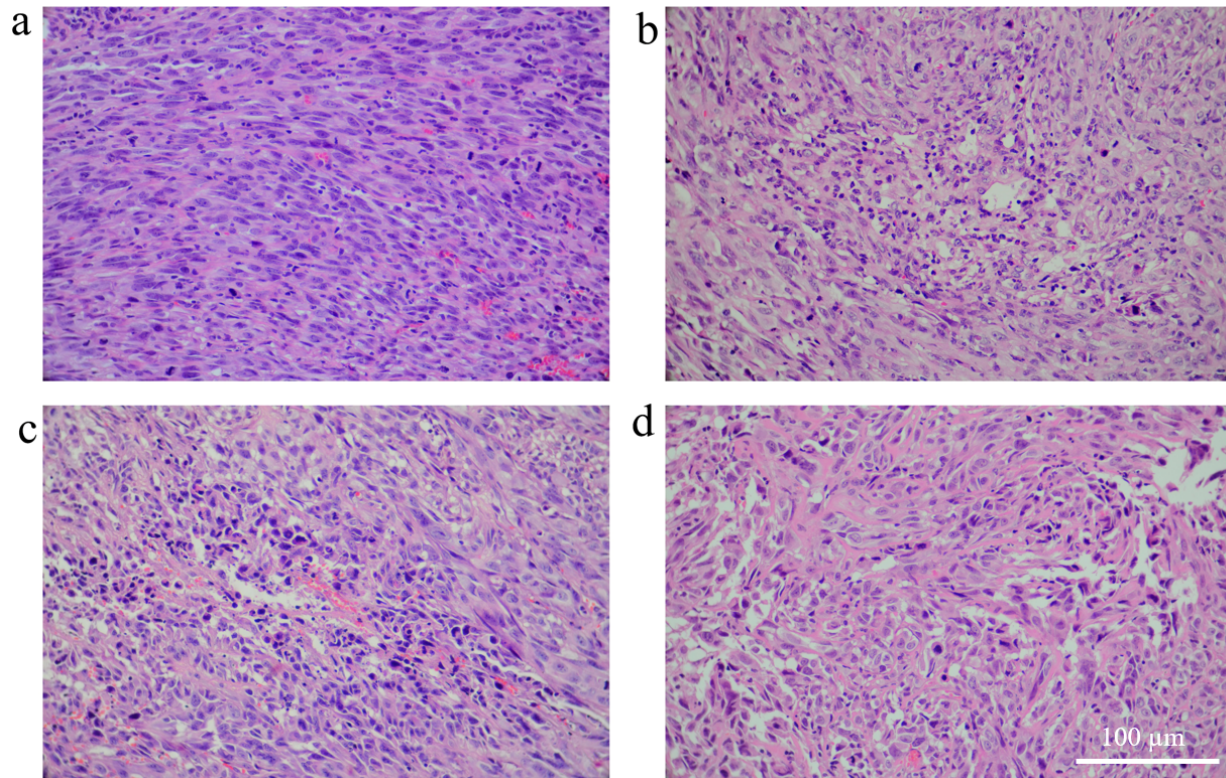


Fig. 4.10. Images of H&E stained-tumor tissues of mice received (a) PBS, (b) Pluronic, (c) salinomycin, and (d) Pluronic-salinomycin, 12 days post-treatment.

#### 4.4. Conclusion

In this study, two salinomycin-loaded thermosensitive injectable hydrogels were examined as drug delivery systems for local chemotherapy of GBM. Pluronic showed a faster degradation rate than PLGA-PEG-PLGA *in vitro*, with complete release of salinomycin from Pluronic hydrogel within a one-week period compared to ca. 35% drug release from the PLGA-PEG-PLGA over the same period of time. The difference in drug release was attributed to the stronger intermolecular forces between the ester group in the PLGA core, compared to the ether group in the core of Pluronic, as well as the role of PEG in stabilizing the micellar structure. Cytotoxicity studies revealed that both salinomycin-loaded hydrogels were more effective than free salinomycin to induce apoptosis and generate intracellular ROS, which can be attributed to the improved drug's bioavailability and modified microviscosity of the plasma membrane. Moreover, gene studies showed upregulation of Caspase-3 and tumor suppressors i.e. Rb1 and Rb2, while downregulation of Wnt1 in GBM cells treated with salinomycin-loaded hydrogels. In the comparative study, Pluronic was determined to provide a better hydrogel platform for local delivery of salinomycin compared to PLGA-PEG-PLGA due to the desired drug release profile, superior substrate's biocompatibility and greater anti-cancer synergistic effect. Animal studies in subcutaneous U251 xenografted nude mice showed reduced tumor growth in the Pluronic+salinomycin-treated group compared to either PBS or free salinomycin-treated mice. This superior anti-tumor activity of the Pluronic+salinomycin can be attributed to the sustained release of salinomycin from the hydrogel at the tumor site, while preventing the drug from enzymatic degradation and enhancing its bioavailability. The results indicate a potential application of Pluronic+salinomycin as an injectable drug delivery system for local chemotherapy

of brain tumors, while bypassing the BBB and providing a sustained release as well as a therapeutic concentration of salinomycin at the tumor site.

## 4.5. References

- 1 Hathout, L. et al. (2016) Modeling the efficacy of the extent of surgical resection in the setting of radiation therapy for glioblastoma. *Cancer science* 107 (8), 1110-1116
- 2 Shi, W. et al. (2018) Investigating the Effect of Reirradiation or Systemic Therapy in Patients With Glioblastoma After Tumor Progression: A Secondary Analysis of NRG Oncology/Radiation Therapy Oncology Group Trial 0525. *International Journal of Radiation Oncology\* Biology\* Physics* 100 (1), 38-44
- 3 Grauwet, K. and Chiocca, E.A. (2016) Glioma and microglia, a double entendre. *Nature immunology* 17 (11), 1240
- 4 Kenny, G.D. et al. (2013) Multifunctional receptor-targeted nanocomplexes for the delivery of therapeutic nucleic acids to the brain. *Biomaterials* 34 (36), 9190-9200
- 5 Norouzi, M. (2018) Recent advances in brain tumor therapy: application of electrospun nanofibers. *Drug discovery today*
- 6 Norouzi, M. et al. (2016) Injectable hydrogel-based drug delivery systems for local cancer therapy. *Drug discovery today*
- 7 Norouzi, M. et al. (2016) Injectable hydrogel-based drug delivery systems for local cancer therapy. *Drug discovery today* 21 (11), 1835-1849
- 8 Norouzi, M. et al. (2017) Electrospun-based systems in cancer therapy. In *Electrospun Materials for Tissue Engineering and Biomedical Applications*, pp. 337-356, Elsevier
- 9 Wolinsky, J.B. et al. (2012) Local drug delivery strategies for cancer treatment: gels, nanoparticles, polymeric films, rods, and wafers. *Journal of Controlled Release* 159 (1), 14-26
- 10 Norouzi, M. et al. (2015) PLGA/gelatin hybrid nanofibrous scaffolds encapsulating EGF for skin regeneration. *Journal of biomedical materials research Part A* 103 (7), 2225-2235
- 11 Norouzi, M. et al. (2015) Advances in Skin Regeneration: Application of Electrospun Scaffolds. *Advanced Healthcare Materials* 4 (8), 1114-1133
- 12 Turabee, M.H. et al. (2018) A pH-and temperature-responsive bioresorbable injectable hydrogel based on polypeptide block copolymers for the sustained delivery of proteins in vivo. *Biomaterials science* 6 (3), 661-671
- 13 Phan, V.G. et al. (2017) Temperature and pH-sensitive injectable hydrogels based on poly (sulfamethazine carbonate urethane) for sustained delivery of cationic proteins. *Polymer* 109, 38-48
- 14 Nguyen, M.K. and Lee, D.S. (2010) Injectable biodegradable hydrogels. *Macromolecular bioscience* 10 (6), 563-579
- 15 Elias, P.Z. et al. (2015) A functionalized, injectable hydrogel for localized drug delivery with tunable thermosensitivity: Synthesis and characterization of physical and toxicological properties. *Journal of Controlled Release* 208, 76-84
- 16 Mano, J.F. (2008) Stimuli-responsive polymeric systems for biomedical applications. *Advanced Engineering Materials* 10 (6), 515-527
- 17 Nagahama, K. et al. (2015) Self-assembling polymer micelle/clay nanodisk/doxorubicin hybrid injectable gels for safe and efficient focal treatment of cancer. *Biomacromolecules* 16 (3), 880-889
- 18 Chen, Y.-Y. et al. (2013) Injectable and thermoresponsive self-assembled nanocomposite hydrogel for long-term anticancer drug delivery. *Langmuir* 29 (11), 3721-3729

- 19 Zhang, N. et al. (2016) Nanocomposite hydrogel incorporating gold nanorods and paclitaxel-loaded chitosan micelles for combination photothermal–chemotherapy. *International journal of pharmaceutics* 497 (1), 210-221
- 20 Lei, N. et al. (2012) Therapeutic application of injectable thermosensitive hydrogel in preventing local breast cancer recurrence and improving incision wound healing in a mouse model. *Nanoscale* 4 (18), 5686-5693
- 21 Mao, Y. et al. (2016) Thermosensitive Hydrogel System with Paclitaxel Liposomes Used in Localized Drug Delivery System for In Situ Treatment of Tumor: Better Antitumor Efficacy and Lower Toxicity. *Journal of pharmaceutical sciences* 105 (1), 194-204
- 22 Wang, Y. et al. (2010) 5-FU-hydrogel inhibits colorectal peritoneal carcinomatosis and tumor growth in mice. *BMC cancer* 10, 402-2407-2410-2402
- 23 Seo, H.W. et al. (2013) Injectable intratumoral hydrogel as 5-fluorouracil drug depot. *Biomaterials* 34 (11), 2748-2757
- 24 Valtonen, S. et al. (1997) Interstitial chemotherapy with carmustine-loaded polymers for high-grade gliomas: a randomized double-blind study. *Neurosurgery* 41 (1), 44-49
- 25 Naujokat, C. and Steinhart, R. (2012) Salinomycin as a drug for targeting human cancer stem cells. *BioMed Research International* 2012
- 26 Jangamreddy, J.R. et al. (2013) Salinomycin induces activation of autophagy, mitophagy and affects mitochondrial polarity: differences between primary and cancer cells. *Biochimica et Biophysica Acta (BBA)-Molecular Cell Research* 1833 (9), 2057-2069
- 27 Gupta, P.B. et al. (2009) Identification of selective inhibitors of cancer stem cells by high-throughput screening. *Cell* 138 (4), 645-659
- 28 Huczynski, A. (2012) Salinomycin—a new cancer drug candidate. *Chemical biology & drug design* 79 (3), 235-238
- 29 Lagas, J.S. et al. (2008) P-glycoprotein limits oral availability, brain penetration, and toxicity of an anionic drug, the antibiotic salinomycin. *Antimicrobial agents and chemotherapy* 52 (3), 1034-1039
- 30 Urquhart, B.L. and Kim, R.B. (2009) Blood– brain barrier transporters and response to CNS-active drugs. *European journal of clinical pharmacology* 65 (11), 1063
- 31 Wu, Z.M. et al. (2009) Disulfide-crosslinked chitosan hydrogel for cell viability and controlled protein release. *European Journal of Pharmaceutical Sciences* 37 (3), 198-206
- 32 Siepmann, J. and Peppas, N.A. (2001) Modeling of drug release from delivery systems based on hydroxypropyl methylcellulose (HPMC). *Advanced Drug Delivery Reviews* 48 (2), 139-157
- 33 Jin, J.-I. et al. (2011) PTD4-apoptin protein and dacarbazine show a synergistic antitumor effect on B16-F1 melanoma in vitro and in vivo. *European journal of pharmacology* 654 (1), 17-25
- 34 Kaech, S.M. and Ahmed, R. (2001) Memory CD8+ T cell differentiation: initial antigen encounter triggers a developmental program in naive cells. *Nature immunology* 2 (5), 415
- 35 Dubey, P. and Gopinath, P. (2016) Fabrication of electrospun poly (ethylene oxide)–poly (caprolactone) composite nanofibers for co-delivery of niclosamide and silver nanoparticles exhibits enhanced anti-cancer effects in vitro. *Journal of Materials Chemistry B* 4 (4), 726-742
- 36 Lee, J.-Y. et al. (2017) Chemosensitizing indomethacin-conjugated chitosan oligosaccharide nanoparticles for tumor-targeted drug delivery. *Acta biomaterialia* 57, 262-273
- 37 Huang, P. et al. (2016) Zwitterionic nanoparticles constructed from bioreducible RAFT–ROP double head agent for shell shedding triggered intracellular drug delivery. *Acta biomaterialia* 40, 263-272
- 38 Zhang, T. et al. (2019) Multitargeted Nanoparticles Deliver Synergistic Drugs across the Blood–Brain Barrier to Brain Metastases of Triple Negative Breast Cancer Cells and Tumor-Associated Macrophages. *Advanced healthcare materials*, 1900543
- 39 Barreiro-Iglesias, R. et al. (2004) Solubilization and stabilization of camptothecin in micellar solutions of pluronic-g-poly (acrylic acid) copolymers. *Journal of controlled release* 97 (3), 537-549

- 40 Dumortier, G. et al. (2006) A review of poloxamer 407 pharmaceutical and pharmacological characteristics. *Pharmaceutical research* 23 (12), 2709-2728
- 41 Lin, Z. et al. (2014) Novel thermo-sensitive hydrogel system with paclitaxel nanocrystals: High drug-loading, sustained drug release and extended local retention guaranteeing better efficacy and lower toxicity. *Journal of Controlled Release* 174, 161-170
- 42 Song, Z. et al. (2011) Curcumin-loaded PLGA-PEG-PLGA triblock copolymeric micelles: Preparation, pharmacokinetics and distribution in vivo. *Journal of colloid and interface science* 354 (1), 116-123
- 43 Yu, L. et al. (2006) A Subtle End-Group Effect on Macroscopic Physical Gelation of Triblock Copolymer Aqueous Solutions. *Angewandte Chemie International Edition* 45 (14), 2232-2235
- 44 Jeong, B. et al. (1999) Thermoreversible gelation of PEG- PLGA- PEG triblock copolymer aqueous solutions. *Macromolecules* 32 (21), 7064-7069
- 45 Yu, L. and Ding, J. (2008) Injectable hydrogels as unique biomedical materials. *Chemical Society Reviews* 37 (8), 1473-1481
- 46 Jeong, B. et al. (2000) In situ gelation of PEG-PLGA-PEG triblock copolymer aqueous solutions and degradation thereof. *Journal of Biomedical Materials Research Part A* 50 (2), 171-177
- 47 Norouzi, M. et al. (2018) Salinomycin-loaded Nanofibers for Glioblastoma Therapy. *Scientific reports* 8 (1), 9377
- 48 Wang, F. et al. (2012) Salinomycin inhibits proliferation and induces apoptosis of human hepatocellular carcinoma cells in vitro and in vivo. *PLoS one* 7 (12), e50638
- 49 Mao, J. et al. (2014) Roles of Wnt/beta-catenin signaling in the gastric cancer stem cells proliferation and salinomycin treatment. *Cell death & disease* 5, e1039
- 50 Minko, T. et al. (2005) Pluronic block copolymers alter apoptotic signal transduction of doxorubicin in drug-resistant cancer cells. *Journal of Controlled Release* 105 (3), 269-278
- 51 Batrakova, E.V. et al. (2006) Alteration of genomic responses to doxorubicin and prevention of MDR in breast cancer cells by a polymer excipient: pluronic P85. *Molecular pharmaceutics* 3 (2), 113-123
- 52 Kabanov, A.V. et al. (2002) Pluronic® block copolymers for overcoming drug resistance in cancer. *Advanced Drug Delivery Reviews* 54 (5), 759-779
- 53 Alakhov, V. et al. (1999) Block copolymer-based formulation of doxorubicin. From cell screen to clinical trials. *Colloids and Surfaces B: Biointerfaces* 16 (1), 113-134
- 54 Rapoport, N.Y. et al. (2004) Ultrasound-triggered drug targeting of tumors in vitro and in vivo. *Ultrasonics* 42 (1), 943-950
- 55 Batrakova, E.V. and Kabanov, A.V. (2008) Pluronic block copolymers: evolution of drug delivery concept from inert nanocarriers to biological response modifiers. *Journal of Controlled Release* 130 (2), 98-106
- 56 Muniruzzaman, M. et al. (2002) Intracellular uptake of Pluronic copolymer: effects of the aggregation state. *Colloids and Surfaces B: Biointerfaces* 25 (3), 233-241
- 57 Pitto-Barry, A. and Barry, N.P. (2014) Pluronic® block-copolymers in medicine: from chemical and biological versatility to rationalisation and clinical advances. *Polymer Chemistry* 5 (10), 3291-3297
- 58 Batrakova, E.V. et al. (2010) Effects of pluronic and doxorubicin on drug uptake, cellular metabolism, apoptosis and tumor inhibition in animal models of MDR cancers. *Journal of controlled release* 143 (3), 290-301
- 59 Chang, G. et al. (2011) Enhancement of the fraction of the active form of an antitumor drug topotecan via an injectable hydrogel. *Journal of Controlled Release* 156 (1), 21-27
- 60 Prasad, N.K. et al. (2007) Mechanism of cell death induced by magnetic hyperthermia with nanoparticles of  $\gamma$ -Mn x Fe 2-x O 3 synthesized by a single step process. *Journal of Materials Chemistry* 17 (48), 5042-5051

- 61 Zhang, X.-F. and Gurunathan, S. (2016) Combination of salinomycin and silver nanoparticles enhances apoptosis and autophagy in human ovarian cancer cells: an effective anticancer therapy. *International journal of nanomedicine* 11, 3655
- 62 Zhang, Y. et al. (2017) Salinomycin Exerts Anticancer Effects on PC-3 Cells and PC-3-Derived Cancer Stem Cells In Vitro and In Vivo. *BioMed Research International* 2017
- 63 Roulston, G.D. et al. (2016) Low-dose salinomycin induces anti-leukemic responses in AML and MLL. *Oncotarget* 7 (45), 73448-73461
- 64 Schenk, M. et al. (2015) Salinomycin inhibits growth of pancreatic cancer and cancer cell migration by disruption of actin stress fiber integrity. *Cancer letters* 358 (2), 161-169
- 65 Xipell, E. et al. (2016) Salinomycin induced ROS results in abortive autophagy and leads to regulated necrosis in glioblastoma. *Oncotarget* 7 (21), 30626-30641
- 66 Zhao, S.-J. et al. (2017) Induction of G1 Cell Cycle Arrest in Human Glioma Cells by Salinomycin Through Triggering ROS-Mediated DNA Damage In Vitro and In Vivo. *Neurochemical research* 42 (4), 997-1005
- 67 Wang, Q.-F. et al. (2002) Regulation of Bcl-2 family molecules and activation of caspase cascade involved in gypenosides-induced apoptosis in human hepatoma cells. *Cancer letters* 183 (2), 169-178
- 68 Boehmerle, W. and Endres, M. (2011) Salinomycin induces calpain and cytochrome c-mediated neuronal cell death. *Cell death & disease* 2, e168
- 69 Kim, K.-Y. et al. (2011) Salinomycin-induced apoptosis of human prostate cancer cells due to accumulated reactive oxygen species and mitochondrial membrane depolarization. *Biochemical and biophysical research communications* 413 (1), 80-86
- 70 Zhao, H. et al. (2015) Bufalin promotes apoptosis of gastric cancer by down-regulation of miR-298 targeting bax. *International journal of clinical and experimental medicine* 8 (3), 3420-3428
- 71 Zhou, J. et al. (2013) Salinomycin induces apoptosis in cisplatin-resistant colorectal cancer cells by accumulation of reactive oxygen species. *Toxicology letters* 222 (2), 139-145
- 72 Kaplan, F. and Teksen, F. (2016) Apoptotic effects of salinomycin on human ovarian cancer cell line (OVCAR-3). *Tumor Biology* 37 (3), 3897-3903
- 73 Reynolds, M.R. et al. (2014) Control of glutamine metabolism by the tumor suppressor Rb. *Oncogene* 33 (5), 556-566
- 74 Kaur, N. et al. (2013) Wnt3a mediated activation of Wnt/ $\beta$ -catenin signaling promotes tumor progression in glioblastoma. *Molecular and Cellular Neuroscience* 54, 44-57
- 75 Rampazzo, E. et al. (2013) Wnt activation promotes neuronal differentiation of glioblastoma. *Cell death & disease* 4, e500
- 76 Lu, D. et al. (2011) Salinomycin inhibits Wnt signaling and selectively induces apoptosis in chronic lymphocytic leukemia cells. *Proceedings of the National Academy of Sciences of the United States of America* 108 (32), 13253-13257
- 77 King, T.D. et al. (2012) The wnt/ $\beta$ -catenin signaling pathway: A potential therapeutic target in the treatment of triple negative breast cancer. *Journal of cellular biochemistry* 113 (1), 13-18
- 78 Fourniols, T. et al. (2015) Temozolomide-loaded photopolymerizable PEG-DMA-based hydrogel for the treatment of glioblastoma. *Journal of Controlled Release* 210, 95-104
- 79 Bastiancich, C. et al. (2016) Lauroyl-gemcitabine-loaded lipid nanocapsule hydrogel for the treatment of glioblastoma. *Journal of controlled release* 225, 283-293
- 80 Calzolari, A. et al. (2014) Salinomycin potentiates the cytotoxic effects of TRAIL on glioblastoma cell lines. *PloS one* 9 (4), e94438
- 81 Qin, L.-s. et al. (2015) ROS-p53-cyclophilin-D signaling mediates salinomycin-induced glioma cell necrosis. *Journal of Experimental & Clinical Cancer Research* 34 (1), 57

## **Chapter 5**

# **Conclusion and Future Directions**

## 5.1. Conclusion

The blood-brain barrier (BBB) limits the penetration of many therapeutic agents into the brain and is the main challenge for the development of effective chemotherapeutic regimens for malignant gliomas. In this context, TMZ is a single-agent chemotherapeutic that is currently indicated in glioma therapy, while it has not been found effective to eradicate cancer cells and the media survival of GBM patients receiving the current standard of care (TMZ plus radiotherapy) is limited to 14.6 months post-diagnosis. In this study, we selected two effective and more potent chemotherapeutics (i.e. doxorubicin, and salinomycin), whose pre-clinical indications are restricted for brain tumors *ipso facto* their inability to penetrate the BBB and low bioavailability in the brain. Nevertheless, not only are doxorubicin (IC<sub>50</sub>: 330 ng/mL), and salinomycin (IC<sub>50</sub>: 700 ng/mL) more potent than TMZ (IC<sub>50</sub>: 9600 ng/mL) in U251 GBM cells *in vitro*, but also they can be utilized in combination with temozolomide to show synergistic anti-cancer effects in GBM cells and sensitize them to TMZ [1-3]. Therefore, in this study, we developed various drug delivery systems to enable the delivery of Doxorubicin, and Salinomycin into the brain, while overcoming the limited permeability of the BBB.

In the first scenario, magnetic IONPs were developed as drug delivery systems of Doxorubicin, and Salinomycin. For this purpose, negatively charged EDT-IONP and positively charged PEI-PEG-IONP were developed as carriers of Doxorubicin, and Salinomycin, respectively. Both EDT-IONP and PEI-PEG-IONP at various concentrations (1-30 µg/mL) were found biocompatible in bEnd.3 and U251 cells, while both cell lines could efficiently take up the nanoparticles. The drug-loaded IONPs released their payload entirely over 4 days with the capability of an accelerated initial release at the acidic microenvironments. Both DOX-EDT-

IONPs and Sali-PEI-PEG-IONPs were found to be effective in causing apoptosis-induced cell death, proliferation inhibition, and ROS-induction in U251 cells. In fact, the DOX-EDT-IONPs and Sali-PEI-PEG-IONPs (with 1  $\mu\text{g}/\text{mL}$  of either DOX or Sali) were found to be effective in apoptotic-induced GBM cell death by approximately 80% and 100% within 48 hours of treatment. Moreover, DOX-EDT-IONPs augmented the DOX's uptake in U251 cells by  $2.2\pm 0.6$  (without an external magnetic field) and  $2.8\pm 0.5$ -fold (with an external magnetic field) compared to that of free DOX. To study the anti-cancer mechanisms of the developed formulations, gene studies were conducted that revealed an upregulation in Caspase 3 (key mediator of apoptosis), along with p53 and GAS5 (tumor suppressors), while a downregulation in TOP II and Ku70 (essential enzymes for DNA repair and replication), along with MiR-155 (an oncogene) in U251 cells upon treatment with either DOX-EDT-IONPs or Sali-PEI-PEG-IONPs. Thereafter, the permeability and anti-cancer effect of the drug-loaded IONPs were examined in an *in vitro* BBB-GBM co-culture model. The DOX-EDT-IONPs showed a permeability of  $5.2\pm 0.4\%$  across the MDCK-MDR monolayer over 4 hours that was significantly enhanced to  $8.5\pm 0.36\%$  using a cyclic ADT peptide as a transient disruption agent of the cell monolayer in combination with an external magnetic field. It is noteworthy to mention that surveying the literature in a 10-year period reveals that only 0.7% (median) of the administered nanoparticle dose is found to be delivered to a solid tumour in pre-clinical studies [4]. This suggests that this combinational approach of using magnetic convective diffusion of IONPs and transient disruption of the BBB can significantly enhance the efficacy of drug delivery to brain tumors. Furthermore, using DOX-EDT-IONPs, the permeability of DOX across the MDCK-MDR monolayer was augmented over 2-fold and provided significantly higher anti-cancer effect than free DOX in GBM cells (cell viability:  $66\pm 3.3\%$  and  $45\pm 3.7\%$  for cells treated with free DOX and DOX-EDT-IONPs, respectively) in the presence of a magnetic field

and ADTC5. On the other hand, Sali-PEG-PEI-IONPs showed a limited permeability of  $1.0 \pm 0.1\%$  across the bEnd.3 monolayers that was significantly enhanced to  $3.2 \pm 0.1\%$  using an external magnetic field and a hyperosmotic mannitol solution for transient disruption of the bEnd.3 monolayer. Correspondingly, using Sali-PEG-PEI-IONPs concomitant with administration of an external magnetic field and mannitol decreased GBM cell viability more effectively than that of free Salinomycin (cell viability: 60% and 38% for cells treated with free Salinomycin and Sali-PEG-PEI-IONPs, respectively). In a comparative study, the DOX-EDT-IONPs were found to be superior to the Sali-PEG-PEI-IONPs in terms of nanoparticle coating stability in biological media, anti-cancer effect against human GBM cells, and diffusion across the BBB model.

Generally, utilizing magnetic IONPs as a delivery system of chemotherapeutics in the presence of an external magnetic field not only can enhance nanoparticles' permeability across the BBB and augments their accumulation within the brain, but also can potentially draw the drug-loaded IONPs to the tumor target site, by which the systemic drug exposure and toxicity are reduced. In addition, transient enhanced permeability of the BBB using either hyperosmotic mannitol or cadherin peptide was found an effective approach to enhance the diffusion of the drug-loaded IONPs across the BBB model and potentially increase their accumulation within the brain. Herein, we reported that using ADTC5 shows the advantage of not causing an extensive change in permeability of large molecules compared to that of mannitol, as evidenced by the IRDye permeability ( $2.7 \pm 0.4\%$  and  $3.1 \pm 0.3\%$  without and with ADTC5, respectively, compared to  $15.6 \pm 0.6\%$  with mannitol (supplementary materials: Fig. S 2.2). across the MDCK-MDR monolayer in the BBB-GBM co-culture model). Therefore, using this peptide is expected to enable the BBB to stay relatively intact to large macromolecules and correspondingly diminish the risk

neurological toxicity [5], while facilitating the magnetic enhanced convective diffusion of the IONPs across the BBB in the presence of an external magnetic field.

In the second scenario, local drug delivery systems were utilized to bypass the BBB and provide a sustained release of a chemotherapeutic at the brain tumor site, by which the systemic exposure to the drug is diminished. Among the two common thermosensitive hydrogels examined, Pluronic F127 was preferred to PLGA-PEG-PLGA due to the superior gradual release profile of the payload and superior biocompatibility on various cell lines. Therefore, the Pluronic-Salinomycin was employed as an injectable thermosensitive local drug delivery system. The Pluronic-Salinomycin released 100% of the encapsulated Salinomycin over a week that was consistent with the Pluronic degradation rate *in vitro*. The Pluronic-Salinomycin was also found effective in inhibiting GBM cell proliferation, inducing apoptosis and generating intracellular ROS. In this context, Pluronic-Salinomycin significantly decreased GBM cell viability over 90% within 48 h compared to that of free Salinomycin (ca. 50%). Furthermore, Pluronic-Salinomycin could upregulate Caspase-3, as well as tumor suppressors Rb1, Rb2 and Bax as the suggested mechanisms involved in apoptosis induction in GBM cells. Animal studies in subcutaneous U251 xenografted nude mice also revealed that Pluronic-Salinomycin reduced the tumor size compared to the PBS and free Salinomycin-treated mice ( $V/V_0$ : 4.7, 3.5, and 1.8 for mice received either PBS, free Salinomycin or Pluronic-Salinomycin, respectively at day 11 post-treatment). The superior anti-tumor activity of the Pluronic-Salinomycin could be attributed to the sustained release of Salinomycin from the hydrogel at the tumor site, while preventing the drug from enzymatic degradation and enhancing its bioavailability. Therefore, the results suggested a potential application of Pluronic-Salinomycin as an injectable drug delivery system for local chemotherapy of brain tumors, while bypassing the BBB, providing a sustained release and a

therapeutic concentration of Salinomycin at the tumor site, and synergistically enhancing the Salinomycin's anti-cancer effects. Since the developed Pluronic-Salinomycin can be less invasively re-administered on demand, it can potentially be a better substitution for the FDA-approved Gliadel<sup>®</sup> wafers, which are implanted at the brain tumor cavity upon surgical resection.

As another local drug delivery system of Salinomycin, electrospun nanofibers (diameter:  $170\pm 57$  nm) encapsulating Salinomycin (NFs-Salinomycin) were fabricated in this project, as reported previously elsewhere [6]. The NFs-Salinomycin have the potential to be recruited as an implantable drug delivery system in the brain cavity after surgical resection of the tumor while providing a sustained release of Salinomycin at the target site. The NFs-Salinomycin released Salinomycin over 2 weeks *in vitro*, and showed a significantly higher anti-tumor effect than that of free Salinomycin in GBM cells by further decreasing cell viability and inducing intracellular ROS. The superior anti-tumor effect of NFs-Salinomycin was attributed to the gradual release of the drug from the nanofibers over the treatment period. The developed NFs-Salinomycin, which can be implanted at the brain tumor cavity, is potentially a substitution for the FDA-approved Gliadel<sup>®</sup> wafers with a more sustained release of the chemotherapeutic.

In summary, in this set of projects, two magnetic IONP-based formulations (i.e. DOX-EDT-IONPs and Sali-PEI-PEG-IONPs) were developed to potentially deliver Doxorubicin, and Salinomycin into the brain, while overcoming the limitations of the BBB permeability and providing a magnetic site-specific targeting. By the magnetic site-specific targeting, the drug-loaded IONPs can be drawn to the target site in the presence of an external magnetic field that reduces the systemic drug exposure and side effect. Moreover, the magnetic site-specific targeting in combination with the transient enhanced permeability of the BBB (using either mannitol or cadherin peptide) was found to be effective to augment the penetration of the drug-loaded IONPs

across the BBB and enhance the anti-cancer effect of the payload chemotherapeutics compared to the free drug *in vitro*.

Moreover, two local drug delivery systems (i.e. Pluronic-Salinomycin and NFs-Salinomycin) providing a sustained release of Salinomycin were developed to bypass the BBB and provide therapeutic doses of the drug at the tumor cavity or the tumor site within the brain. Similarly, by the local drug delivery approach, the systemic exposure to the drug and the systemic side effect can be efficiently diminished. Although subcutaneous tumor models have been commonly used to assess local drug delivery systems to provide a proof-of-concept for their final applications, they do not necessarily resemble the brain tumor microenvironment including high interstitial pressure within the brain.

Taken together, subsequent intracranial tumor studies of the developed systems will be beneficial to prove the efficacy of these formulations *in vivo*. Generally, it is speculated that the developed DOX-EDT-IONPs in combination with magnetic enhanced-convective diffusion and transient disruption of the BBB can overcome the limited permeability of the BBB and provides therapeutic concentrations of DOX within the brain through either paracellular diffusion of the DOX-EDT-IONPs across the BBB or their endocytosis by the endothelial cells. Moreover, the rapid release of DOX (within an hour) from the DOX-EDT-IONPs that magnetically has been drawn to the target site, can increase the chance of DOX entering the brain through the transiently open tight junctions of the BBB. Therefore, the DOX-EDT-IONPs in juxtaposition with the developed combinational approach can potentially enable DOX to be considered as a candidate in multi-agent chemotherapy regimen of GBM. Moreover, it is envisaged that Pluronic-Salinomycin can provide therapeutic concentrations of Salinomycin within the brain as an adjuvant therapy in GBM with minimal systemic distribution and toxicity. This formulation can be re-administered

locally on demand, which potentially makes it be a better substitution for the FDA-approved Gliadel<sup>®</sup> wafers.

Finally, since rodents do not necessarily mimic humans with respect to tumor's growth rate, size relative to body mass, and microenvironment [7,8], it is also suggested that subsequent pilot studies are required to appraise the efficacy of the developed systems in GBM patients.

## 5.2. Future Directions

Since the surface coating of IONPs can be degraded over time in biological media, this may lead to aggregation and precipitation of the nanoparticles in the bloodstream. This fact is often considered as a hurdle in the clinical applications of IONPs. In order to address this shortcoming, both IONPs and therapeutic agents can be encapsulated within liposomes, polymeric or lipid nanoparticles, serving as magnetic responsive nanocarriers for the therapeutic agents [9-11]. This strategy not only enhances encapsulation efficiency for a wide range of molecules within the nanoparticles, but also can ameliorate the IONP stability in the bloodstream [12]. Moreover, loading IONPs into liposomes, polymeric or lipid nanoparticles can protect the therapeutic agents from inactivation and degradation while offering well-defined *in vivo* behavior, independent of size or surface characteristics of IONPs [13,14]. Similar to PEGylated IONPs, lipid-anchored PEG stabilizes liposomes or lipid nanoparticles, and prevents them from being rapidly recognized and cleared by the MPS [15]. Additionally, the surface of the liposomes or lipid nanoparticles can be decorated with various ligands capable of binding to the receptors overexpressed by cancer cells or angiogenic endothelial cells, thus enhancing their cellular uptake and tumor internalization via the receptor-mediated endocytosis. Last but not least, incorporation of magnetic IONPs into

liposomes, polymeric or lipid nanoparticles enables controlled release of payload that is triggered with an alternating magnetic field (AMF) [16].

Having considered that, our lab is currently investigating encapsulation of the EDT-IONPs within various lipid-based structures to find optimum formulations. This formulation needs to meet the following criteria: (i) high encapsulation efficiency of various chemotherapeutics (including Doxorubicin, and Salinomycin) to show synergistic anti-tumor effect. In this context, the chemotherapeutics are encapsulated within the lipid nanoparticles regardless of surface coating of IONPs, while being protected from inactivation and degradation during blood circulation. (ii) high encapsulation efficiency of EDT-IONPs to provide magnetic-responsive lipid nanoparticles; (iii) surface decoration of the lipid nanoparticles with various ligands (like EGFRvIIIAb, binding to EGFRvIII on GBM cells [17,18], and Angiopep-2, recognizing low density lipoprotein-related protein 1 (LRP-1) expressed on the brain capillary endothelial cells [19]). By targeting both angiogenic endothelial and GBM cells, the cellular uptake and tumor internalization of the lipid nanoparticles are augmented via receptor-mediated endocytosis.

This formulation not only overcomes the aggregation problem of IONPs in the biological media, but also can potentially provide a controlled site-specific drug release upon heating the IONP-based lipids using an alternating magnetic field. Moreover, the developed approach of using cadherin peptide in combination with an external magnetic field in this study, is expected to enhance the penetration of IONP-based lipid nanoparticles across the BBB. Pursuant to successful *in vitro* studies, these IONP-based lipid nanoparticles will be evaluated *in vivo* in intracranial GBM tumor-bearing mice to evaluate their pharmacokinetic and anti-cancer efficacy.

### 5.3. References

- 1 Villodre, E.S. et al. (2018) Low Dose of Doxorubicin Potentiates the Effect of Temozolomide in Glioblastoma Cells. *Molecular neurobiology* 55 (5), 4185-4194
- 2 Caraglia, M. et al. (2006) Phase II study of temozolomide plus pegylated liposomal doxorubicin in the treatment of brain metastases from solid tumours. *Cancer chemotherapy and pharmacology* 57 (1), 34-39
- 3 Qin, L.-s. et al. (2015) ROS-p53-cyclophilin-D signaling mediates salinomycin-induced glioma cell necrosis. *Journal of Experimental & Clinical Cancer Research* 34 (1), 57
- 4 Wilhelm, S. et al. (2016) Analysis of nanoparticle delivery to tumours. *Nature reviews materials* 1 (5), 16014
- 5 On, N.H. et al. (2014) Modulation of blood–brain barrier permeability in mice using synthetic E-cadherin peptide. *Molecular pharmaceutics* 11 (3), 974-981
- 6 Norouzi, M. et al. (2018) Salinomycin-loaded Nanofibers for Glioblastoma Therapy. *Scientific reports* 8 (1), 9377
- 7 Danhier, F. (2016) To exploit the tumor microenvironment: Since the EPR effect fails in the clinic, what is the future of nanomedicine? *Journal of Controlled Release* 244, 108-121
- 8 Wolfram, J. and Ferrari, M. (2019) Clinical cancer nanomedicine. *Nano Today*
- 9 Joniec, A. et al. (2016) Magnetoliposomes as potential carriers of doxorubicin to tumours. *Chemistry—A European Journal* 22 (49), 17715-17724
- 10 German, S. et al. (2015) Liposomes loaded with hydrophilic magnetite nanoparticles: preparation and application as contrast agents for magnetic resonance imaging. *Colloids and Surfaces B: Biointerfaces* 135, 109-115
- 11 Ying, X.-Y. et al. (2011) Magnetic lipid nanoparticles loading doxorubicin for intracellular delivery: Preparation and characteristics. *Journal of Magnetism and Magnetic Materials* 323 (8), 1088-1093
- 12 Rostami, E. et al. (2014) Drug targeting using solid lipid nanoparticles. *Chemistry and physics of lipids* 181, 56-61
- 13 Kulkarni, J.A. et al. (2017) Rapid synthesis of lipid nanoparticles containing hydrophobic inorganic nanoparticles. *Nanoscale* 9 (36), 13600-13609
- 14 Allen, T.M. and Cullis, P.R. (2013) Liposomal drug delivery systems: from concept to clinical applications. *Advanced drug delivery reviews* 65 (1), 36-48
- 15 Frascione, D. et al. (2012) Ultrasmall superparamagnetic iron oxide (USPIO)-based liposomes as magnetic resonance imaging probes. *International journal of nanomedicine* 7, 2349
- 16 Amstad, E. et al. (2011) Triggered release from liposomes through magnetic actuation of iron oxide nanoparticle containing membranes. *Nano letters* 11 (4), 1664-1670
- 17 Bouras, A. et al. (2015) Radiosensitivity enhancement of radioresistant glioblastoma by epidermal growth factor receptor antibody-conjugated iron-oxide nanoparticles. *Journal of neuro-oncology* 124 (1), 13-22
- 18 Hadjipanayis, C.G. et al. (2010) EGFRvIII antibody-conjugated iron oxide nanoparticles for magnetic resonance imaging-guided convection-enhanced delivery and targeted therapy of glioblastoma. *Cancer research*, 0008-5472. CAN-0010-1022
- 19 Chen, G.-J. et al. (2014) Angiopep-pluronic F127-conjugated superparamagnetic iron oxide nanoparticles as nanotheranostic agents for BBB targeting. *Journal of Materials Chemistry B* 2 (34), 5666-5675

